Smart Construction Work-Zone Safety with V2I Passive Material Sensing

Apidej Sakulneya
Jeffery Roesler

DISCLAIMER

Suggested APA Format Citation:

Sakulneya, A., & Roesler, J. (2024). *Smart construction work-zone safety with V2I passive material sensing* (Report No. ICT-24-027). Illinois Center for Transportation. https://doi.org/10.36501/0197-9191/24-027

Contacts

For more information:

Jeffery R. Roesler
University of Illinois Urbana-Champaign
2129E Newmark Civil Engineering Bldg
jroesler@illinois.edu
https://ict.illinois.edu

CCAT
University of Michigan Transportation Research Institute
2901 Baxter Road
Ann Arbor, MI 48152
(734) 763-2498
www.ccat.umtri.umich.edu

1. Report No. ICT-24-027	2. Government Accession No. N/A	3. Recipient's Catalog No. N/A
4. Title and Subtitle Smart Construction Work-Zone Safety with V2I Passive Material Sensing		5. Report Date December 2024
		6. Performing Organization Code N/A
7. Authors Apidej Sakulneya (https://orcid.org/0000-0002-0482-0861) and Jeffery Roesler (https://orcid.org/0000-0001-6194-269X)		8. Performing Organization Report No. ICT-24-027 UILU-ENG-2024-2027
9. Performing Organization Name and Address Illinois Center for Transportation Department of Civil and Environmental Engineering University of Illinois Urbana-Champaign 205 North Mathews Avenue, MC-250 Urbana, IL 61801		10. Work Unit No. N/A
		11. Contract or Grant No. Grant No. 69A3552348301
12. Sponsoring Agency Name and Address Center for Connected and Automated Transportation University of Michigan Transportation Research Institute 2901 Baxter Road Ann Arbor, MI 48152		13. Type of Report and Period Covered Final Report
		14. Sponsoring Agency Code

15. Supplementary Notes

16. Abstract

This study explored new vehicle to infrastructure (V2I) technology in construction work zones (CWZ), where speeding, unsafe driving behaviors, and drivers' failure to obey traffic signs contribute significantly to elevated accident rates and fatalities. The objective of this research to advance CWZ safety by evaluating the potential of 3-axis magnetometers attached to a moving cart and traversing over a pavement-assisted passive sensing system can improve vehicle lateral positioning and warning in CWZ. Secondly, to develop a process to implement a programmable ferromagnetic oxide material for roadway coatings to interface with vehicles containing magnetometers on a field site. The research testing used a custom-built cart equipped with multiple 3-axis magnetometer to detect EM signals from invisible markings composed of 10% and 20% CrO_2, that were created to alert for speed, lane merges, and lane-keeping. The invisible marking strips were oriented and positioned in various ways to test the repeatability and ability to reliable detect a signal and signature that could be interpreted with automated algorithm. The experimental test results were acquired in a parking and signal-processing technique was established that normalized the raw signals, removed background EM signals not related to the created EM signatures, filtered high- and low-frequency noise, and took the derivative of the EM flux density with respect to the number of points. The V2I signals in the Y and Z-axes occasionally failed to exceed the minimum threshold set for the experiments, but the X-axis signals consistently exceeded the minimum value of $\pm200nT$ throughout the testing. The minimum threshold signals were used to calculate the speed of the cart, indicate a lane merge, and determine the lateral lane position of the cart. The detected speed signals closely correlated with the GPS speed measurements on the cart as well as provided accurate cart positioning and maneuvering actions. This pilot study demonstrated the potential of V2I communication specifically EM pavement signatures to enhance CWZ safety and provide detectable and actionable feedback to the vehicle.

17. Key Words Construction Work-Zone Safety, Smart-Work-Zone Technology, Pavement-Assisted Passive Sensing, Invisible Marking	18. Distribution Statement No restrictions. This document is available through the National Technical Information Service, Springfield, VA 22161.		
19. Security Classif. (of this report) Unclassified	20. Security Classif. (of this page) Unclassified	21. No. of Pages 47 + appendices	22. Price N/A

Form DOT F 1700.7 (8-72)   **Reproduction of completed page authorized**

ACKNOWLEDGMENT, DISCLAIMER, MANUFACTURERS' NAMES

EXECUTIVE SUMMARY

This report investigated the application of invisible markings arranged in detectable patterns to enhance construction work zone (CWZ) safety. Past research has shown that in-vehicle audio/visual warnings to drivers can potentially alert drivers to the beginning of the CWZ, to reduce speeds, and to produce sooner merge actions. The proposed electromagnetic (EM) markings in CWZ could communicate information to advanced driver-assistance system (ADAS)-equipped vehicles to slow down, merge, or exit. The first research objective was to evaluate the implementation of 3-axis magnetometers on pavement-assisted passive sensing systems for improving safe vehicle movements through CWZs. Second, the research study explored the development of programmable roadway coatings that can be used to provide speed and maneuvering information to ADAS-equipped vehicles.

The initial experimental phase evaluated the implementation of 3-axis fluxgate magnetometers on pavement-assisted passive sensing using ferromagnetic oxide materials (CrO_2) embedded into epoxy-based pavement markings. The experiment used a cart (instead of a vehicle) equipped with 3-axis magnetometers to detect and process EM signals from these markings. The chromium dioxide content varied from 10% to 20% by weight. Test results demonstrated that as the CrO_2 content increased, the EM signals across all three dimensions (X, Y, and Z axes) were more distinguishable for the proposed speed warnings, lane merge alerts, and lane-keeping assistance. Furthermore, the signal output varied based on the distance between the EM specimen and sensor. The x-axis sensor (vertical direction) produced the strongest overall magnetic field signals, followed by the z-direction (forward-backward direction). The y-axis sensor (lateral direction) had the lowest signal strength across all specimen layouts and orientations.

The second phase of the research validated the system's effectiveness in an extended test section with eight EM strips. Each strip contained 20% CrO_2 by weight, with a coating size of 6 inches in width and 28 inches in length. These strips were set up on the pavement surface to simulate CWZ warning applications, including speed warnings and vehicle maneuvering instructions. After the raw sensor signals were processed through several steps—including normalizing signals to their initial values, subtracting background magnetic flux, and applying high- and low-frequency filtering—the processed signals confirmed that the observed EM pavement signatures accurately corresponded to the intended setup. Not only did the speed predictions closely align with GPS data, but lane merge suggestions and cart positioning also accurately matched the intended results.

This pilot study validated the effectiveness of EM signature coated on pavement surface for application to construction work zone safety. The experimental results suggested that this passive material technology can provide valuable feedback for vehicle control systems, improve traffic flow, and reduce congestion. Future work should focus on refining the materials used for EM markings, integrating additional sensors, and validating system performance under various real-world vehicle conditions.

TABLE OF CONTENTS

LIST OF FIGURES

LIST OF TABLES

CHAPTER 1: INTRODUCTION

BACKGROUND

Construction work zones on roadways have been identified as high-risk areas because of the complex activities and traffic patterns associated with them. Previous studies have shown that the risk of accidents, injuries, and fatalities increased when drivers fail to adhere to posted speed limits and disregard warning signs and traffic control devices (Pigman & Agent, 1990; Raub et al., 2001; Bai & Li, 2006). Safety enhancements are continuously being updated to increase work zone safety for drivers and workers. For instance, rumble strips have been installed on road surfaces to vibrate vehicles, make noise, and alert drivers of an approaching work zone area. Warning signs have been placed strategically to provide instructions to drivers that guide them through the work zone safely (El-Rayes et al., 2014; Fontaine & Carlson, 2001). Furthermore, intelligent transportation systems, such as advance-warning mechanisms and real-time traffic updates, have been employed to further improve safety (Azimi et al., 2021; Darwesh et al., 2021; Li et al., 2018). Despite the development of various safety measures, the number of accidents and fatalities have trended upward in work zones over the past decade.

A previous CCAT project by Sakulneya and Roesler (2023) explored the potential of in-vehicle message warning systems to improve driver responses and safety when approaching work zones, particularly focusing on electromagnetic (EM) passive-sensing strips on the road and single-axis fluxgate magnetometer sensor arrays on the vehicle. An experimental plan was executed to test the responses of EM signatures from several EM passive-sensing strip configurations, including varying strip spacing and inclination angle. The laboratory proof-of-concept results demonstrated that the responses of these EM coded signatures exhibited potential for the establishment of a vehicle-to-infrastructure (V2I) system for work zones that includes an in-vehicle speed and lane-merge warning system. Each EM-strip configuration generated response signatures at different shapes, intensities, and offsets. For the initial study, the signal clarity of the passive-sensing signatures was primarily influenced by the spacing between the EM strips. Ultimately, the experimental findings demonstrated that different configurations of these strips could produce unique EM signatures that could be effectively deployed in a V2I system (Sakulneya & Roesler, 2023; Sakulneya & Roesler, 2024).

The purpose of this research project was to advance construction work-zone safety by implementing 3-axis fluxgate magnetometer sensors coupled with programmable ferromagnetic oxide materials on the surface of the road. The current research explored whether 3-axis fluxgate magnetometer sensors can provide additional detection and response benefits compared to single-axis magnetometers, offering enhanced vehicle control within work zones. Additionally, the integration of programmable ferromagnetic oxide material coatings aimed to create passive-sensing signatures on roadways, which can be used for real-time communication with ADAS-equipped vehicles. The purpose of the EM surface coating was to improve the practicality of passive sensing signatures compared to previous embedded methods (Dahal & Roesler, 2021; Dahal 2022; Roesler & Dahal 2024). The passive EM surface coating requires less installation time, is non-evasive to pavement materials, and is easily removable, which is essential for applications in CWZs.

Research Objectives

The objective of this research is to advance construction work-zone safety through integration of 3-axis magnetometers on a cart vehicle, develop and implement programmable ferromagnetic oxide materials for roadway coatings that form the passive sensing communication between vehicles and the roadway, and evaluate this V2I enhancement for determining the cart vehicle's speed, lateral position, and potential future maneuvers. The goal of adding a 3-axis versus a single-axis magnetometer is to assess forward or lateral detection of the approaching passive material sensor as extra positional or coded signature information. These two main efforts seek to improve driver safety through construction work zones by communicating and warning the driver directly, minimizing unplanned congestion, and maintaining the target traffic flow.

Overview of the Report

This report is structured into five chapters, with Chapter 1 providing background on the research problem, research objectives, and scope of work for the enhanced construction work-zone safety study. Chapter 2 demonstrates the potential for V2I communication through invisible passive-sensing signatures on the pavement. This chapter includes documentation of the coded signature algorithms for CWZ safety and the selection of materials for EM-passive sensing signatures coded on the pavement surface (i.e., invisible pavement marking). Chapter 3 details the development of the invisible pavement marking system, including materials, mixing process, procedures for encoding, and establishment of a 3-axis magnetometer array for a field pilot study. Chapter 4 defines the experimental setup and data collection for passive EM-sensing signatures for CWZ warning and safety enhancements as well as the signal-processing techniques. Finally, Chapter 5 synthesizes the experimental research findings into conclusions and recommendations for implementing pavement-assisted, passive-sensing technology to improve work-zone safety.

CHAPTER 2: V2I COMMUNICATION FOR ROAD SAFETY

PAVEMENT SIGNAGE CODED ON ROAD SURFACE

Pavement markings have been one of the most commonly used forms of signage coded on road surfaces to provide indirect messages to drivers for safe vehicle movements. These markings provide essential guidance for drivers by defining travel paths and conveying important information about roadway alignment, lane demarcations, passing zones, etc.

According to AASHTO (2008), a highway fatality occurred every 21 minutes because of lane departures, totaling over 25,000 deaths annually. In response, AASHTO developed a Strategic Highway Safety Plan targeted at reducing these fatalities. The plan's primary goal was to keep vehicles within their lanes and on the roadway. Research has shown that pavement markings can significantly reduce crashes under certain conditions, especially road run-off and head-on collisions that are prevalent on curves and at night. Enhanced or additional markings, like increased width or improved retroreflectivity, have been shown to reduce these types of crashes as well (Hall, 1987; Cottrell, 1987; Hughes et al, 1989).

Maintaining vehicle lane position remains a significant challenge, particularly under varying conditions and adverse weather. According to the National Highway Traffic Safety Administration (NHTSA, 2021), lane departures were still responsible for 50% of fatal crashes from 2015 to 2019, with this figure increasing to 75% during adverse weather. Lane departure incidents contribute to 1.13 million crashes annually, resulting in substantial fatalities, injuries, vehicle damage, and economic costs (Wang, 2019). These statistics highlight the potential need for advanced vehicle technologies such as lane-keeping to save thousands of lives and billions of dollars annually. Despite the reliance of autonomous vehicles (AVs) on GPS and cameras, or LiDAR for lane-keeping system, challenges persist when lane markings are obscured (Dahal & Roesler, 2022).

Passive pavement sensing technology, recently proposed by Roesler and Dahal (2022), offers a potential complementary solution. This technology involves creating passive EM signatures on the road, which can be detected by vehicle-mounted magnetometers. The EM material embedded on the pavement has been shown to successfully detect a vehicle's lateral positioning within the lane in normal conditions and even in adverse weather conditions such as snow (Dahal & Roesler, 2022).

In this study, passive pavement-assisted EM signature technology has been adapted for coating on road surfaces, functioning as pavement coded signage. The goal of integrating this technology with vehicle-to-infrastructure (V2I) strategies is not only to assist vehicle with lane keeping, but also to alert drivers and have drivers respond to real-time in-vehicle warnings about speed limits, merging instructions, and exits in construction work zones. The proposed EM coded signatures oriented on the pavement surface will be tested with 3-axis magnetometer arrays (past research only used 1-axis magnetometers), offering potentially more precise data on vehicle lateral position, vehicle trajectory, and speed from multiple magnetometer sensor axes. This information can be used to guide drivers safely through work zones, ensure compliance with speed limits, and assist with lane-merging instructions.

Construction Work Zone Safety Enhancement

Pavement-assisted passive sensing technologies represent a significant advancement in enhancing safety within construction work zones (CWZs). These technologies utilize EM signatures coded on the roadway to establish passive communication with vehicles with the goal of improving driver awareness and reducing accident risks.

The theoretical application for the single-axis sensor system completed by Sakulneya and Roesler (2023) involved an in-vehicle speed-warning system (Figures 1 and 2), where uniformly spaced EM strips interacted with vehicle-mounted magnetometer sensors. Controlled by the vehicle's electronic control unit (ECU), this system activates upon detecting EM signatures surpassing a predefined magnetic field strength threshold. It compares time intervals between EM peak responses against a universal time constant adjusted for the work-zone speed limit, alerting drivers through visual and audio cues to potential speed limit exceedances. Another previously explored application is the in-vehicle lane-merge warning system (Figure 3 and 4), which employed diagonal EM strips to facilitate lane changes effectively (Sakulneya & Roesler, 2023). Similar to the speed-warning system, the ECU triggers alerts based on EM intensity detections, providing real-time merging instructions (audio and visual) in the vehicle. These integrated systems enhance overall safety by promptly informing drivers about the vehicle's speed limit and imminent lane-merging requirement, which should minimize accidents and maintain the expected CWZ traffic flow.

To extend the previous work, a three-axis magnetometer system was employed to improve the reliability of EM signatures by incorporating algorithms to cross-check calculated actions across the different sensor axes (i.e., x-, y-, and z-axes). The theoretical explanation for the speed and lane-merge warning system of the 3-axis sensor system are illustrated in Figured 5 and 6, respectively. The addition of multiple axes of detection for one sensor provides redundant information to avoid the risk of erroneous maneuvers triggered by unexpected EM noise, which could occur on single-axis systems. By validating the acquired signals on orthogonal axes before issuing instructions to the vehicle control unit, the proposed system ensures more robust performance in diverse operational conditions.

Figure 1. Diagram. Proposed in-vehicle speed-warning system for smart construction work zones.

Processing of the Vehicle's Electronic Control Unit (ECU)

Start

Read EM responses as a function of time period

The system activates when the three EM sensors discover the change in electromagnetic intensity greater than 200 nT within 1 second.

Obtain ΔTsi (time period of sensor (s) between peak response (i) and its preceding peak, which is equivalent to $\frac{X}{V_c}$)

If $\Delta Tsi > \Delta Tlimit$

Yes — Audio and visual in-vehicle suggested maximum allowable speed for work zone area ($Vs = X/\Delta Tlimit$) on vehicle's dashboard

No — Audio and visual In-vehicle speed reduction alert.

$$\Delta \; Tlimit = \frac{X}{V_S}$$

Where,
ΔT_{limit} = Universal constant time period between the strips spacing
X = Strip spacing (varies with suggested speed)
V_s = Suggested speed from the speed warning system

Figure 2. Diagram. Flowchart of the proposed in-vehicle speed-warning system for smart construction work zones (1-axis sensing system).

Work-Zone Advance-Warning Area

ECU

EM Sensors — Left Center Right

Responses

T_0 X T_1 X T_2 X T_3

Electromagnetic Intensity (I)

I, left
T_{l0} ΔT_1 ΔT_2 ΔT_3
Left EM Sensor T_{l1} T_{l2} T_{l3} Time

I, center
T_{c0} ΔT_1 ΔT_2 ΔT_3
Center EM Sensor T_{c1} T_{c2} T_{c3} Time

I, right
T_{r0} ΔT_1 ΔT_2 ΔT_3
Right EM Sensor T_{r1} T_{r2} T_{r3} Time

System activated
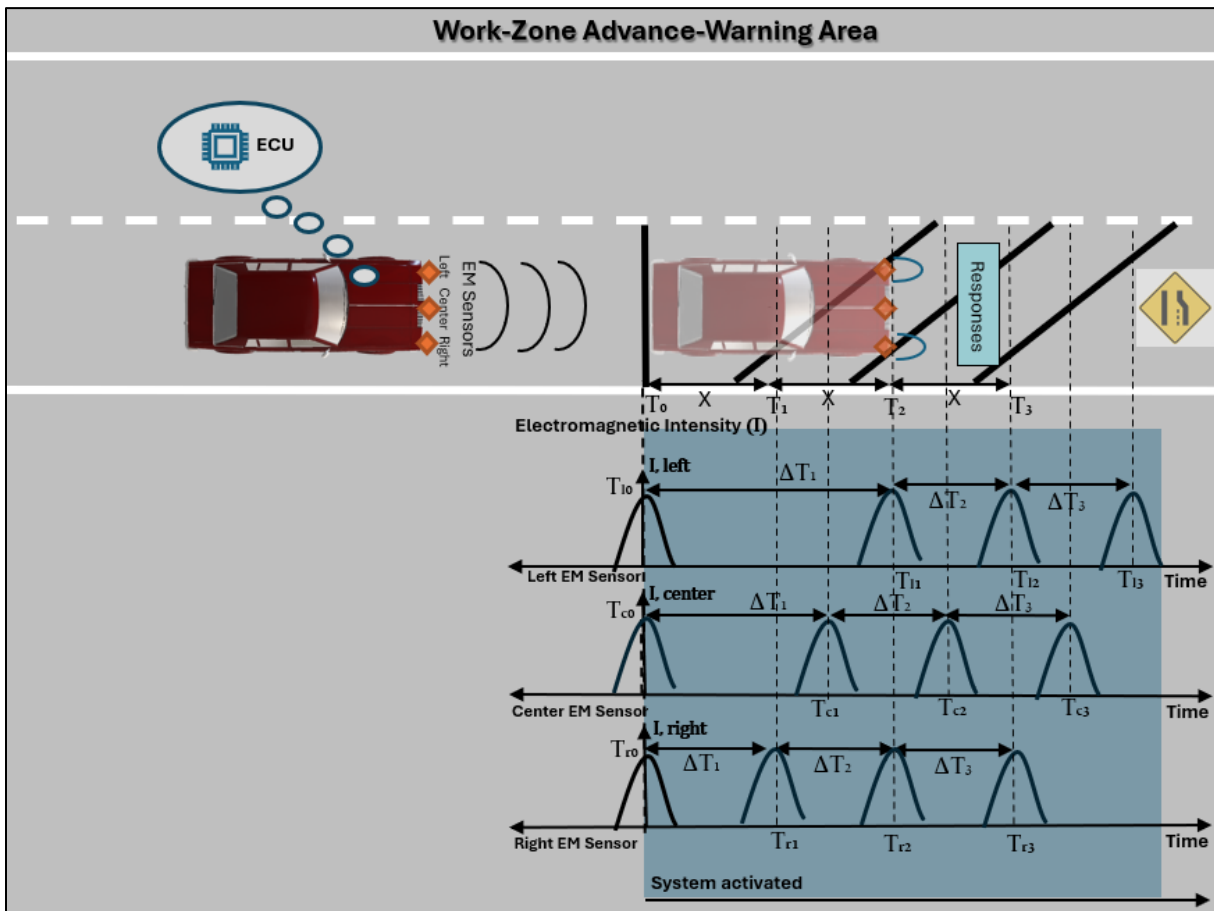
Figure 3. Diagram. Proposed lane-merge warning system for smart construction work zone.

Processing of the Vehicle's Electronic Control Unit (ECU)

Start

Read EM responses as a function of time period

System activate when changes in Ici, Ili, and Iri > 200 nT within 1 second

If
$\Sigma(\Delta Tci) < \Sigma(\Delta Tli)$ and
$\Sigma(\Delta Tci) > \Sigma(\Delta Tri)$

Yes → Audio and visual in-vehicle merge left alert on vehicle's dashboard

No → Audio and visual in-vehicle merge right alert on vehicle's dashboard
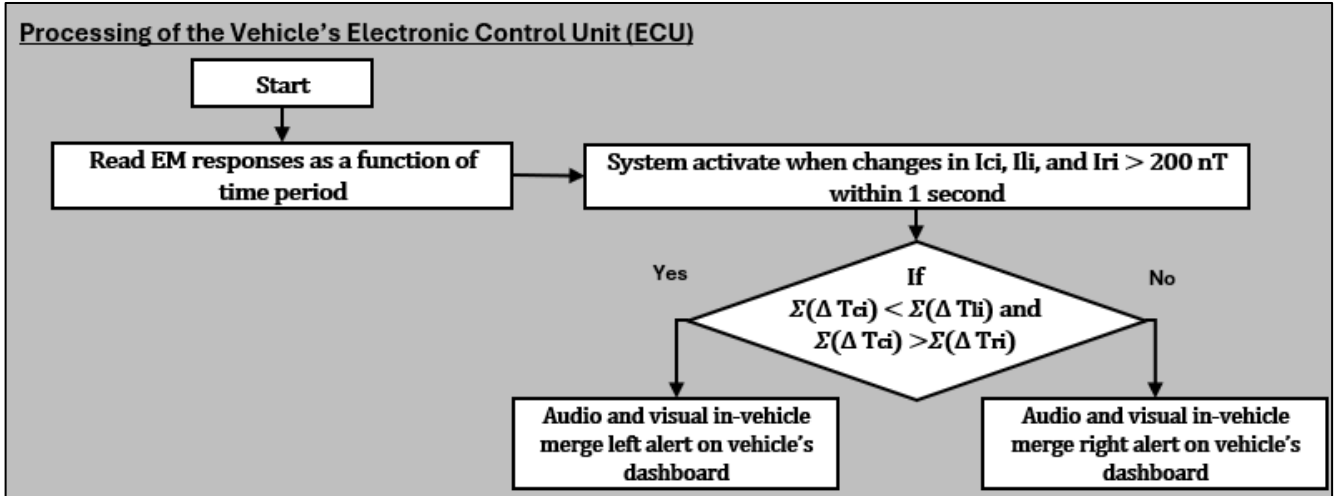
Figure 4. Diagram. Flowchart of the proposed lane-merge warning system for smart construction work zone (1-axis sensing system).

Processing of the Vehicle's Electronic Control Unit (ECU)

Start

Read EM responses from 3 axes as a function of time period

The system activates when the three EM sensors discover the changes in electromagnetic intensity at least in two axes greater than 200 nT within 1 second.

Obtain $\Delta Tsij$ (sensor # (s), time period between the peak (i) and its preceding peak of each axis (j), which is equivalent to $\frac{X}{V_C}$)

$\Delta Tlimit = \frac{X}{V_S}$

Where,
$\Delta Tlimit$ = Universal constant time period between the strips spacing
X = Strip spacing (varies with suggested speed)
V_s = Suggested speed from the speed warning system

If $\Delta Tsi(x) > \Delta Tlimit$

Yes → Audio and visual in-vehicle suggested maximum allowable speed for work zone area $(V_s = X/\Delta Tlimit)$ on vehicle's dashboard

No →

If
$|\Delta Tsi(x) - \Delta Tsi(z)| < 0.5X/V_S$
or
$|\Delta Tsi(x) - \Delta Tsi(y)| < 0.5X/V_S$

No →

Yes → Audio and visual in-vehicle speed reduction alerts on vehicle's dashboard

If
$\frac{\Delta Trij}{\Delta Tlij} \in (0.9, 1.1)$

No →

Yes → Do not alert

Figure 5. Diagram. Flowchart of the proposed speed warning system for smart construction work zone (3-axis sensor system).

Figure 6. Diagram. Flowchart of the proposed lane-merge warning system for smart construction work zone (3-axis sensor system).

Material for Pavement Signage

In general, the pavement surface has no unique or preferred electromagnetic propeties in any directions (Dahal, 2023). The addition of metallic constituents (e.g., iron powder, steel fibers, etc.) enhances the pavement's electric conductivity and magnetic permeability, altering its response to magnetic fields. This change is crucial as it allows for the induction of magnetization within the pavement material. According to the principles of magnetization (M), which is defined as the magnetic moment per unit volume, it depends on the magnetic flux density (B) and magnetic field intensity (H) where, μ_0 is the permeability of free space, equal to $4\pi \times 10^{-7}$ H/m. The relationship between M and H is influenced by the ferromagnetic properties of the material. The induced magnetic flux density (B) in the pavement material can be significantly increased by incorporating ferromagnetic materials with high magnetic permeability such as steel fibers or iron powder (μ_{EM}), compared to normal roadway construction materials (μ_{CM}). This difference ($\mu_{EM} \gg \mu_{CM}$) indicates a higher concentration of magnetic flux density in sections containing EM materials compared to the section without EM materials . Figure 7 illustrates a standard pavement section with uniform (low) magnetic properties influenced by the Earth's magnetic field. In contrast, sections enhanced with ferrous materials exhibit a concentrated magnetic flux pattern, distorting the near-surface magnetic field. This induced magnetization can be detected by magnetometers, with the magnetic field signal strength depending on factors such as magnetic material type, shape, volume, dosage, and distance of sensor to material. These modifications enable the creation of distinct electromagnetic signatures spatially on or near the pavement surface, enabling vehicle-to-infrastructure applications such as vehicle localization in lane and V2I communication like smart construction work zones.
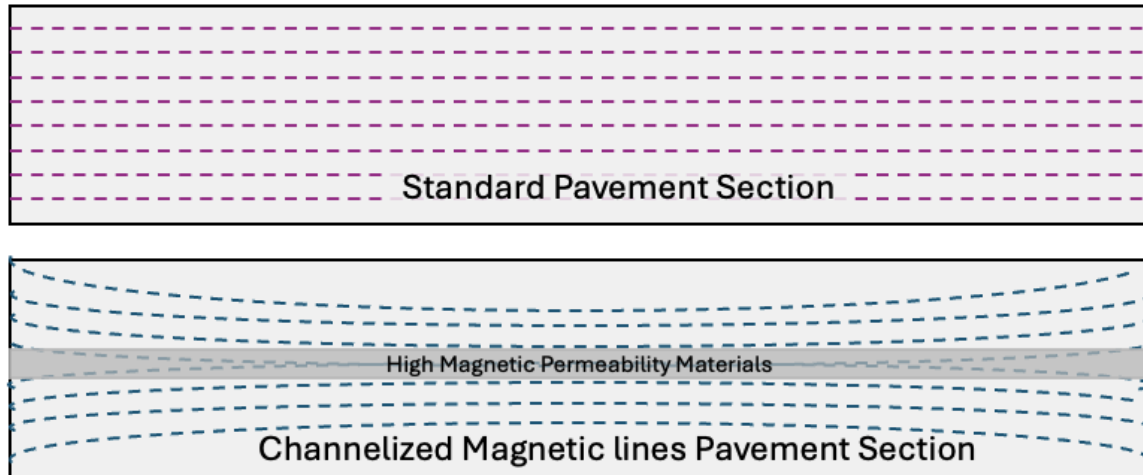
Figure 7. Diagram. Comparison of magnetic lines on a standard pavement section and a pavement section with channelized magnetic lines.

Material selection for coating applications requires specific properties, such as the ability to reorient magnetic polarity in the preferred direction. Chromium dioxide (CrO_2) possesses a low Curie temperature (Tc) of around 120°C, which is promising for generating codable magnetic fields in near pavement surface or surface coating applications. Tc denotes the threshold above which materials lose their permanent magnetic properties in the absence of an external magnetic field. When an external magnetic field is applied above Tc, the material's intrinsic magnetic moment, both in direction and strength, can be altered. As the temperature drops below Tc, this induced magnetism becomes permanently stamped as the material's intrinsic magnetic moment. This characteristic originally allowed magnetic patterns from a master tape, typically made of higher Tc magnetic materials, to be permanently transferred to blank recording tapes composed of γ-iron oxide or chromium dioxide when heated above their respective Tc and subsequently cooled. The Tc of CrO_2 that are embedded in existing paving materials ensures stability under normal roadway conditions (e.g., hot summer) and during the magnetic field creation process. For example, when applied as a powder on concrete surfaces and magnetized, CrO_2 generates a detectable magnetic signature, which can be erased by heating above its Tc of 120°C and then renewed again using an external magnetic field coupled with heating above a Tc of 120°C (Dahal 2022).

CHAPTER 3: INVISIBLE PAVEMENT MARKING FOR PASSIVE SENSING

This chapter develops a procedure to create EM surface markings with ferromagnetic oxides in a host material that can be applied as a coating. This development will be demonstrated and validated on a field pilot study aimed at assessing the process, material proportions, and implementation of a custom EM passive material formulation. This formulation combines CrO_2 with an epoxy mastic paint base and activator. Additionally, this part of the research involves a detection setup that incorporates a 3-axis magnetometer array for capturing and analyzing electromagnetic signatures in three orthogonal directions.

FERROMAGNETIC OXIDE MATERIAL

The EM material explored in this study was CrO_2 as depicted in Figure 8, for its high purity of 99.5% and particle size of less than 45 microns, This EM material was mixed with an epoxy mastic paint base designed to withstand temperatures up to 150°C. Two mixtures compositions (#1 and #2) were formulated (Table 1), where the percentages of epoxy base, epoxy hardener, and CrO_2 were adjusted with the volume fraction of the epoxy base and epoxy hardener fixed at 1 to 1 as recommended by the producer. The CrO_2 was varied between the two mixes to evaluate its effect on the signal response captured by the 3-axis magnetometer array.

Table 1. Mix Composition of Invisible Pavement Marking

Components	Mix #1 (% by wt./wt.)	Mix #2 (% by wt./wt.)
Epoxy Base	45%	40%
Epoxy Hardener	45%	40%
Chromium Dioxide (CrO_2)	10%	20%
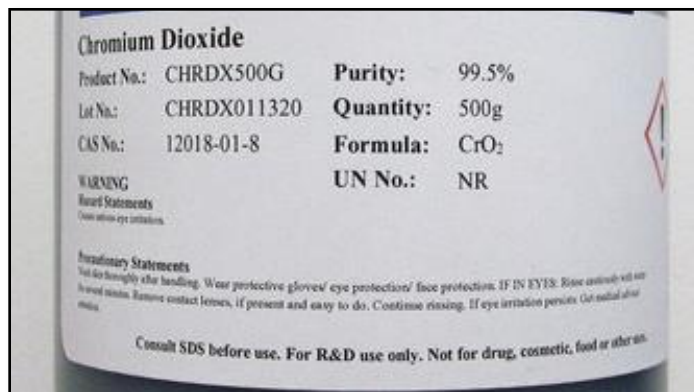
Figure 8. Photo. Chromium dioxide for invisible pavement marking mixture.

Mixing Procedure and Magnetization Steps for Invisible EM Pavement Markings

The weight of each material in Table 1 was batched and then the epoxy base and hardener were thoroughly mixed in a container using an electric paint mixer to homogenize the two components. CrO_2 powder was gradually added to the epoxy paint mixture. The mixing continued until the CrO_2 powder was fully dispersed and uniformly blended, achieving a consistent color throughout the mixture to ensure even coating and CrO_2 distribution on the pavement surface.

The CrO_2 containing pavement marking was applied to the surface of a concrete substrate using a 4-inch-wide paint brush. The next step was to establish the desired EM signature on the pavement surface through the magnetization process. The magnetization step introduced an external magnetic field after the invisible lane-marking coating had sufficiently cured. The magnetization setup is shown in Figure 9. Initially, a 2,500 W infrared heating lamp was used to heat the coated specimens, and an infrared laser thermometer was used to evaluate when the surface temperature exceeded 120°C. Permanent magnets were then positioned 6 inches apart (see Figure 9) at approximately 1 inch above the concrete surface, to align the magnetic field of the invisible pavement marking sample. After alignment of the sample's magnetic field, the specimen's temperature was cooled to below 60°C before removing the external magnets over the coated specimens to ensure that the new CrO_2 polarity orientation was fixed. Figure 10 presents the final concrete specimen coated with the invisible pavement marking after the magnetization process. For this test series, a green pigment was applied to distinguish the marking. Due to the black color of the CrO_2 powder, the specimens with a darker green hue represented the 20% CrO_2 mixture, while the lighter green specimens corresponded to the 10% CrO_2 mixture.
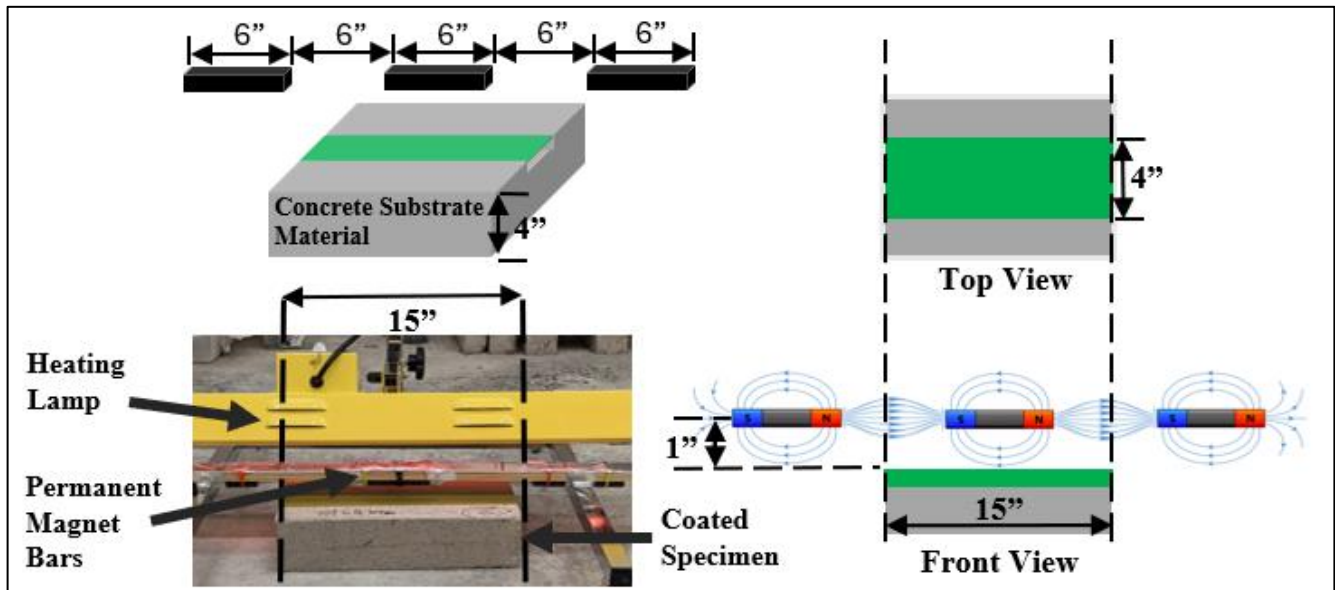
Figure 9. Diagram. Magnetization setup for invisible pavement marking.
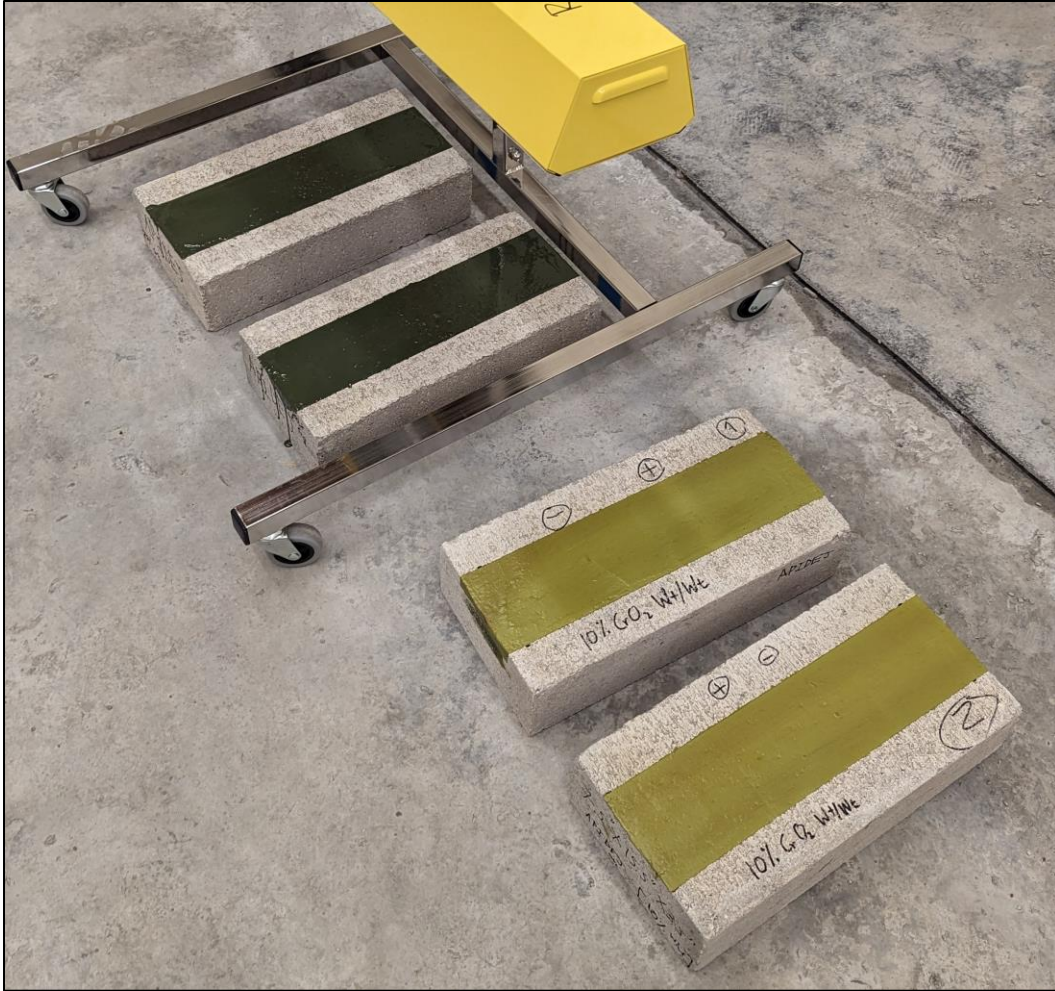
Figure 10. Photo. Final concrete specimens (10% and 20% CrO₂) with coated invisible pavement marking after magnetization.

3-AXIS MAGNETOMETER ARRAY SETUP

In order to simulate a vehicle with sensors that can detect the higher magnetic field surrounding the invisible lane markings, this study constructed a small cart equipped with an array of 3-axis magnetometer sensors, as shown in Figure 11. The cart features six 3-axis fluxgate magnetometers arranged in the lower row with a spacing of 6 inches and an upper row containing two additional 3-axis fluxgate magnetometers specifically designed to mitigate background noise in the test environment. The fluxgate magnetometer model used during this experiment was the Stefan Mayer FLC3-70, characterized by its measurement capability ranging from −200 μT to 200 μT with a maximum bandwidth of 1 kHz. Each 3-axis magnetometer independently detects variations in magnetic flux in the X, Y, and Z dimensions. In this study, the X-direction corresponds to the vertical axis relative to the vehicle's movement path, while the Z-direction represents the forward-moving axis direction, and the Y-direction indicates the lateral axis perpendicular to the vehicle movement. The magnetometer array setup is called a gradiometer, where the upper row records all background magnetic flux density components, including the Earth's magnetic field and nearby ferromagnetic

materials (steel, buried utilities, etc.) present around the testing location. By subtracting the upper row from the bottom row magnetic field signals, the sensor system effectively captures the intended engineered magnetic signature for the work zone instructions or vehicle lane positioning and guidance and the background noise is cancelled out or minimized.
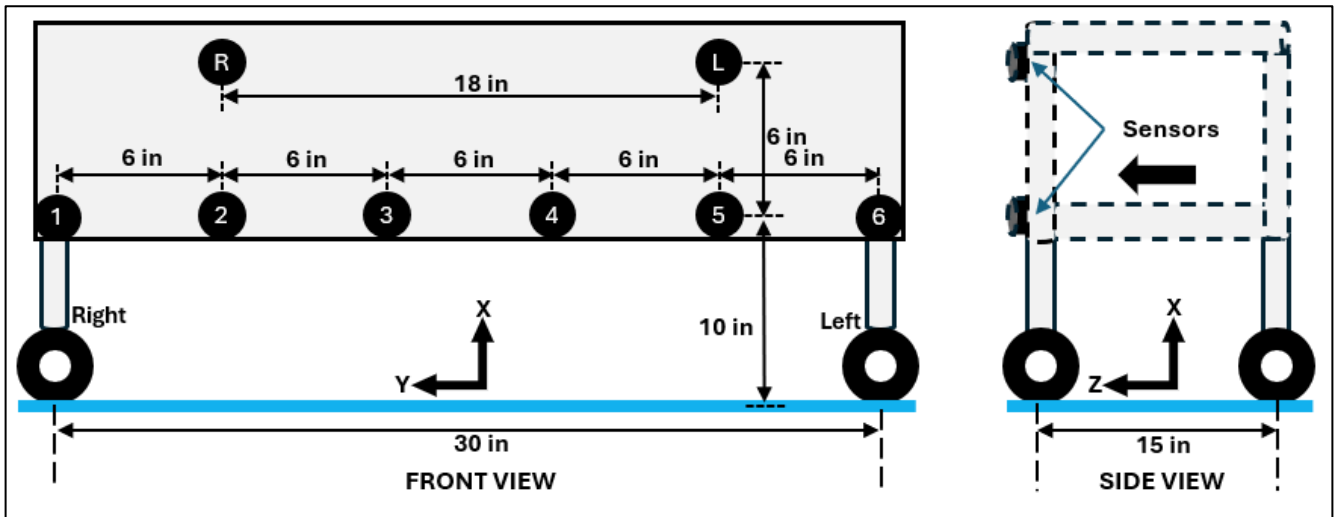
Figure 11. Diagram. Magnetometer sensor array setup oriented as gradiometer on a mobile cart.

EXPERIMENTAL SETUP FOR FIELD PILOT STUDY

The field pilot study conducted in a parking lot area encompassed a comprehensive range of experimental setups of the markings to test the invisible pavement markings and the 3-axis magnetometer. As illustrated in Figure 12, invisible pavement markings were placed in various orientations (transverse or longitudinal), offset from the centerline (right, left, and variable), and strength of magnetic field (commercial magnetic tape, 10% CrO_2, or 20% CrO_2). The transverse orientations of the invisible markings were spaced 9 feet and were analogous to a construction work zone application where a speed check or warning would be given to a vehicle. These test cases were conducted at different speed conditions, ranging from slow walking pace (<10 km/h), normal walking speed ($\approx$ 10 km/h), and running speed (> 10 km/h). Collectively, this experimental test factorial was designed to investigate the sensitivity of the signal responses generated by the EM materials in the coatings as well as a means for reading and interpreting the sensor responses to the magnetic field changes for near future implementation into a Level 4 autonomous vehicle that would alter the vehicle trajectory based on the sensor output.
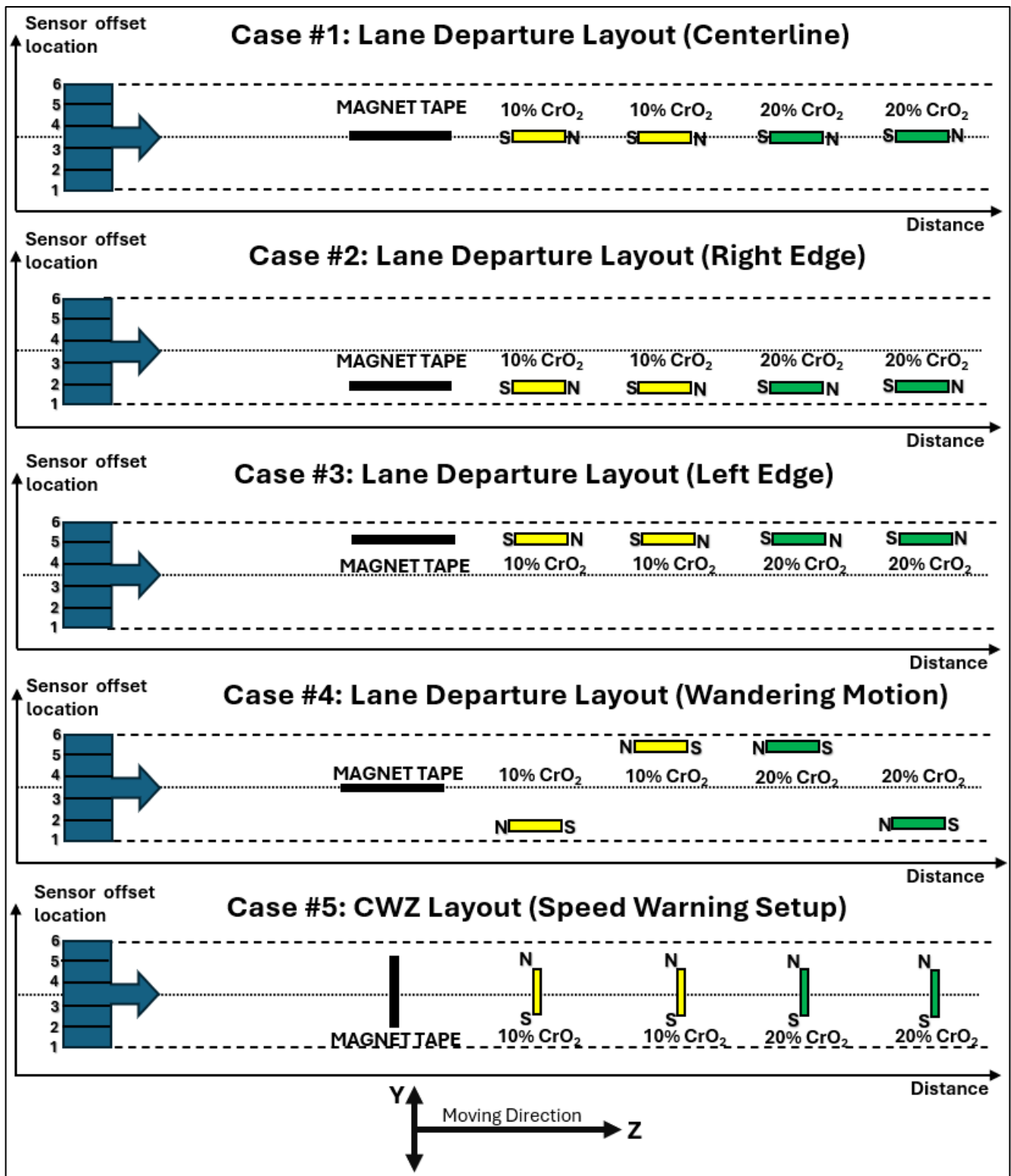
Figure 12. Diagram. Test cases for field pilot experiment in a university parking lot.

Field Pilot Experimental Results

Although the fluxgate magnetometer used in this experiment had a bandwidth capacity of up to 1,000 Hz, the data collection rate was set at 100 Hz, as this frequency was sufficient to capture the speeds utilized in the experiment. The raw output of each magnetometer was largely influenced by the Earth's magnetic field, ranging from 22,000 to 67,000 nT depending on the location and orientation of the specimens reading. To extract the distinguishable EM flux patterns from the EM signature strips, signal processing for both high- and low-frequency noise components was essential because of the significant background noise (earth's magnetic field, locally buried ferromagnetic materials, and other EMF noise affecting signal output). The signal-processing procedure involved several steps to refine the raw output data from the main sensors:

1. Each sensor's initial reading was zeroed at approximately t= 0 seconds by subtracting the initial data point (magnetic flux reading) from subsequent readings.

2. Background magnetic flux, comprising the Earth's magnetic field and nearby ferromagnetic materials, was minimized using a gradiometer setup where each bottom row sensor's data (e.g., sensor 1 to 6) was adjusted by subtracting the nearest top row sensor's data (e.g., sensors R or L in Figure 11).

3. High-frequency noise was reduced by using a 4-point moving average technique.

4. The effect of low-frequency noise was reduced by taking the derivative of the processed signal to achieve the rate of change of the EM flux density between consecutive data points collected ($\frac{dEM_i}{d_i} = \frac{(EM_{i+1} - EM_i)}{(i+1) - i}$). This processing step also allowed for determining more reliable the spacing between EM strips for speed or orientation calculations.

The signal responses, including those with Earth's magnetic field removed and fully processed responses under various moving speed conditions, are detailed in the appendices. One observation was that by increasing cart speed, there was increased low-frequency signal noise, which highlighted the need for effective filtering to distinguish the unique EM signatures. This chapter focuses on evaluating the magnitude of the final processed signal responses from the invisible markings spaced along the pilot sections. Detailed discussions on signal-processing techniques will follow in the subsequent chapter. The signal responses from five distinct cases are illustrated next.

Case #1: Lane Departure Layout (Centerline Travel)

Figure 13 to Figure 15 show the processed signal results of case #1 for the 3-axis magnetometer array under slow moving speed condition. The maximum signal was between sensors 3 and 4 (spaced 6 inches apart) in Figure 13. The shape of the signals was consistent for the four invisible marking specimens, but the magnitude level reflected the amount of CrO_2 (last two signals) or if the cart and one of sensors (#3) passed closely over the invisible marking specimen (see time 20 to 21 seconds). The magnetic tape at the beginning of the section was detected but generally below the acceptable threshold of 300 nT.
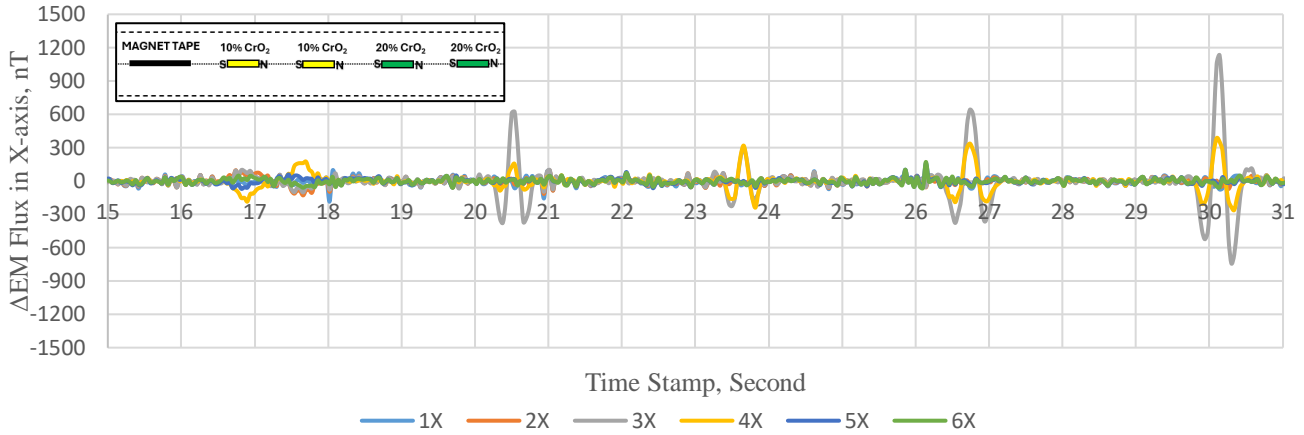
Figure 13. Graph. Processed ΔEM Flux in X-direction with time for Case #1.

In Figure 14, the y-axis magnetometer (lateral detection of magnetic field) had relatively low signal strength except for the 20% CrO_2 specimens. The specimen was between sensors 3Y and 4Y as the cart passed over it. The magnetic tape at the beginning of the section was detected but below the acceptable threshold of 300 nT for the y-axis sensors (3Y and 4Y). The absolute value of the peaks in the y-axis correspond to the times of the peaks of the x-axis sensors (Figure 13).
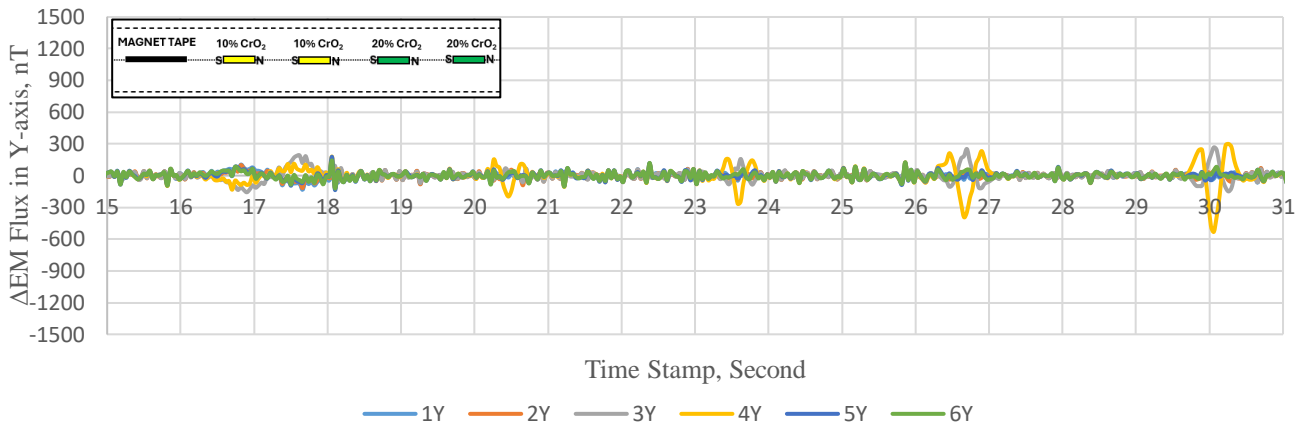
Figure 14. Graph. Processed ΔEM Flux in Y-direction with time for Case #1.

In Figure 15, the z-axis magnetometer (forward detection of magnetic field) had higher signal strength than the y-axis sensors but signal clarity for some specimens was not as good and repeatable as seen in the x-axis sensors. The highest signal came from the 20% CrO_2 specimens. Again, the activated sensors were 3Z and 4Z. The magnetic tape at the beginning of the section was not detectable even though there was a signal recorded at 18 seconds for sensor 5Z. The absolute value of the peaks in the y-axis correspond to the times of the peaks of the x-axis sensors. Even with filtering, the signal still has around ±100 nT of baseline noise.

Figure 15. Graph. Processed ΔEM Flux in Z-direction with time for Case #1.

Case #2: Lane Departure Layout (Right Edge)

Figure 16 to Figure 18 show the processed signal results of case #2 for the 3-axis magnetometer array under slow moving speed condition. The EM signatures were placed longitudinally along the right edge of the sensor array. As shown in Figure 16, the x-axis signals peaked predominantly at sensor 2, followed by sensor 1 for the four invisible marking specimens. The magnitude of the signals was strongly influenced by the CrO_2 content, with the last two signals (occurring between 24 to 25 seconds and 26.5 to 27.5 seconds) significantly surpassing the 10% CrO_2 content. Although the magnetic tape at the beginning of the section was detected, its ΔEM flux remained noticeably low. While the magnitude of the raw EM flux from the magnetic tape was generally higher than that of the invisible marking specimens, the EM flux change of the tape was more gradual. Consequently, the ΔEM of the invisible marking specimens was more prominent compared to that of the magnetic tape.
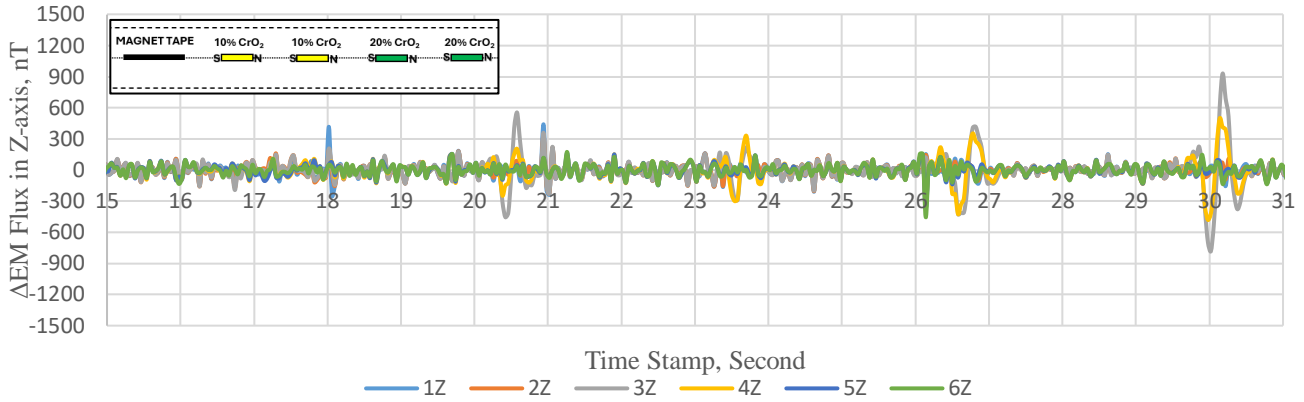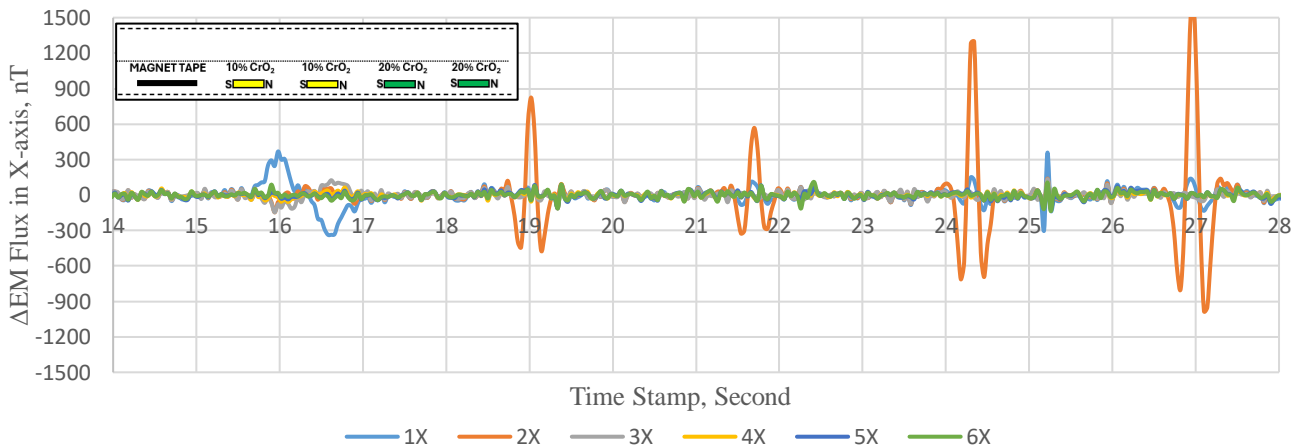

Figure 16. Graph. Processed ΔEM Flux in X-direction with time of Case #2.

In Figure 17, the y-axis magnetometer (lateral detection of the magnetic field) exhibited relatively low signal strength, with the 20% CrO_2 specimens producing the highest signal strength compared to the other specimens. The observable signals were predominantly detected by sensors 1, 2, and 3. This pattern can be attributed to the fact that these sensors were nearest to the offset specimens from

the centerline. When the cart, passed directly over the EM specimens, sensors 1 and 2 were more likely to detect the lateral flux generated by the specimens.

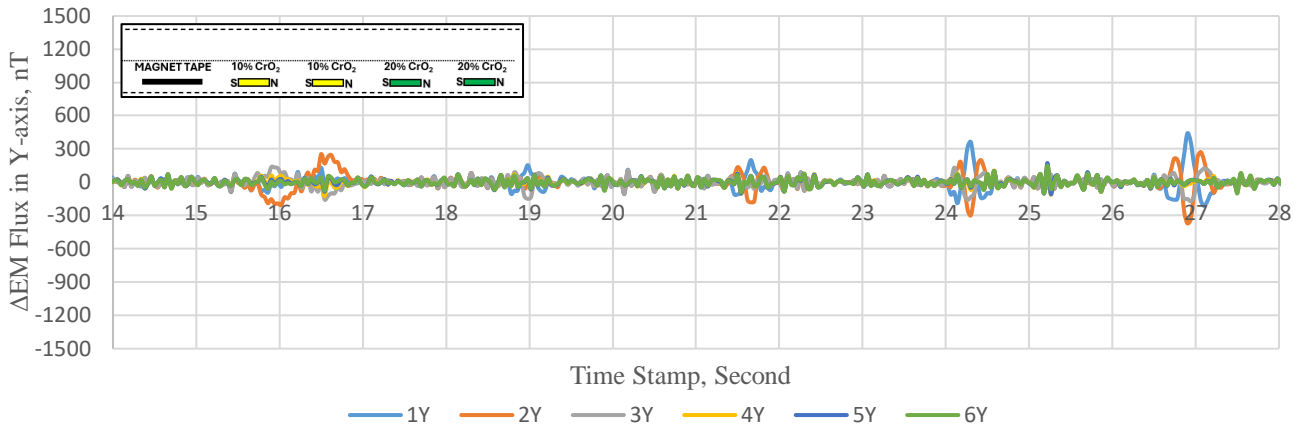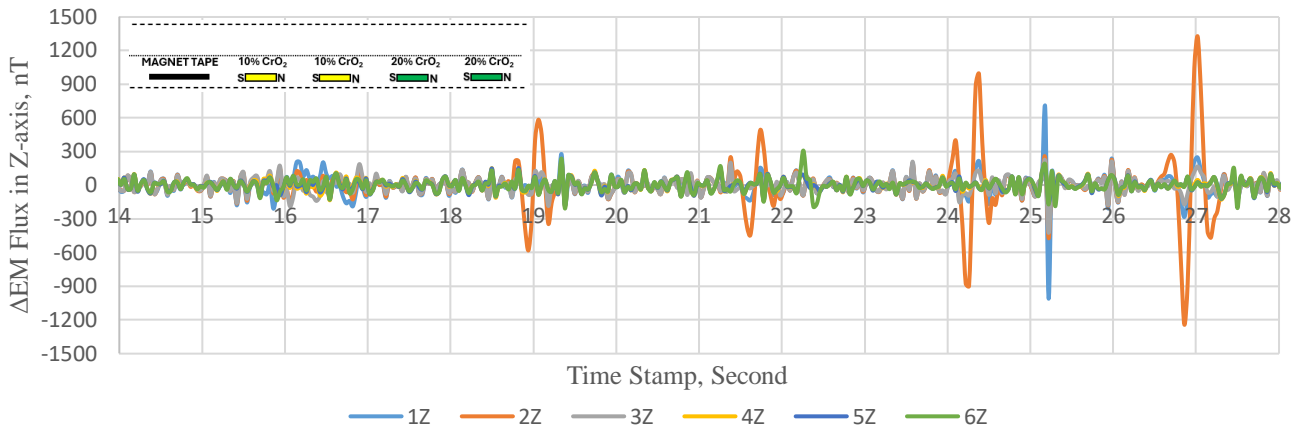**Figure 17. Graph. Processed ΔEM Flux in Y-direction with time of Case #2.**

In Figure 18, the z-axis magnetometer (forward detection of the magnetic field) exhibited higher signal strength compared to the y-axis sensors; however, the clarity of the magnetic tape signal was not as distinct, similar to the x-axis results. The highest signal was detected from the 20% CrO_2 specimens, with sensor 2 recording the strongest signal, which aligned well with the signals observed in the other axes. Unexpected ΔEM noise, approximately 300 nT in the x-axis and 900 nT in the z-axis, was observed at around 25.2 seconds on sensor 1. These anomalies could be attributed to interference from a strong magnetic source beneath the parking lot, such as an electrical cable.

Figure 18. Graph. Processed ΔEM Flux in Z-direction with time of Case #2.

Case #3: Lane Departure Layout (Left Edge)

Figure 19 to Figure 21 show the processed signal results of case #3 for the 3-axis magnetometer array under slow moving speed condition. The EM specimens were placed longitudinally along the left edge of the sensor array. In Figure 19, the x-axis magnetometer (vertical detection) shows that sensor 5 captured the highest signal strength, aligning with the placement of the EM specimens near the left

edge of the array. The 20% CrO_2 specimens displayed the strongest signals, particularly between 26.5 and 27 seconds. The magnetic tape at the beginning of the section was detected but exhibited lower ΔEM flux compared to the invisible marking specimens.
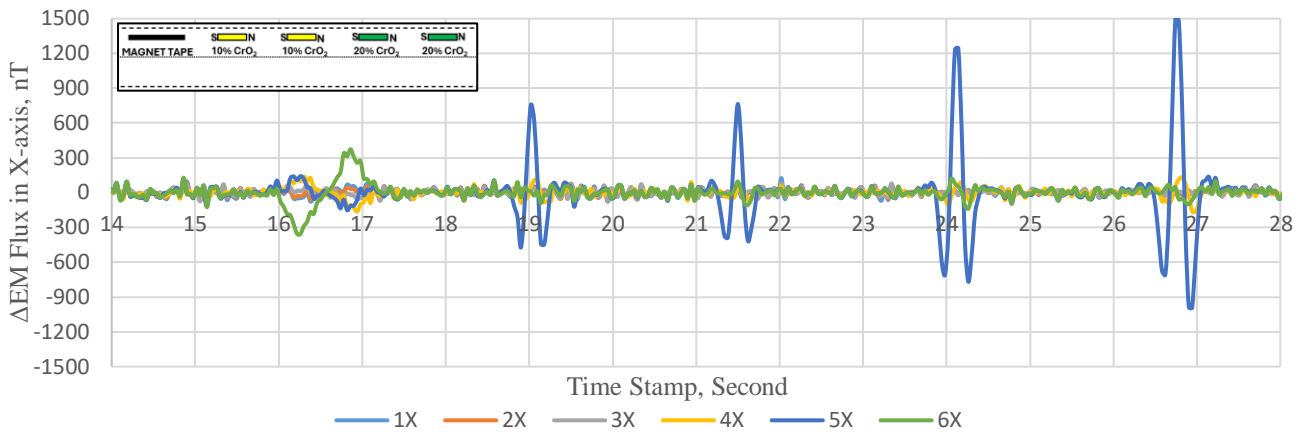
Figure 19. Graph. Processed ΔEM Flux in X-direction with time of Case #3.

In Figure 20, the y-axis magnetometer (lateral detection of the magnetic field) displayed relatively low signal strength, except for the 20% CrO_2 specimens. While sensor 5 remained, the primary sensor detecting the signals, some detectable responses were also observed on sensors 4 and 6. These additional responses can be attributed to the lateral flux influence as the cart passed over the EM specimens, causing the nearby sensors to capture some lateral magnetic field variations.

Figure 20. Graph. Processed ΔEM Flux in Y-direction with time of Case #3.

In Figure 21, the z-axis magnetometer (forward detection) produced higher signal strengths than the y-axis and remained consistent in time and peak sensor with the results from the x-axis. The highest signal was recorded at sensor 5, correlating with the placement of the EM specimens near the left edge of the array. The ambient EM noise remained below 300 nT, indicating there were no significant external disturbances in the z-direction of the signal data in this trial.
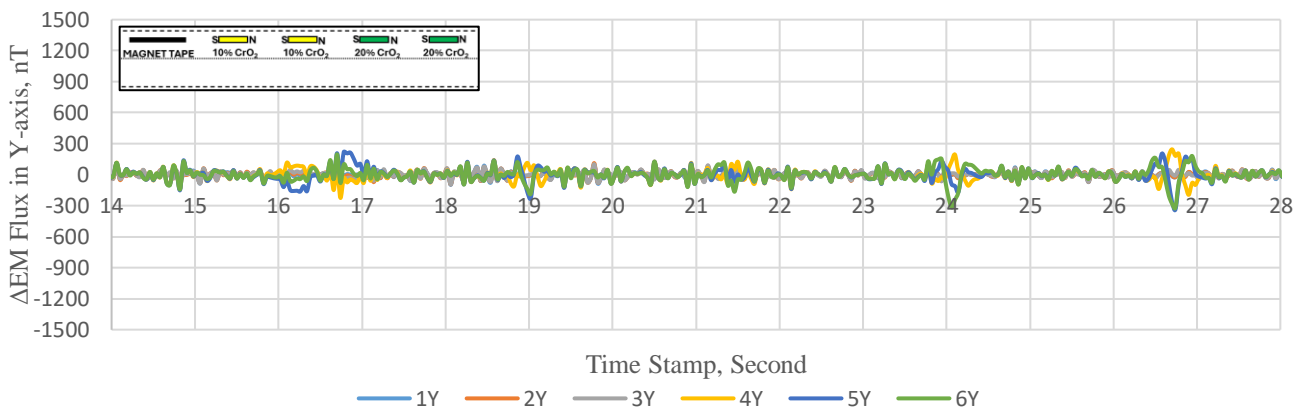
Figure 21. Graph. Processed ΔEM Flux in Z-direction with time of Case #3.

Case #4: Lane Departure Layout (Wandering Motion)

Figures 22 to 24 present the processed signal results of case #4 for the 3-axis magnetometer array, where the EM specimens were placed strategically to simulate a wandering motion of the cart despite the cart actually moving straight forward. This configuration included a magnetic tape placed along the centerline of the path, followed by alternating invisible marking specimens positioned along the right and left edges of the sensor array. Specifically, one invisible marking specimen was placed on the right edge, the next on the left edge, followed by a 20% CrO_2 specimen on the left edge, and finally, the last specimen on the right edge.

In Figure 22, the x-axis magnetometers (vertical detection) revealed distinct peaks for different sensors that corresponded to the placement of the invisible marking specimens. The highest signals observed at each specimen were the following in sequence: sensor 2, followed by sensor 5, with another peak at sensor 5, and concluding with signals at sensor 2 (See Figure 22). The signal patterns were consistent with the position of the sensors on the cart relative to the EM specimens. The 20% CrO_2 specimen generated the most prominent peak because of the higher concentration of ferromagnetic material. In contrast, the magnetic tape, positioned along the path's centerline, exhibited the lowest ΔEM flux compared to all invisible marking specimens.
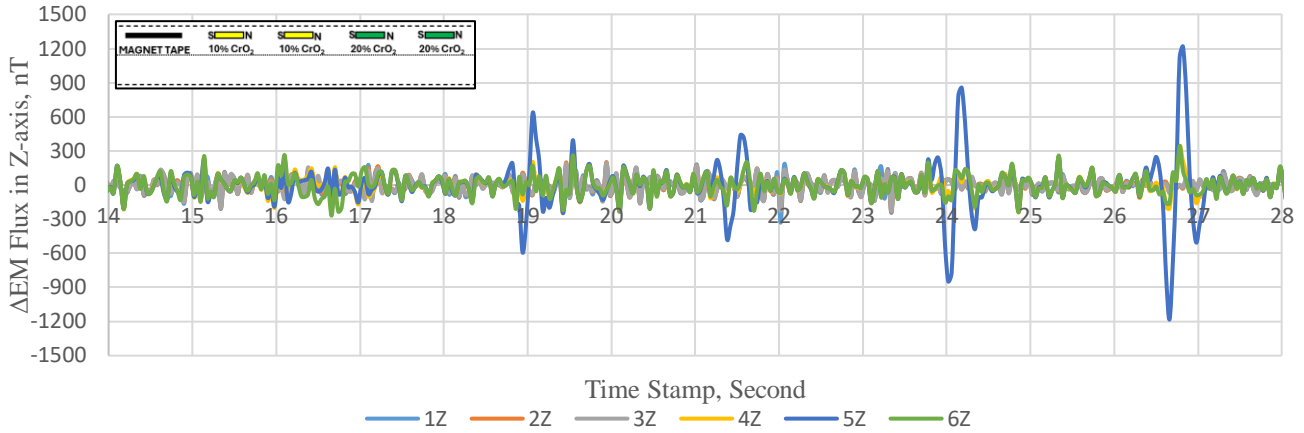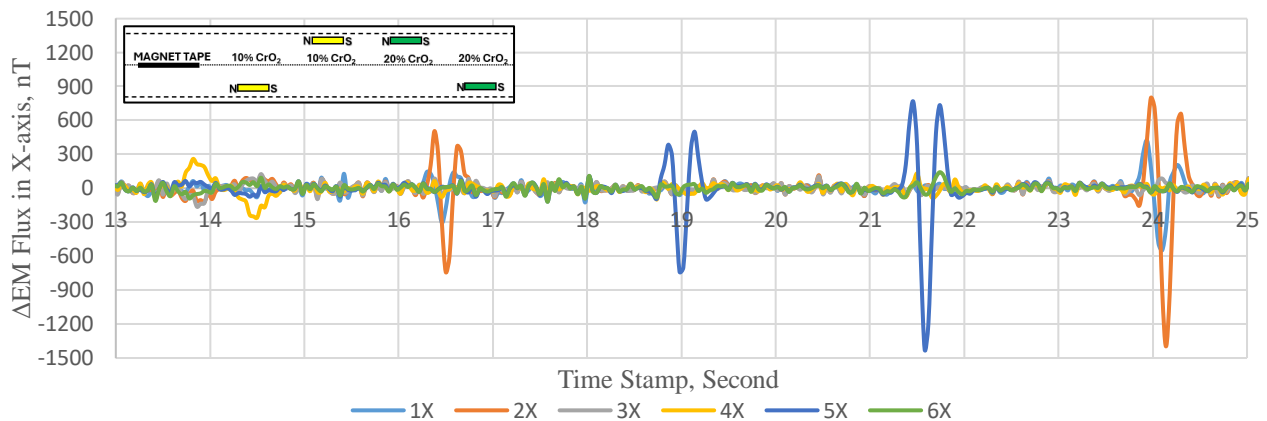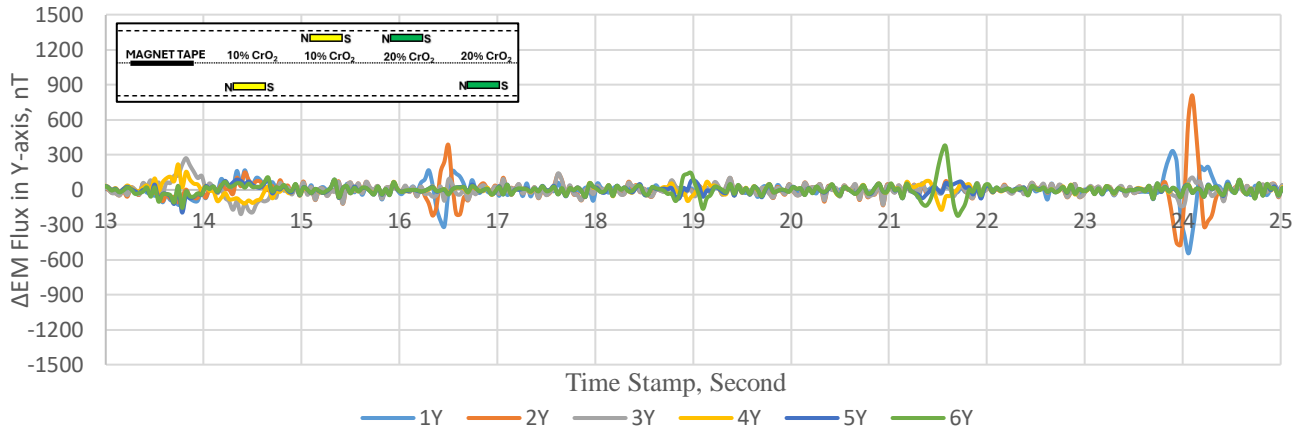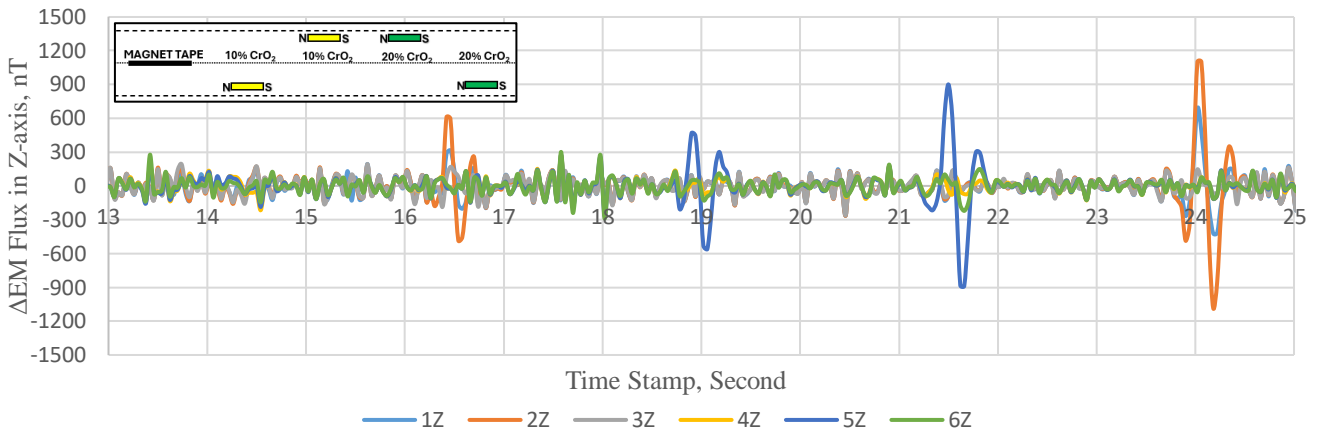

Figure 22. Graph. Processed ΔEM Flux in X-direction with time of Case #4.

In Figure 23, the y-axis magnetometer (lateral detection) detected weaker signals overall compared to the x-axis, but the sensors still followed the pattern of the invisible marking specimens but slightly different than Figure 22. As expected, the 20% CrO_2 specimen produced the most significant peak in the y-axis. The last two invisible marking specimens recorded the dominant signal on sensors 4, 5, and 6, followed by sensors 1, 2, and 3, respectively.

Figure 23. Graph. Processed ∆EM Flux in Y-direction with time of Case #4.

In Figure 24, the z-axis magnetometer (forward detection) showed consistent peak signals aligning with the positions of the invisible marking specimens. The strongest peaks were found at sensors 2 and 5, correlating well with the data from the x-axis in Figure 22. The 20% CrO_2 specimen displayed the highest signal, while the magnetic tape produced a lower and less distinct ∆EM flux.
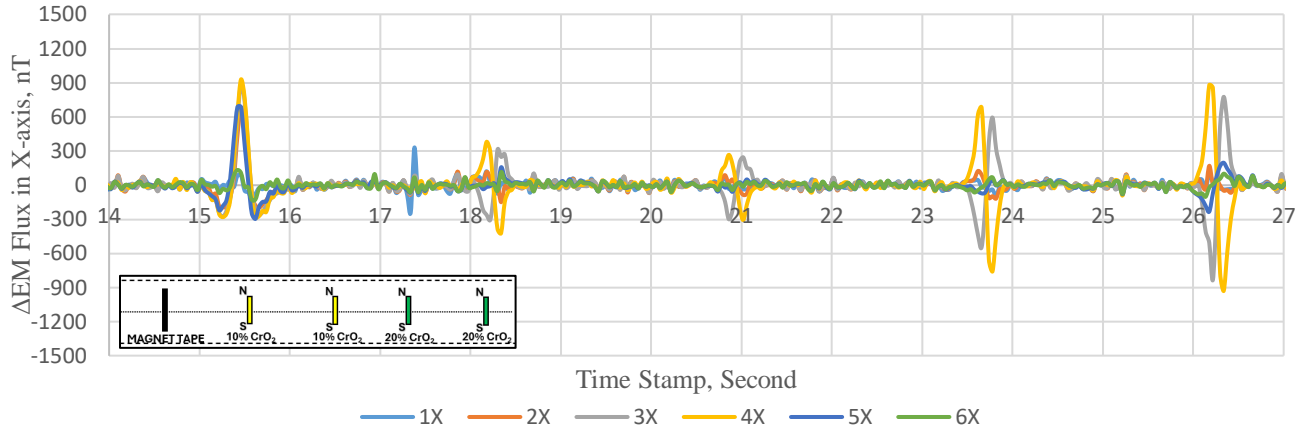

Figure 24. Graph. Processed ∆EM Flux in Z-direction with time of Case #4.

Case #5: CWZ Layout (Speed Warning Setup)

Figure 25 to Figure 27 show the processed signal results of case #5 for the 3-axis magnetometer array under slow moving speed condition for the speed warning configuration in a CWZ. In Figure 25, the x-axis magnetometer (vertical detection) demonstrated noticeable peak signals for both the magnetic tape and the 20% CrO_2 specimens. The ∆EM flux ranged between 600 and 900 nT for the 20% CrO_2

specimens, showing a similar intensity to the magnetic tape. However, the 10% CrO_2 specimens failed to generate distinguishable signals, with ΔEM flux values below 300 nT. Furthermore, for the CWZ setup, simultaneous peak responses from sensors 3 and 4 were expected, and as shown in this figure, both sensors peaked at the same time, confirming the intended output of the system.

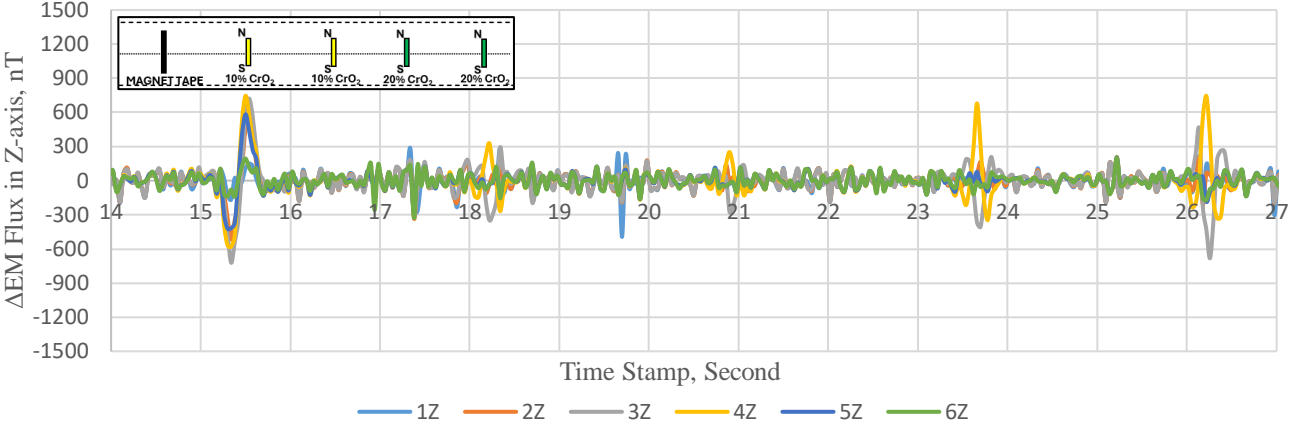**Figure 25. Graph. Processed ΔEM Flux in X-direction with time of Case #5.**

In Figure 26, the y-axis magnetometer (lateral detection) did not show any distinguishable peaks, and signals were weak across all specimens (< 300 nT), including the magnetic tapes. The absence of clear peaks indicates that the y-axis detection did not capture significant lateral variations in the magnetic flux from either the magnetic tapes or the invisible marking specimens for this transverse orientation of the EM specimens.
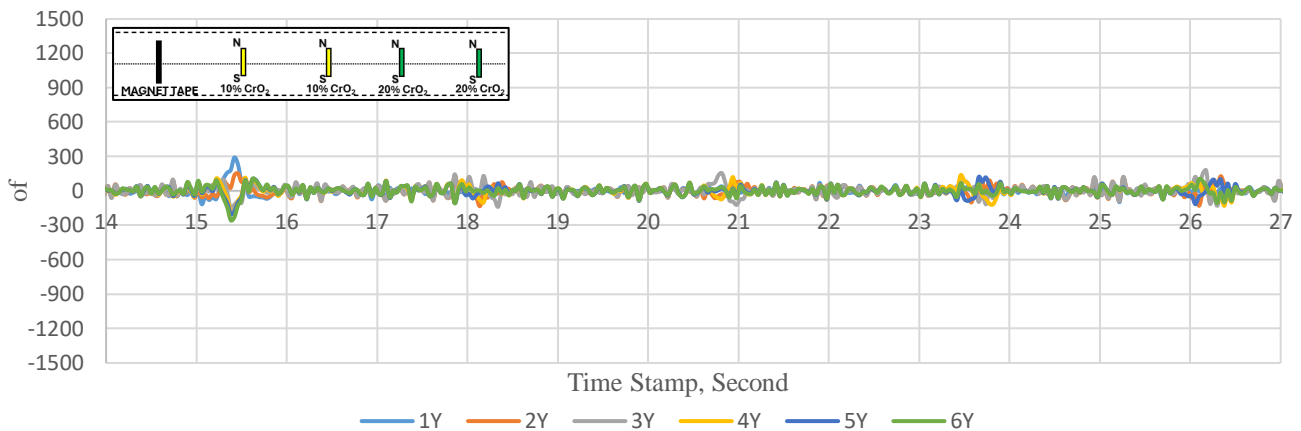
Figure 26. Graph. Processed ΔEM Flux in Y-direction with time of Case #5.

In Figure 27, the z-axis magnetometer (forward detection) produced distinct peaks corresponding to the magnetic tape and 20% CrO_2 specimens. The signals from the 20% CrO_2 specimens aligned well with those observed in the x-axis, further supporting the reliability of the transverse setup for speed warning in CWZ applications. As with the x-axis, the 10% CrO_2 specimens failed to generate clear signals, with flux values consistently below 300 nT. Additionally, the simultaneous peak responses

from sensors 3 and 4 in the z-axis further validated the system's ability to detect EM signals consistently when the cart passed over the specimens, as expected in the CWZ setup.

Figure 27. Graph. Processed ΔEM Flux in Z-direction with time of Case #5.

The results of the field pilot study show that all sensors and respective axes can detect a signal if the EM specimen is in very close proximity to the sensor. The magnitude of the signal output depended on the relative distance between the EM specimen and the sensor. The x-axis sensor produced the largest signals overall followed by the z-direction, which closely followed the time activation as the x-axis sensor. The y-axis sensor had the lowest signal strength for all specimen layout and orientations.

CHAPTER 4: EXPERIMENTAL SETUP FOR PASSIVE EM SENSING SIGNATURES FOR CWZ

The goal of this chapter was to further investigate the applicability of EM signatures generated by invisible markings under various configurations and patterns especially looking at coded signatures that communicate a warning or required/optional maneuver to a vehicle. For example, these EM pavement signatures in distinct orientation and patterns can be identified and provide specific instructions for vehicles approaching, traversing, or exiting a construction work zone. These V2I safety instructions could be speed warnings, lane-merge warnings, lane-keeping assistance, or entrance/exit ramps. Unlike the initial pilot study, which had five EM specimens, the field experimental setup involved an extended test section with eight EM strips with the ability to run the test at several cart speeds.

EXPERIMENTAL SETUP

The experimental setup for this phase maintained the invisible marking composition used in the initial pilot study but with only 20% of CrO_2. Figure 28 illustrates the magnetization setup and specimen size specifically for this expanded test matrix. The invisible marking was now 28 inches long instead of 15 inches in the pilot study (Chapter 3). The sensor configuration on the cart also was adjusted, with sensors positioned 8 inches above the ground (instead of 10 inches in the pilot study) and equipped with a GPS camera (GoPro HERO11), as shown in Figure 29.

The invisible marking strip patterns tested in this field experiment include the speed warning signatures, lane-merge warning signatures, and lane-keeping signatures for construction work zones, which are illustrated in Figure 30 and detailed in Cases #1 to #3 in Table 2. Figure 31 is an example of the field experimental setup in a parking lot near Newmark Laboratory on campus. This experiment was conducted at the highest possible speed the cart could achieve in order to observe the recorded EM signatures relative to previous slow-moving experiments and to recheck the accuracy of the back-calculated speed from the speed warning setup. These test cases were performed under running speed conditions exceeding 10 km/h (See Figure 31c).
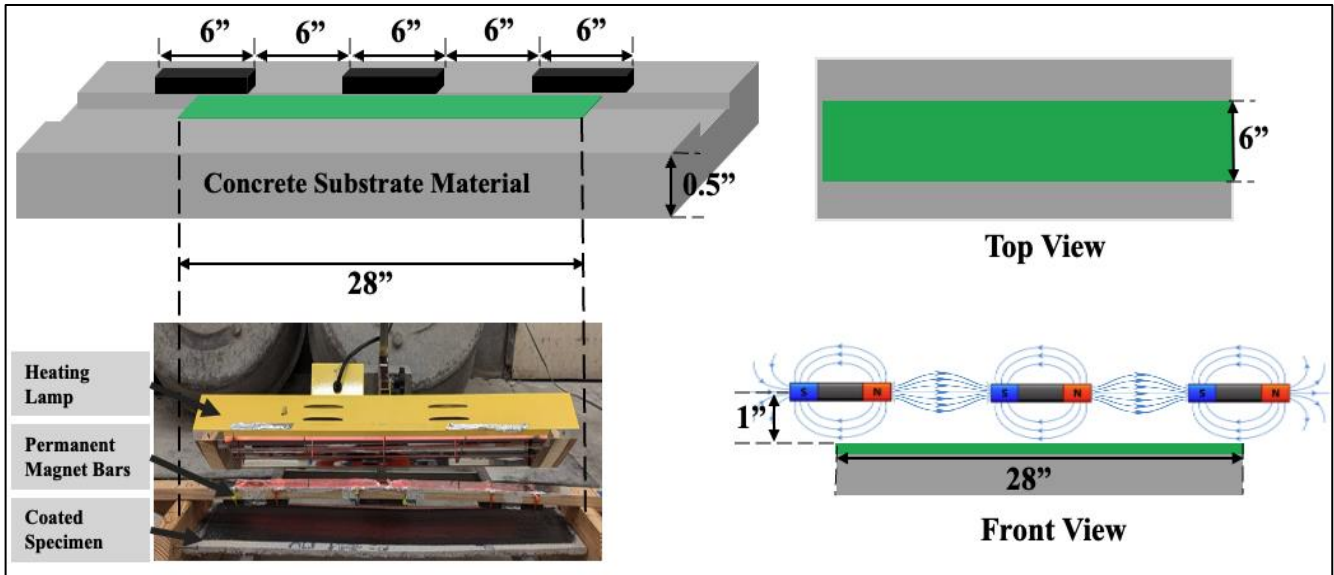
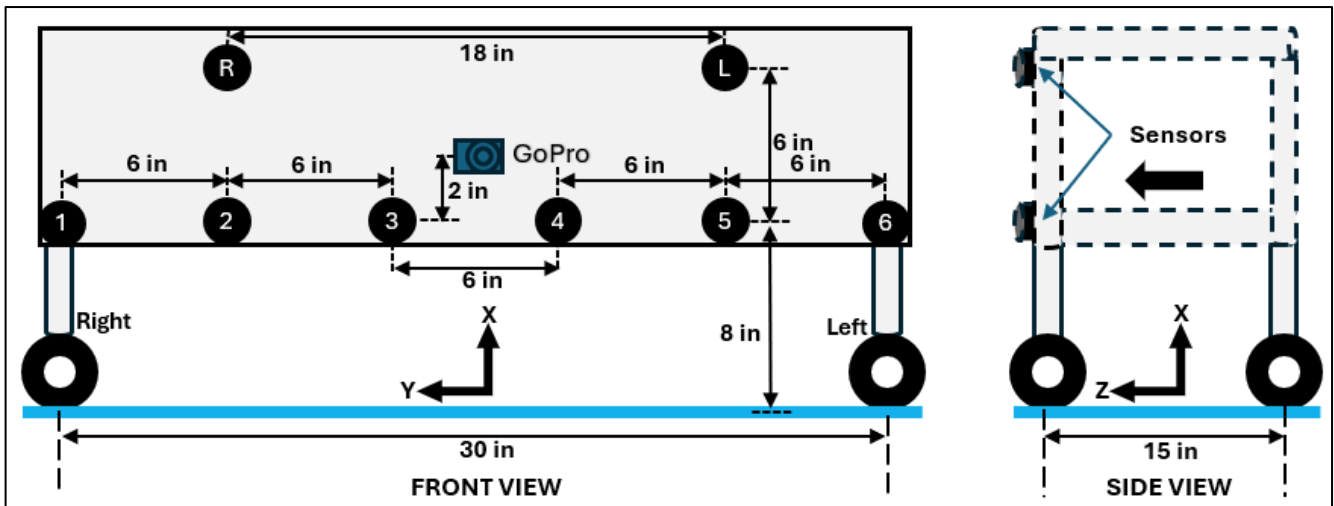**Figure 28. Diagram. Magnetization setup for invisible marking for field experiment.**

Figure 29. Diagram. Magnetometer sensor array setup.

Table 2. Cases with Strip Number and Inclination Angle for Speed and Lane-Merge Warning Test

| Case Number	Inclination angle of strip #1	Inclination angle of strip #2	Inclination angle of strip #3	Inclination angle of strip #4	Inclination angle of strip #5	Inclination angle of strip #6	Inclination angle of strip #7	Inclination angle of strip #8
1	90	90	90	90	90	90	90	90
2	90	90	90	90	60	60	60	60
3	180	180	180	180	180	180	180	180
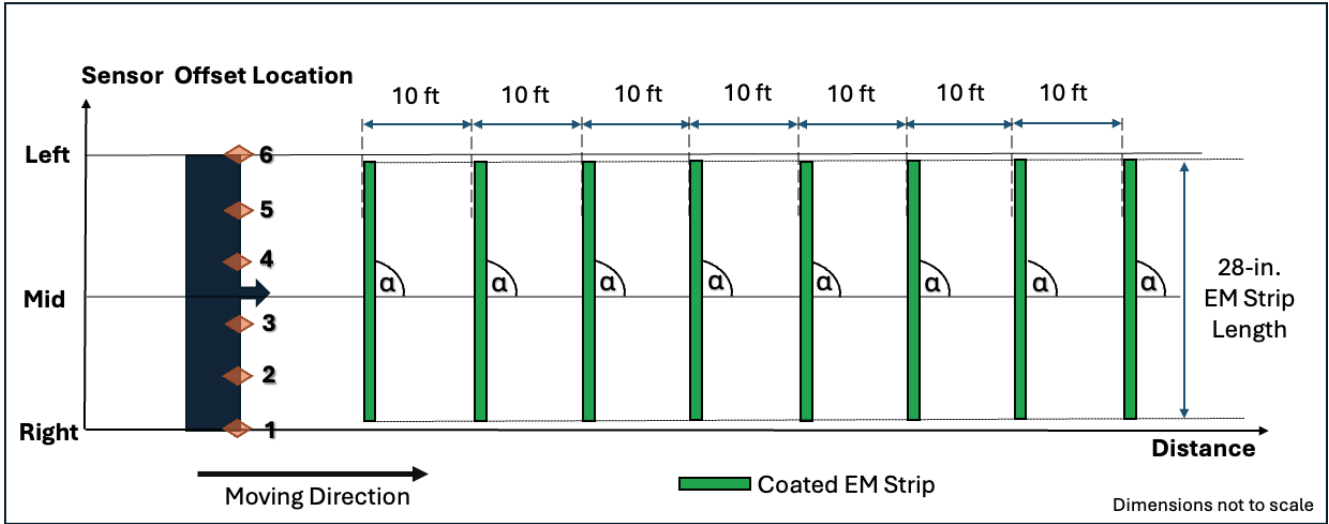
Figure 30. Diagram. Schematic for experimental setup of speed and lane-merge warning.

A. Front view of sensor and data collection cart setup
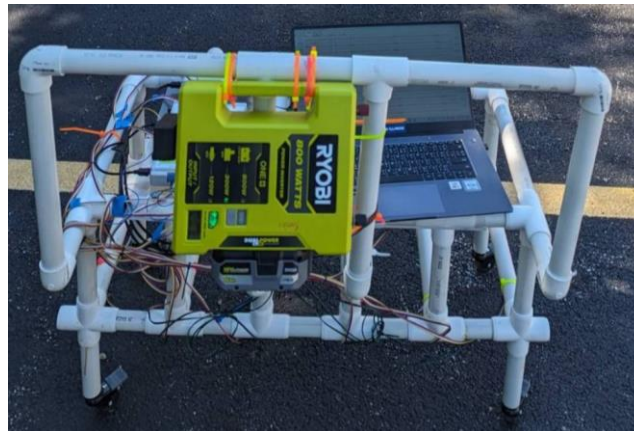
B. Rear view of cart setup

C. Field experimental setup sample with moving cart

Figure 31. Photo. Field experimental setup with cart traversing over transverse specimens in a parking lot near the Newmark research laboratory.

FIELD EXPERIMENTAL RESULTS

Speed Warning Signatures

Signal Processing for EM Signatures

This section will first discuss the signal-processing requirements for interpreting correctly the speed warning EM signatures. Figure 32 illustrates the raw EM flux density for 3-axis magnetometers along the cart path for Case #1, where all strips are 90° from the direction of travel. Figure 32 demonstrates the variation in initial EM flux values across all sensors (2 to 5) and axes, which was attributable to both the Earth's magnetic field and local magnetic disturbances. To accurately interpret the signals from each axis, it was essential to normalize each sensor to the initial values. Next, the background magnetic flux (earth and other local environmental factors) was removed further by subtracting the signal data from the nearest top row sensor signal.

Figure 33 shows the EM flux for the X-axis sensor after normalizing the signal to the initial data points and removing the background magnetic flux for Case #1. Note, the high- and low-frequency noise persisted in these processed signals. To address high-frequency noise, a 4-point moving average technique was applied, with the resulting EM flux shown in Figure 34. Low-frequency noise was further reduced by taking the stepwise differential of each data point relative to its preceding point ($\Delta EM/\Delta i$), as depicted in Figure 35. In the final step, signals below ±200 nT threshold were filtered out as shown in Figure 36 to focus on the primary signals representing the encoded EM signature.

Figures 32 through 36 illustrate the progression from raw to fully processed EM flux signals for the X-axis sensors 2 to 5. Figures 32 through 36 illustrate the progression from raw to fully processed EM flux signals for the X-axis sensors 2 to 5. For the EM flux in the Y and Z axes, similar processing steps are detailed in the appendices, with fully processed signals shown in Figures 37 and 38 for the Y- and Z-axes, respectively. From the results obtained in Figures 36 to 38, the X-axis exhibited the highest

signal magnitudes and successfully captured all eight peak signals corresponding to the eight transverse specimen strips. However, two peak signals were missed in the Y-axis (around 12.1 and 16.7 seconds), and one peak signal was undetected in the Z-axis (around 17.4 seconds). Because the Y-and Z-axes captured flux on the lateral plane to the moving direction, their ability to detect signals was more sensitive to the vertical distance between the sensor and the EM source compared to the X-axis. In contrast, the X-axis demonstrated consistent and reliable EM flux detection across the specimens and setup.

Verification of Processed EM Signatures for Speed Warning Signatures

The final processed EM signatures for the 3-axis of the magnetometer sensors are illustrated in Figures 36 to 38. They revealed distinct and consistent patterns in both the X-axis and Z-axis directions. The responses from the signal-processed data with ΔEM flux values below the absolute value of 150 nT were excluded to make the speed calculation more automated. Figure 39 provides an example of the X-axis responses for the first two EM strips, as recorded by sensors 2 through 5. To determine what value of time should be selected for the cart's speed calculation, the peak of the differentiated EM flux was selected because it represents the point of maximum rise in the EM flux signal. This peak signal is approximately when the cart is beginning to move across the EM strip. For instance, as shown in Figure 39, the time stamp for the peak response of the first EM strip is 12.18 seconds, while the peak response of the second strip occurs at 13.06 seconds. These time intervals translate to an approximate speed of 12 km/h.

To validate the accuracy of the calculated cart speed derived from the peak responses of the EM strips, these calculations were compared with the GPS speed recorded by the GPS camera on the cart, as detailed in Table 3 and 4. Furthermore, a comparison between the z-axis and x-axis calculated speeds, as observed in Table 3 and 4, showed that the average speed derived from the peak responses of the EM strips correlated well between the x-axis and z-axis.
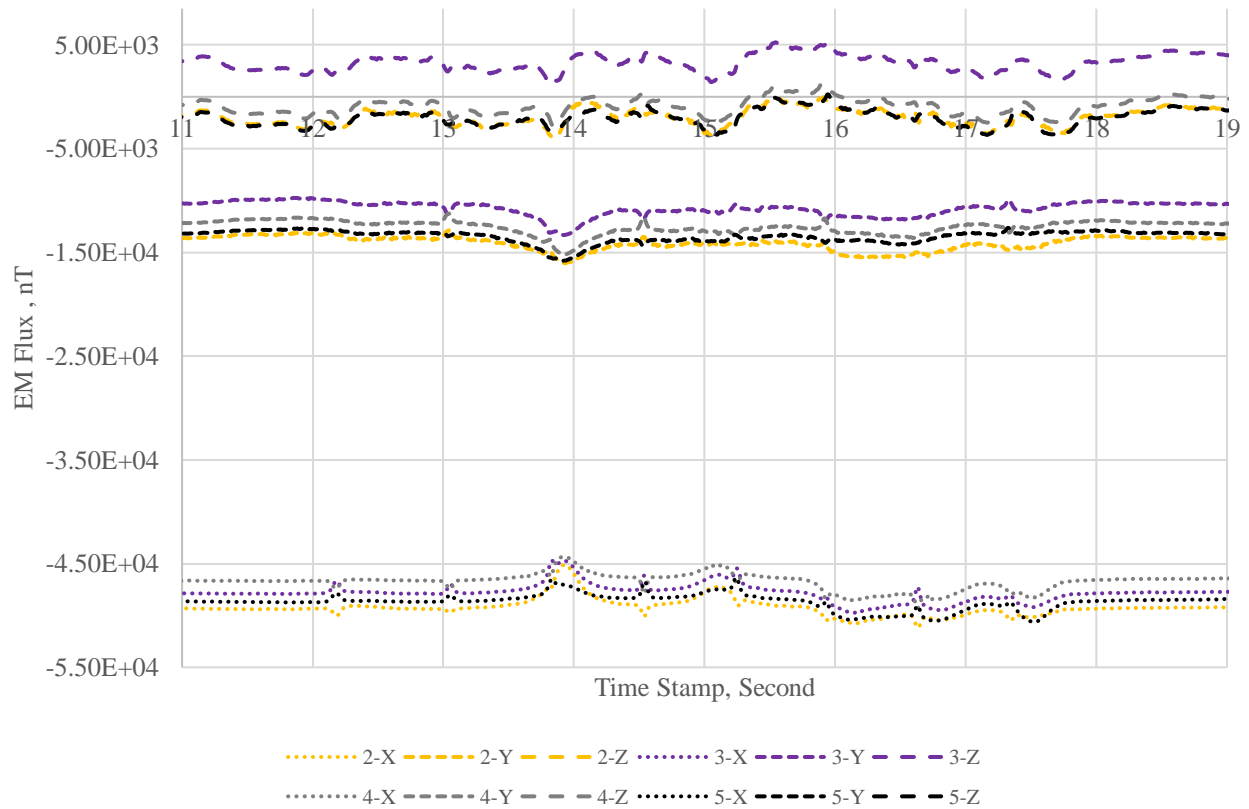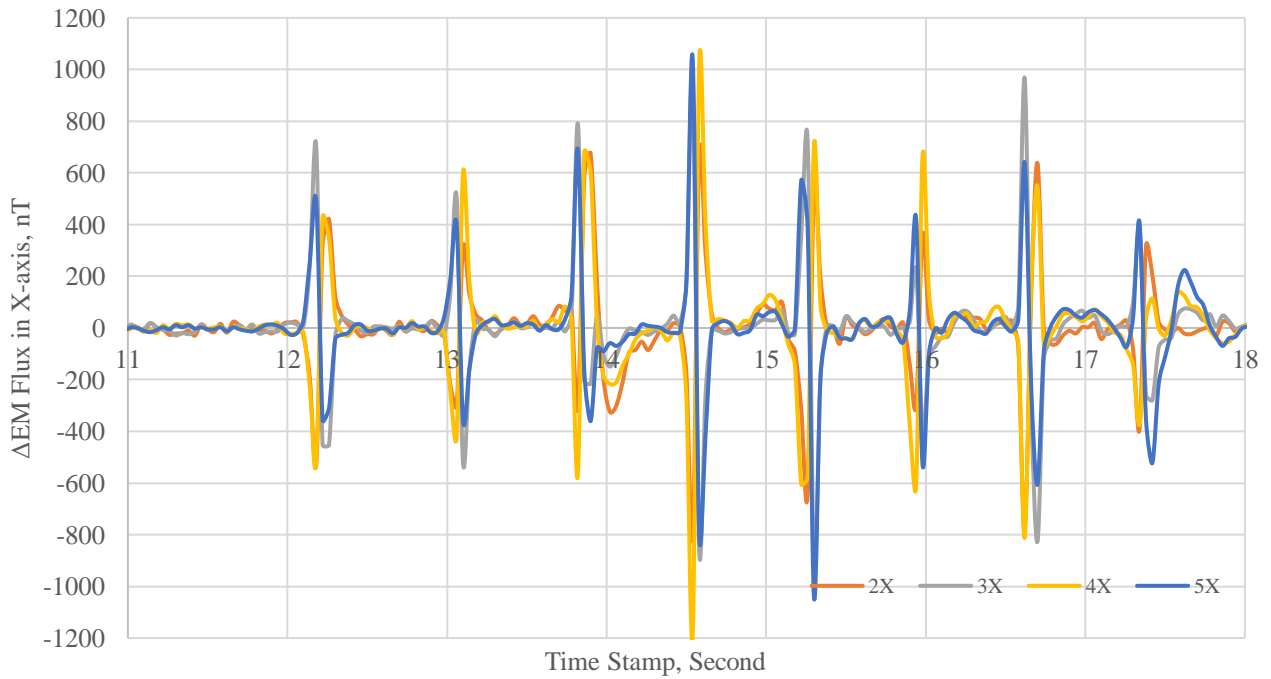
Figure 32. Graph. Raw sensor signals (EM flux) for 3-axis magnetometer sensors 2 to 5 (Case #1).
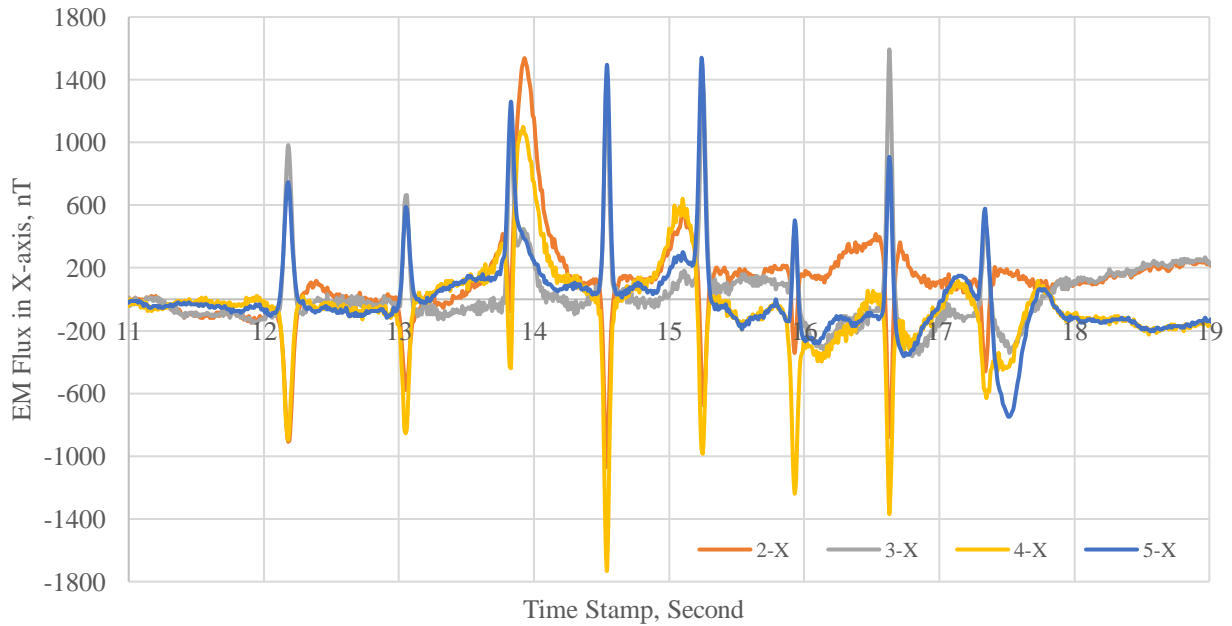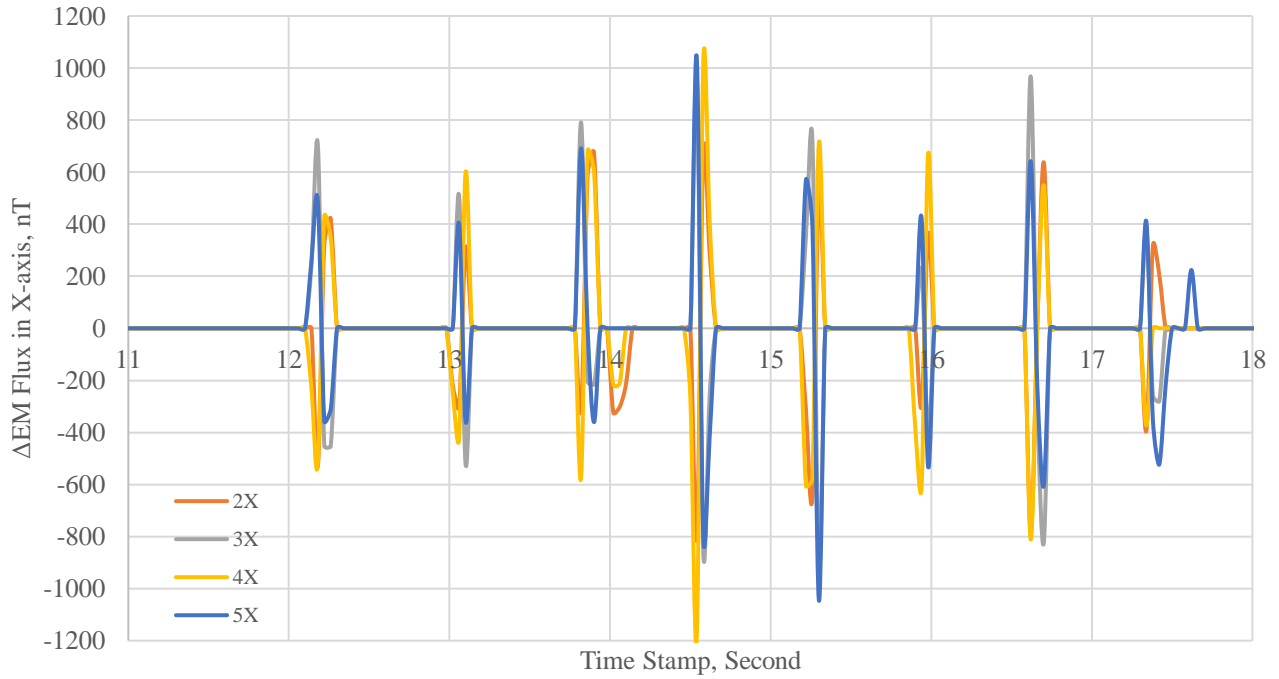

Figure 33. Graph. X-axis signals (EM flux) for sensors 2 to 5 after normalizing signal to time zero data points and subtracting out background magnetic flux (Case #1).
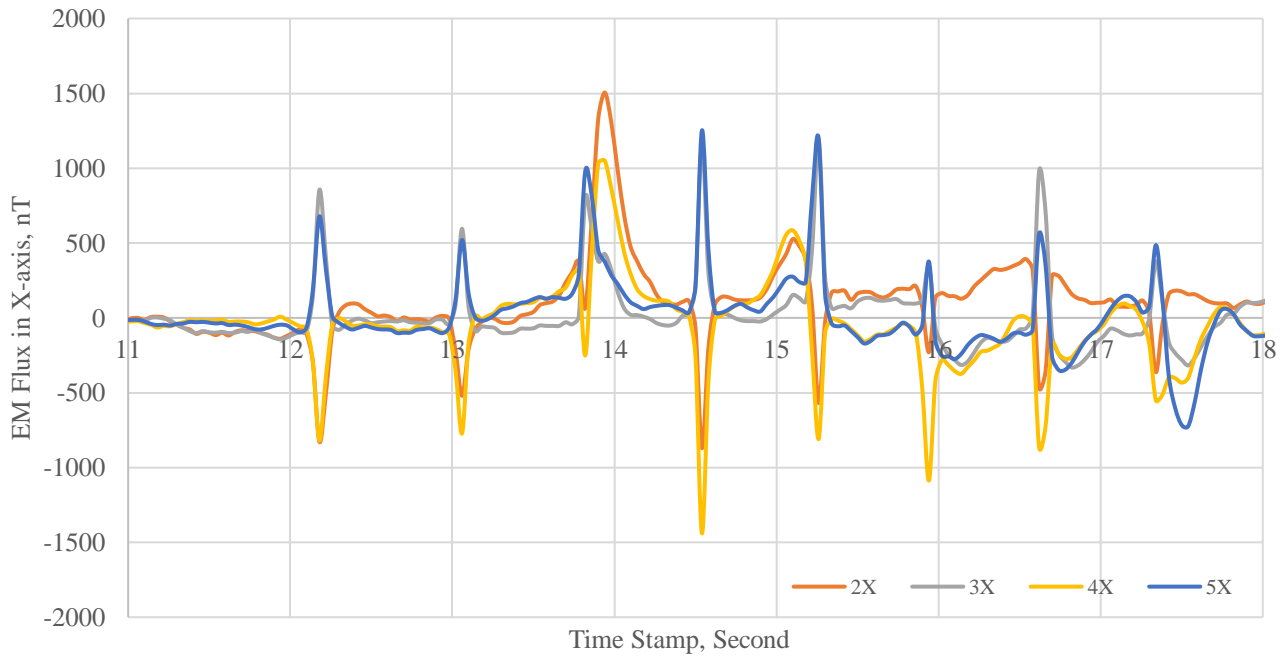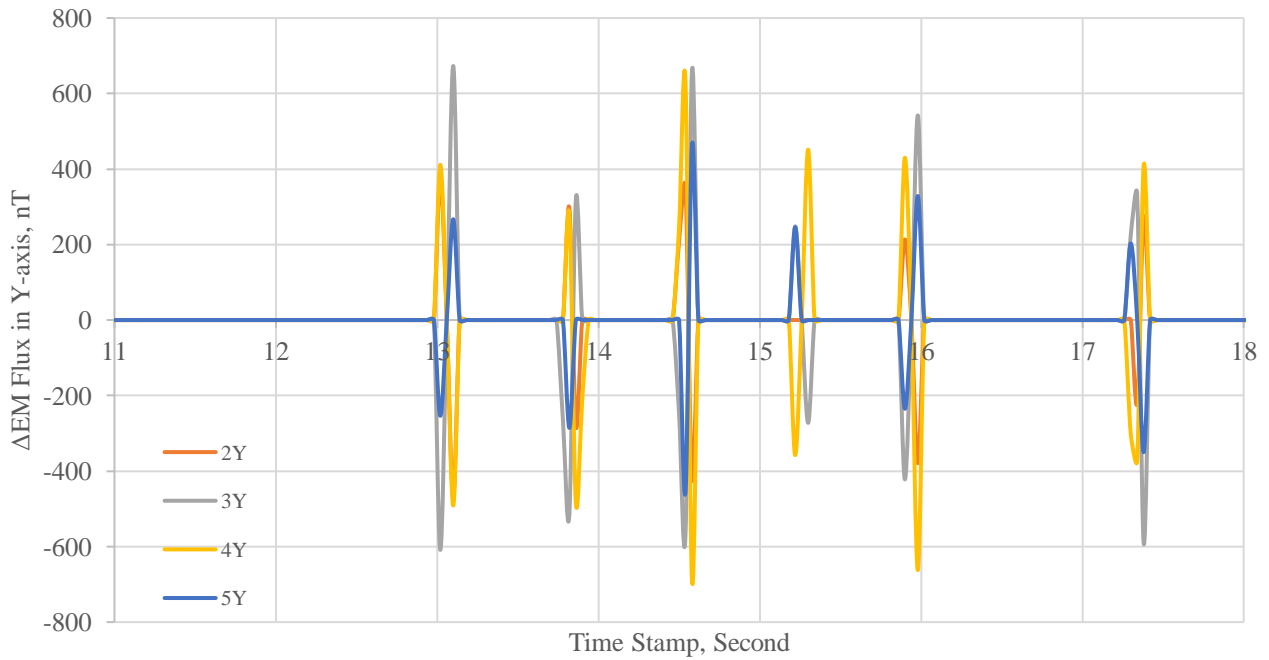
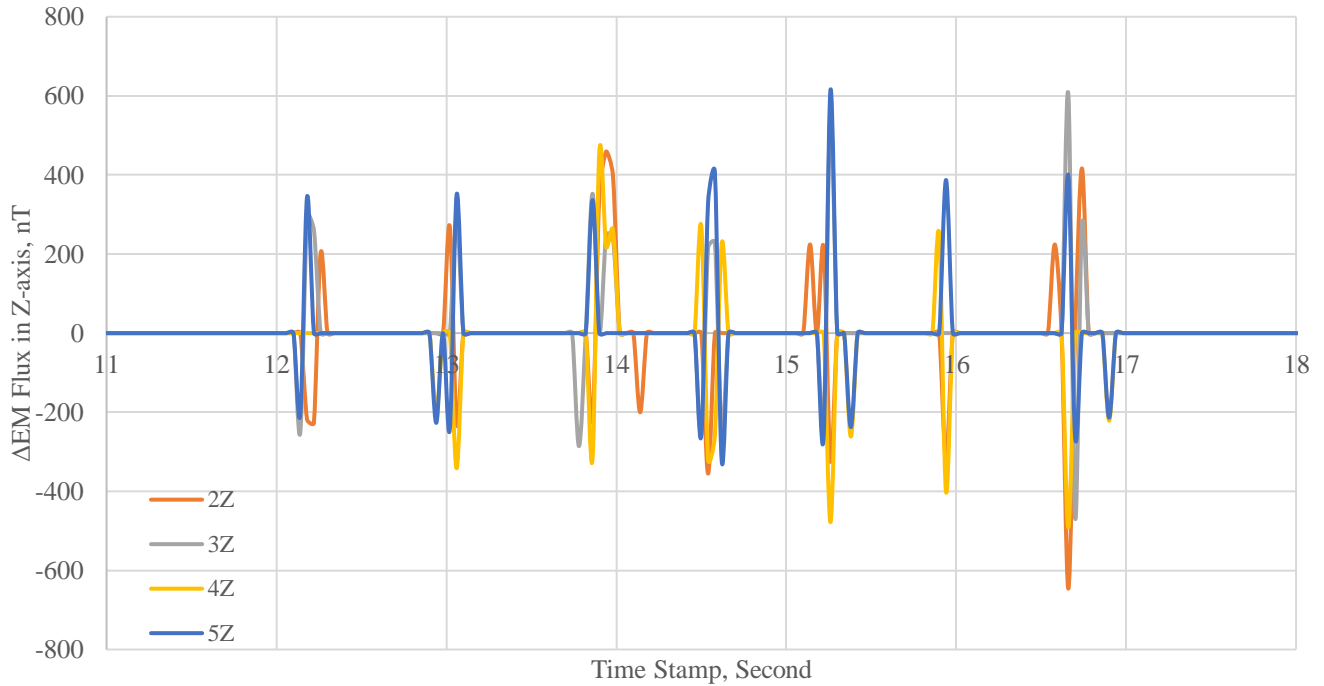**Figure 34. Graph. High-frequency filtered responses (ΔEM flux) for the X-axis of sensors 2–5 (Case #1).**

Figure 35. Graph. Low-frequency filtered responses (ΔEM flux) for the X-axis of sensors 2–5 (Case #1).

Figure 36. Graph. Signal-processed responses (ΔEM flux) for the X-axis of sensors 2–5 (Case #1).

Figure 37. Graph. Signal-processed responses (ΔEM flux) for the Y-axis of sensors 2–5 (Case #1).

Figure 38. Graph. Signal-processed responses (ΔEM flux) for the Z-axis of sensors 2–5 (Case #1).
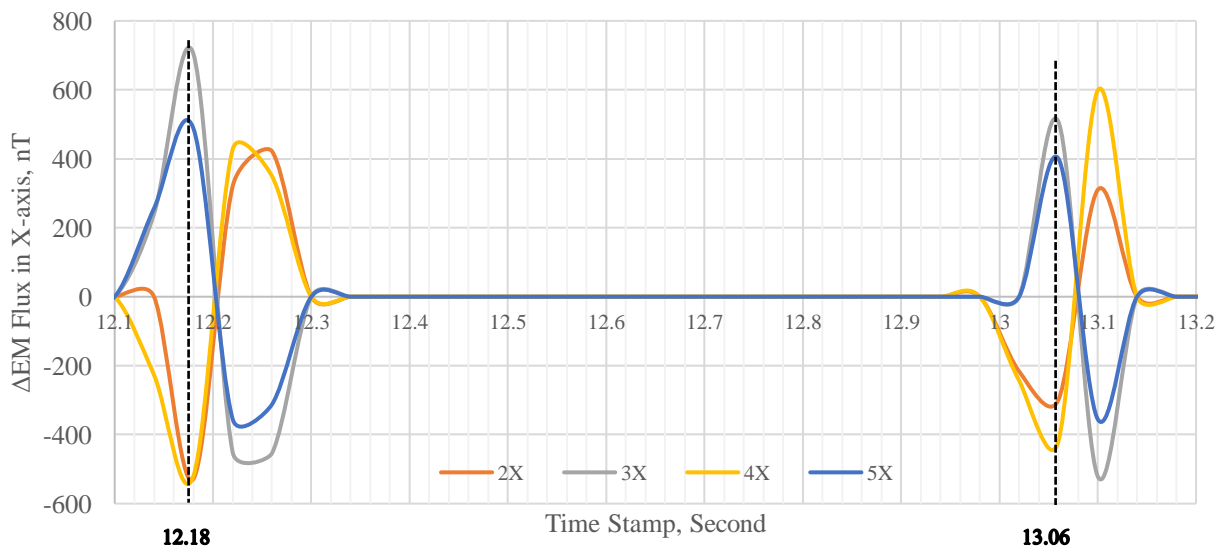
Figure 39. Graph. Example of two consecutive processed signals (ΔEM flux) with peaks for the X-axis of sensors 2 to 5 (Case #1—Cart Speed).
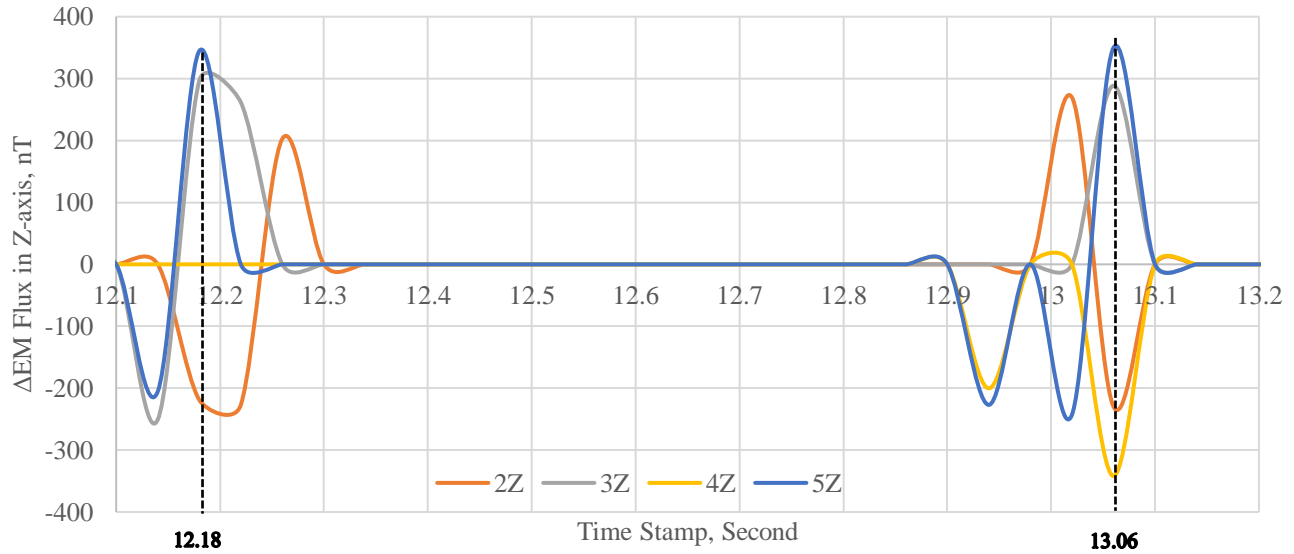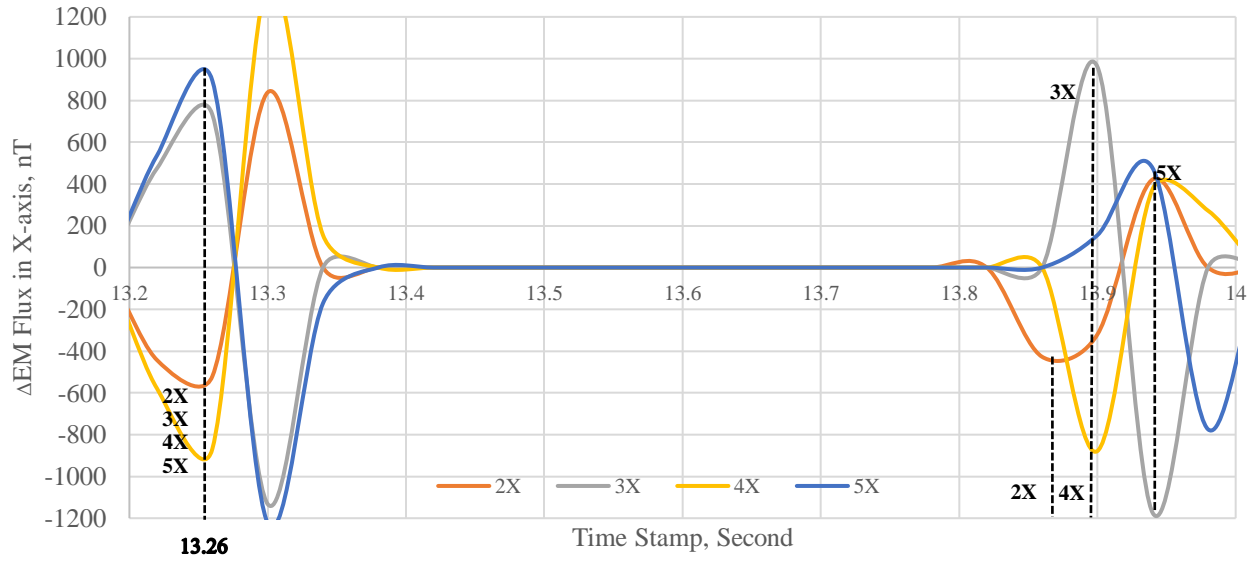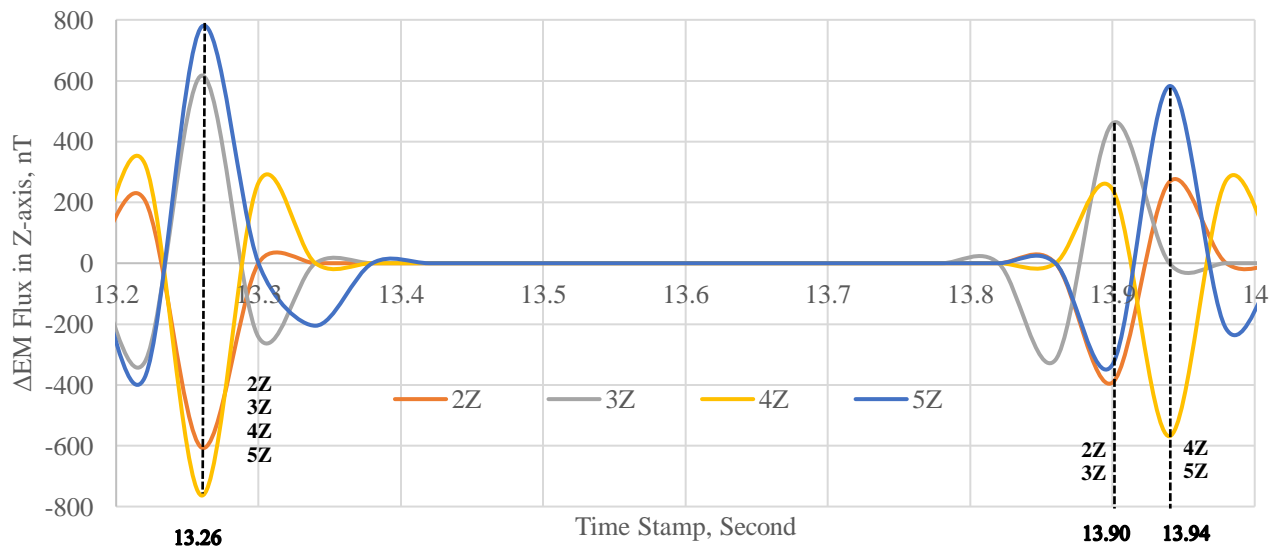
Figure 40. Graph. Example of two consecutive processed signals (ΔEM flux) with peaks for the Z-axis of sensors 2 to 5 (Case #1—Cart Speed).

Table 3. Calculated Cart and GPS Speeds of Test Case#1 for X-axis and Z-axis Magnetometer

Time Stamp (s) at Peak in X-Axis	EM Strip 1	EM Strip 2	EM Strip 3	EM Strip 4	EM Strip 5	EM Strip 6	EM Strip 7	EM Strip 8
Sensor 2	12.18	13.06	13.82	14.54	15.26	15.94	16.62	17.34
Sensor 3	12.18	13.06	13.82	14.54	15.26	15.94	16.62	17.34
Sensor 4	12.18	13.06	13.82	14.54	15.26	15.94	16.62	17.34
Sensor 5	12.18	13.06	13.82	14.54	15.26	15.94	16.62	17.34
Calculated Speed (km/h)	–	12	14	15	15	16	16	15
GPS Speed (km/h)	–	12–13	14–15	15	15	15	15	15–14

Table 4. Calculated Cart and GPS Speeds of Test Case#1 for Z-axis Magnetometer

Time Stamp (s) at Peak in Z-Axis	EM Strip 1	EM Strip 2	EM Strip 3	EM Strip 4	EM Strip 5	EM Strip 6	EM Strip 7	EM Strip 8
Sensor 2	12.22	13.06	13.86	14.54	15.26	15.94	16.66	NA
Sensor 3	12.18	13.06	13.86	14.54	15.26	NA	16.66	NA
Sensor 4	NA	13.06	13.86	14.54	15.26	15.94	16.66	NA
Sensor 5	12.18	13.06	13.86	14.54	15.26	15.94	16.66	NA
Calculated Speed (km/h)	–	12	14	16	15	16	15	NA
GPS Speed (km/h)	–	12–13	14–15	15	15	15	15	15–14

Lane-Merge Warning Signatures

Signal Processing for EM Signatures

The signal-processing techniques for lane-merge warning signatures followed the same approach as for speed warnings. Figure 41 illustrates raw EM flux variations for lane-merge test cases, influenced similarly by both the Earth's magnetic field and local disturbances. The standardization process involved adjusting initial readings, mitigating background EM flux, and applying filtering techniques to refine the data for calculations. The final processed EM flux for these signatures is presented in Figures 42 to 44.
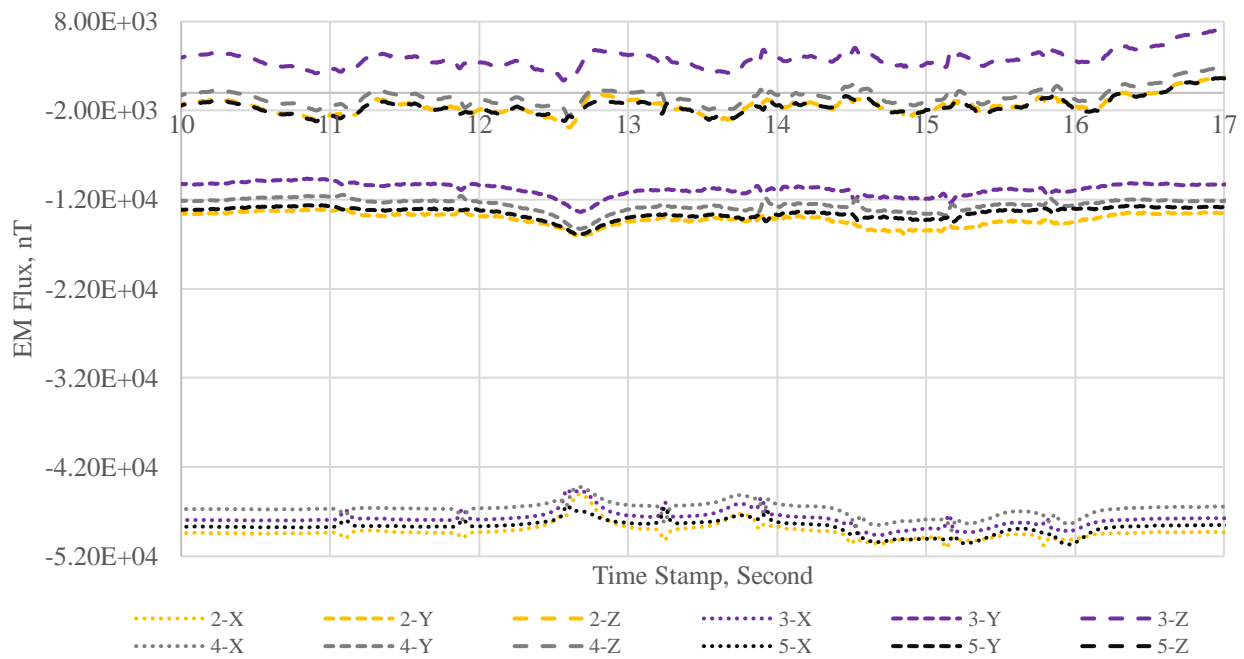
Figure 41. Graph. Raw sensor signals (EM flux) for 3-axis magnetometer sensors 2 to 5 (Case #2).
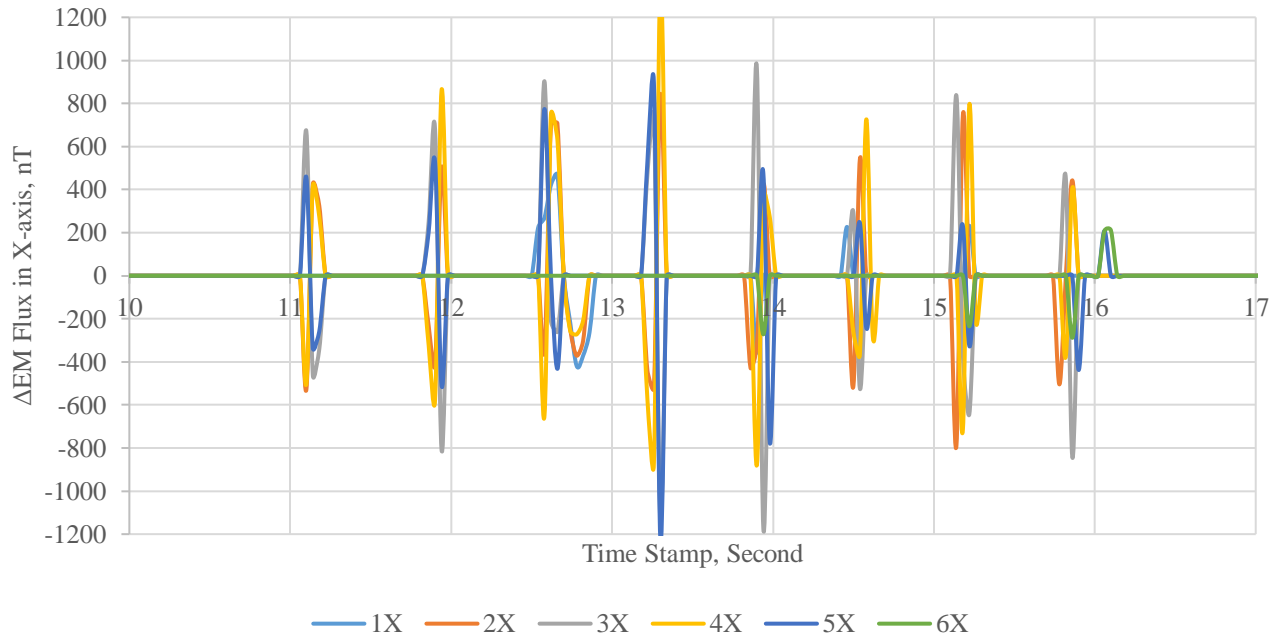
Figure 42. Graph. Signal-processed responses (ΔEM flux) for X-axis sensors 2–5 (Case #2).
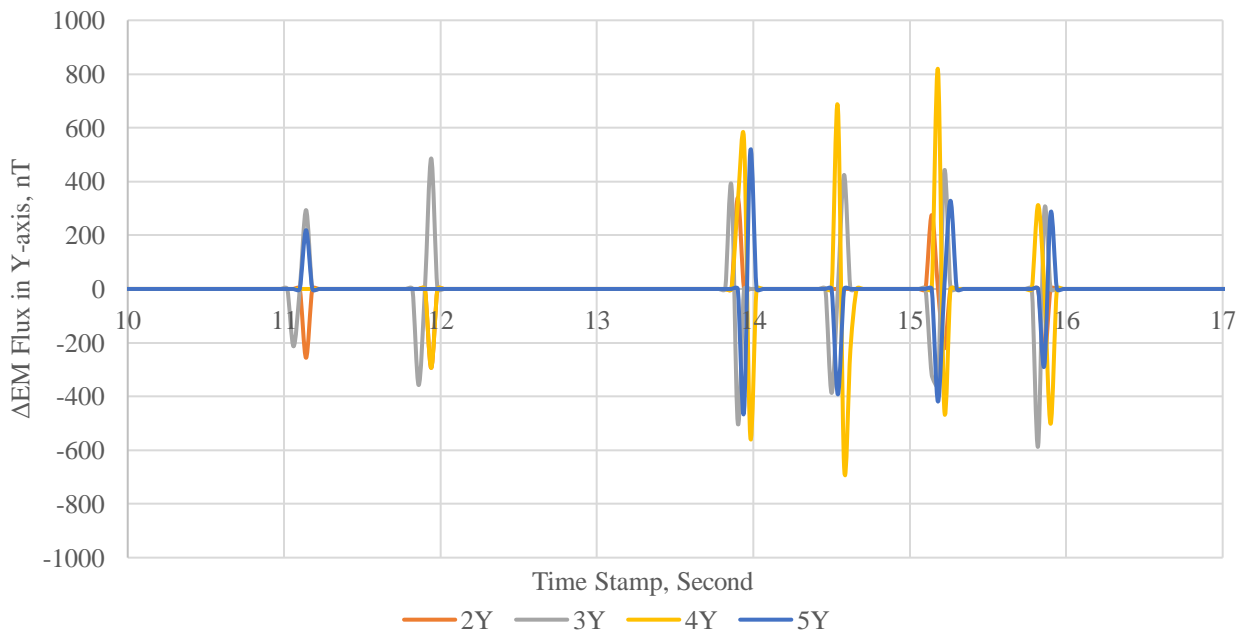
Figure 43. Graph. Signal-processed responses (ΔEM flux) for Y-axis sensors 2–5 (Case #2).
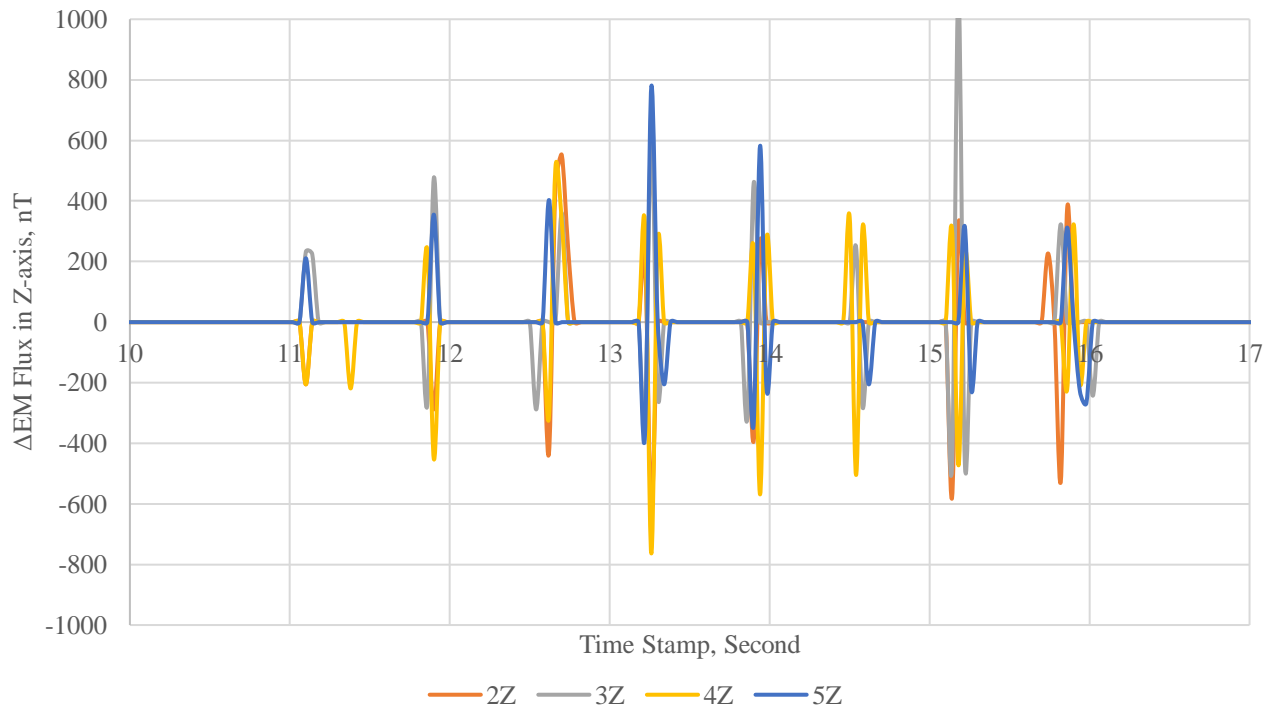
Figure 44. Graph. Signal-processed responses (ΔEM flux) for Z-axis sensors 2–5 (Case #2).

Verification of Processed EM Signatures for Lane-Merge Warning Signatures

For the lane-merge warning system, the results from Case #2, which included four series of EM strips at a 90-degree inclination and four series at a 60-degree inclination, were used for verification. Figure 45 provides an example of peak observations for EM strip number 4 (90-degree inclination) and EM strip number 5 (60-degree inclination) within the lane-merge scenario. The processed data and calculations from Case #2 are detailed in Table 5 and 6, including comparisons of back-calculated speed, GPS speed, and lane-merge actions. The time differences of peak responses from sensors on the left, center, and right of the cart were analyzed to determine the suggested merge-direction, as shown in Table 5 and 6.

Figure 45. Graph. Example of two consecutive processed signals (ΔEM flux) with observable peaks for sensors 2 to 5 in the X-axis direction (Case #2—cart speed and merging direction).

Figure 46. Graph. Example of two consecutive processed signals (ΔEM flux) with observable peaks for sensors 2 to 5 in the Z-axis direction (Case #2—cart speed and merging direction).

Table 5. Comparison of Back-Calculated and GPS Cart Speed of Test Case #2 for X-axis Magnetometer

Time Stamp (s) at Peak in X-axis	Strip #1	Strip #2	Strip #3	Strip #4	Strip #5	Strip #6	Strip #7	Strip #8
Sensor 2 (R)	11.1	11.90	12.58	13.26	13.86	14.5	15.14	15.78
Sensor 3	11.1	11.90	12.58	13.26	13.90	14.5	15.14	15.82
Sensor 4	11.1	11.90	12.58	13.26	13.90	14.54	15.18	15.82
Sensor 5 (L)	11.1	11.90	12.58	13.26	13.94	14.54	15.18	15.9
Average Speed (km/h)	–	14	16	16	17	18	17	16
GPS Speed (km/h)	–	13–15	15–16	16–17	17	17	17	16–14
ΔT_r (Sensor 2)	0.00	0.80	1.48	2.16	2.76	3.40	4.04	4.68
ΔT_c, (Sensor 3 & 4)	0.00	0.80	1.48	2.16	2.80	3.42	4.06	4.72
ΔT_l (Sensor 5)	0.00	0.80	1.48	2.16	2.84	3.44	4.08	4.80
Suggested Lane-Merge Action	–	–	–	–	LEFT	LEFT	LEFT	LEFT

Table 6. Comparison of Back-Calculated and GPS Cart Speed of Test Case #2 for Z-axis Magnetometer

Time Stamp (s) at Peak in Z-axis	Strip #1	Strip #2	Strip #3	Strip #4	Strip #5	Strip #6	Strip #7	Strip #8
Sensor 2 (R)	11.1	11.9	12.62	13.26	13.9	NA	15.14	15.82
Sensor 3	11.1	11.9	12.62	13.26	13.9	14.54	15.18	15.82
Sensor 4	11.1	11.9	12.62	13.26	13.94	14.54	15.18	15.9
Sensor 5 (L)	11.1	11.9	12.62	13.26	13.94	14.62	15.22	15.98
Average Speed (km/h)	–	14	15	17	17	18	17	16
GPS Speed (km/h)	–	13–15	15–16	16–17	17	17	17	16–14
ΔT_r (Sensor 2)	0.00	0.80	1.52	2.16	2.80	NA	4.04	4.72
ΔT_c, (Sensor 3&4)	0.00	0.80	1.52	2.16	2.82	3.44	4.08	4.76
ΔT_l (Sensor 5)	0.00	0.80	1.52	2.16	2.84	3.52	4.12	4.88
Suggested Lane-Merge Action	–	–	–	–	LEFT	LEFT	LEFT	LEFT

Lane-Keeping Signatures

Signal Processing for EM-Sensing Signatures

For lane-keeping signatures, the signal-processing employed the same methodology as described for speed and lane-merge warnings. Figure 47 depicts the raw EM flux sensor data as the cart path for the lane-keeping cases. The processing steps included normalizing the data, mitigating background magnetic flux, and applying high- and low-frequency filters. The processed ΔEM flux across the three axes is shown in Figures 48 to 50.

The results indicate that the peak responses from all invisible marking strips were simultaneously detected along the moving path of sensors #3 and #4. As these sensors are centrally located in the cart's sensor array, their responses align closely with the placement of the invisible markings, which were positioned along the centerline of the cart's path.

The detection of the two highest peaks as the cart approaches the invisible markings can be used to approximate the cart's offset from the centerline of the path, as summarized in Table 7. The peak signals reflect their relative influence on the cart's offset from the centerline. Specifically, if two high peak signals were detected on sensors #3 and #4, it indicated that the cart's path was at the centerline and situated between these sensors. The offset distance from the centerline is approximated by comparing the peak intensities of these sensors. For example, if sensor #3 registered a higher peak than sensor #4, it suggested that the cart's path was offset more toward sensor #3, which means the car is left of center.

For example, in the case of strip #1, the highest peak signal was sensor #3, followed by sensor #4. Given that the sensor array spacing is 6 inches, it is inferred that the centerline path lies between sensors #3 and #4, but closer to sensor #3. Because sensor #3 is positioned 3 inches to the right of the center of the cart's sensor array, the EM path was offset more toward sensor #3. The cart's center was therefore positioned between 0 and 3 inches to the left of the centerline of the EM path.
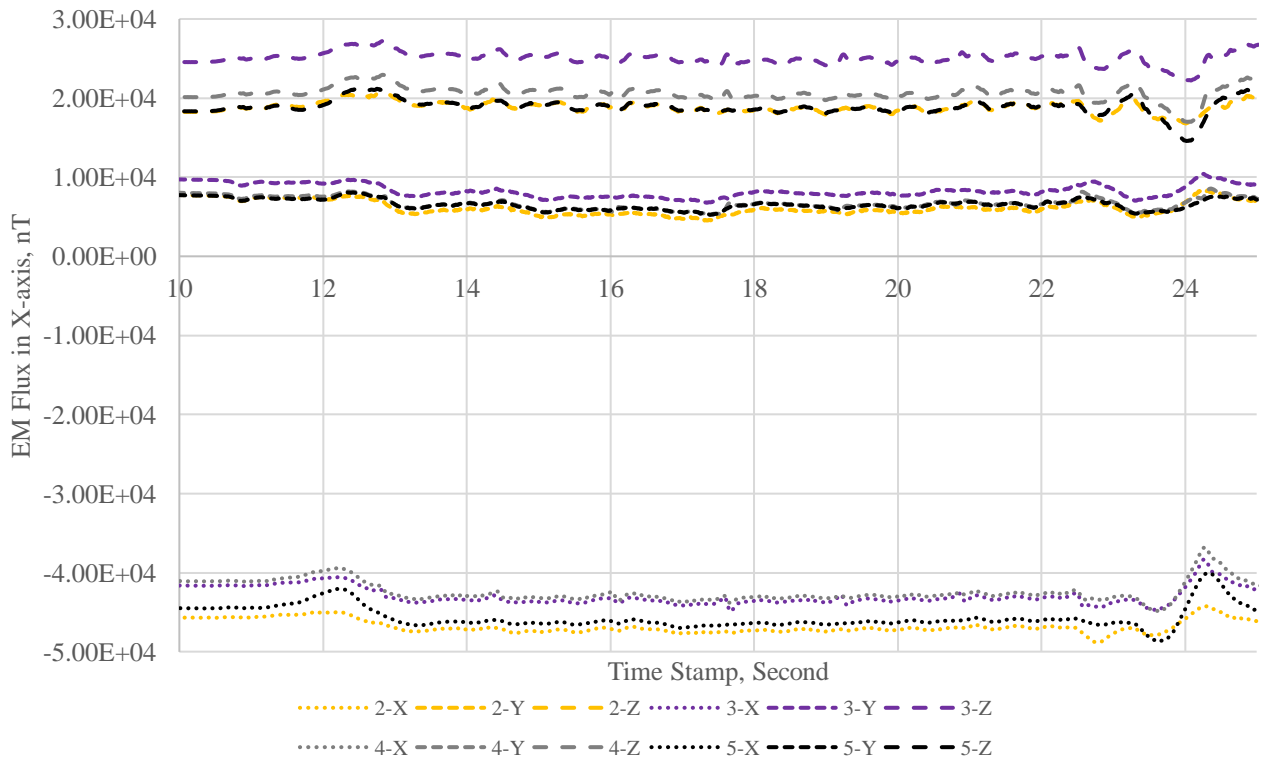
Figure 47. Graph. Raw sensor signals for 3-axis magnetometer sensors 2 to 5 (Case #3).
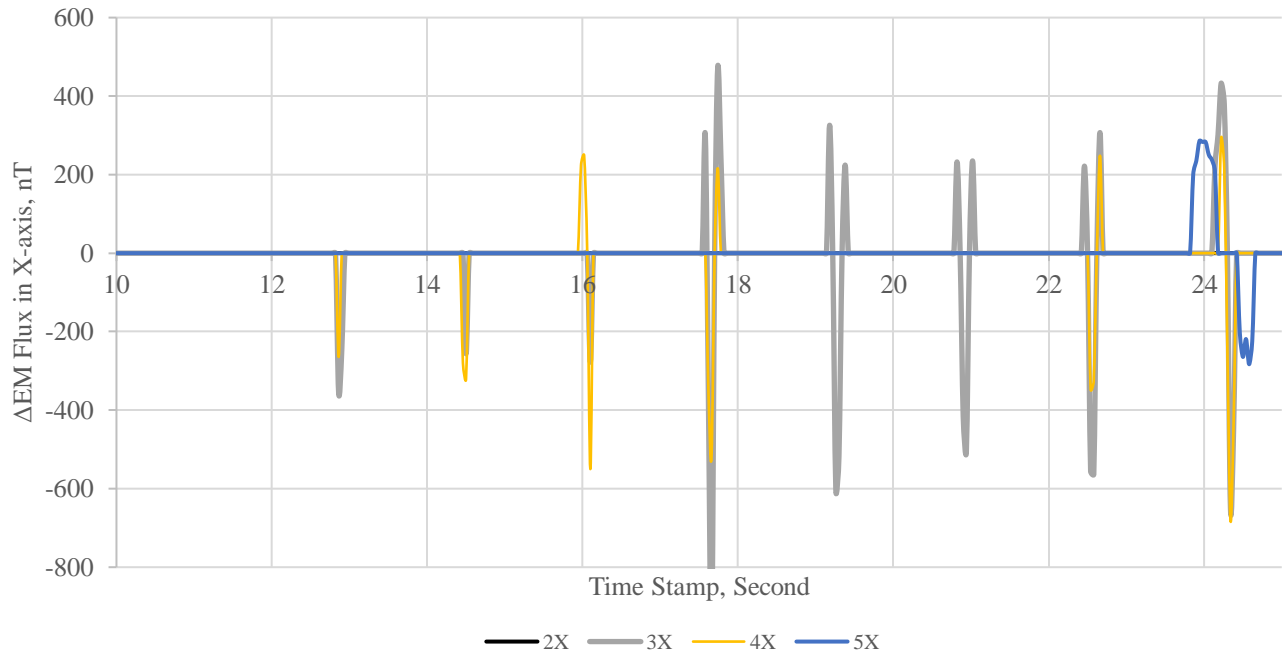
Figure 48. Graph. Signal-processed responses (ΔEM flux) for X-axis sensors 2–5 (Case #3).
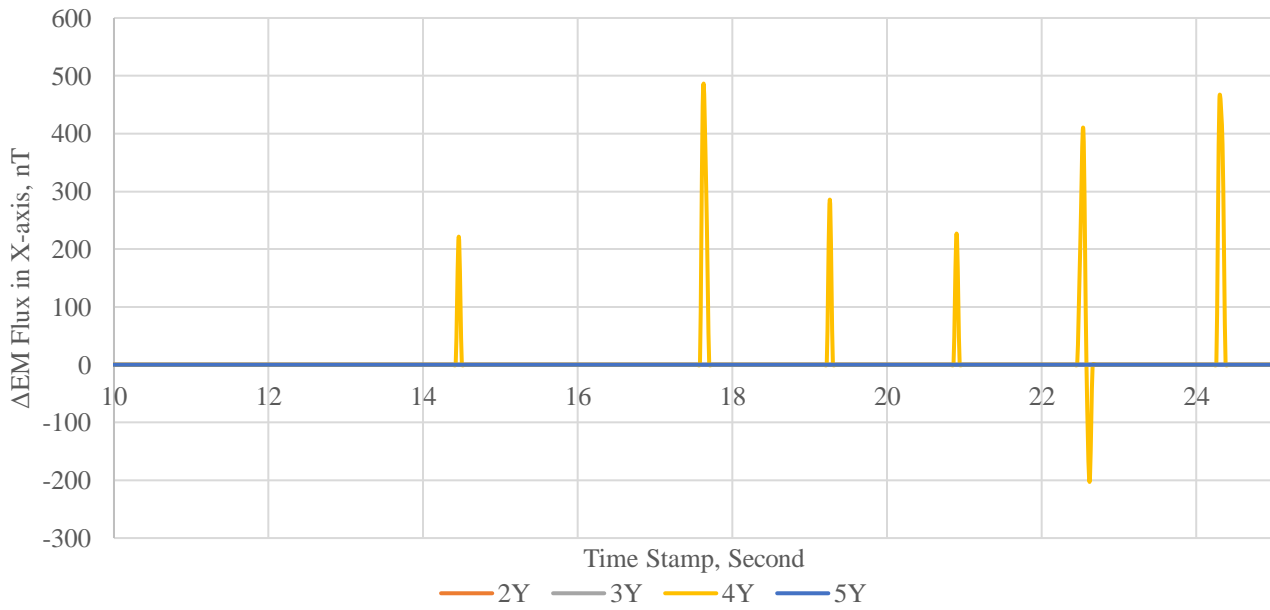
Figure 49. Graph. Signal-processed responses (ΔEM flux) for Y-axis sensors 2–5 (Case #3).
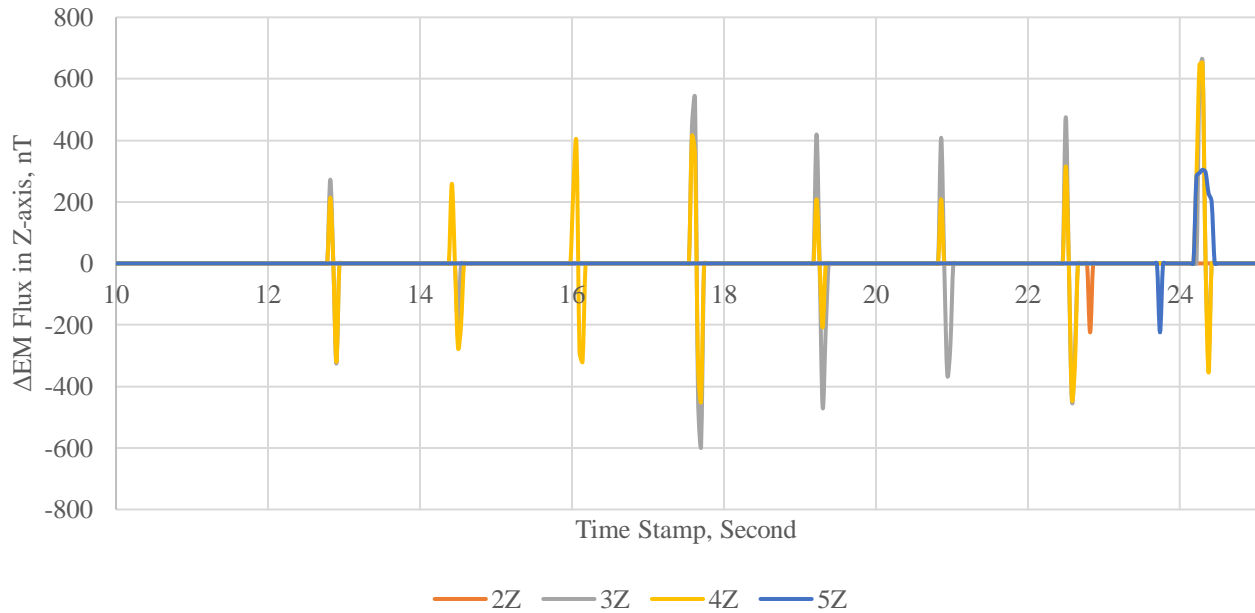
Figure 50. Graph. Signal-processed responses (ΔEM flux) for Z-axis sensors 2–5 (Case #3).

Table 7. Summary of Cart Offset from Centerline of Lane

Location of Highest Peak	Axis	Strip #1	Strip #2	Strip #3	Strip #4	Strip #5	Strip #6	Strip #7	Strip #8
1st Highest Peak Sensor	X	3	4	4	3	3	3	3	3
	Y	–	4	–	4	4	4	4	4
	Z	3	4	4	3	3	3	3	4
2nd Highest Peak Sensor	X	4	3	3	4	4	4	4	4
	Y	–	–	–	3	–	–	3	3
	Z	4	3	3	4	4	4	4	4
Cart Offset from C_L of Lane Path (in.)		0-3 L	0-3 R	0-3 R	0-3 L	0-3 L	0-3 L	0-3 L	0-3 L

FINDINGS

The experimental field results revealed several important findings about the invisible lane-markings and 3-axes magnetometers. First, the invisible marking containing 20% CrO_2 by weight successfully generated a distinct electromagnetic pavement signature for both speed and maneuvering actions. This demonstrated the material's ability to create a reliable EM signature. Second, signal-processing techniques, including signal normalization to time zero, the removal of Earth's background magnetic field, and high- and low-frequency noise filtering, effectively eliminated EM noises from the raw data that would prevent accurate interpretation of speed, maneuvering, or lane offset. This improvement allowed the system to accurately interpret encoded EM signatures and ultimately convey correct instructions to a driver. Third, speed predictions of the cart using the 3-axis magnetometers

consistently produced accurate and precise results, closely matching GPS speed measurements. Signal data from both X- and Z-axes of the magnetometers provided reliable verification for speed and maneuvering actions. Some peaks were unclear in the Y-axis direction, and, thus, this sensor could not always be used with this configuration of strips, material, and sensor arrangement. Additionally, lane-merge actions for Case #2 were accurately predicted by all sensors, utilizing data from both the X- and Z-axes. Finally, the cart positioning system, derived from the lane-keeping signatures in Case #3, successfully indicated the EM path based on the two highest peak signals from the sensor array, which closely correlated with the actual path of the cart's movement.

CHAPTER 5: SUMMARY, CONCLUSIONS, AND RECOMMENDATIONS

This study investigated the use of invisible roadway markings with electromagnetic signatures for enhancing safety in construction work zones. The experimental setup involved a series of tests using a cart equipped with a 3-axis magnetometer to detect and process EM signals from invisible markings composed of 10% and 20% CrO_2 as well as commercially available magnetic tape. The goal of the project was to evaluate the effectiveness of these signatures for in-vehicle speed warnings, lane-merge warnings, and lane-keeping assistance. The field study looked at detection of invisible lane-marking specimens at various test offsets (left, right, center, or variable lateral positions) and orientation angles (0, 60, 90, and 180 degrees). Overall, passive sensing signatures were captured reliably and as expected with 3-axis magnetometers.

The results of the field study demonstrated that the addition of multiple detection axes of the magnetometer sensor offers redundant information, mitigating the risk of erroneous maneuvers triggered by unexpected EM noise, which could occur in single-axis sensor systems. By validating the acquired signals on orthogonal axes before issuing instructions to the vehicle control unit, the proposed system can achieve enhanced reliability and robustness across a variety of operational conditions. The EM invisible markings acquired in the field provided clear and consistent signals for speed and maneuvering actions. The signal-processing techniques employed, including zero-shifting, background noise removal, and frequency filtering, were successful in refining the raw EM signals to achieve accurate and actionable data for further processing. Speed predictions derived from both the X- and Z-axes of the magnetometers successfully aligned with GPS measurements, confirming the reliability of the system. The lane-merge actions were also accurately predicted by the sensor system and EM specimens, emphasizing the system's capability to guide vehicle maneuvers effectively. The lane-keeping signatures, which were EM strips oriented longitudinally, also proved effective, with the peak signals closely matching the actual path of the cart. This alignment demonstrated that the system could reliably approximate the cart's position relative to the centerline of the test lane. The results indicated that the highest peak signals can be used to estimate the cart's offset from the centerline, providing useful feedback for lane-keeping or other vehicle trajectory algorithms.

In summary, the experimental study validated the potential of EM pavement signature technology for improving safety in construction work zones by using ADAS vehicles. The consistent performance across different EM specimen arrangements, sensor axes, and scenarios (orientation of strips) highlights the feasibility of integrating this technology into practical applications. Furthermore, a simple method to magnetize an epoxy-based marking with CrO_2 powder was successfully demonstrated.

The recommendations for future work include further refinement of the EM marking materials to enhance signal clarity, exploring the integration of additional sensors for more comprehensive data capture, and conducting actual roadway trials with the sensor system on an ADAS vehicle to validate the system's performance in varied environmental conditions. Since the speed and merging instruction signatures could be precisely observed by the pavement-assisted passive sensing system,

investigating the potential to expand the system's capabilities to include other maneuvering actions, such as enhancing steering control of automated vehicles or vehicle path trajectory planning with the pavement-assisted passive sensing system, could provide enhanced safety, operational efficiency, and comfort.

PROJECT OUTPUTS, OUTCOMES, AND IMPACTS

OUTPUTS

Presentations:

1. "Enhancing Concrete Pavement Work Zone Safety Through Passive Material Sensing," 13th International Conference on Concrete Pavement, Minneapolis, MN, August 2024.

2. "Smart Construction Work Zone Safety with ADAS and Passive Road Sensing," CCAT Safety Working Group, Sept 27, 2024.

3. "Lane Keeping & Construction Work Zone Safety with ADAS and Passive Road Sensing," U-M/NHTSA Webinar Series, Oct. 3, 2024.

4. Transportation Research Board 2025 Annual Meeting, Washington, DC, Accepted, JAN 2025.

Journal/Conference Papers:

1. Sakulneya, A., and J. Roesler, Enhancing Concrete Pavement Work Zone Safety Through Passive Material Sensing, 13th International Conference on Concrete Pavement, Minneapolis, MN, 2024. (Accepted for publication)

2. Sakulneya, and J. Roesler, V2I Work Zone Communication through Pavement Signage Coded on Road Surface, Transportation Research Board 2025 Annual Meeting, Washington, DC, 2025. (Under reviewed)

Inventions:

1. Roesler, J. and Sakulneya, A. (2023), Passive on-Vehicle Sensing of Pavement Signage Coded on Roadways, Non-Provisional Patent No. 63/591,657.

OUTCOMES

The project outcomes will lead to policy changes that address and improve CWZ safety by V2I communication through EM material sensing and invisible and programmable markings. This research has increased understanding and awareness of how electromagnetic signatures on pavements can improve vehicle guidance and safety in construction zones, contributing to the broader knowledge of transportation safety. This specific project validated the effectiveness of 3-axis magnetometers, invisible lane markings, and signal processing techniques to indicate a vehicle action leading to improved safety in CWZ.

IMPACTS

As this research progresses and is communicated to key stakeholders, it should allow for pilot studies on vehicles through actual CWZ. This research has the potential to significantly enhance safety in construction work zones by integrating invisible electromagnetic (EM) markings on surface of the road along with new vehicle magnetometer sensors. The research impact will require additional studies with vehicles equipped with the sensors and in-vehicle messaging. By providing precise speed warnings and lane merge alerts, the system should mitigate accidents from inattentiveness and excessive speeds particular in high-risk areas. Additionally, the use of programmable materials allows for real-time communication with Advanced Driver Assistance Systems (ADAS) in vehicles. The findings could lead to broader applications of EM signature technology on roadways for CWZ as well as lane departure warning, which should improve overall roadway safety and reduction in accidents.

CHALLENGES AND LESSONS

The main challenge for adoption of this invisible lane marking and vehicle sensing system is coordination of CWZ changes with adding of several magnetometer sensors to new vehicles. Without cooperation with OEMs and owners of the road then this V2I will never see adoption. Even with agreement and cooperation, the technology would take several years, e.g., 10-years, to enable a significant number of vehicles using the roadway with the technology to have a measurable impact on CWZ safety.

REFERENCES

American Association of State Highway and Transportation Officials. (n.d.). Implementation of the AASHTO Strategic Highway Safety Plan. Retrieved July 2008, from http://safety.transportation.org/

Azimi, M., Oyelade, I., Aremu, A. M., Balal, E., Cheu, R. L., & Qi, Y. (2021). "Selection and implementation of intelligent transportation systems for work zone construction projects." *Future Transportation, 1*(2), 169–187.

Bai, Y., & Li, Y. (2006). *Determining the major causes of highway work zone accidents in Kansas* (No. K-TRAN: KU-05-1). Kansas Department of Transportation.

Cottrell, B. H. (1987). Evaluation of wide edge lines on two-lane rural roads (Publication FHWA-VA-85-37). Virginia Highway and Transportation Research Council, Virginia Department of Transportation.

Dahal, Sachindra & Roesler, Jeffery. (2021). Passive Sensing of Electrically Conductive Concrete for Lateral Vehicle Positioning. In Proceedings of the 12th International Conference on Concrete Pavements. http://dx.doi.org/10.33593/a0gjkkah

Dahal, S., & Roesler, J. (2022). Passive sensing of electromagnetic signature of roadway material for lateral positioning of vehicle (Report No. ICT-21-039, UILU-ENG-2021-2039). Illinois Center for Transportation.

Dahal, S. (2022). "Vehicle lane keeping through pavement-assisted passive sensing." [Doctoral dissertation, University of Illinois at Urbana-Champaign].

Darwesh, A., Wu, D., Le, M., & Saripalli, S. (2021). "Building a smart work zone using roadside lidar." In *2021 IEEE International Intelligent Transportation Systems Conference (ITSC)* (pp. 2602–2609). Institute of Electrical and Electronics Engineers.

El-Rayes, K., Liu, L., El-Gohary, N., & Abdelmohsen, A. Z. (2014). *Effect of flaggers and spotters in directing work zone traffic for Illinois expressways and freeways.* Illinois Center for Transportation Series No. 14-001.

Federal Highway Administration. (2003). Manual on uniform traffic control devices for streets and highways. U.S. Department of Transportation.

Fontaine, M. D., & Carlson, P. J. (2001). "Evaluation of speed displays and rumble strips at rural-maintenance work zones." *Transportation Research Record: Journal of the Transportation Research Board, 1745*(1), 27–38.

Hughes, W. E., McGee, H. W., Hussain, S., & Keegel, J. (1989). Field evaluation of edge line widths (Publication FHWA-89-111). Federal Highway Administration, United States Department of Transportation.

Li, J., Li, Q., Qiao, F., & Yu, L. (2018). Assessment of in-vehicle messages in the advance warning area of a work zone. Journal of Civil and Environmental Engineering, 8(2), 1–10

National Highway Traffic Safety Administration. (2021). Fatality and injury reporting system tool

(FIRST). Retrieved from https://cdan.dot.gov/query

Pigman, J. G., & Agent, K. R. (1990). "Highway accidents in construction and maintenance work zones." *Transportation Research Record: Journal of the Transportation Research Board, 1270,* 12-21.

Raub, R. A., Sawaya, O. B., Schofer, J. L., & Ziliaskopoulos, A. (2001). Enhanced crash reporting to explore workzone crash patterns. *Proceedings of the Annual Meeting of the Transportation Research Board, Washington DC, January 2001*, Paper No. 01, 166.

Roesler, J. R., & Dahal, S. (2024). U.S. Patent Application No. 18/368,866.

Sakulneya, A., & Roesler, J. (2023). Enhancing construction work-zone safety by passive pavement-to-vehicle communication (Report No. ICT-23-016). Illinois Center for Transportation. https://doi.org/10.36501/0197-9191/23-016

Sakulneya, A., & Roesler, J. (2024). Enhancing Concrete Pavement Work Zone Safety Through Passive Material Sensing. In Proceedings of the 13th International Conference on Concrete Pavements, Minneapolis MN, August 2024.

Wang, J. S. (2019). Target crash population for crash avoidance technologies in passenger vehicles (No. DOT HS 812 653)

APPENDIX A: SIGNAL-PROCESSING RESULTS OF PILOT STUDY (CHAPTER 3)

CASE #1

Raw EM Flux
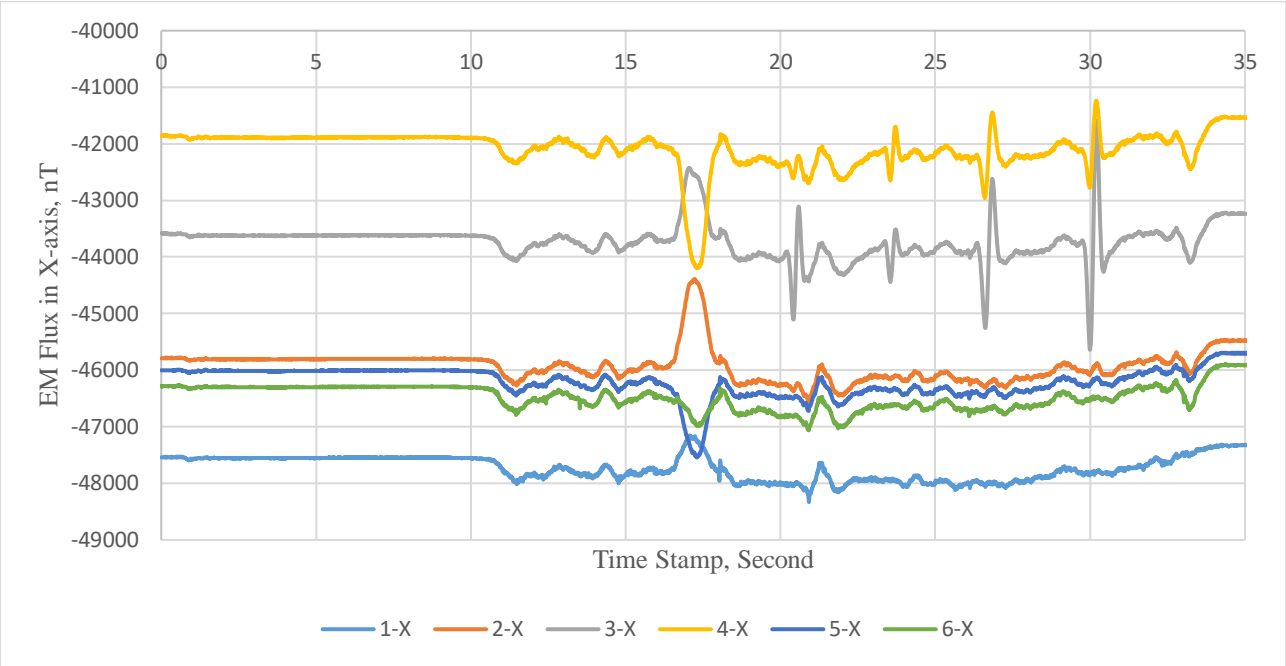
Figure 51. Graph. Raw EM flux signals for sensors X-axis (Case #1).
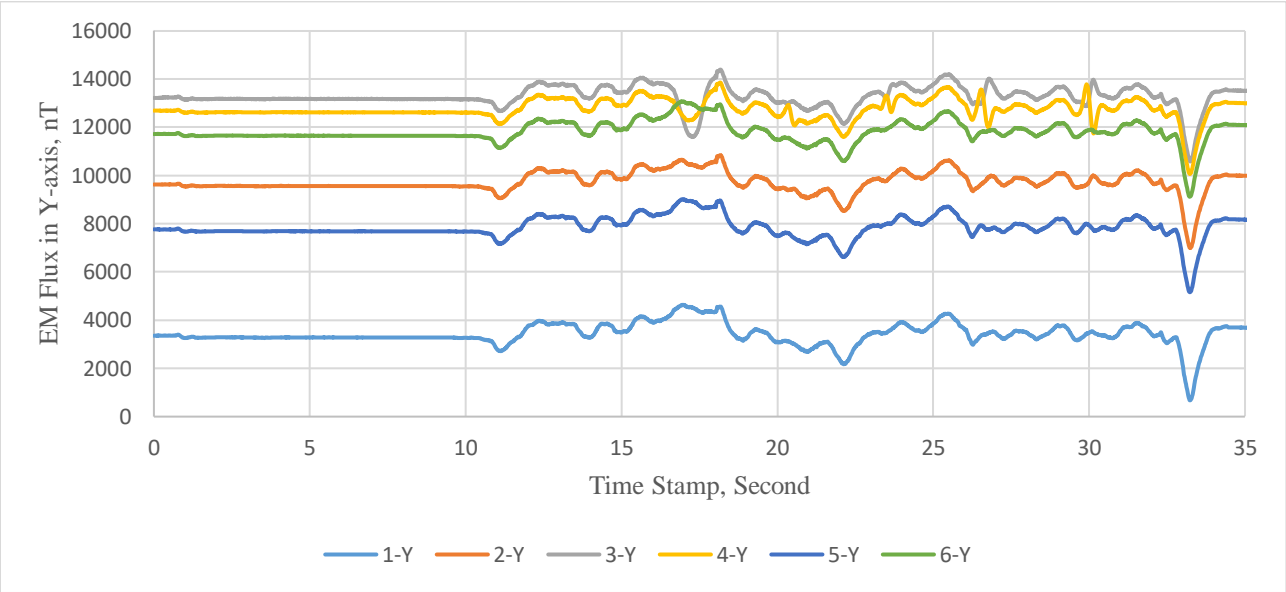
Figure 52. Graph. Raw EM flux signals for sensors Y-axis (Case #1).
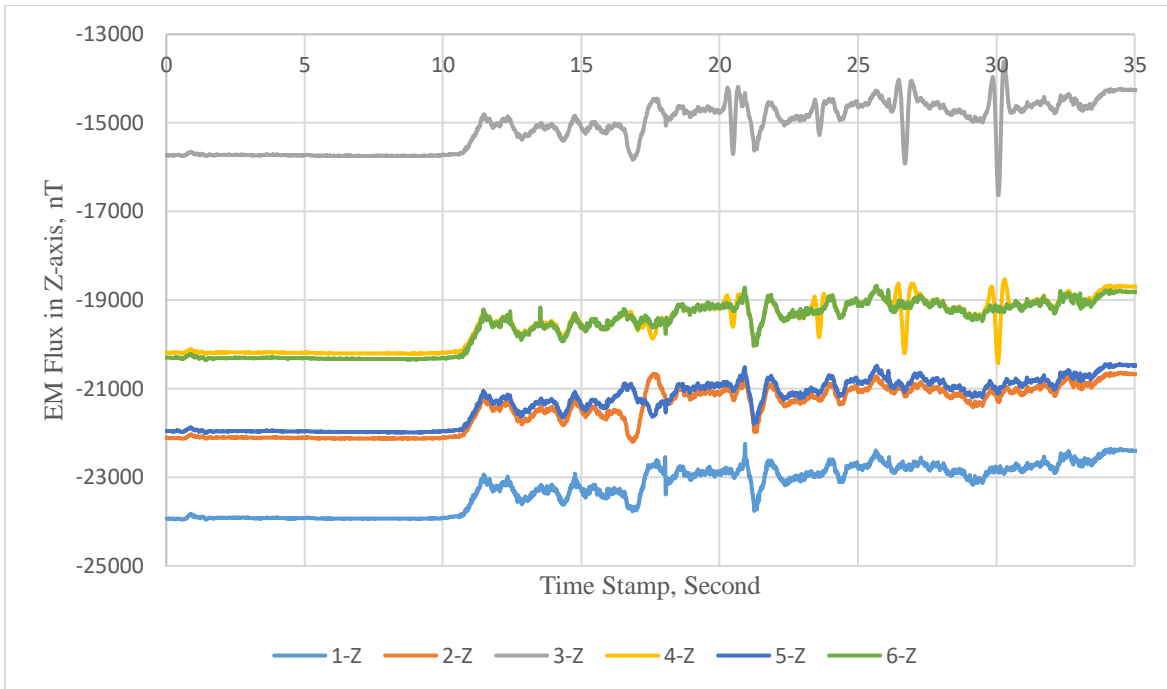
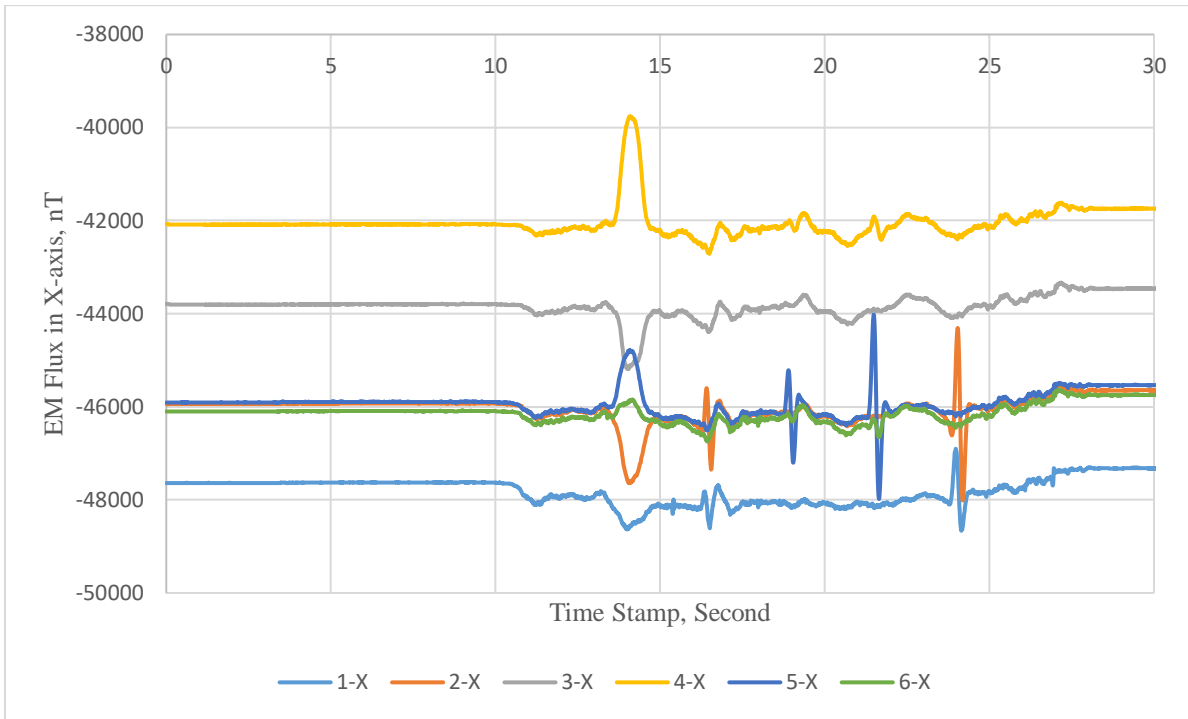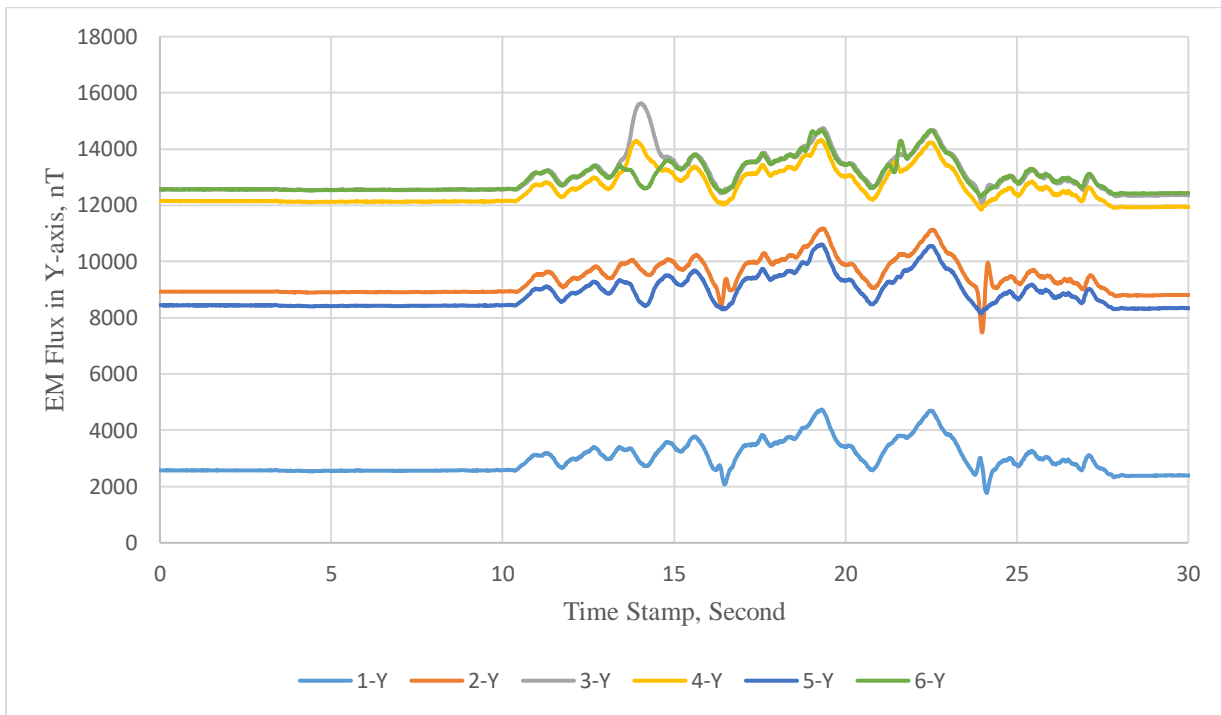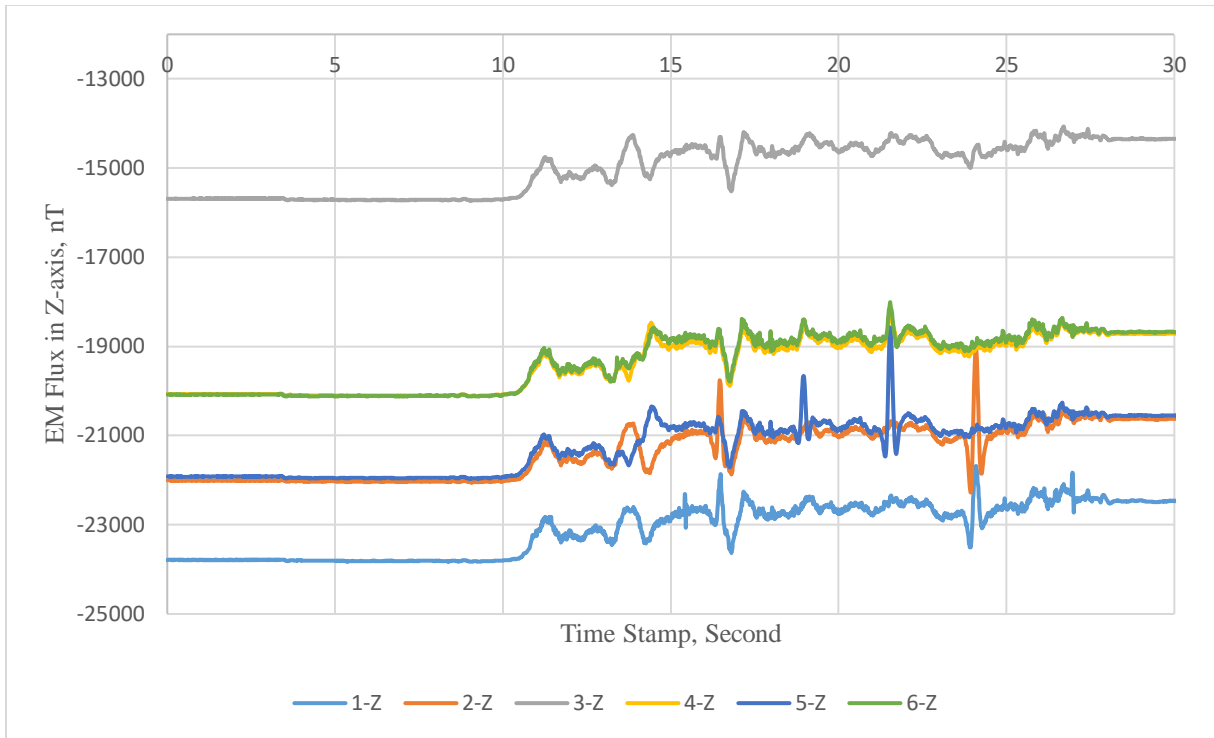**Figure 53. Graph. Raw EM flux signals for sensors Z-axis (Case #1).**

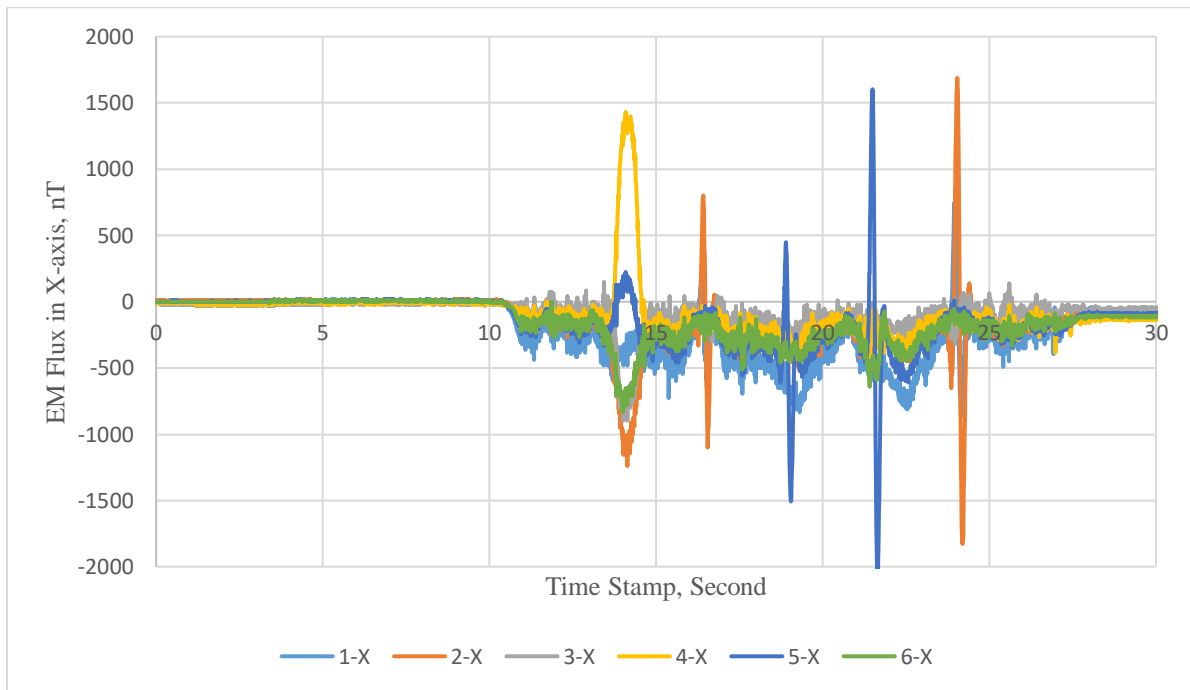## Referenced EM Flux Signal after Initializing Initial Reading Value at Zero and Gradiometer Processing
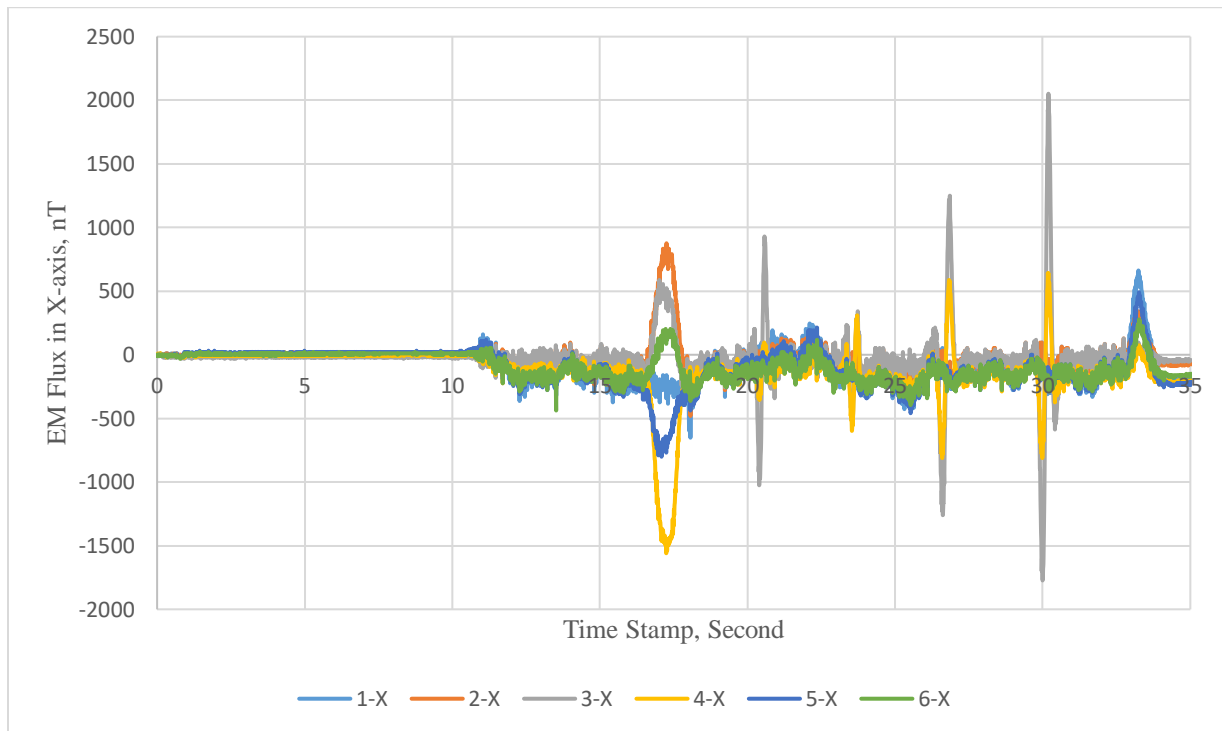
Figure 54. Graph. Referenced EM Flux Signal after initializing initial reading value at zero and gradiometer processing for sensors X-axis (Case #1).

Figure 55. Graph. Referenced EM Flux Signal after initializing initial reading value at zero and gradiometer processing for sensors Y-axis (Case #1).
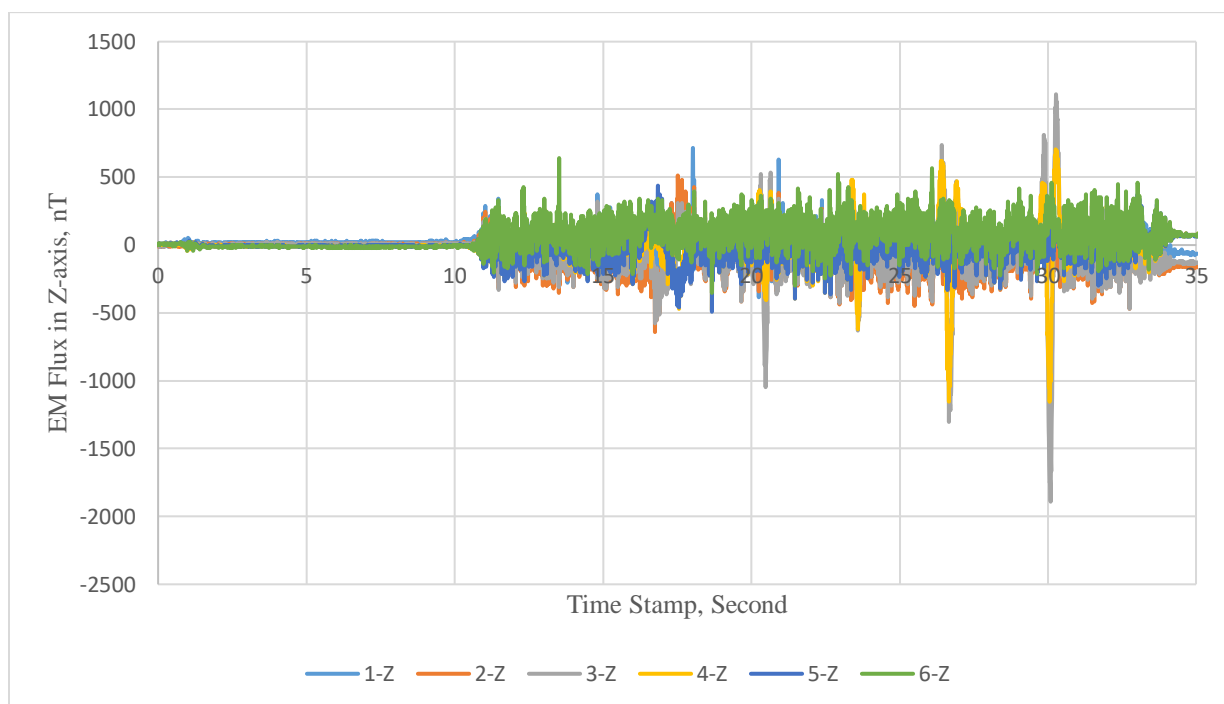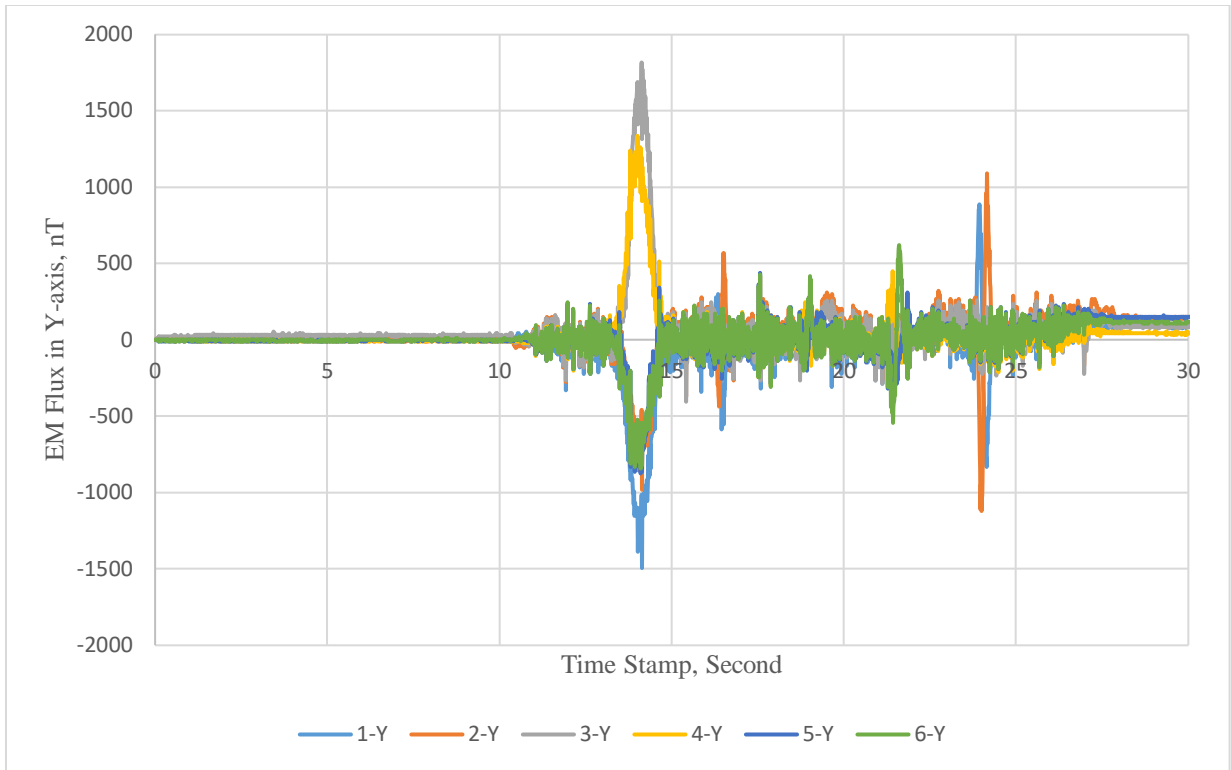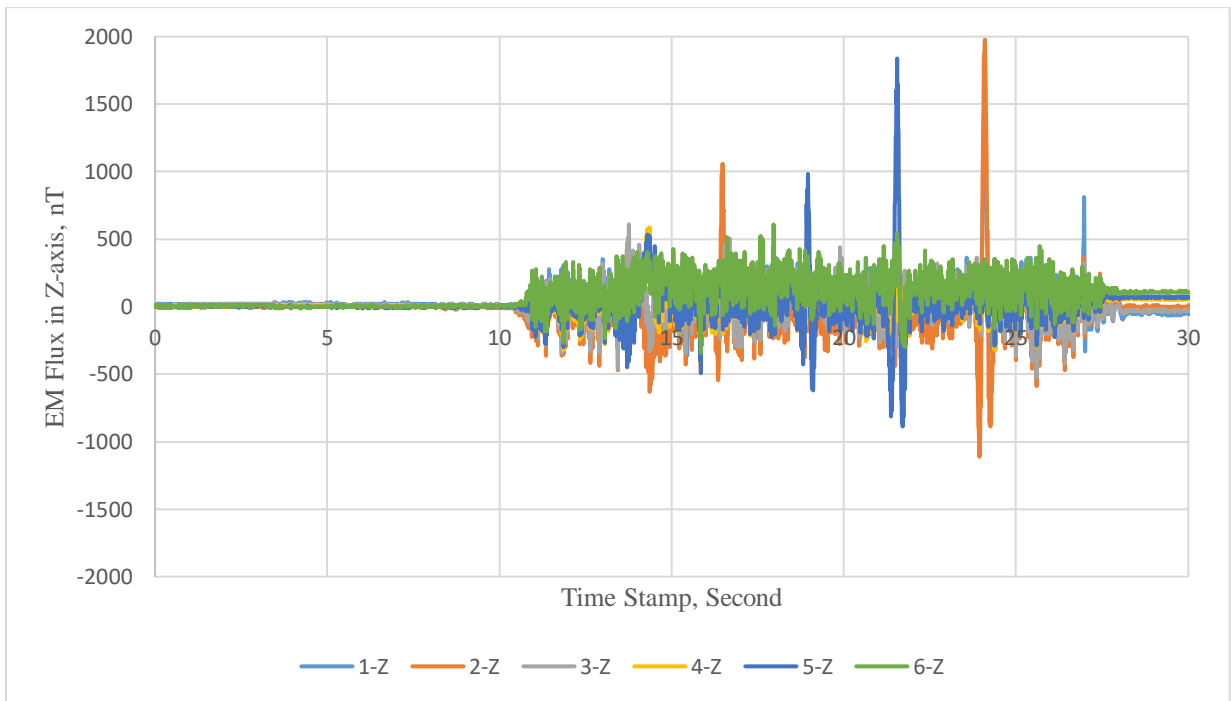

Figure 56. Graph. Referenced EM Flux Signal after initializing initial reading value at zero and gradiometer processing for sensors Z-axis (Case #1).
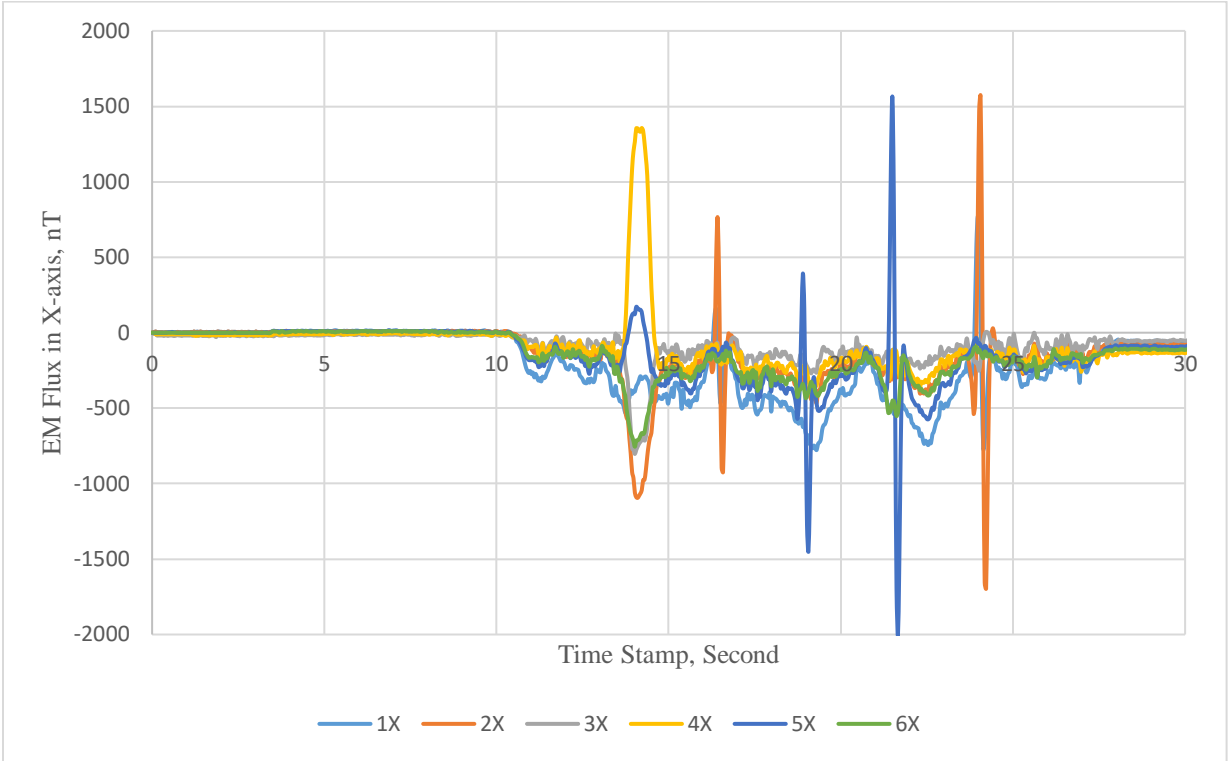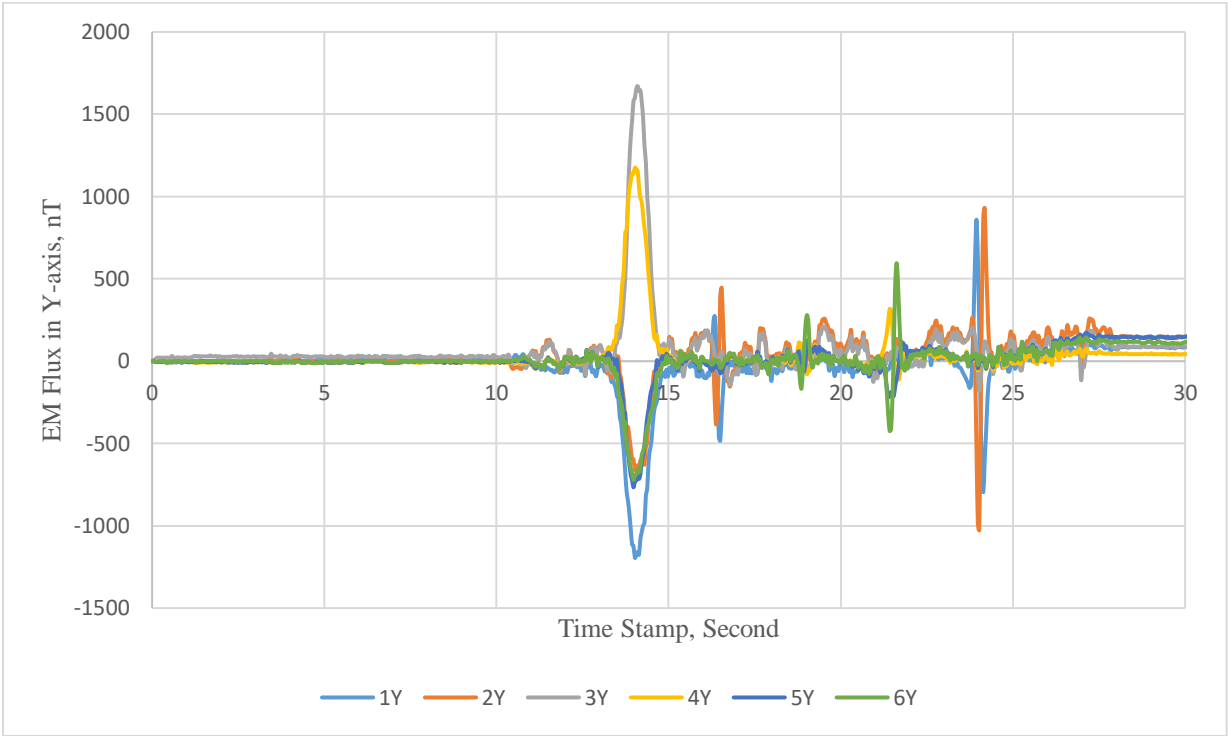
High-Frequency Filtered EM Flux
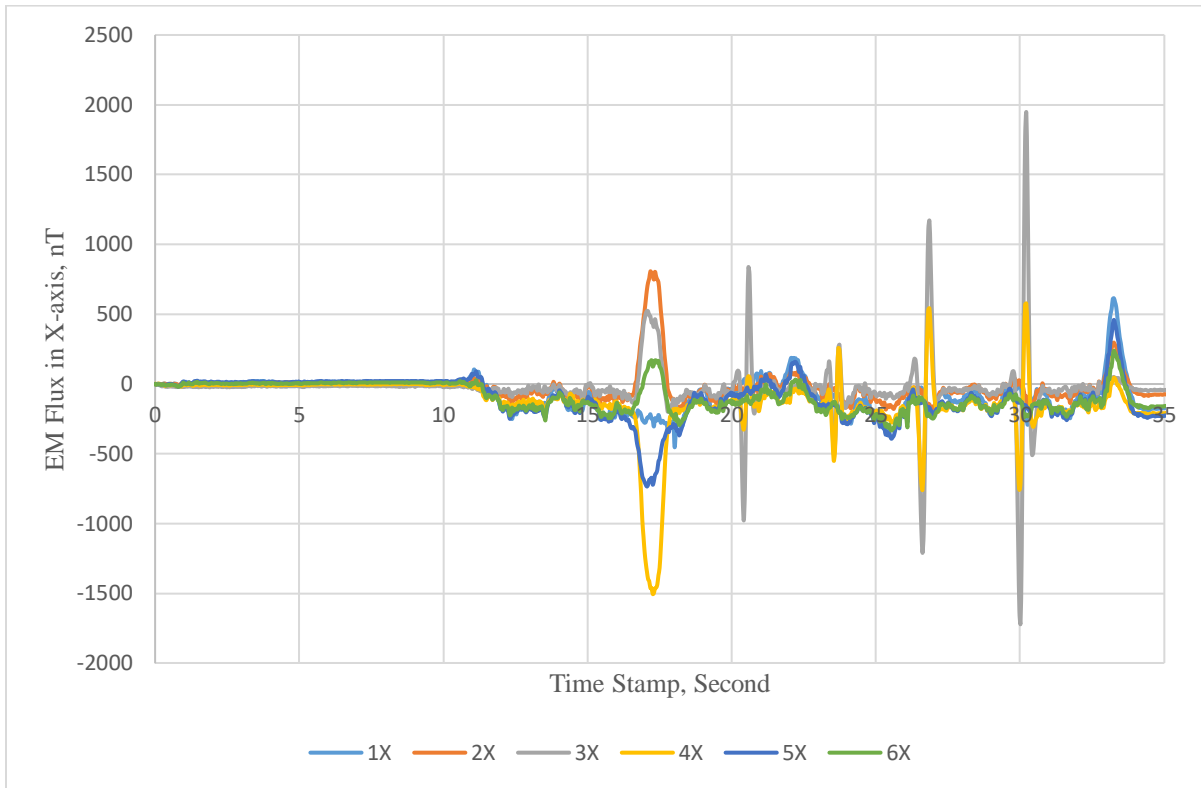
Figure 57. Graph. High-frequency filtered EM flux for sensors in X-axis (Case #1).
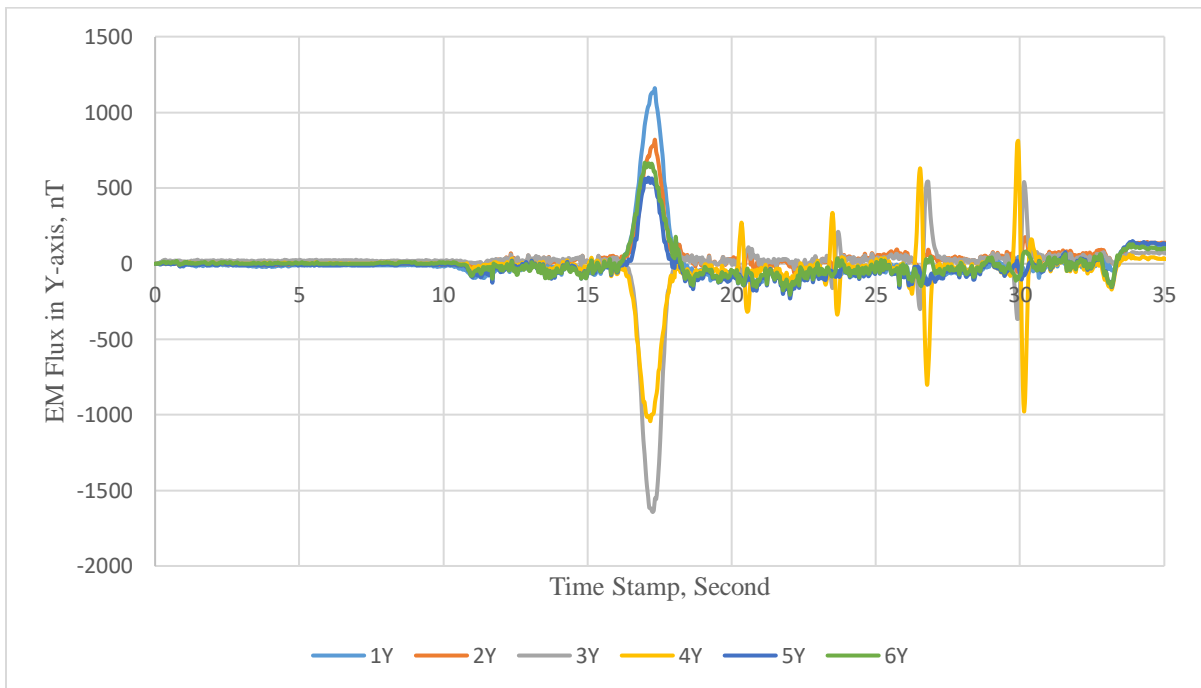
Figure 58. Graph. High-frequency filtered EM flux for sensors in Y-axis (Case #1).
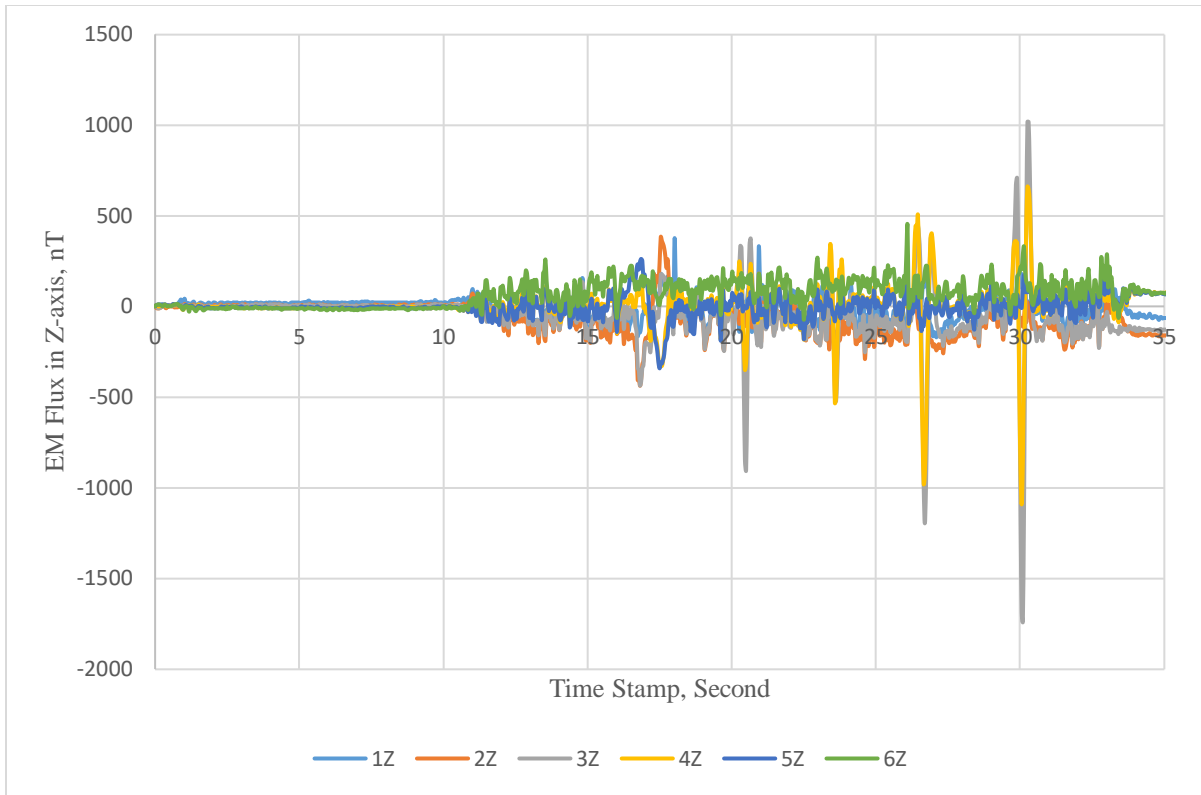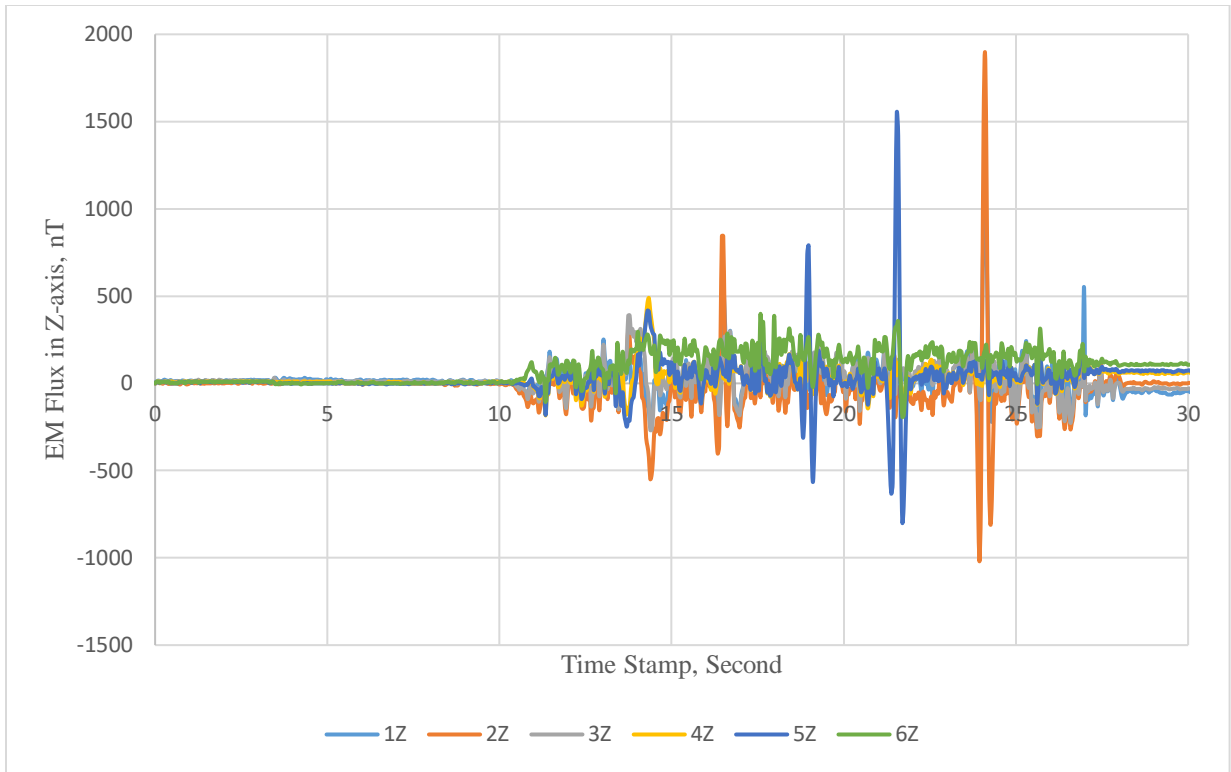
Figure 59. Graph. High-frequency filtered EM flux for sensors in Z-axis (Case #1).
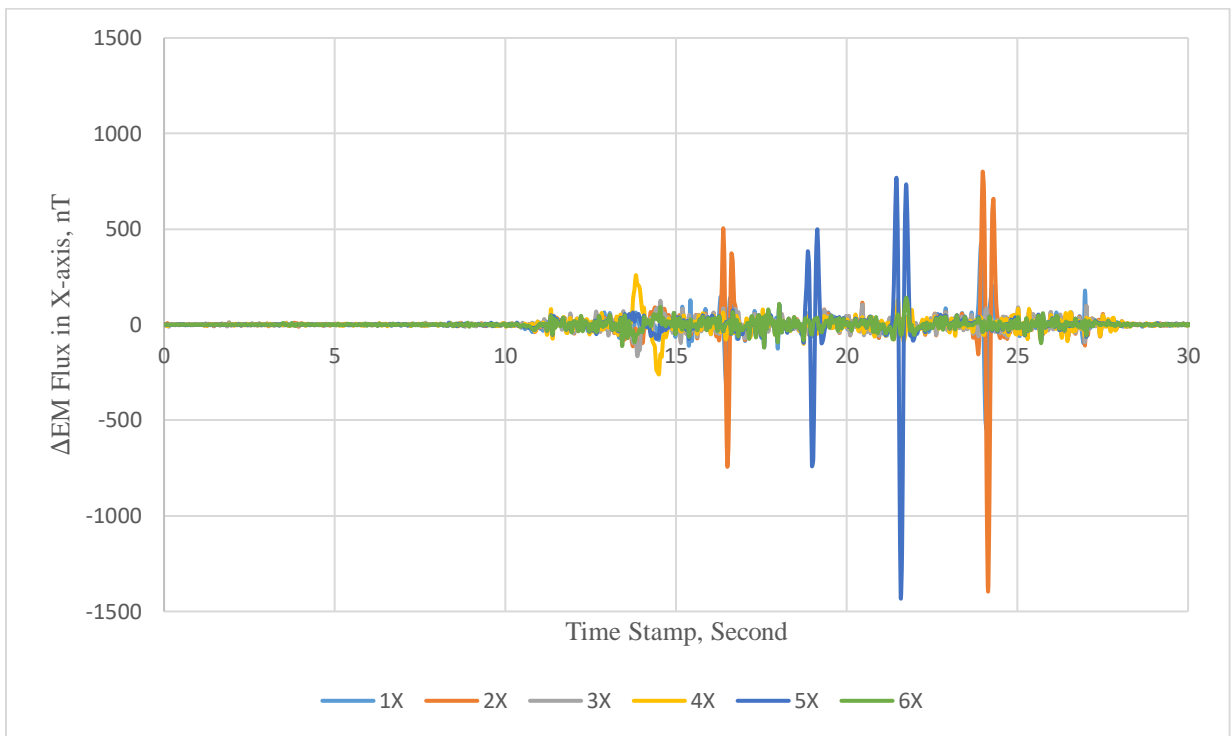
Low- and High-Frequency Filtered EM Flux
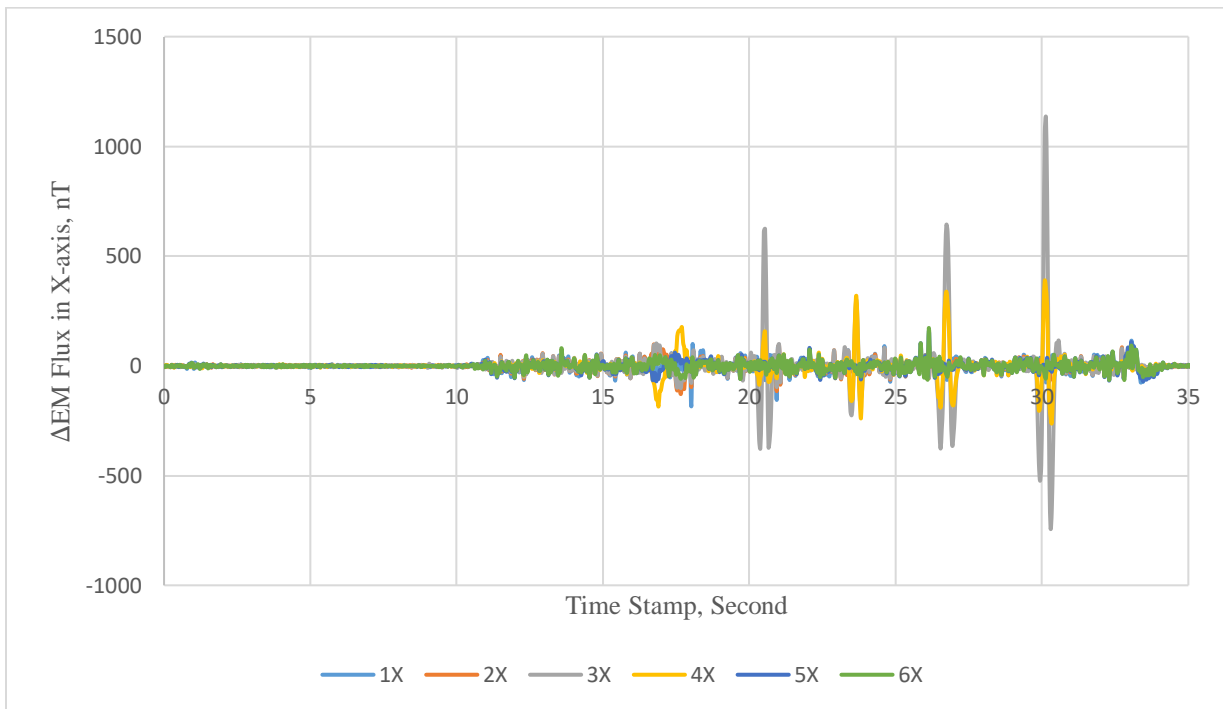
Figure 60. Graph. Low- and high-frequency filtered ΔEM flux for sensors in X-axis (Case #1).
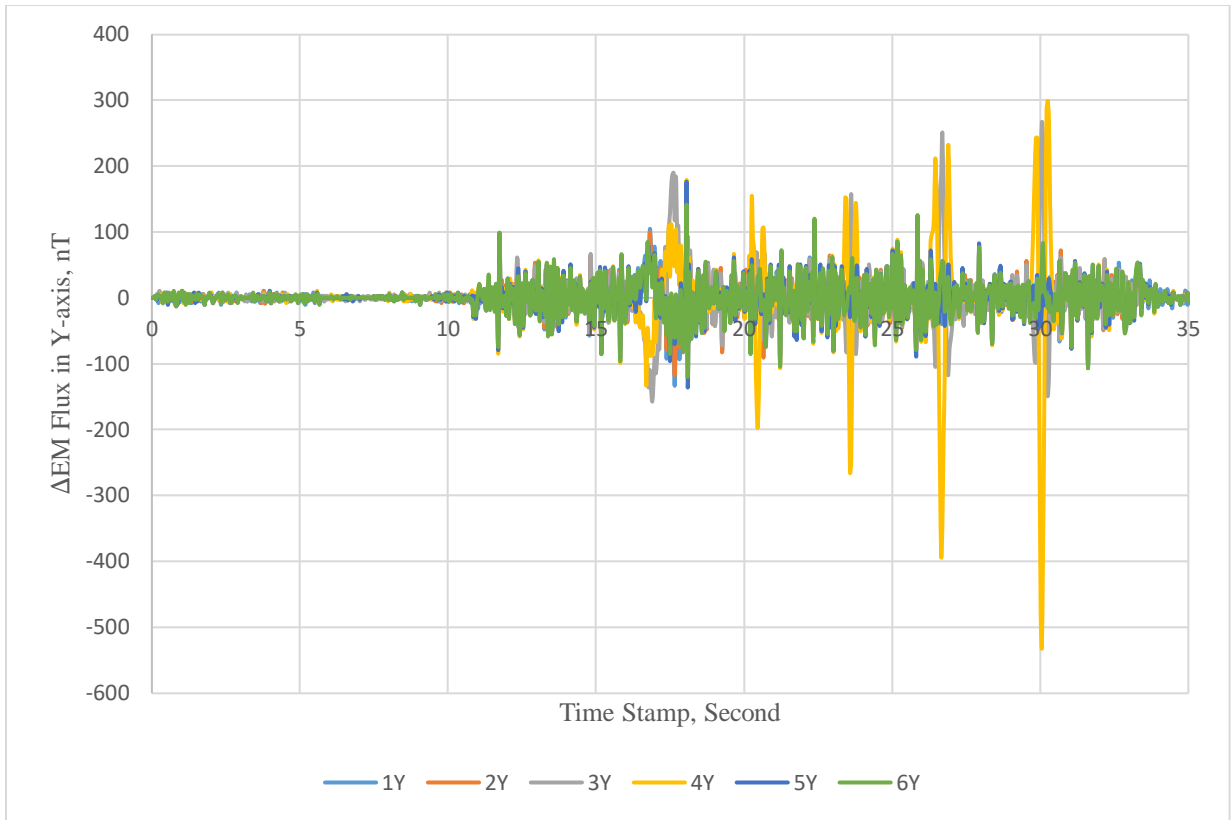
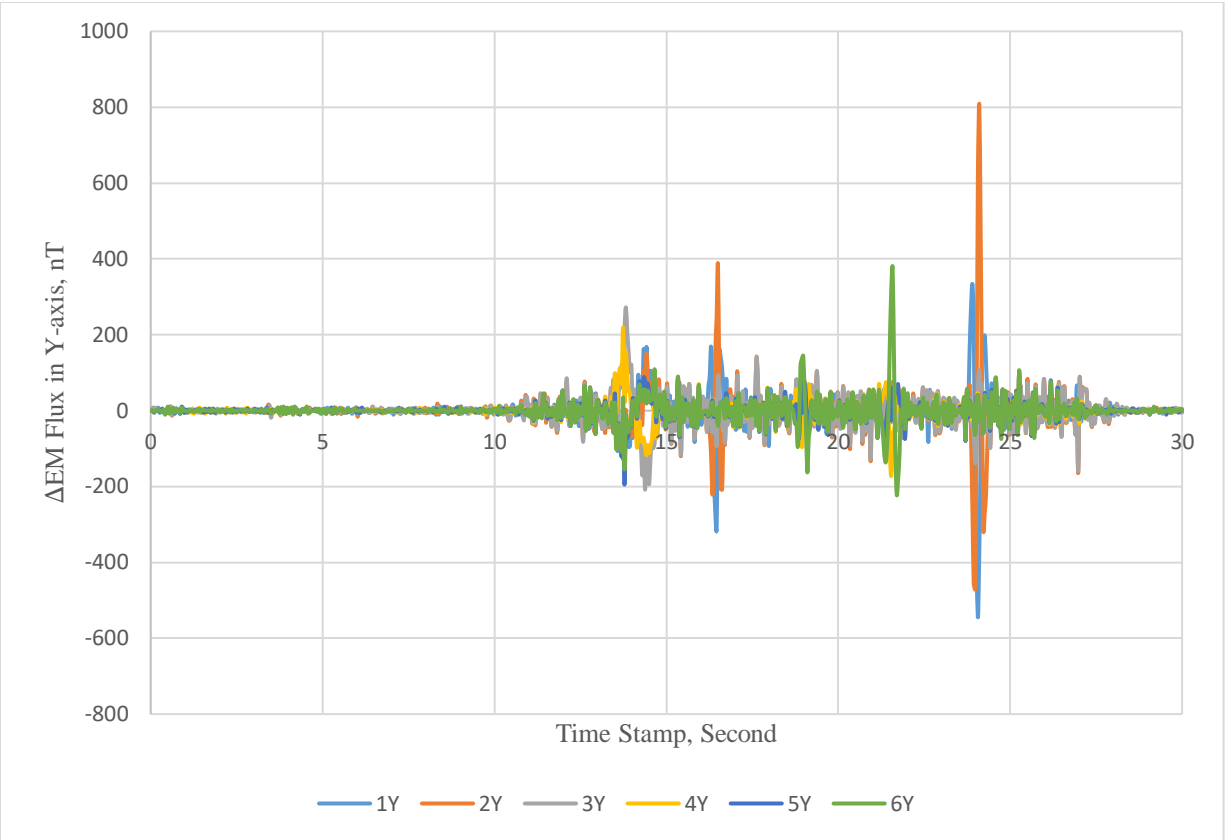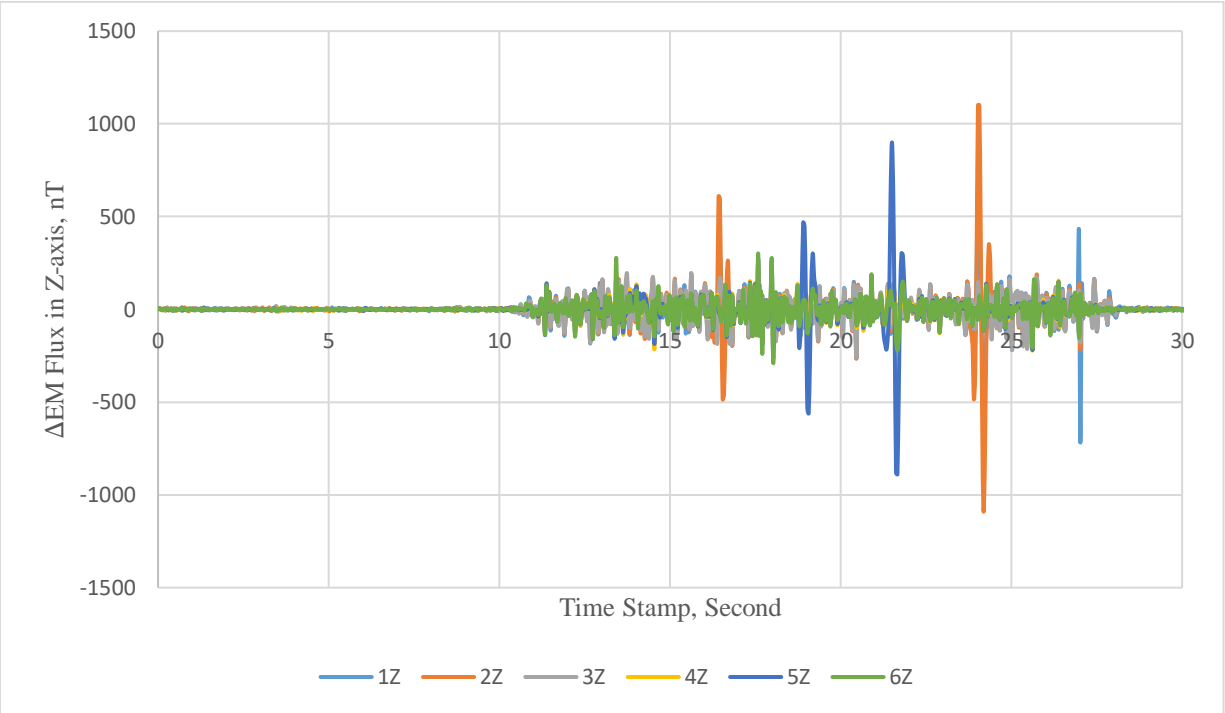**Figure 61. Graph. Low- and high-frequency filtered ΔEM flux for sensors in Y-axis (Case #1).**
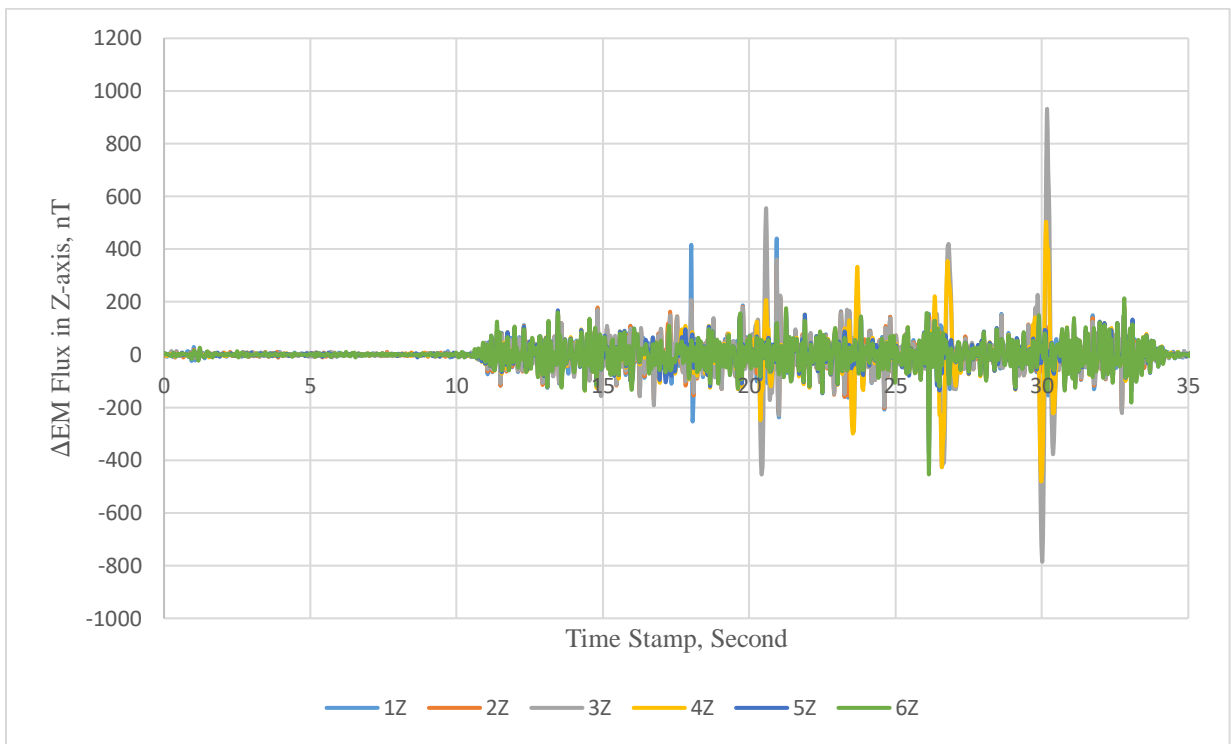
Figure 62. Graph. Low- and high- frequency filtered ΔEM flux for sensors in Z-axis (Case #1).
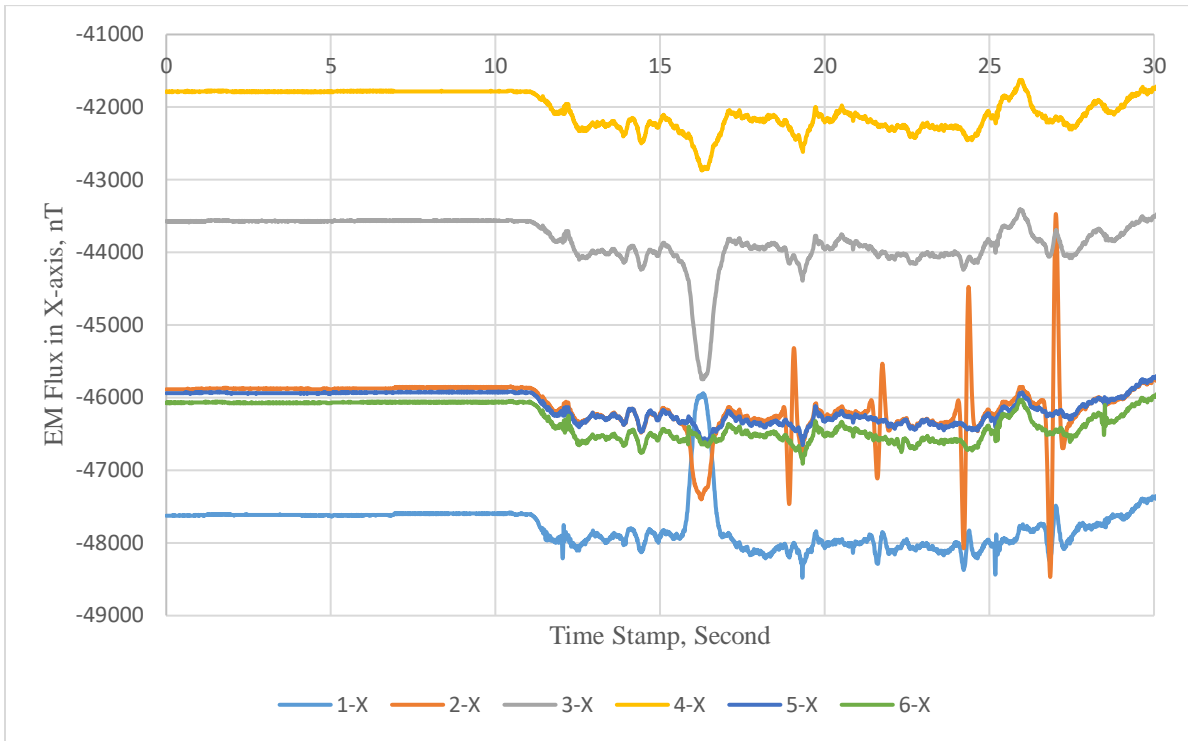
CASE #2

Raw EM Flux

Figure 63. Graph. Raw EM flux signals for sensors in X-axis (Case #2).
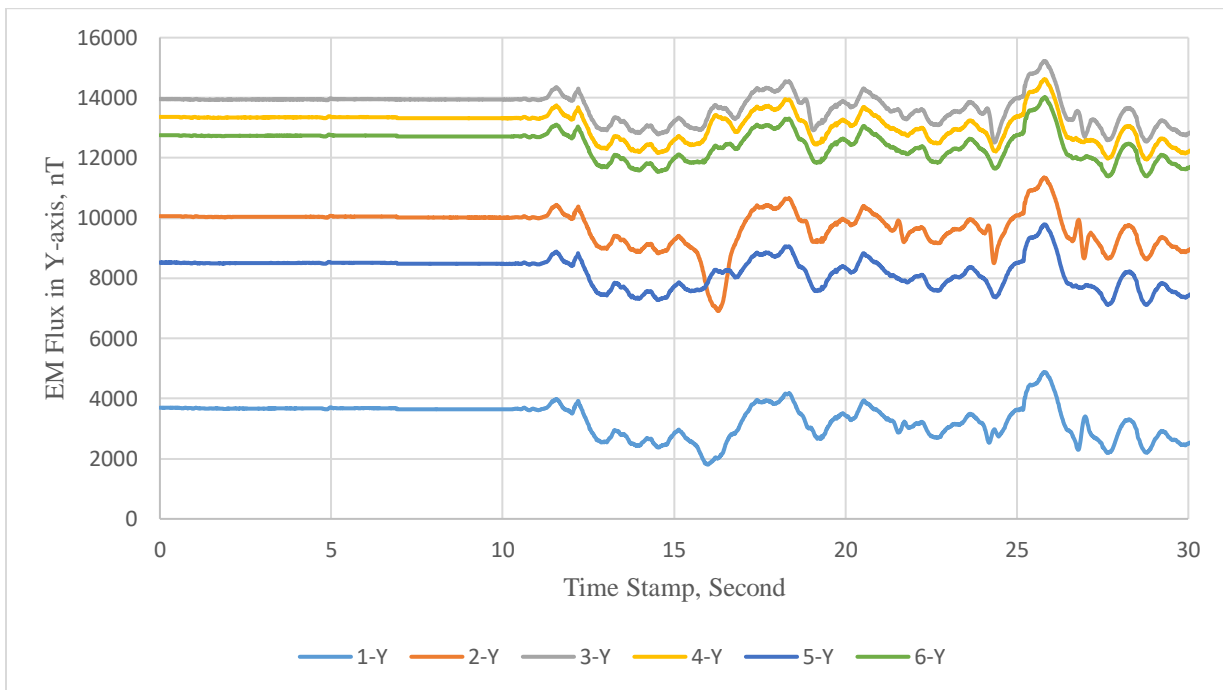
Figure 64. Graph. Raw EM flux signals for sensors in Y-axis (Case #2).
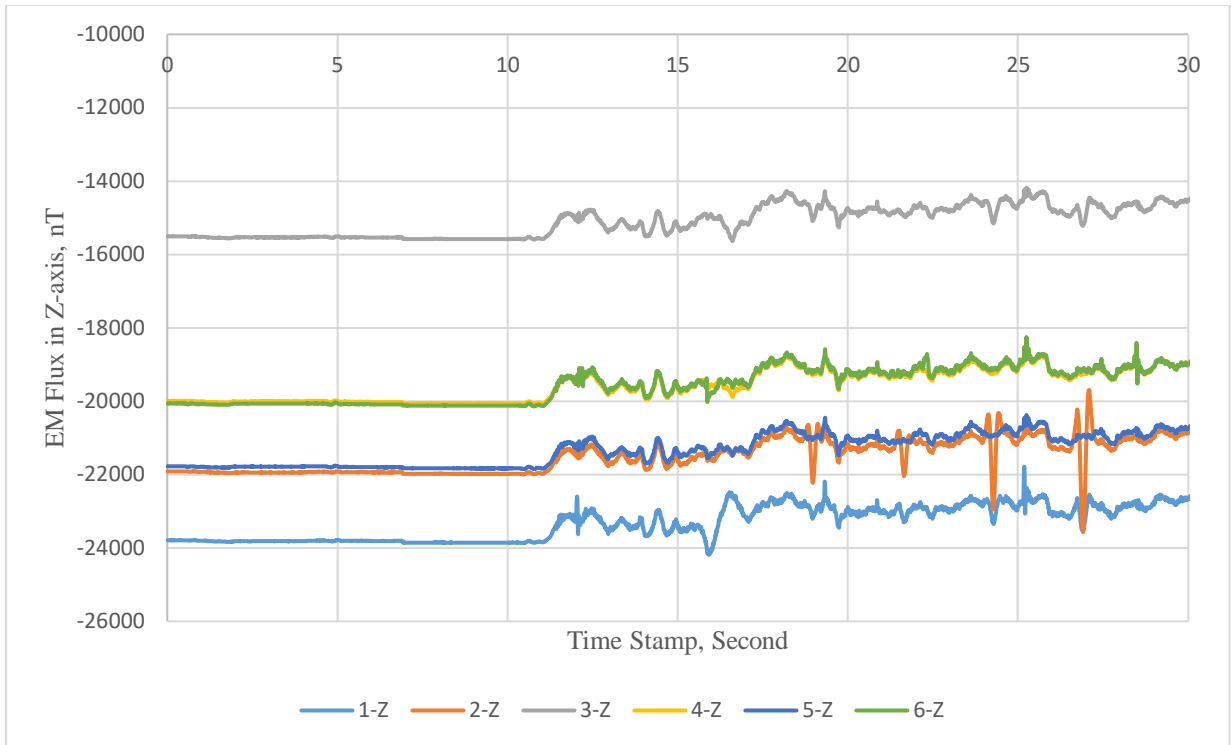
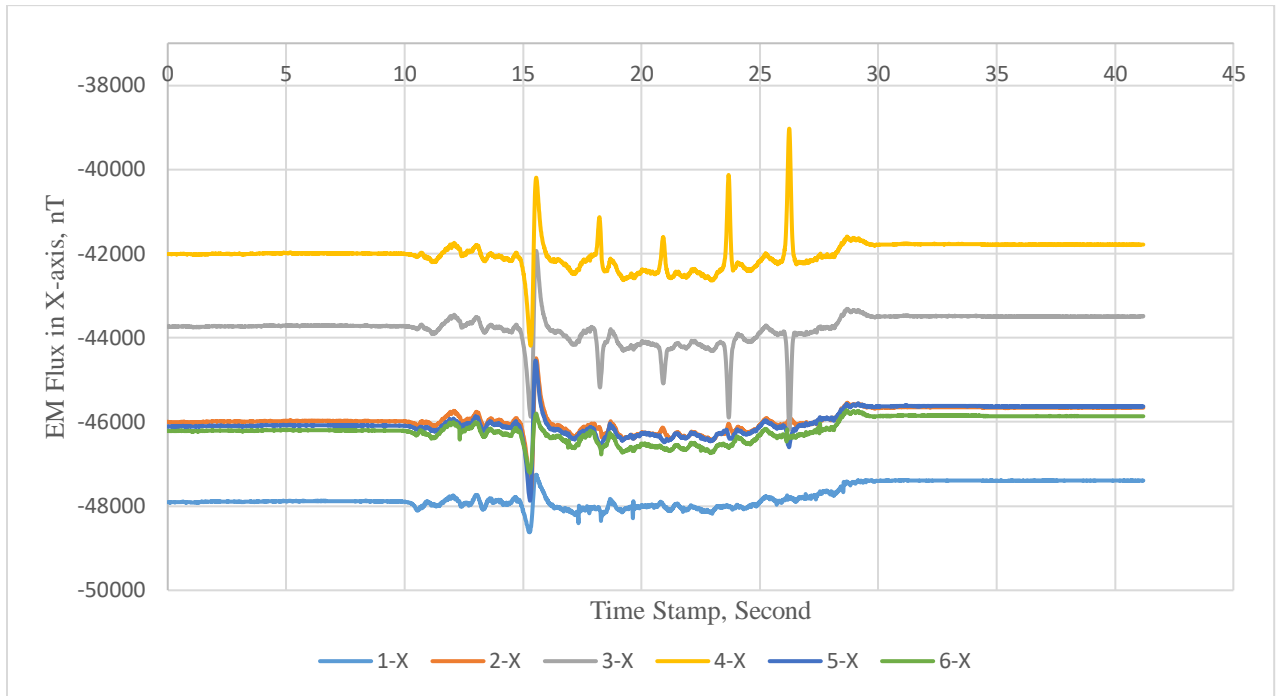**Figure 65. Graph. Raw EM flux signals for sensors in Z-axis (Case #2).**

Referenced EM Flux Signal after Initializing Initial Reading Value at Zero and Gradiometer Processing
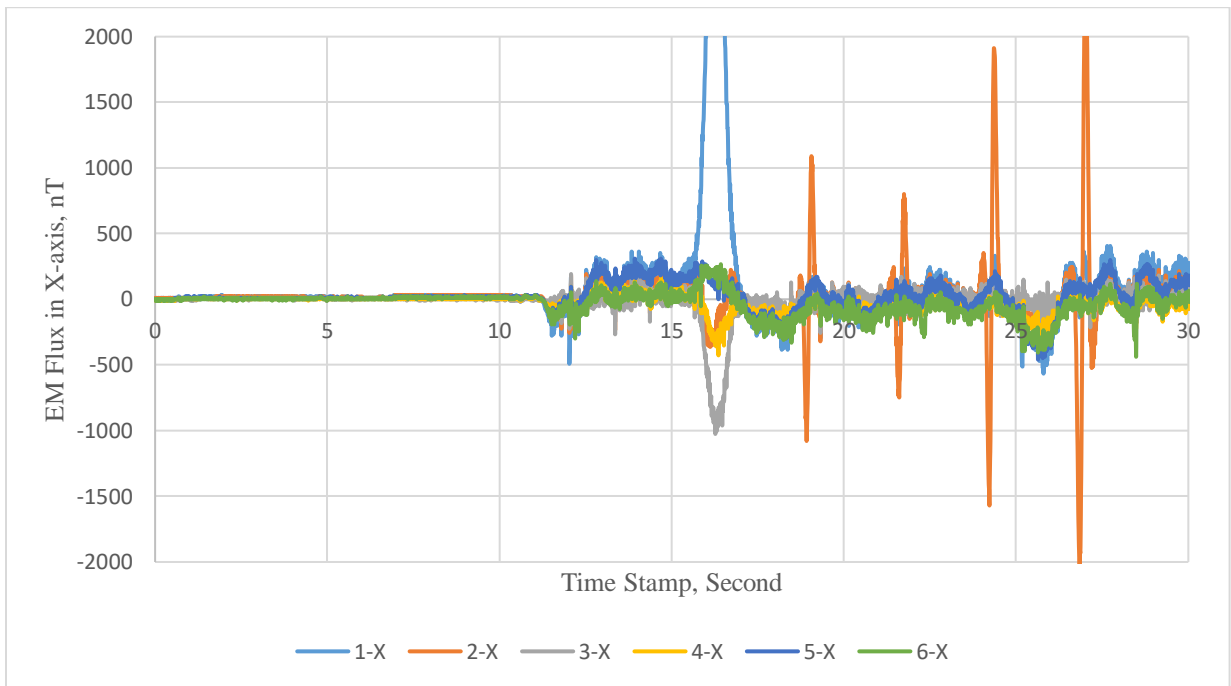
Figure 66. Graph. Referenced EM Flux Signal after initializing initial reading value at zero and gradiometer processing for sensors in X-axis (Case #2).
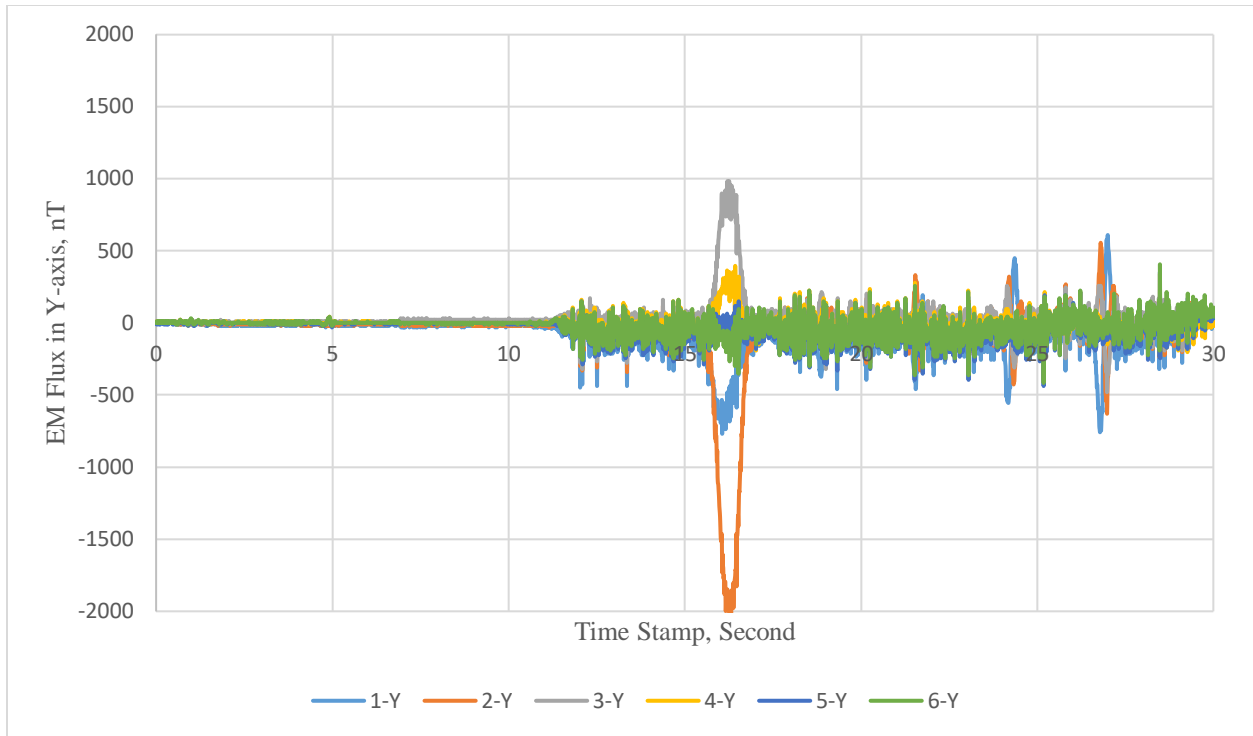
Figure 67. Graph. Referenced EM Flux Signal after initializing initial reading value at zero and gradiometer processing for sensors in Y-axis (Case #2).
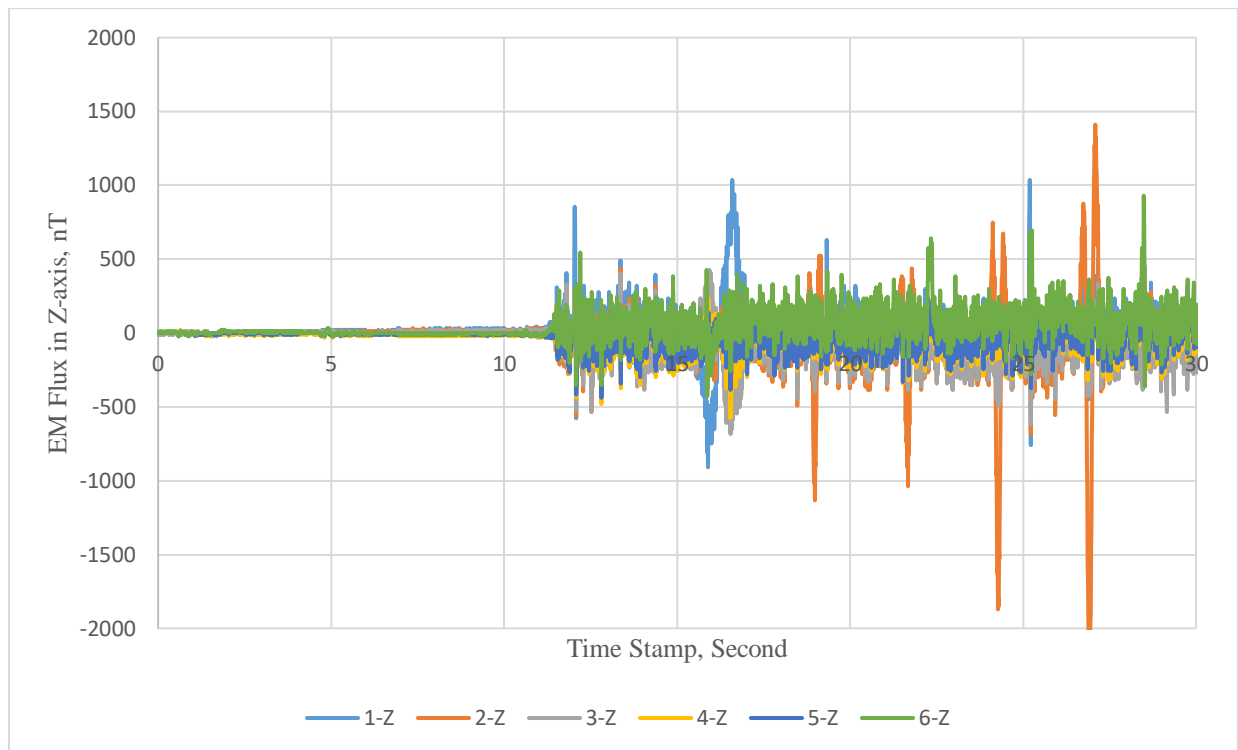
Figure 68. Graph. Referenced EM Flux Signal after initializing initial reading value at zero and gradiometer processing for sensors in Z-axis (Case #2).

High-Frequency Filtered EM Flux
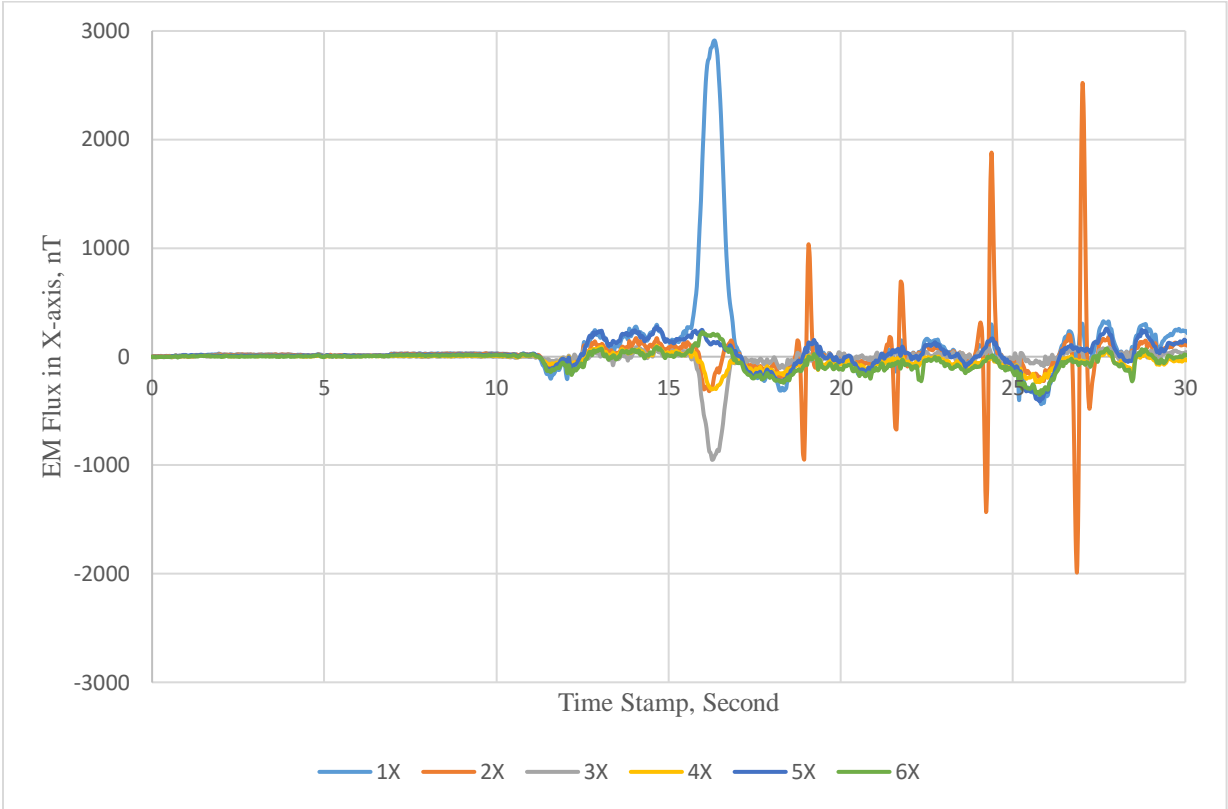
Figure 69. Graph. High-frequency filtered EM flux for sensors in X-axis (Case #2).
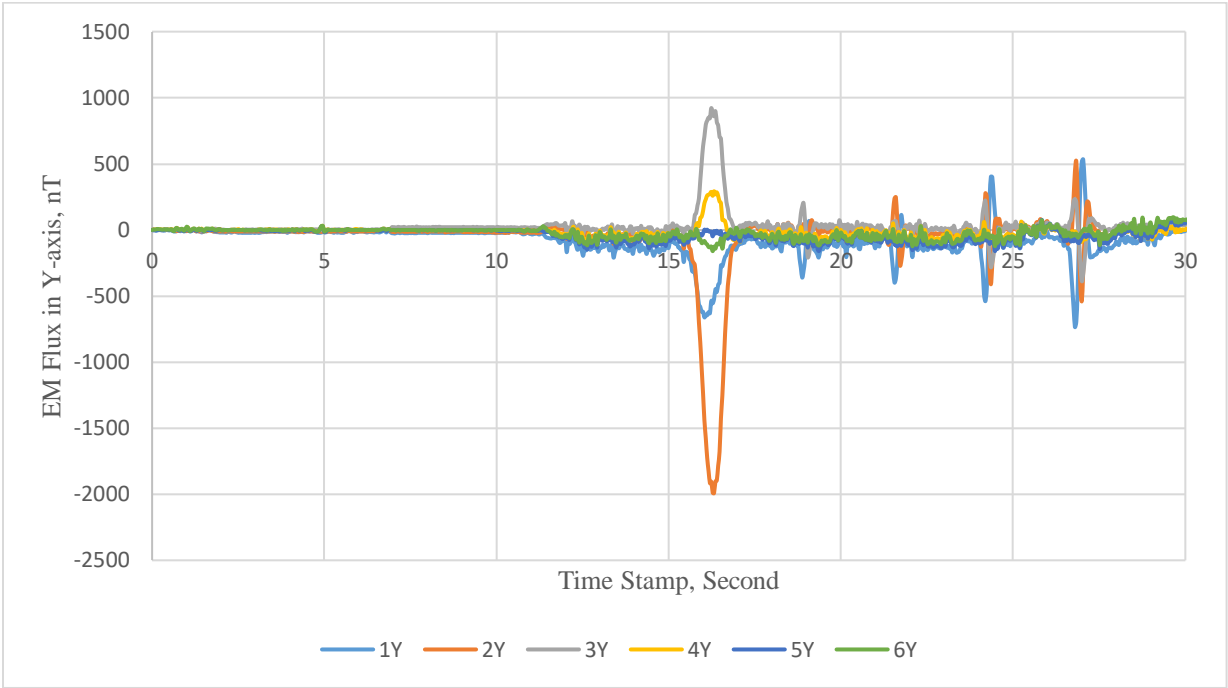
Figure 70. Graph. High-frequency filtered EM flux for sensors in Y-axis (Case #2).
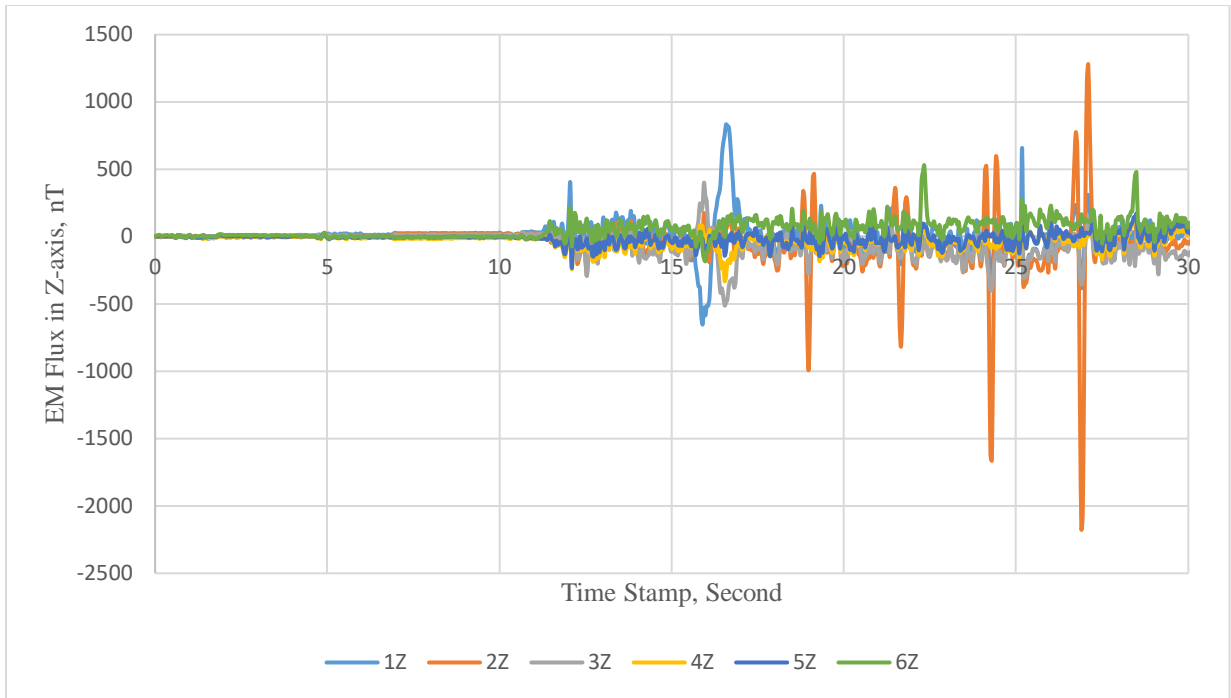
Figure 71. Graph. High-frequency filtered EM flux for sensors in Z-axis (Case #2).

Low- and High-Frequency Filtered EM Flux
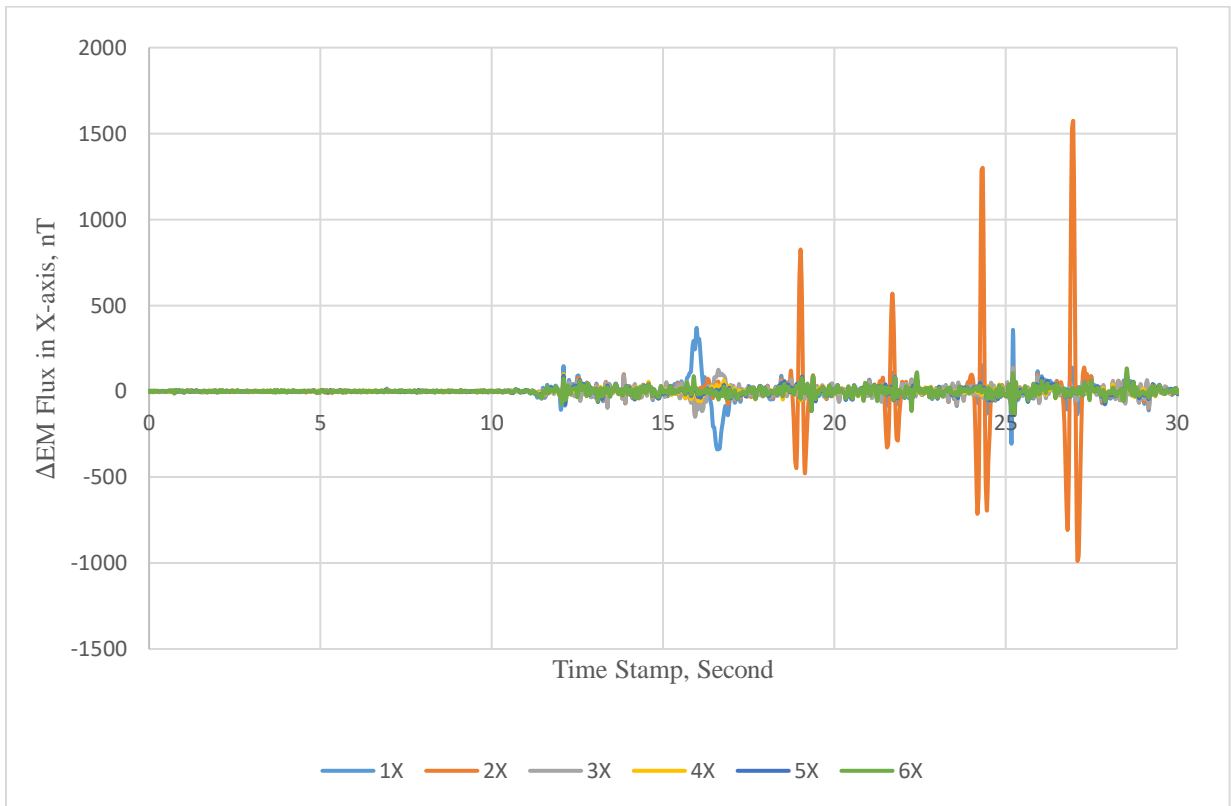
Figure 72. Graph. Low- and high-frequency filtered ∆EM flux for sensors in X-axis (Case #2).
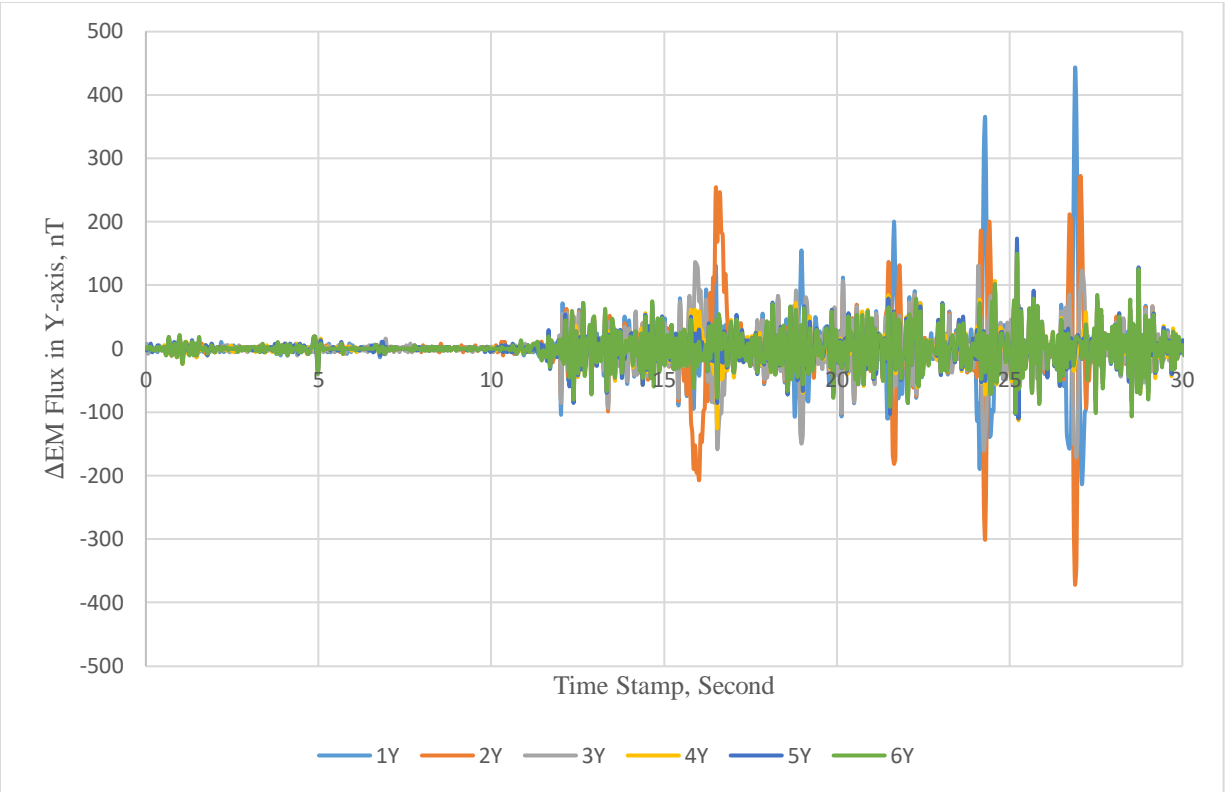
Figure 73. Graph. Low- and high-frequency filtered ΔEM flux for sensors in Y-axis (Case #2).
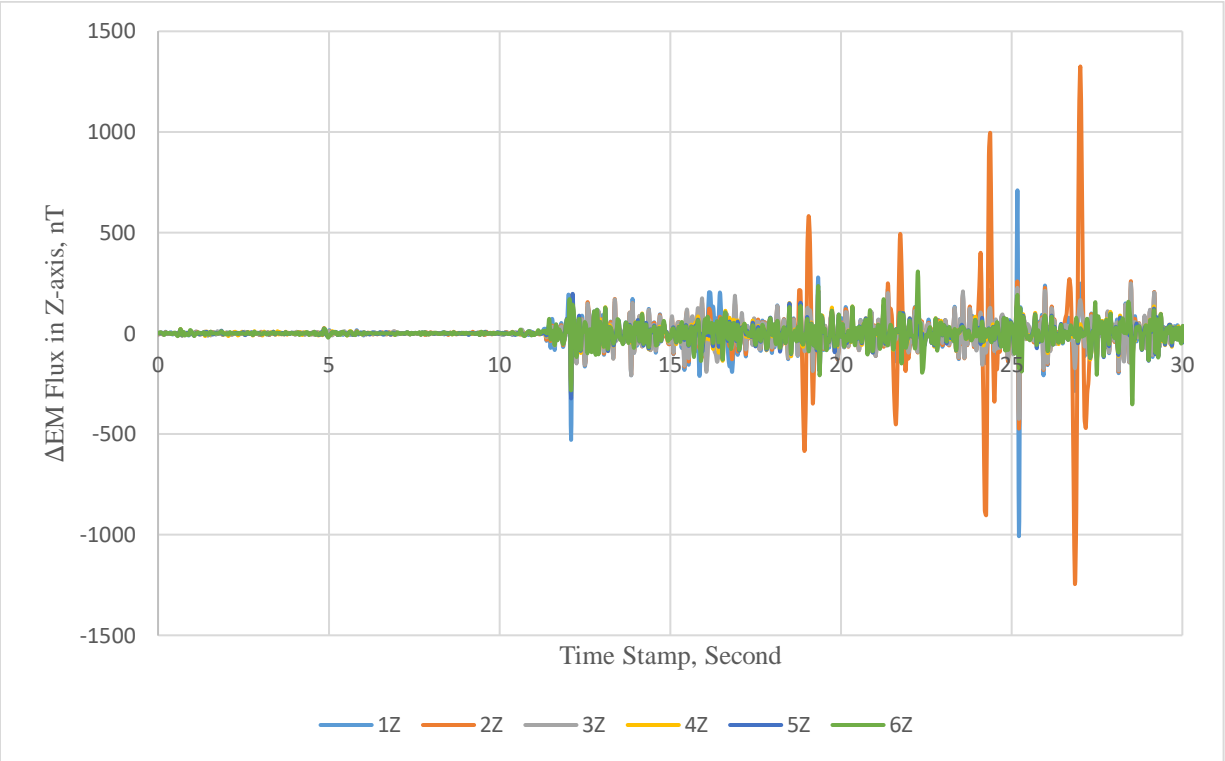
Figure 74. Graph. Low- and high-frequency filtered ΔEM flux in for sensors Z-axis (Case #2).

CASE #3
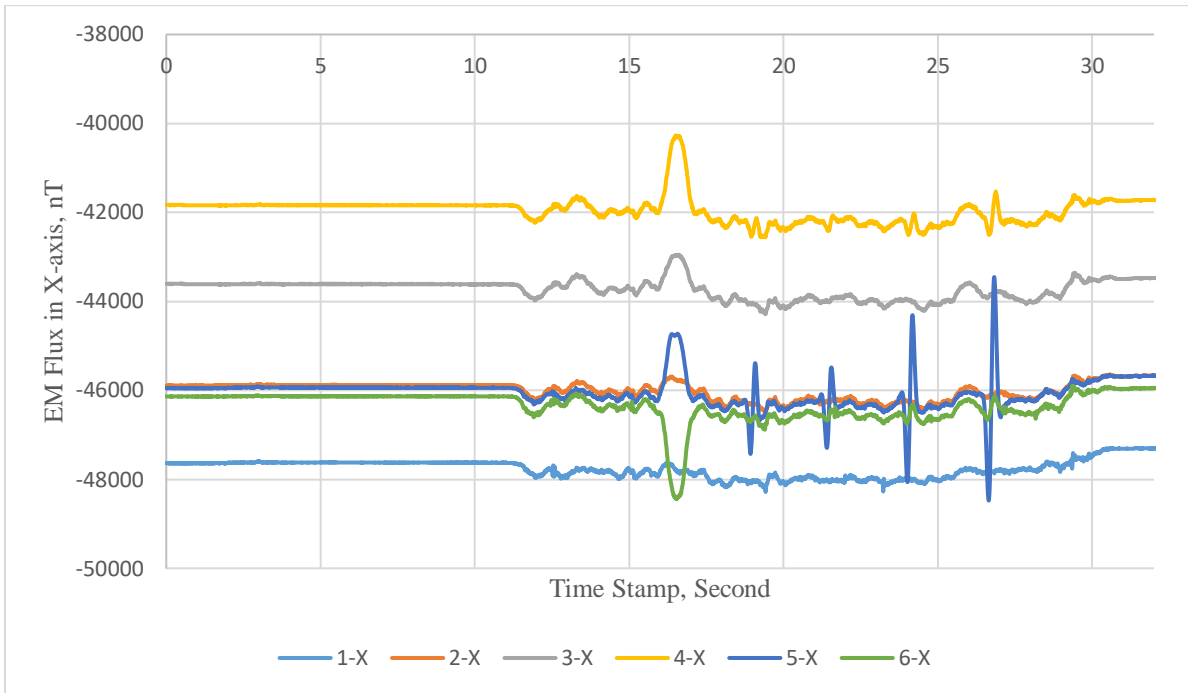
Raw EM Flux

Figure 75. Graph. Raw EM flux signals for sensors in X-axis (Case #3).
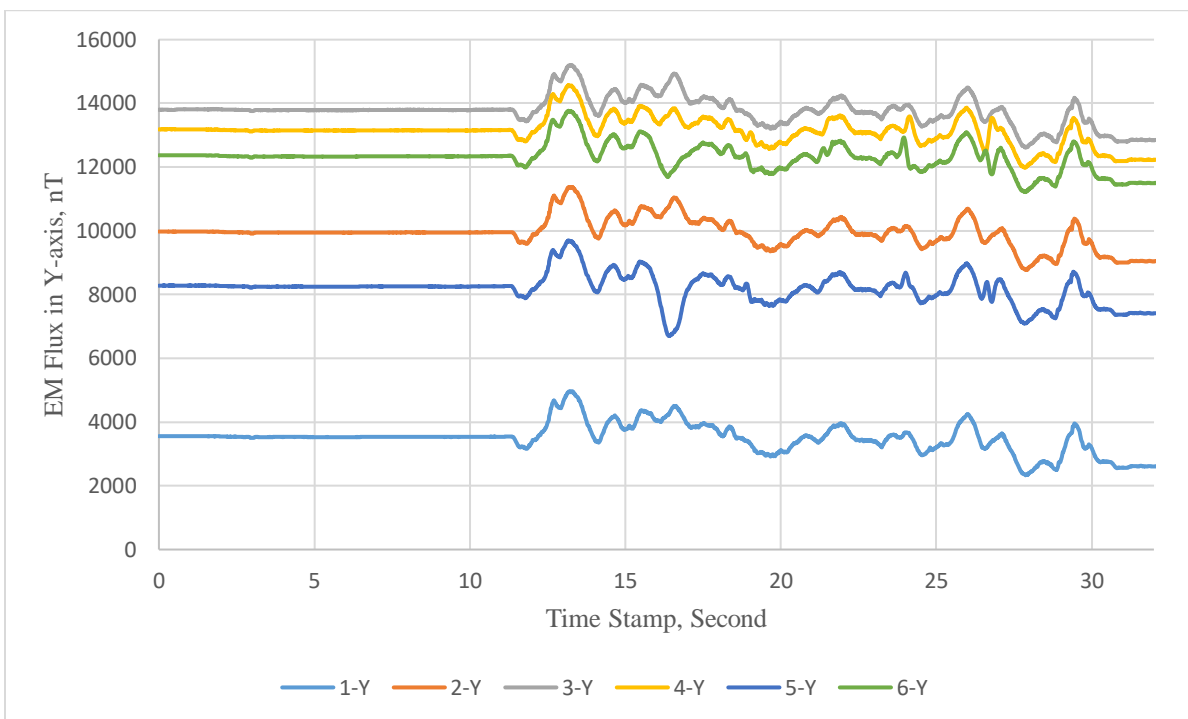
Figure 76. Graph. Raw EM flux signals for sensors in Y-axis (Case #3).
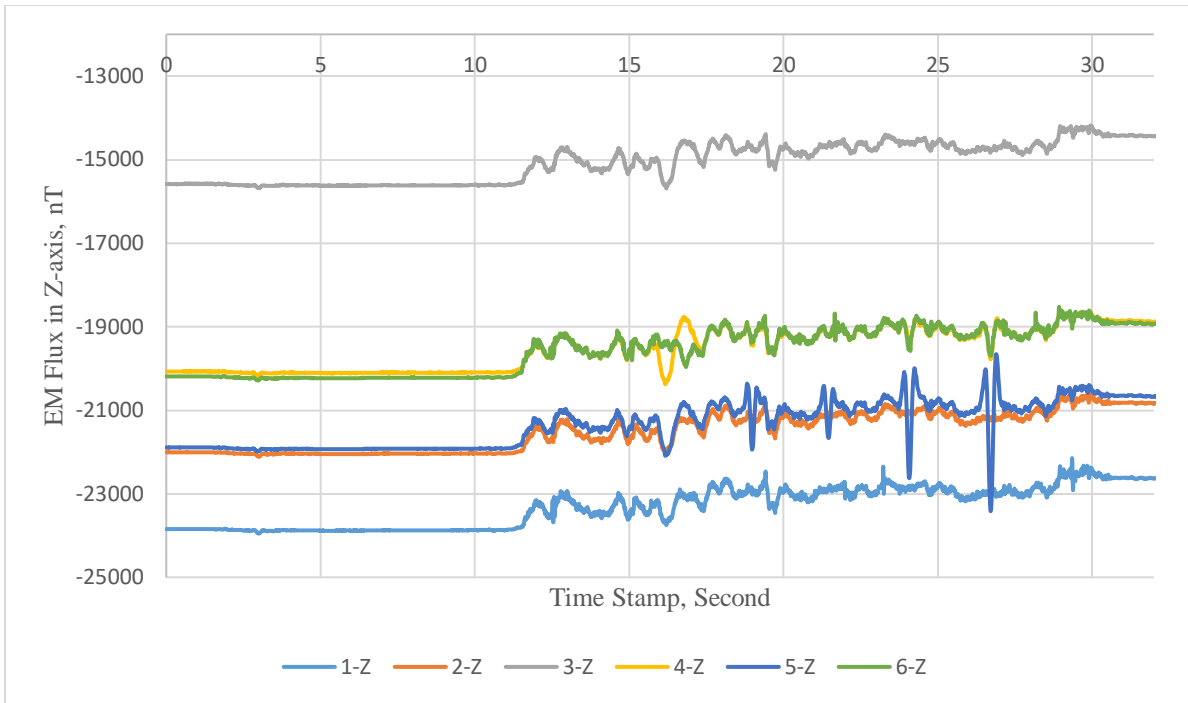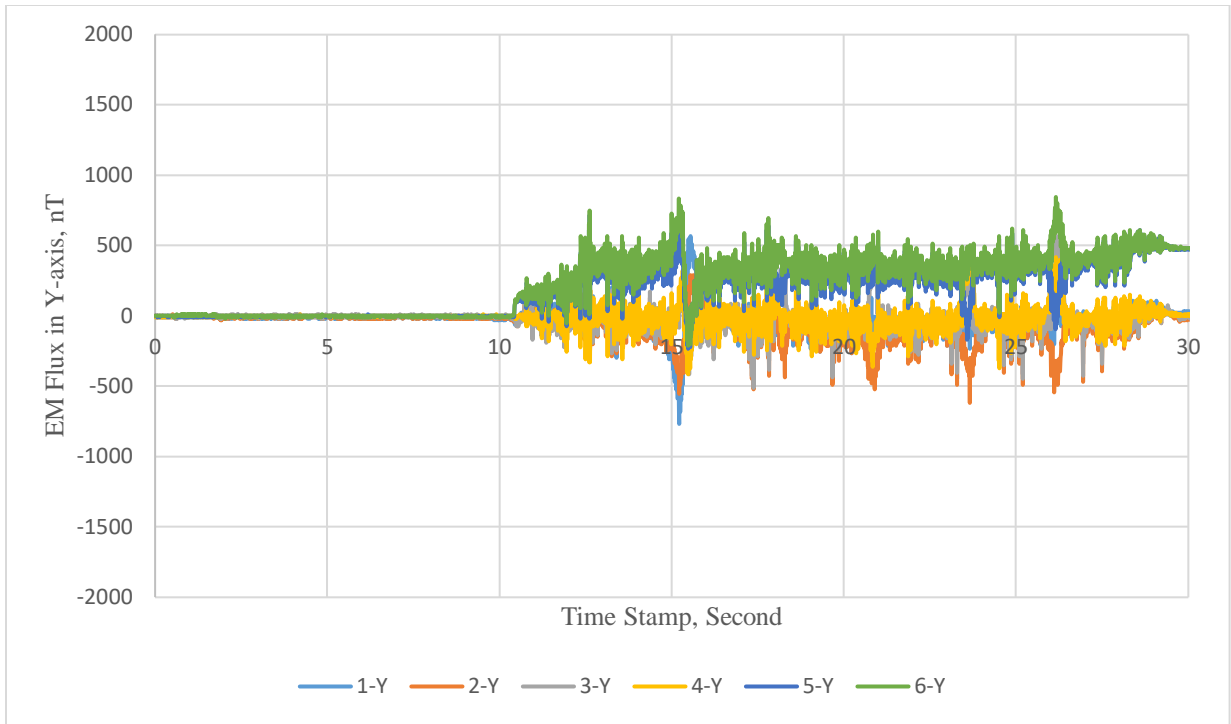
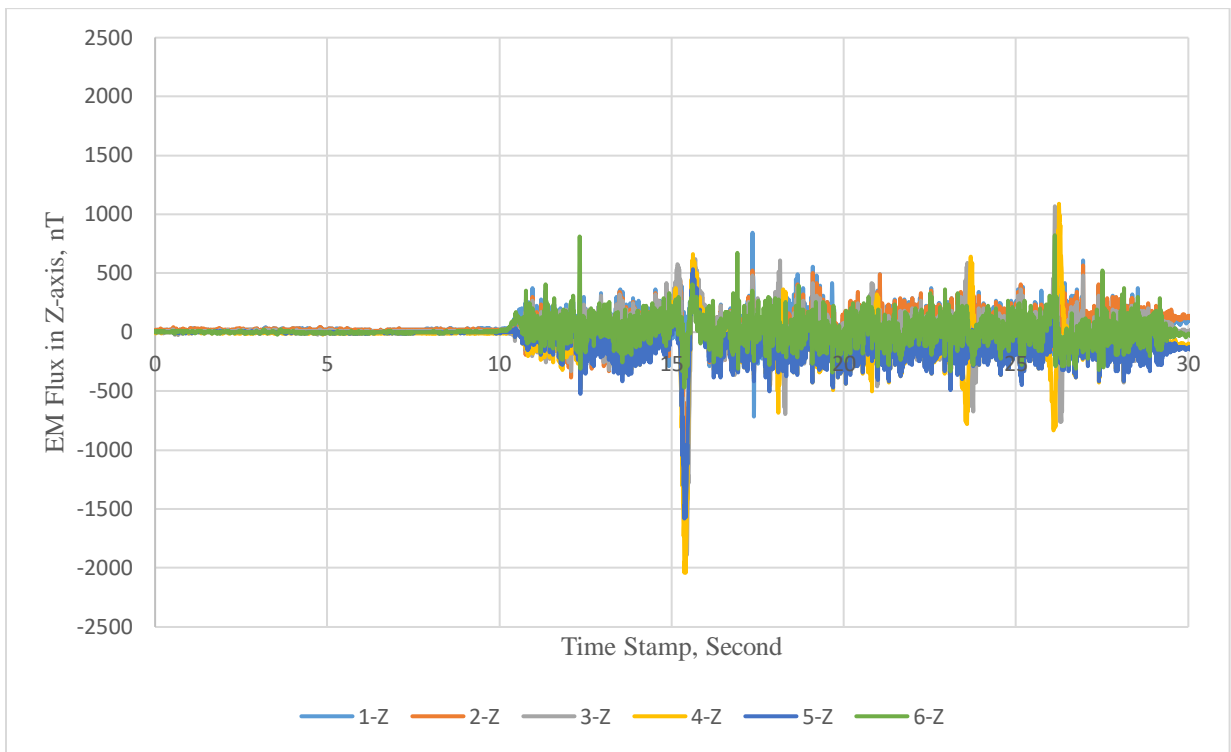**Figure 77. Graph. Raw EM flux signals for sensors in Z-axis (Case #3).**

Referenced EM Flux Signal after Initializing Initial Reading Value at Zero and Gradiometer Processing
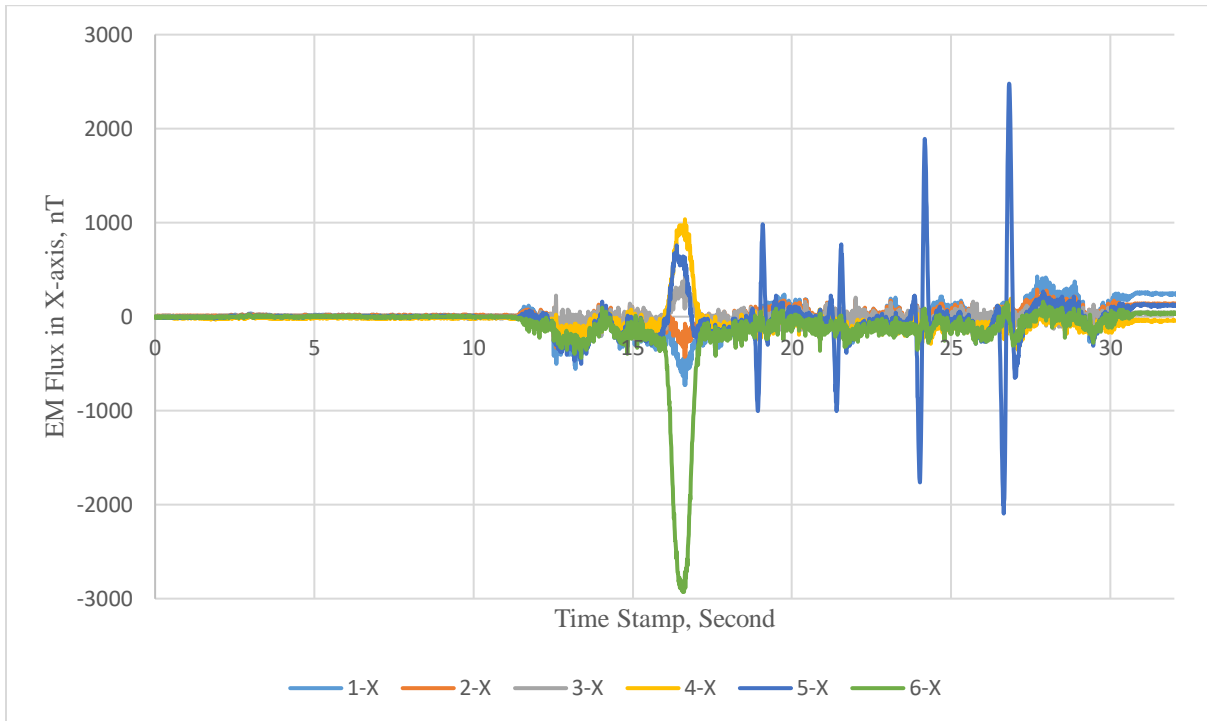
Figure 78. Graph. Referenced EM Flux Signal after initializing initial reading value at zero and gradiometer processing for sensors in X-axis (Case #3).
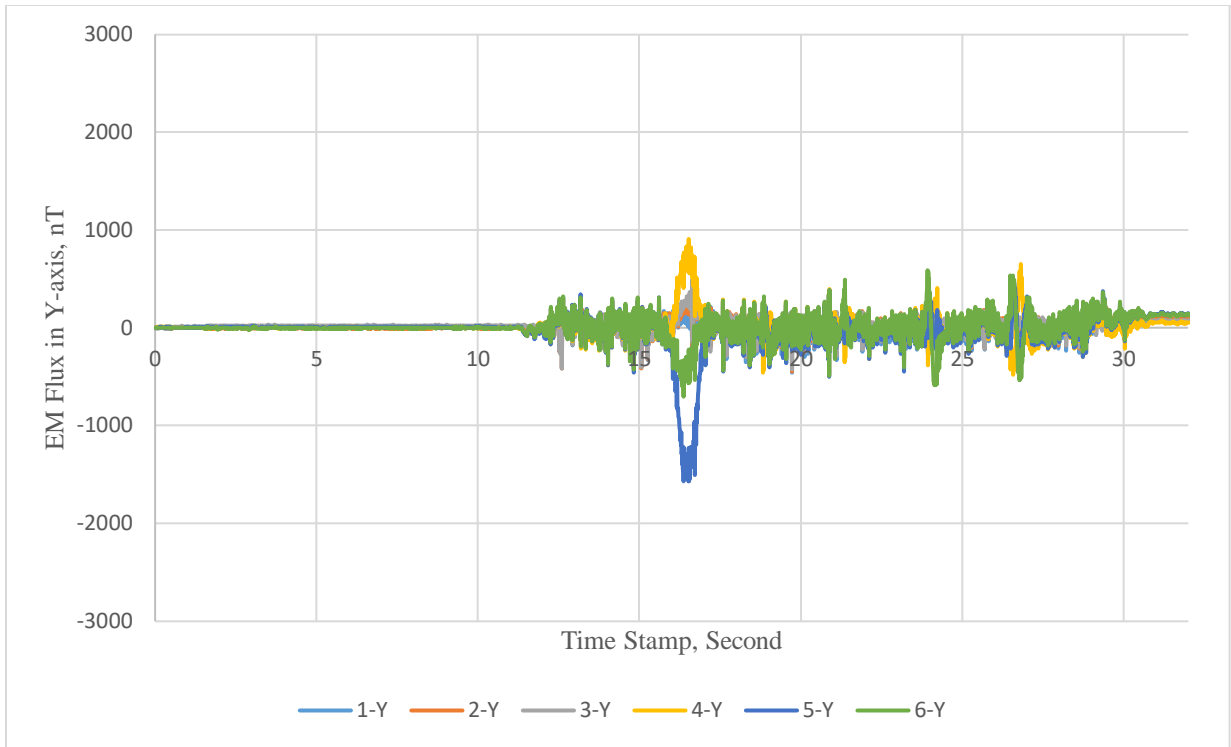
Figure 79. Graph. Referenced EM Flux Signal after initializing initial reading value at zero and gradiometer processing for sensors in Y-axis (Case #3).
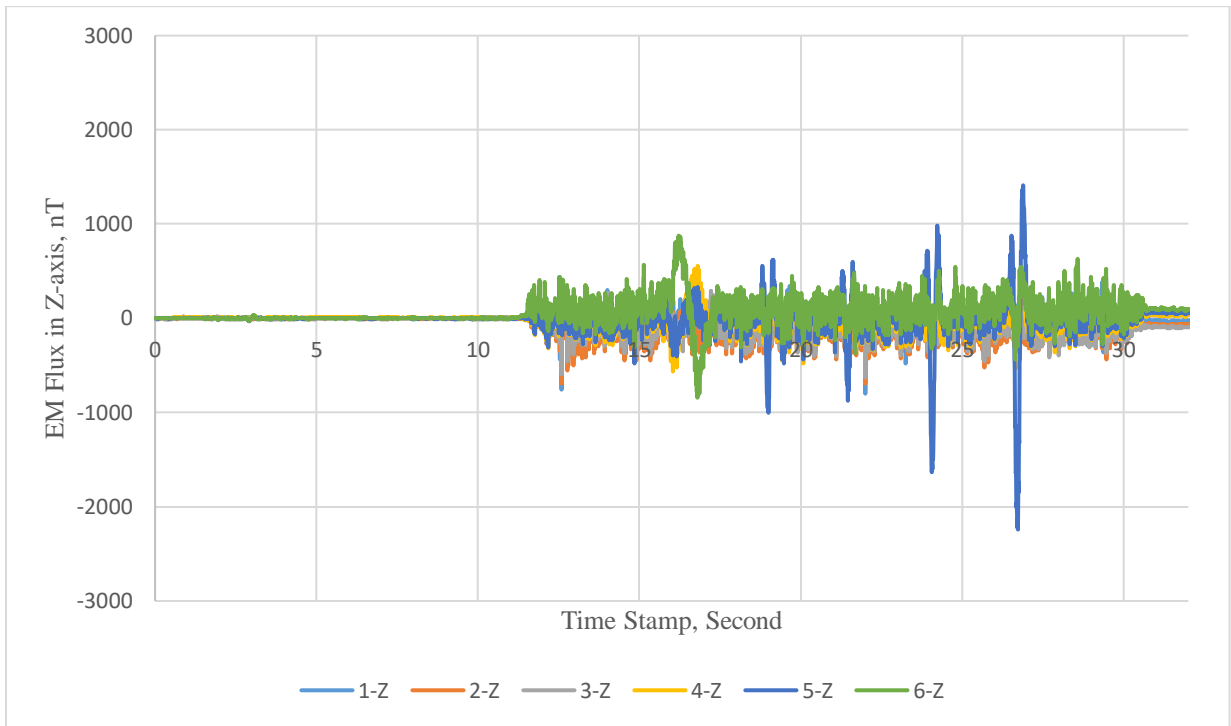
Figure 80. Graph. Referenced EM Flux Signal after initializing initial reading value at zero and gradiometer processing for sensors in Z-axis (Case #3).
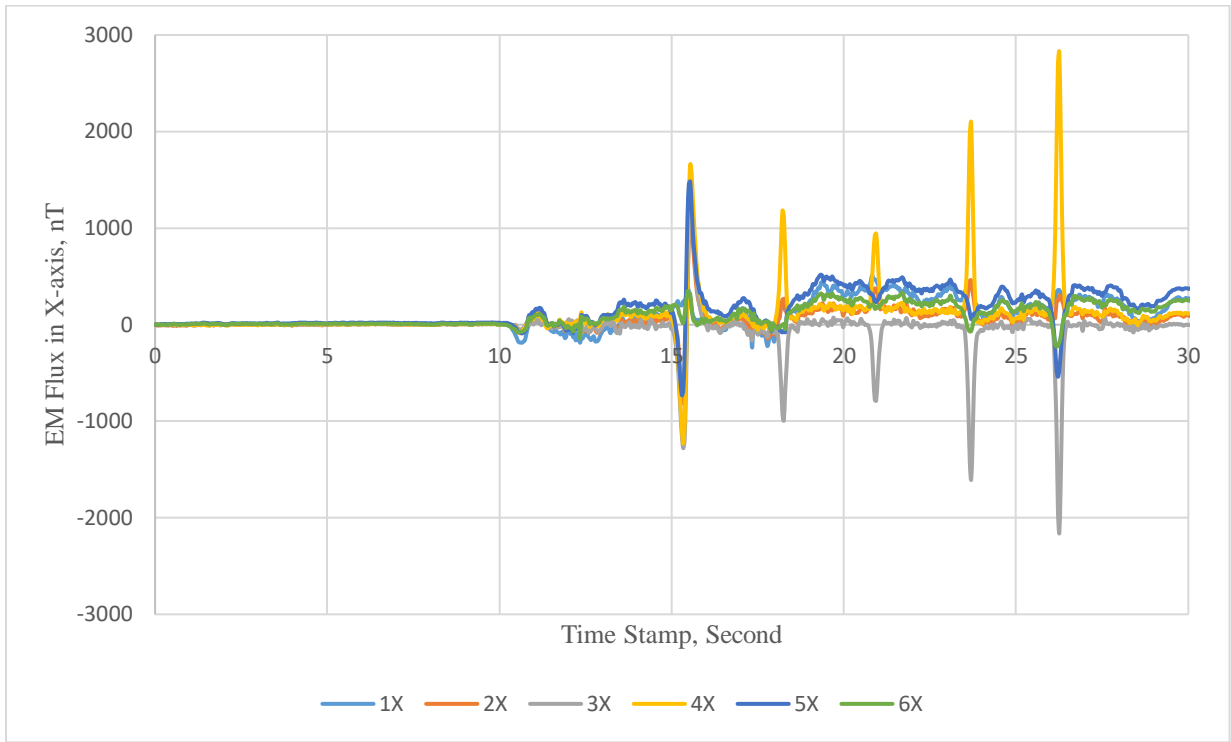
High-Frequency Filtered EM Flux
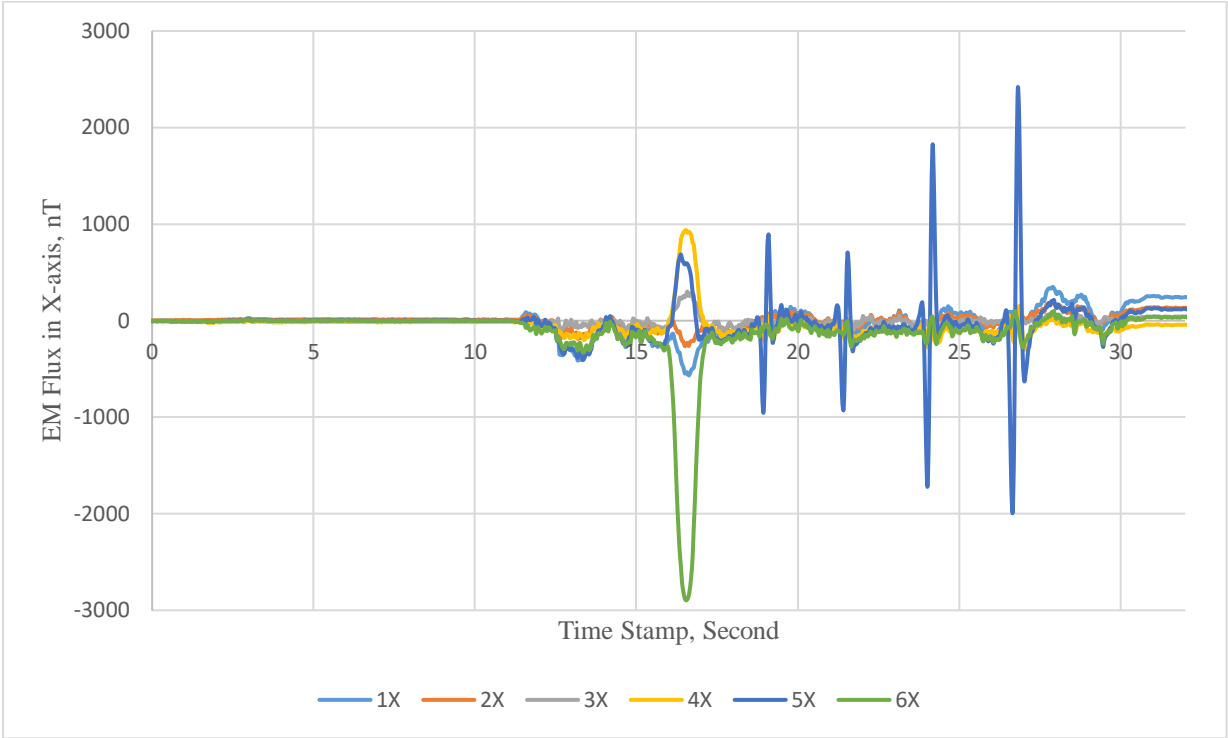
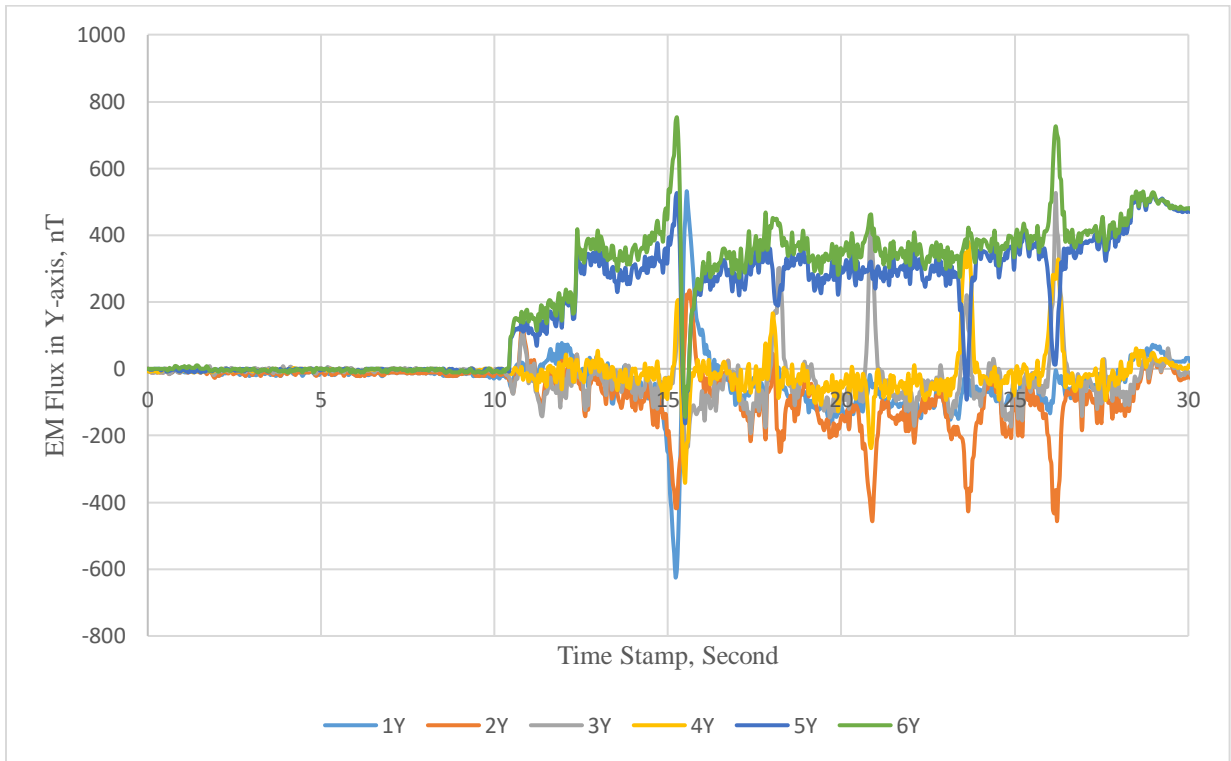**Figure 81. Graph. High-frequency filtered EM flux for sensors in X-axis (Case #3).**
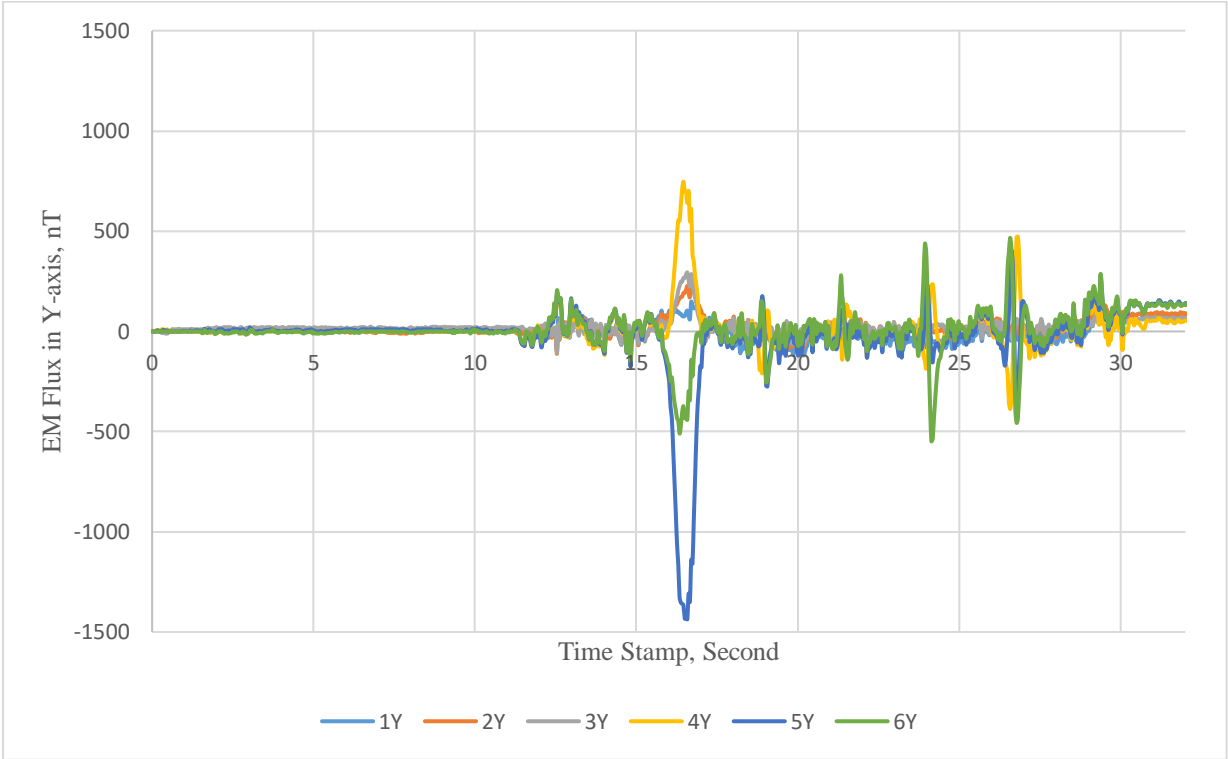
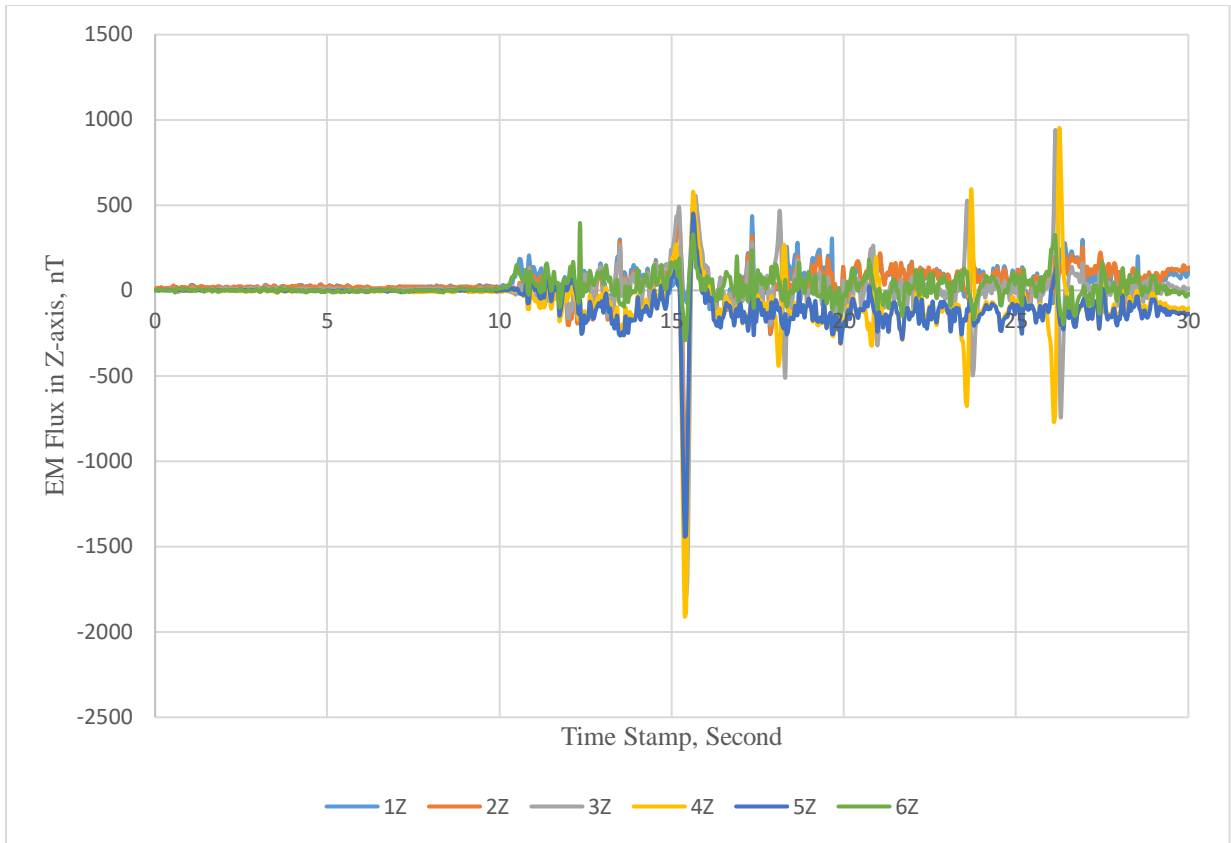**Figure 82. Graph. High-frequency filtered EM flux for sensors in Y-axis (Case #3).**
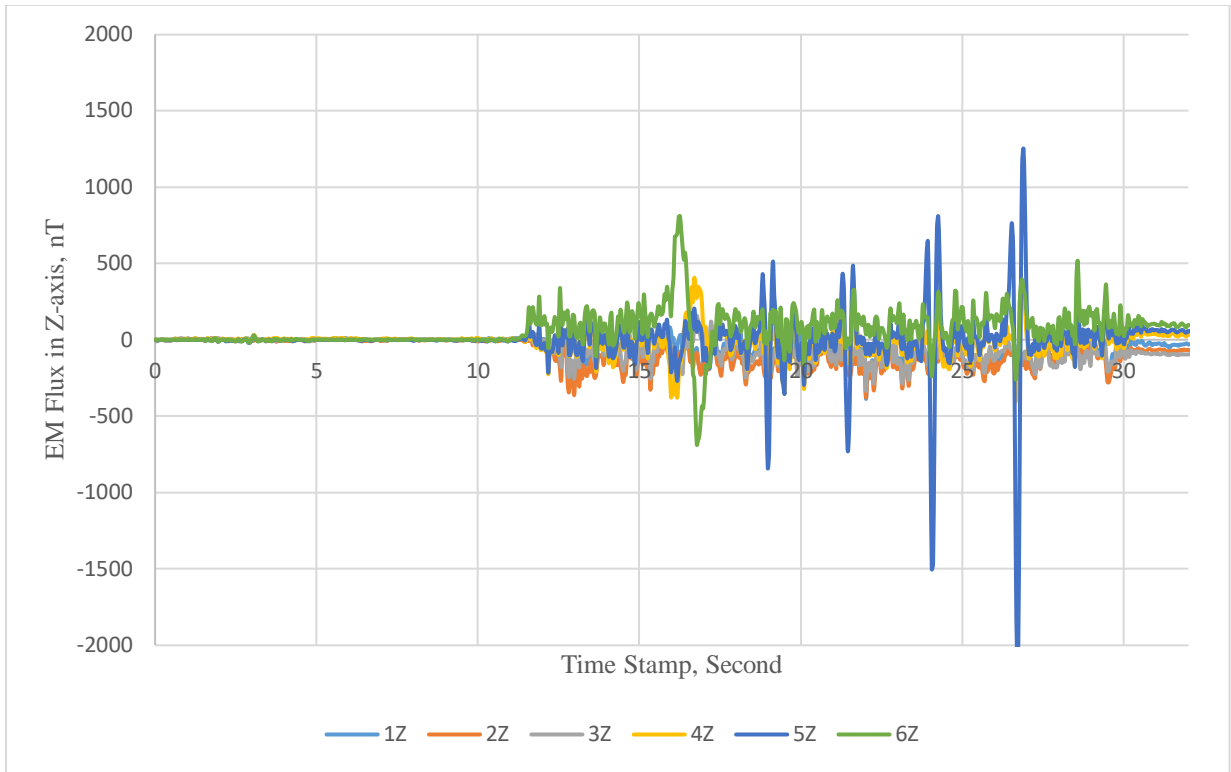
Figure 83. Graph. High-frequency filtered EM flux for sensors in Z-axis (Case #3).
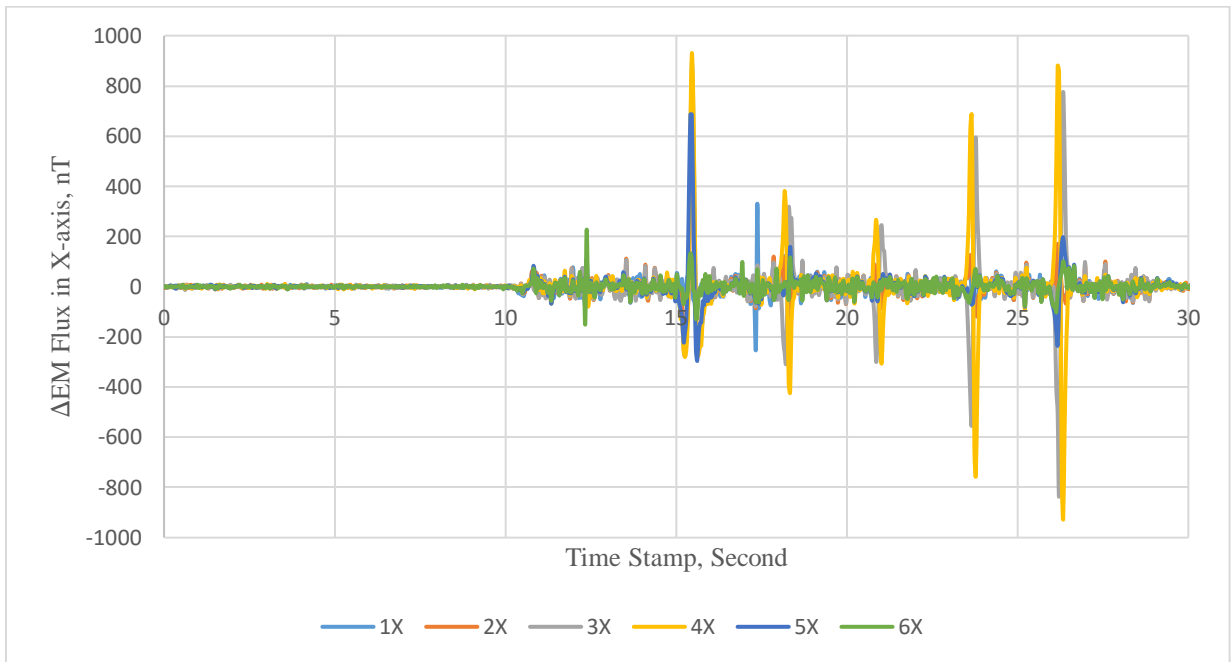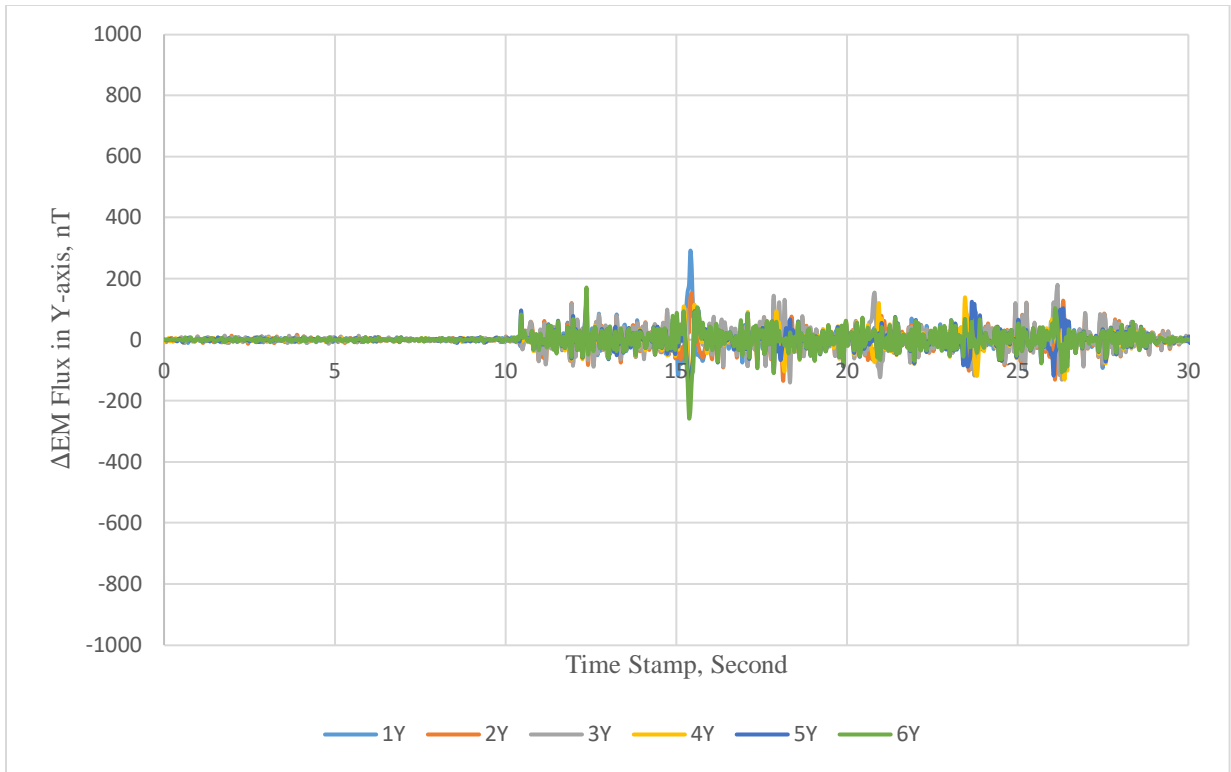
Low- and High-Frequency Filtered EM Flux
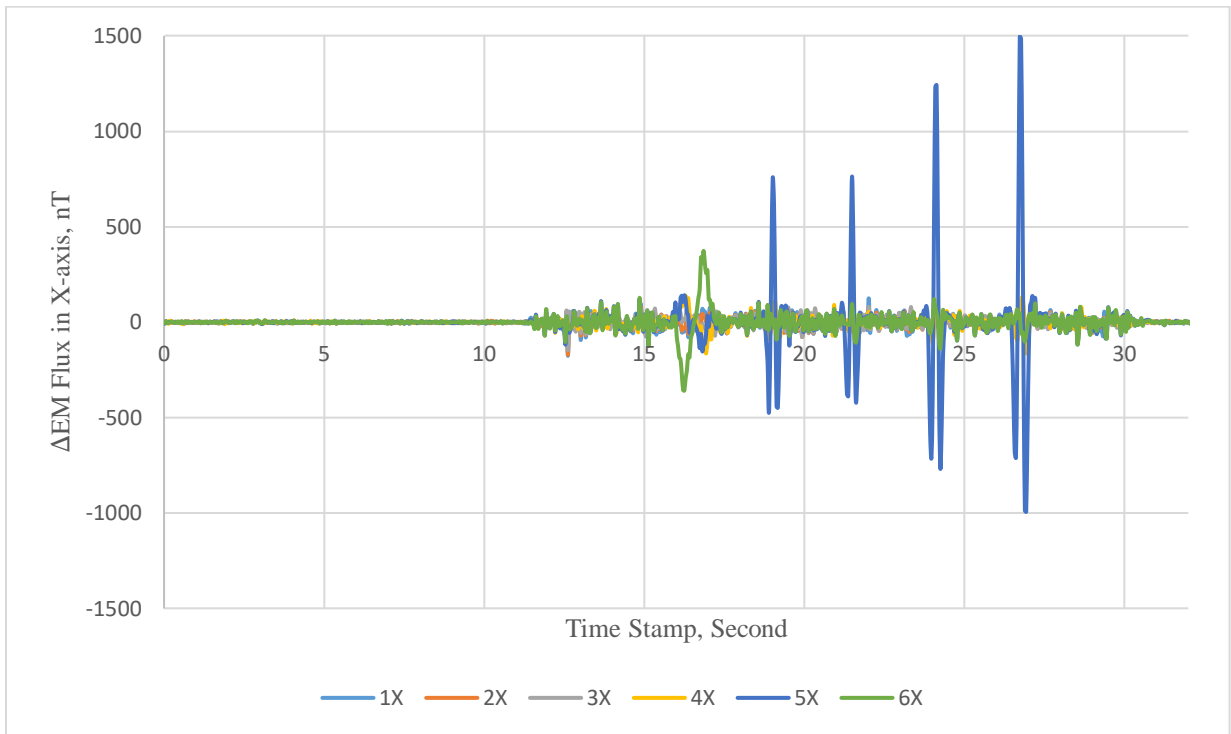
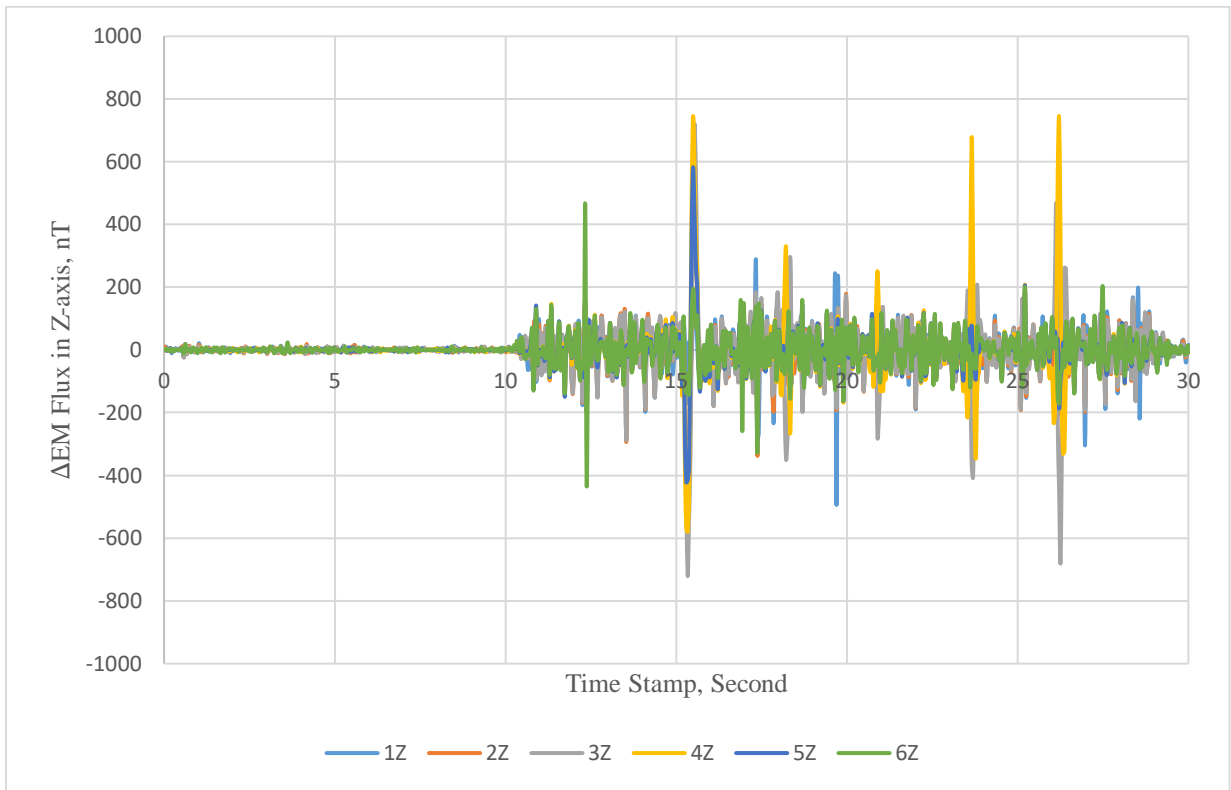**Figure 84. Graph. Low- and high-frequency filtered ΔEM flux for sensors in X-axis (Case #3).**
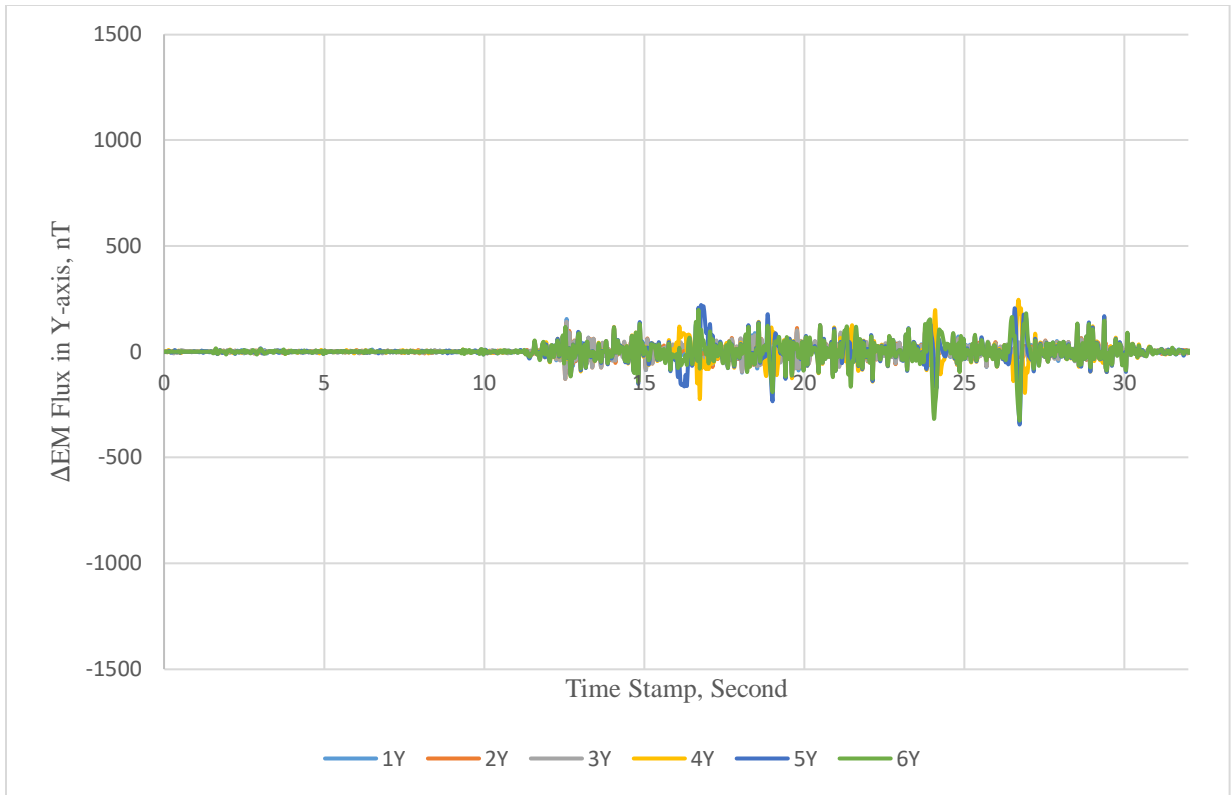
Figure 85. Graph. Low- and high-frequency filtered ΔEM flux for sensors in Y-axis (Case #3).
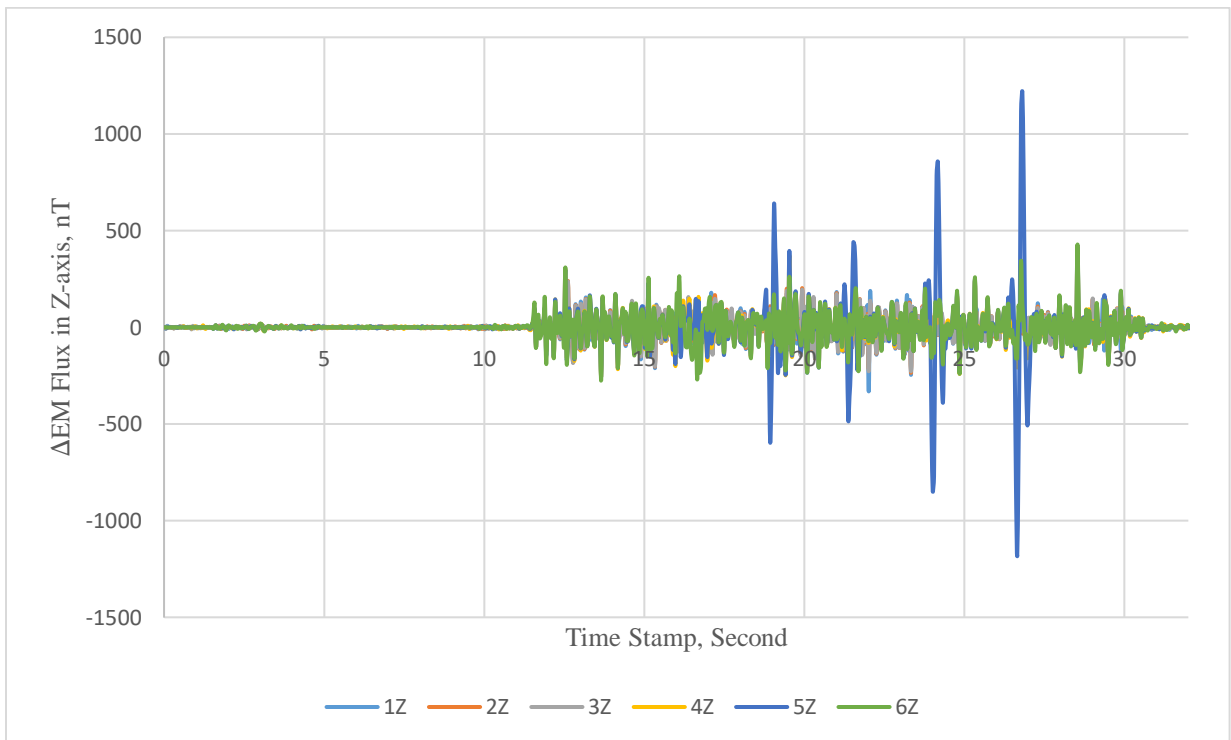
Figure 86. Graph. Low- and high-frequency filtered ΔEM flux for sensors in Z-axis (Case #3).
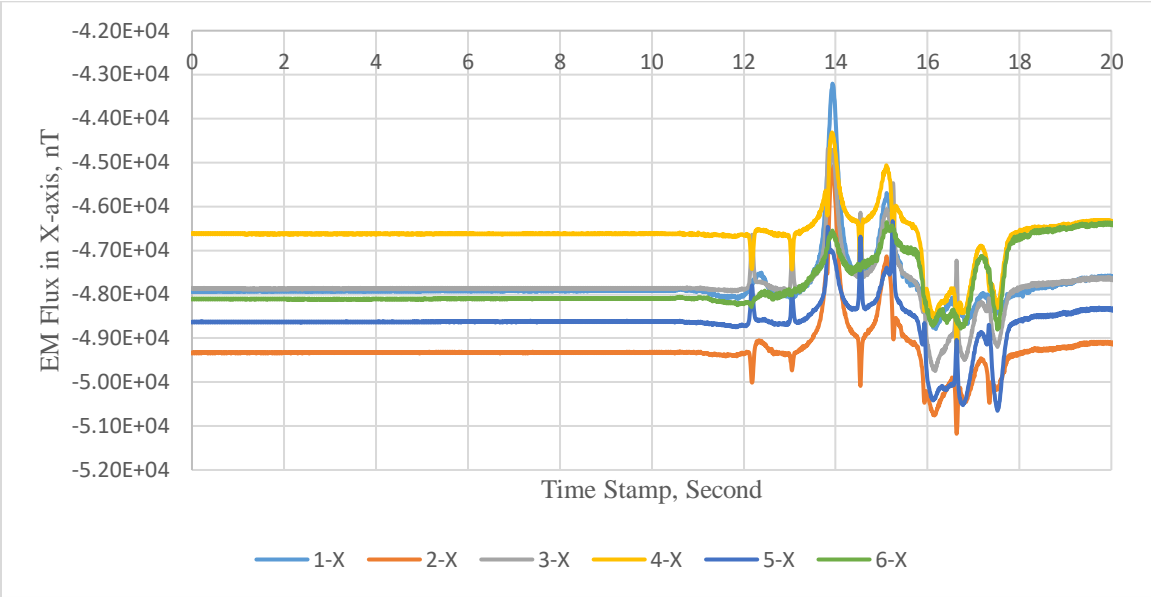
CASE #4

Raw EM Flux

Figure 87. Graph. Raw EM flux signals for sensors in X-axis (Case #4).

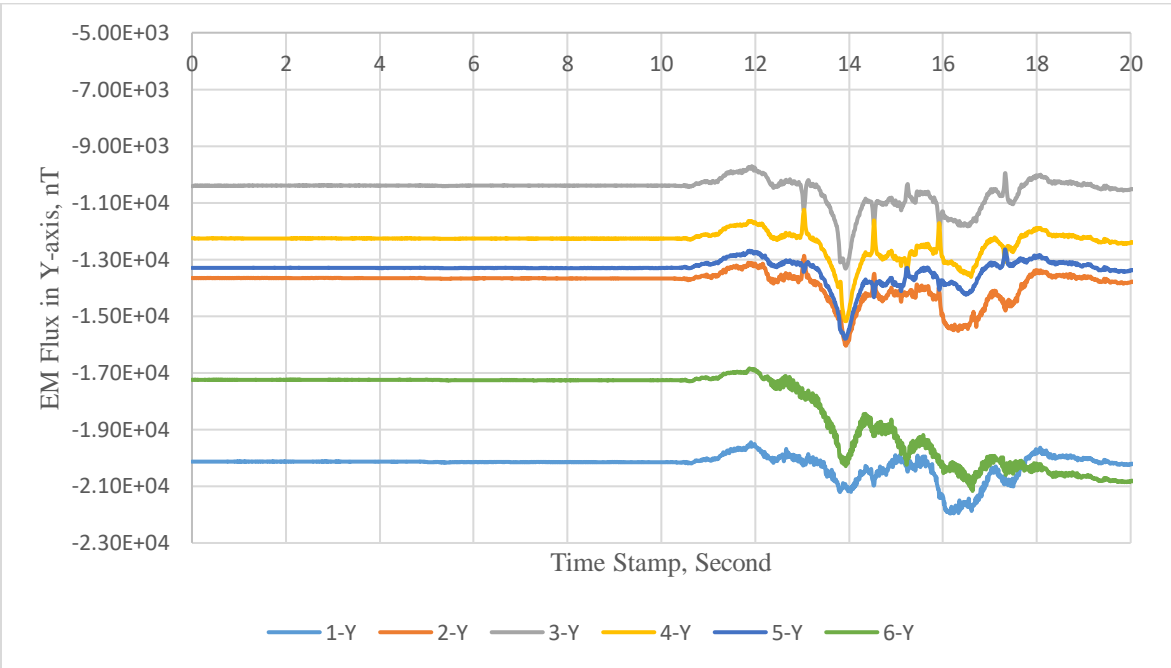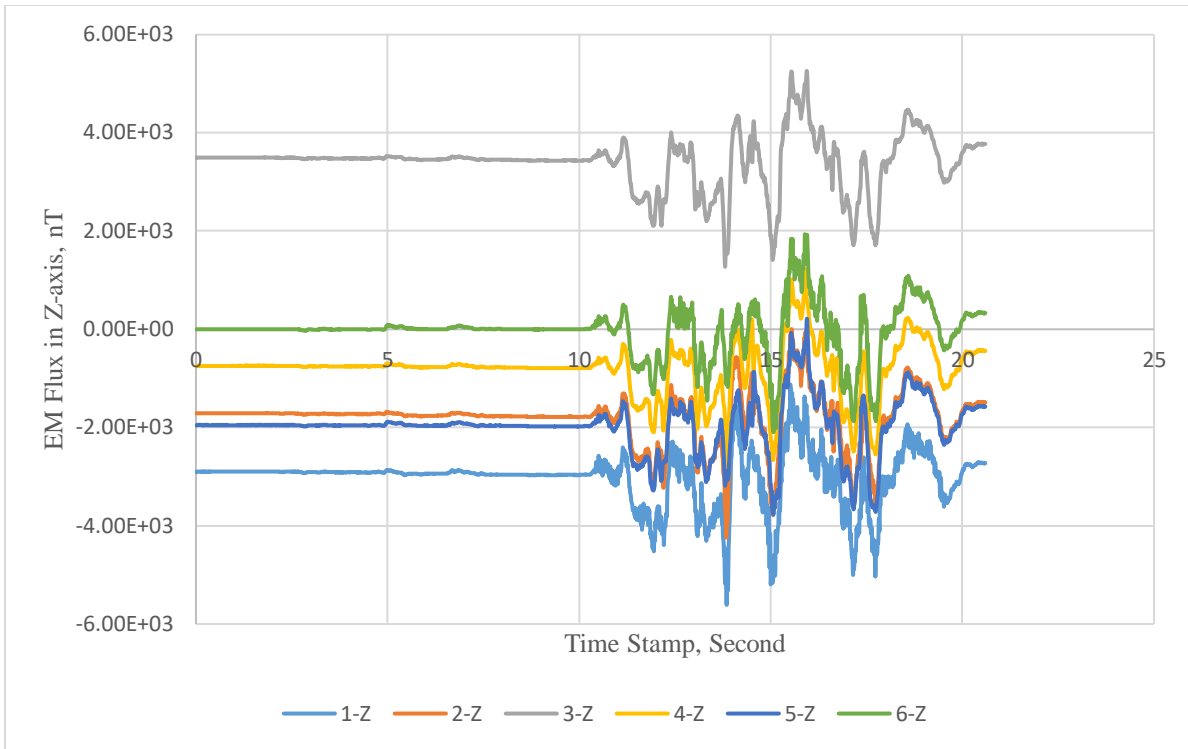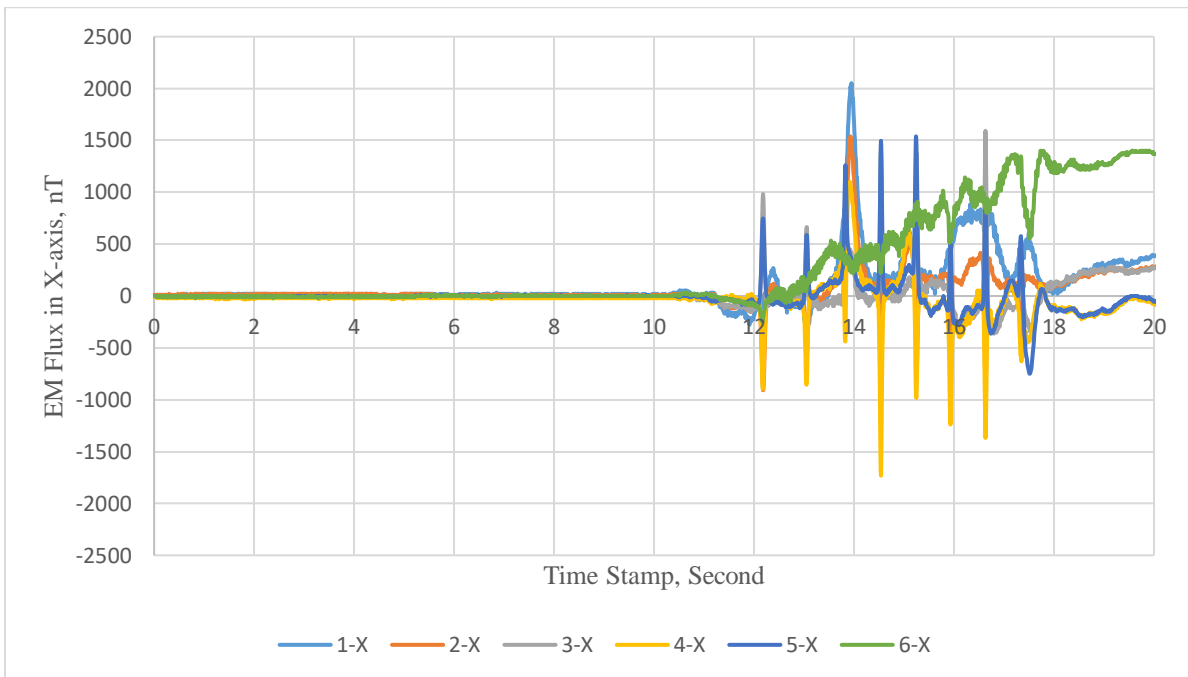**Figure 88. Graph. Raw EM flux signals for sensors in Y-axis (Case #4).**

Figure 89. Graph. Raw EM flux signals for sensors in Z-axis (Case #4).

Referenced EM Flux Signal after Initializing Initial Reading Value at Zero and Gradiometer Processing

Figure 90. Graph. Referenced EM Flux Signal after initializing initial reading value at zero and gradiometer processing for sensors in X-axis (Case #4).

Figure 91. Graph. Referenced EM Flux Signal after initializing initial reading value at zero and gradiometer processing for sensors in Y-axis (Case #4).

Figure 92. Graph. Referenced EM Flux Signal after initializing initial reading value at zero and gradiometer processing for sensors in Z-axis (Case #4).

High-Frequency Filtered EM Flux

Figure 93. Graph. High-frequency filtered EM flux for sensors in X-axis (Case #4).

Figure 94. Graph. High-frequency filtered EM flux for sensors in Y-axis (Case #4).

Figure 95. Graph. High-frequency filtered EM flux for sensors in Z-axis (Case #4).

Low- and High-Frequency Filtered EM Flux

Figure 96. Graph. Low- and high-frequency filtered ∆EM flux for sensors in X-axis (Case #4).

Figure 97. Graph. Low- and high-frequency filtered ΔEM flux for sensors in Y-axis (Case #4).

Figure 98. Graph. Low- and high-frequency filtered ΔEM flux for sensors in Z-axis (Case #4).

CASE #5

Raw EM Flux

Figure 99. Graph. Raw EM flux signals for sensors in X-axis (Case #5).
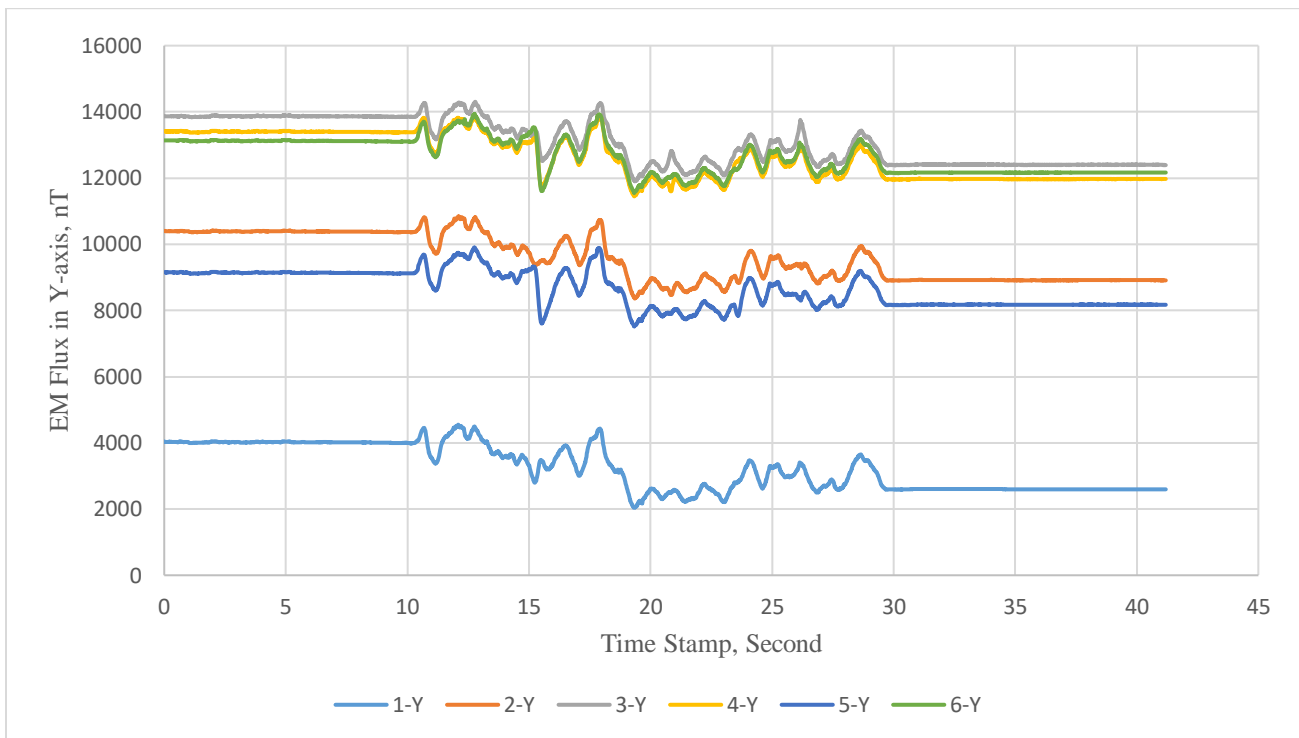
Figure 100. Graph. Raw EM flux signals for sensors in Y-axis (Case #5).
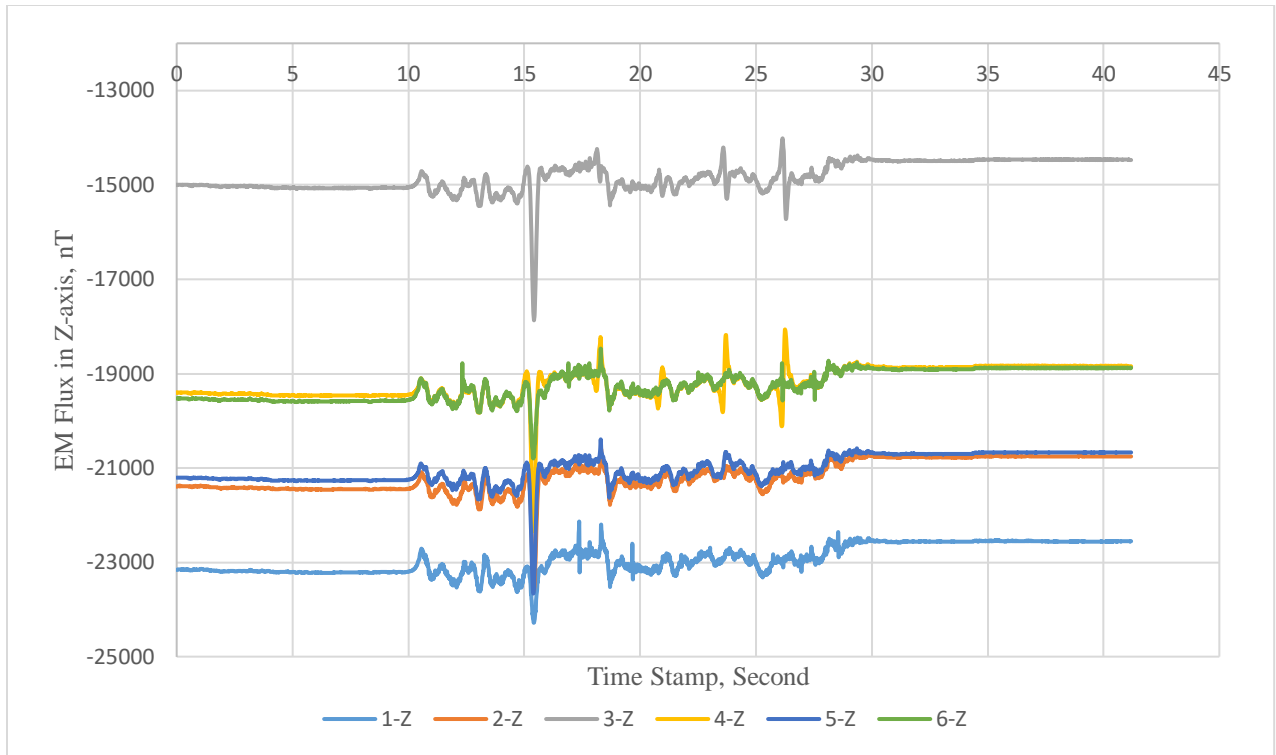
Figure 101. Graph. Raw EM flux signals for sensors in Z-axis (Case #5).

Referenced EM Flux Signal after Initializing Initial Reading Value at Zero and Gradiometer Processing
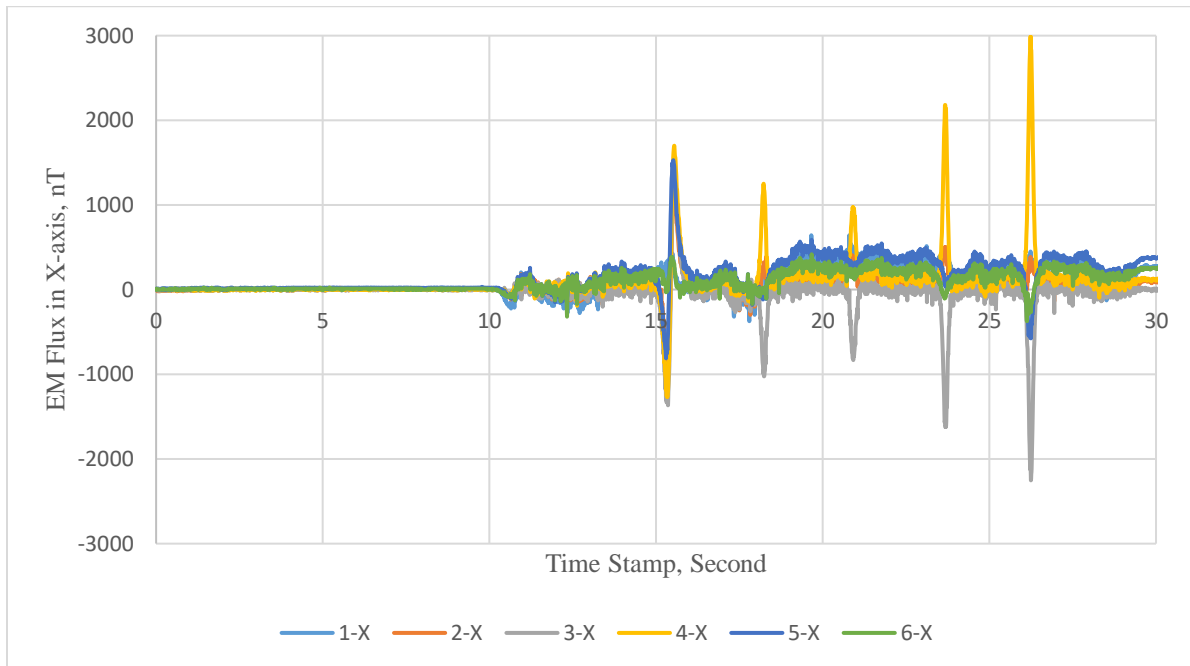
Figure 102. Graph. Referenced EM Flux Signal after initializing initial reading value at zero and gradiometer processing for sensors in X-axis (Case #5).

**Figure 103. Graph. Referenced EM Flux Signal after initializing initial reading value at zero and gradiometer processing for sensors in Y-axis (Case #5).**

Figure 104. Graph. Referenced EM Flux Signal after initializing initial reading value at zero and gradiometer processing for sensors in Z-axis (Case #5).

High-Frequency Filtered EM Flux

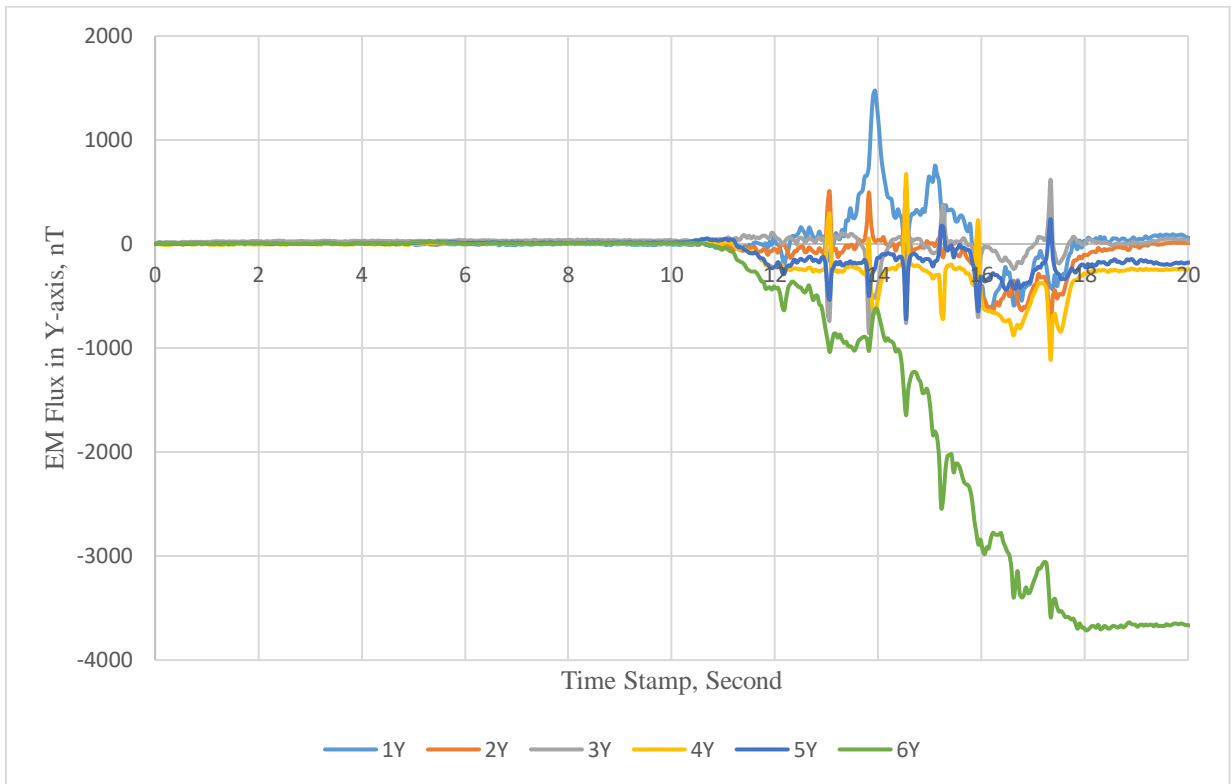**Figure 105. Graph. High-frequency filtered EM flux for sensors in X-axis (Case #5).**

Figure 106. Graph. High-frequency filtered EM flux for sensors in Y-axis (Case #5).

Figure 107. Graph. High-frequency filtered EM flux for sensors in Z-axis (Case #5).
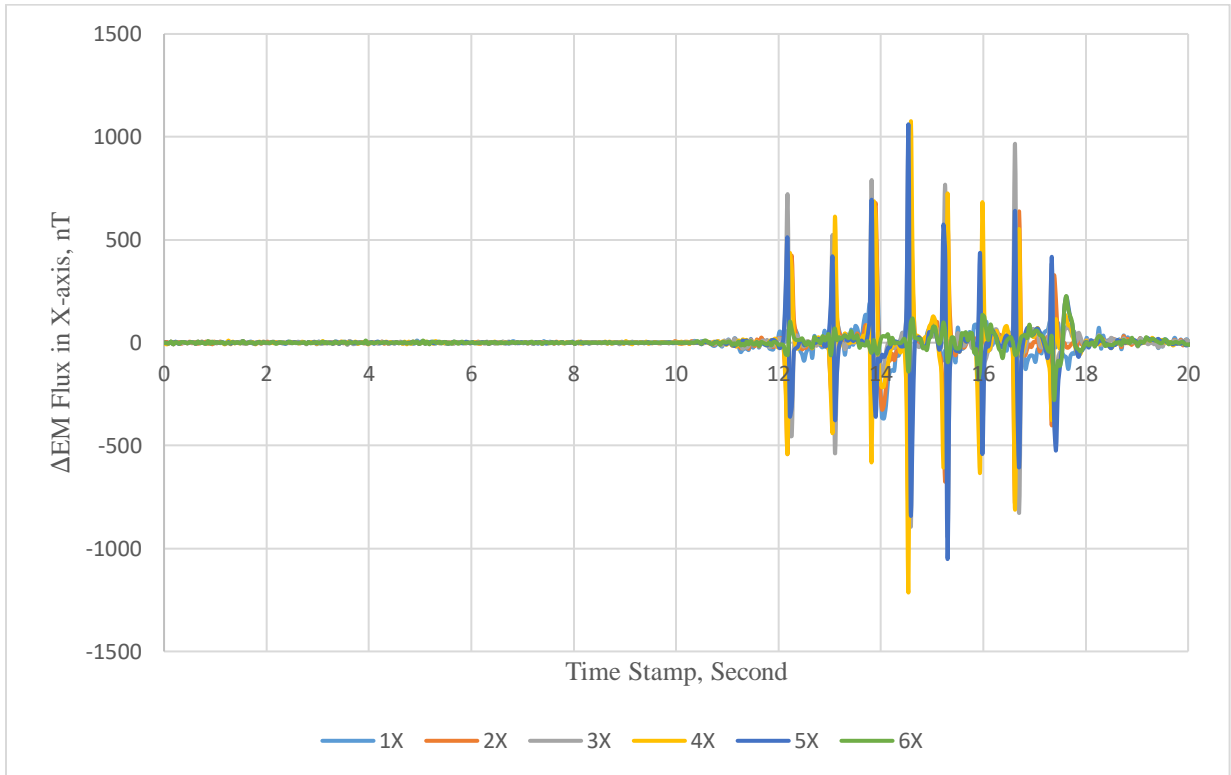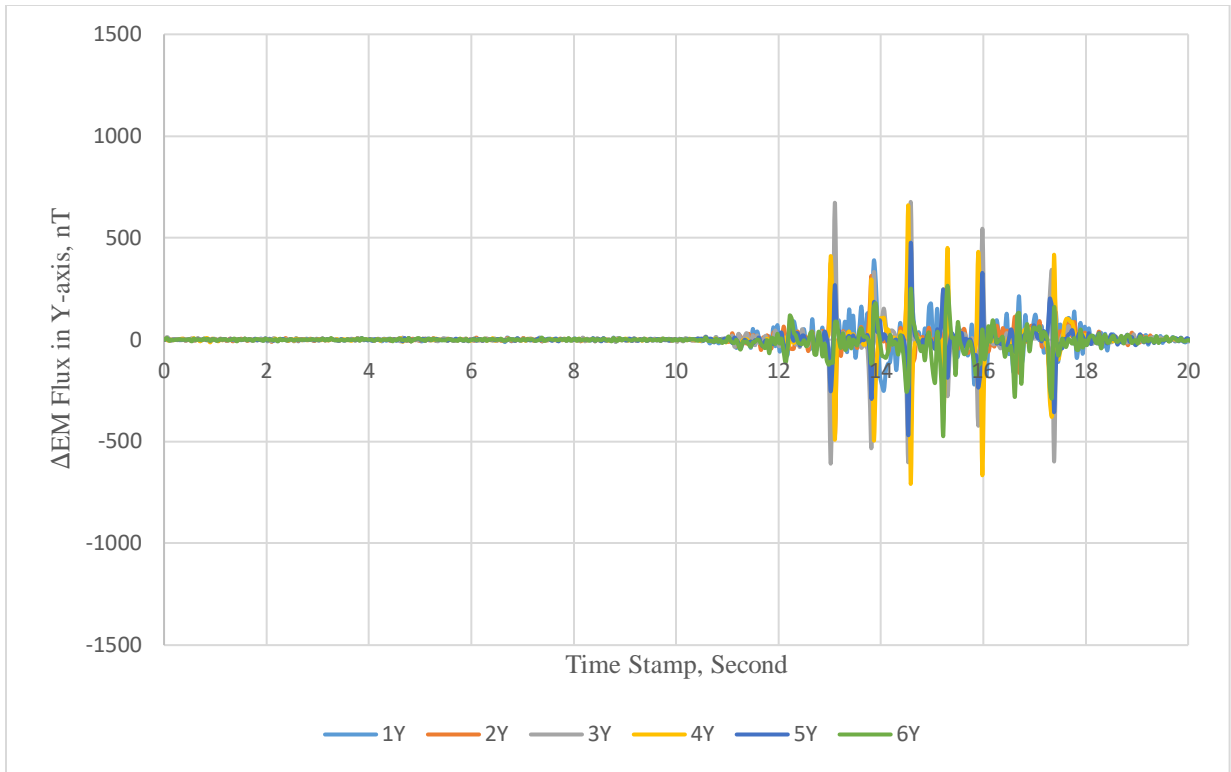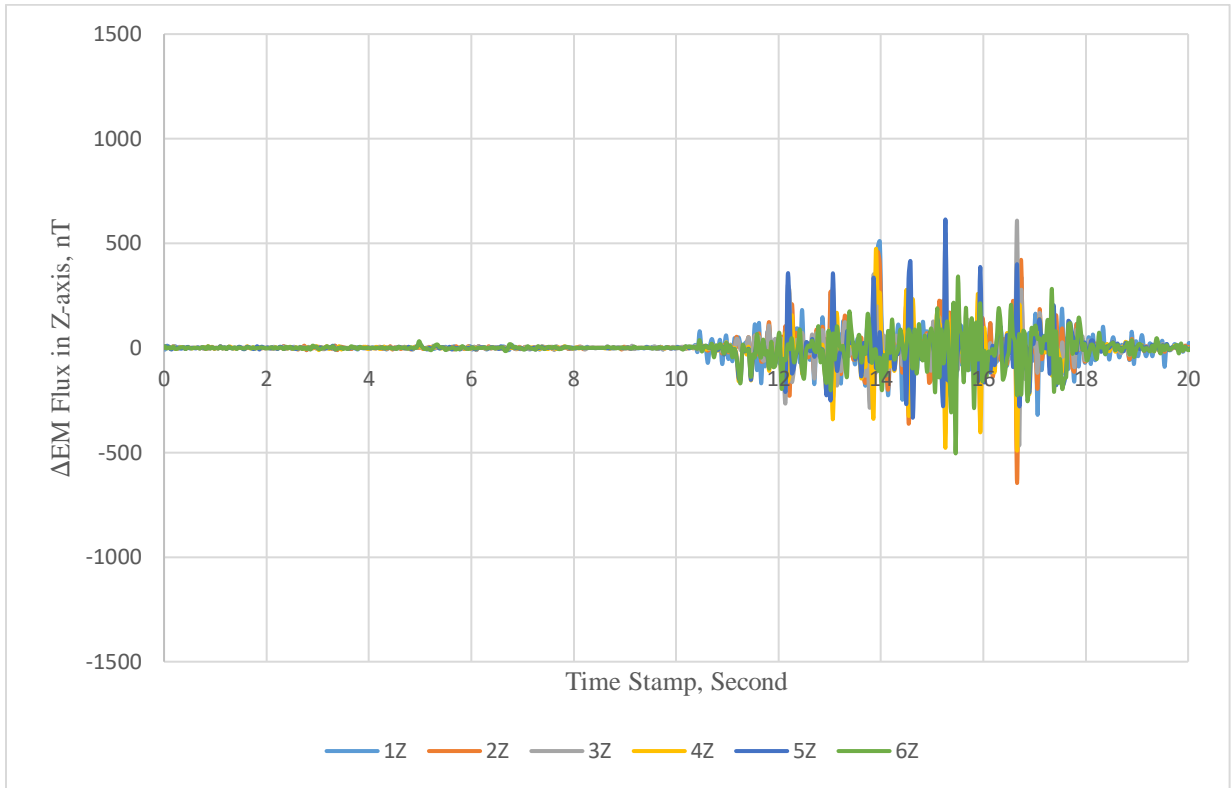
Low- and High-Frequency Filtered EM Flux

Figure 108. Graph. Low- and high-frequency filtered ∆EM flux for sensors in X-axis (Case #5).

Figure 109. Graph. Low- and high-frequency filtered ΔEM flux for sensors in Y-axis (Case #5).

Figure 110. Graph. Low- and high-frequency filtered ΔEM flux for sensors in Z-axis (Case #5).

APPENDIX B: SIGNAL-PROCESSING RESULTS OF EXPERIMENTAL STUDY (CHAPTER 4)
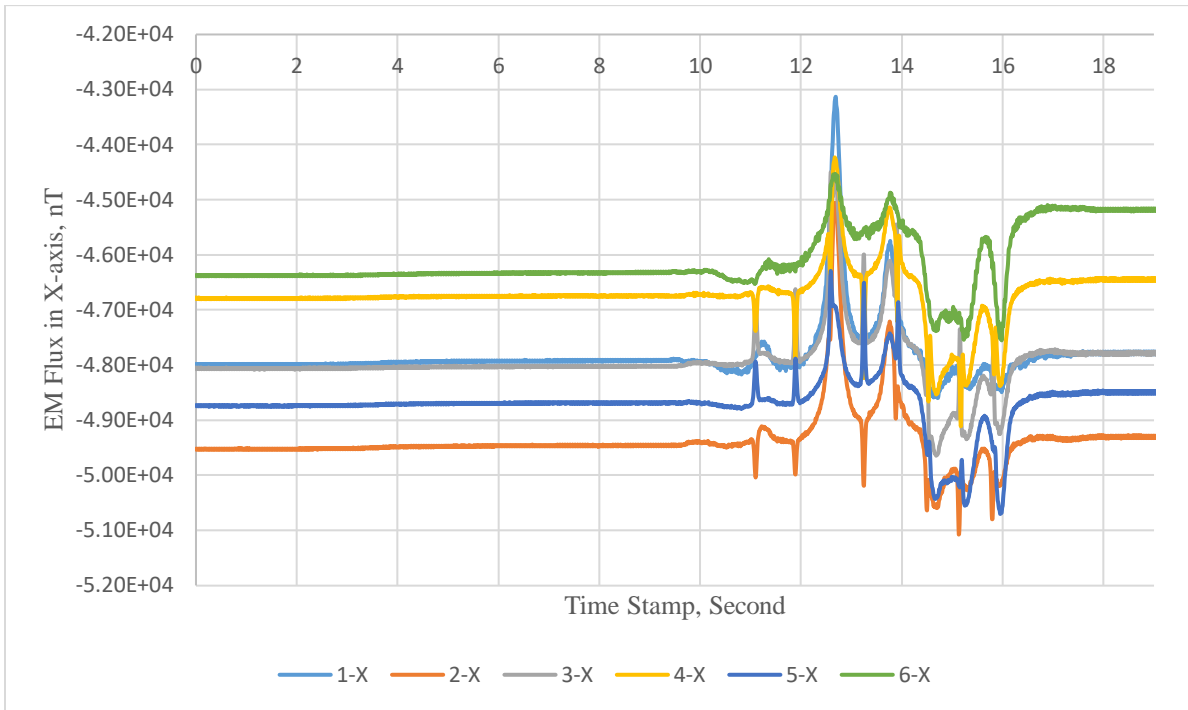
CASE #1

Raw EM Flux

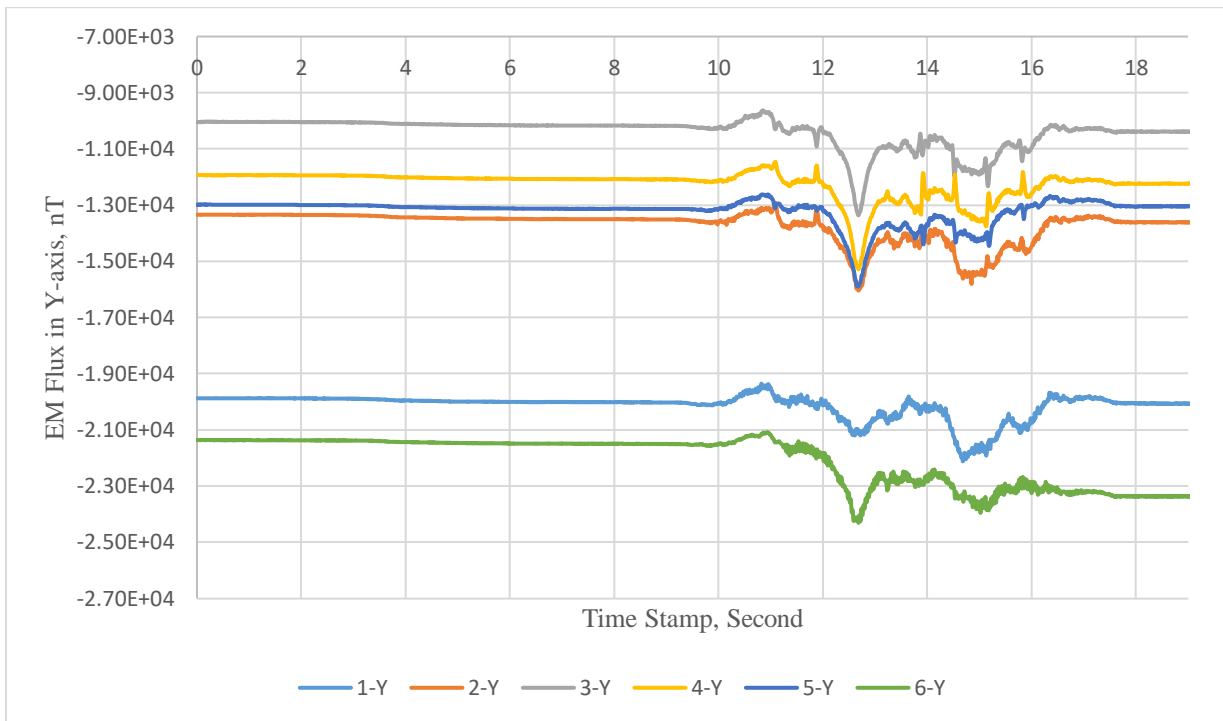**Figure 111. Graph. Raw EM flux signals for sensors in X-axis (Case #1).**
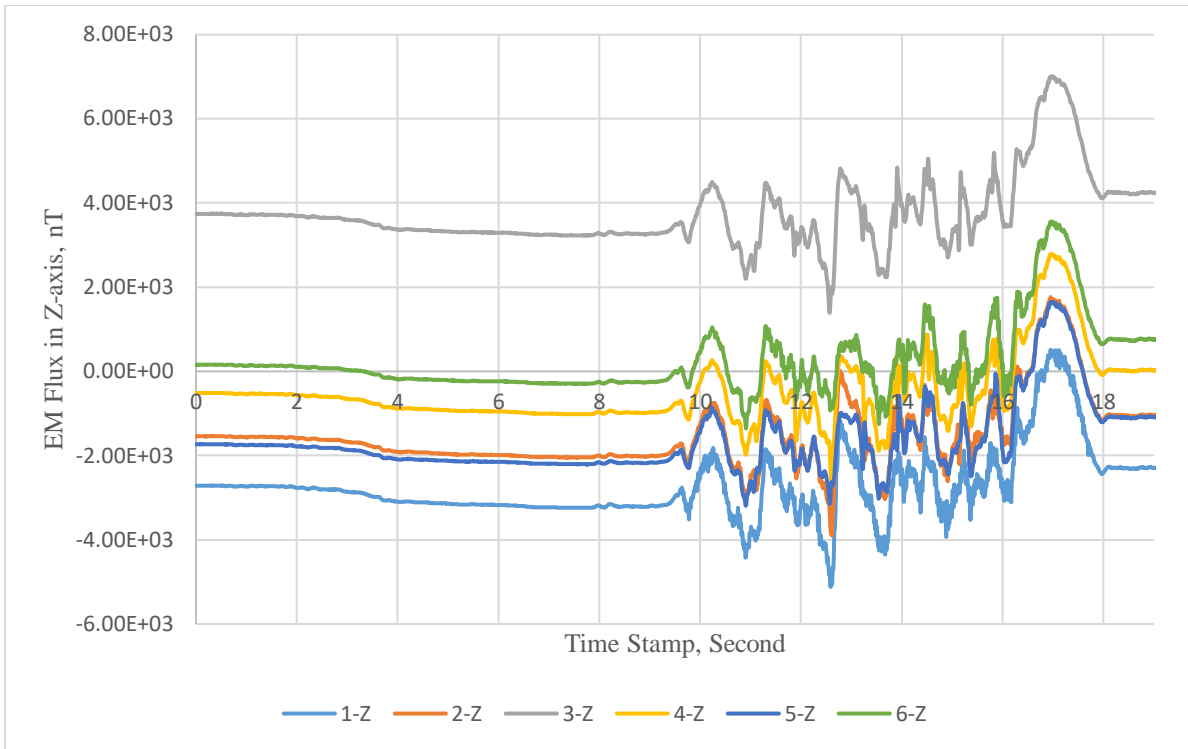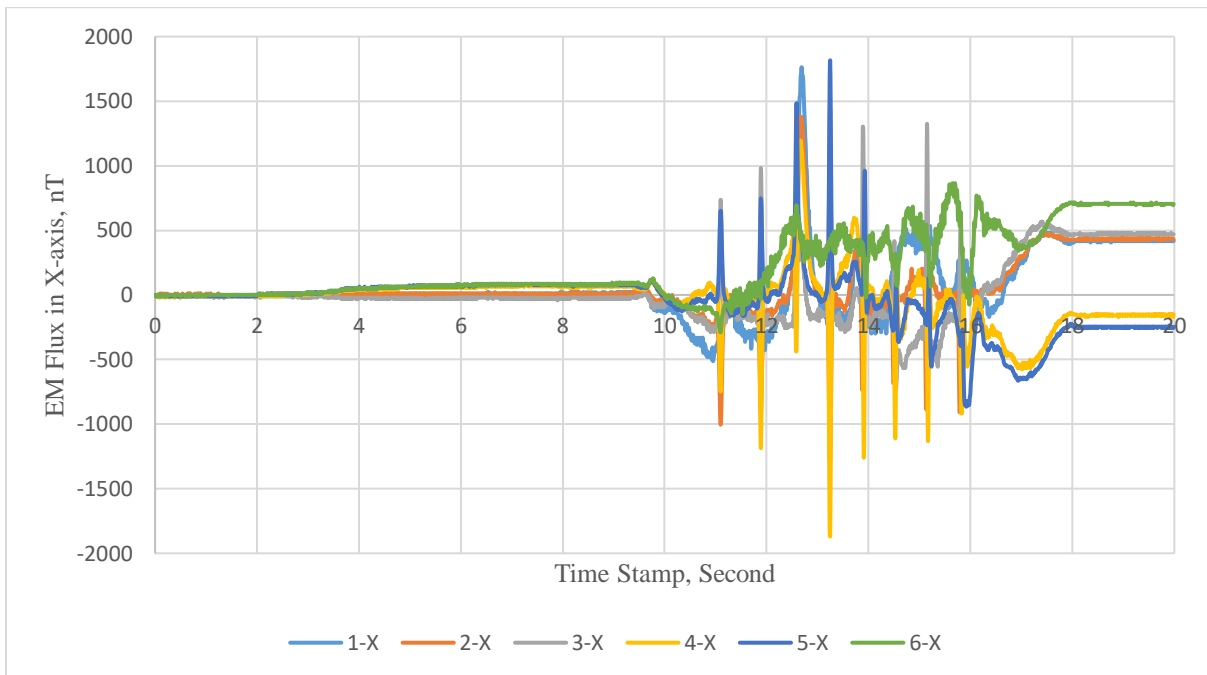

Figure 112. Graph. Raw EM flux signals for sensors in Y-axis (Case #1).
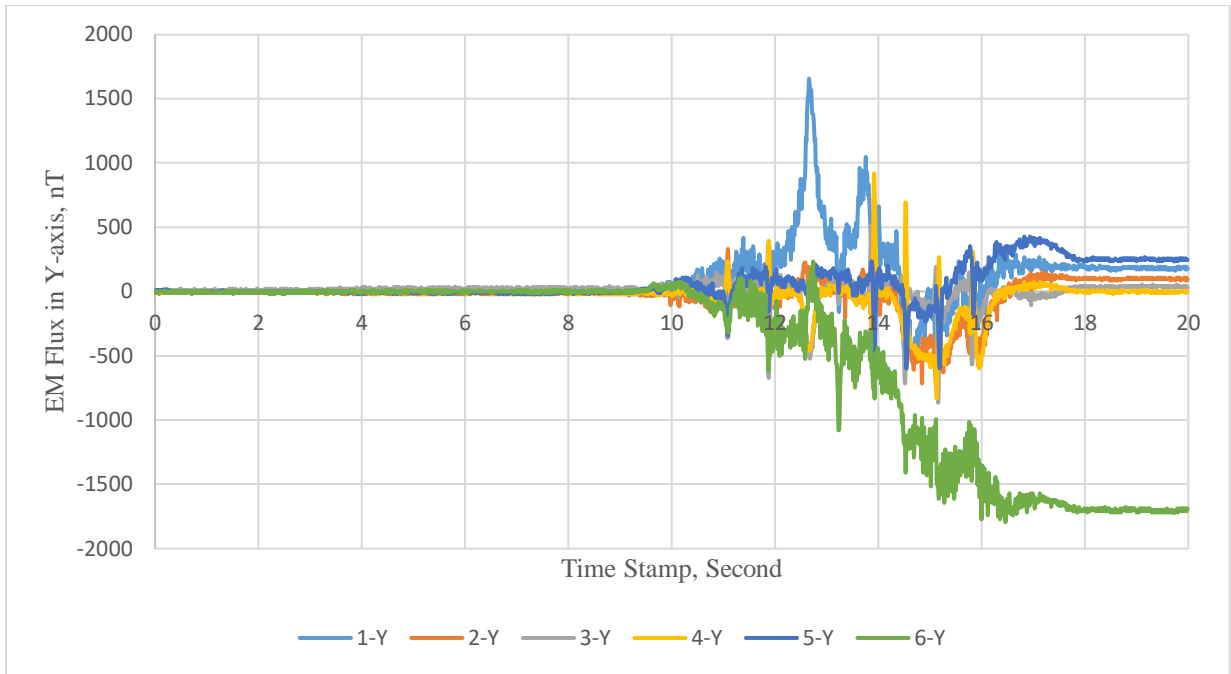
Figure 113. Graph. Raw EM flux signals for sensors in Z-axis (Case #1).

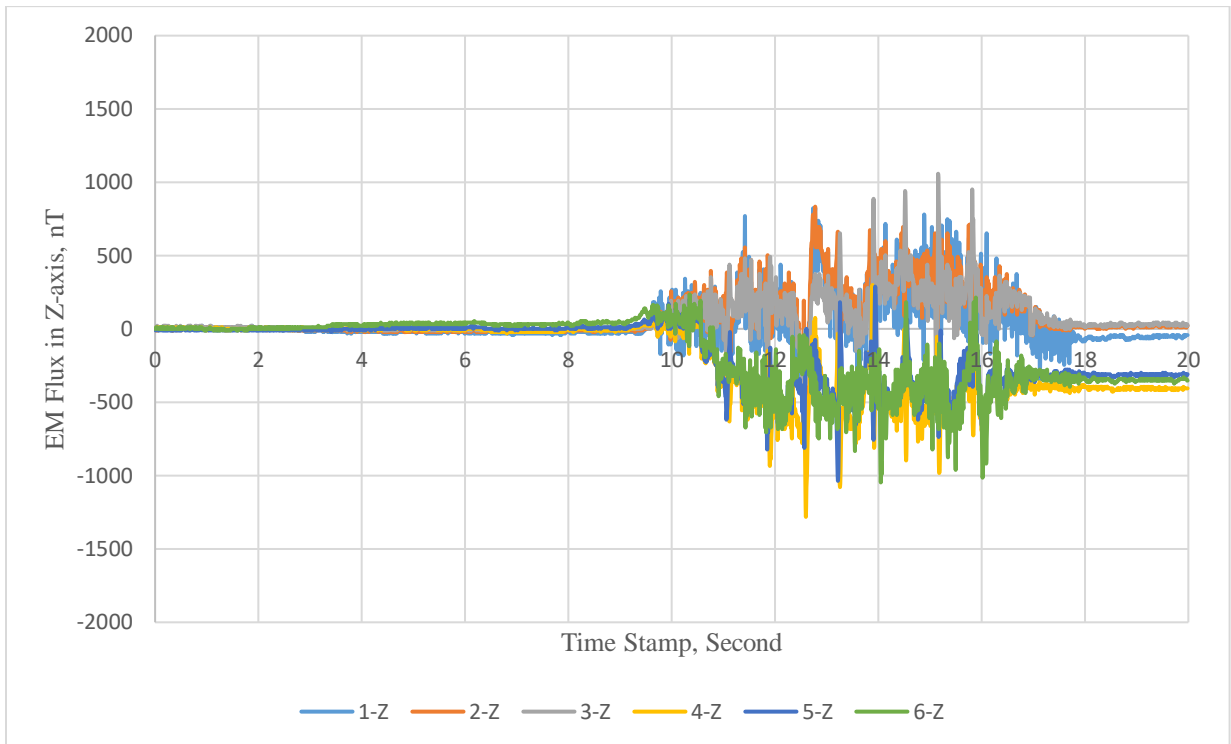## Referenced EM Flux Signal after Initializing Initial Reading Value at Zero and Gradiometer Processing

Figure 114. Graph. Referenced EM Flux Signal after initializing initial reading value at zero and gradiometer processing for sensors in X-axis (Case #1).
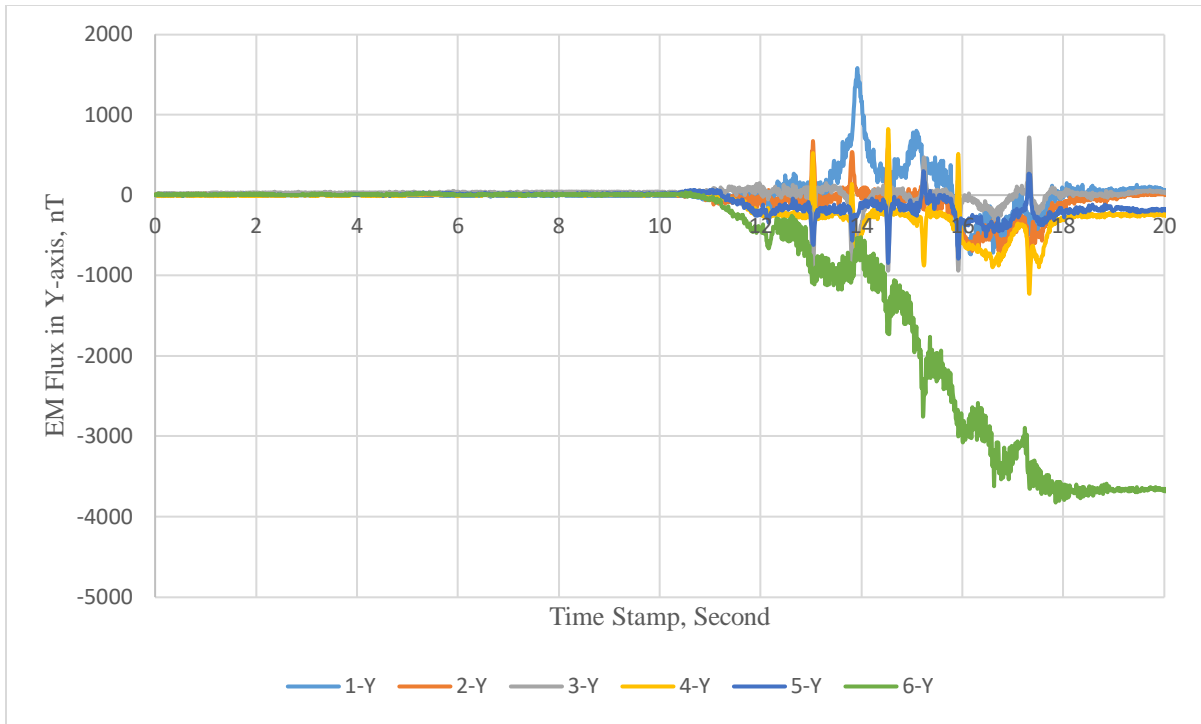
Figure 115. Graph. Referenced EM Flux Signal after initializing initial reading value at zero and gradiometer processing for sensors in Y-axis (Case #1).
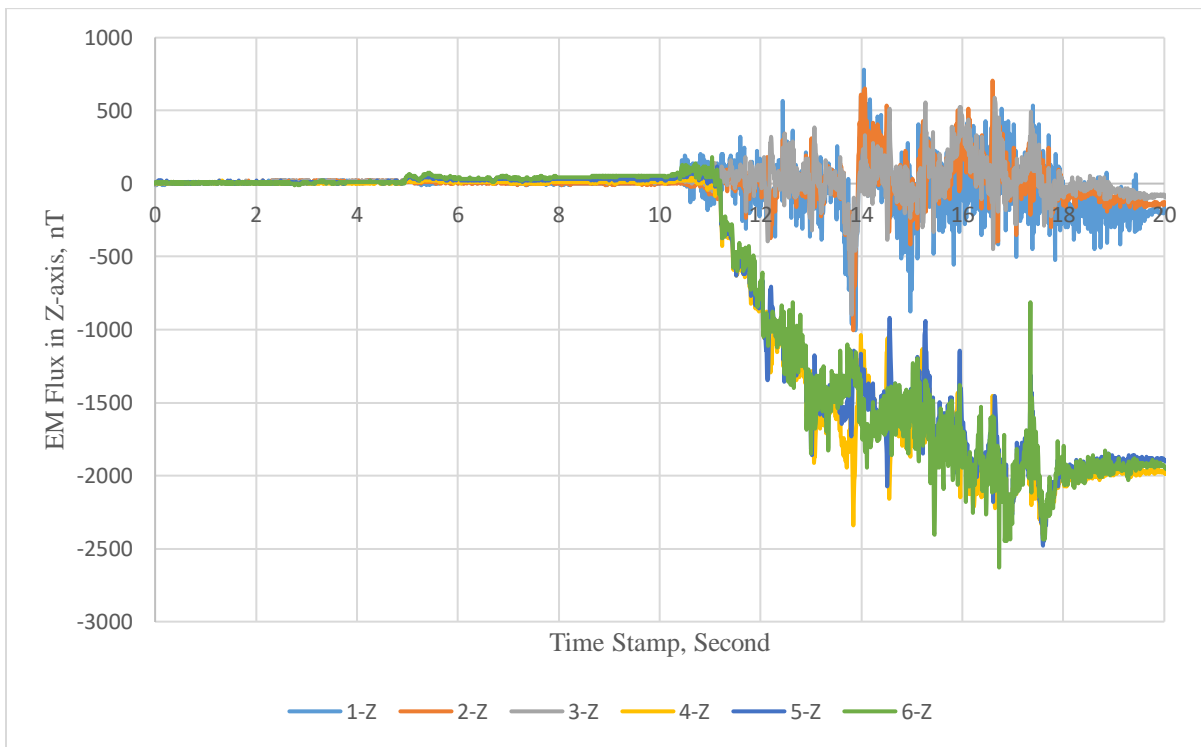
Figure 116. Graph. Referenced EM Flux Signal after initializing initial reading value at zero and gradiometer processing for sensors in Z-axis (Case #1).
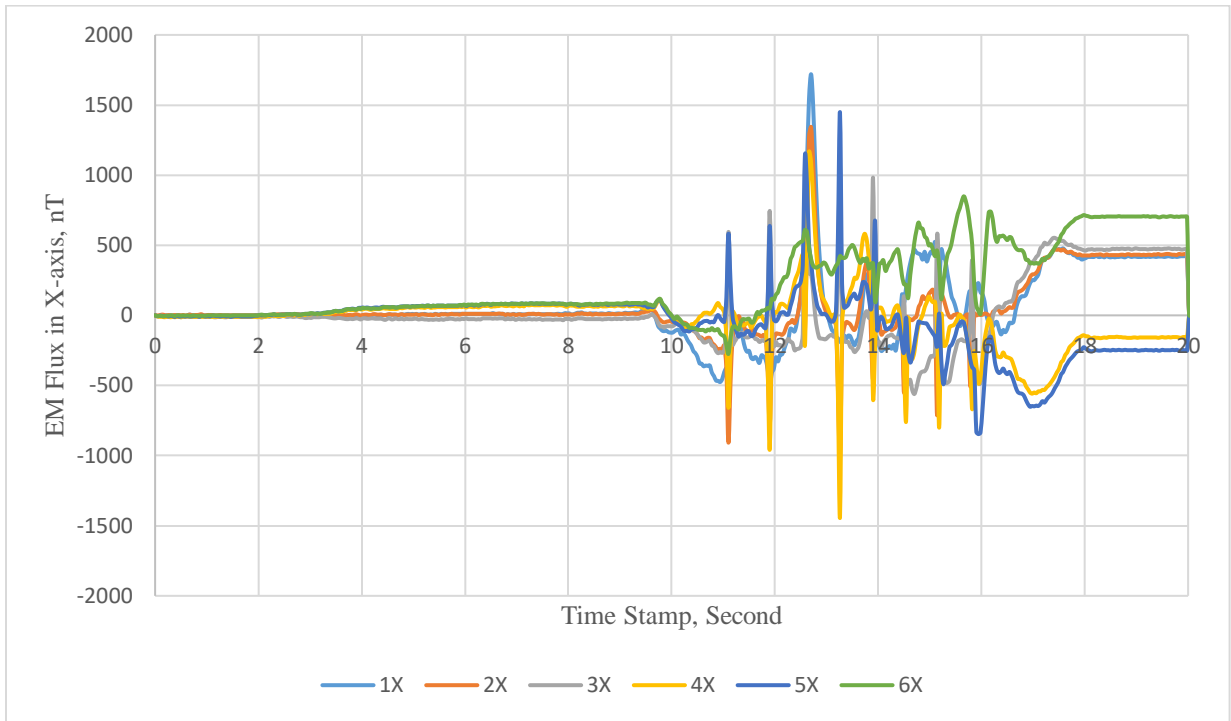
High-Frequency Filtered EM Flux
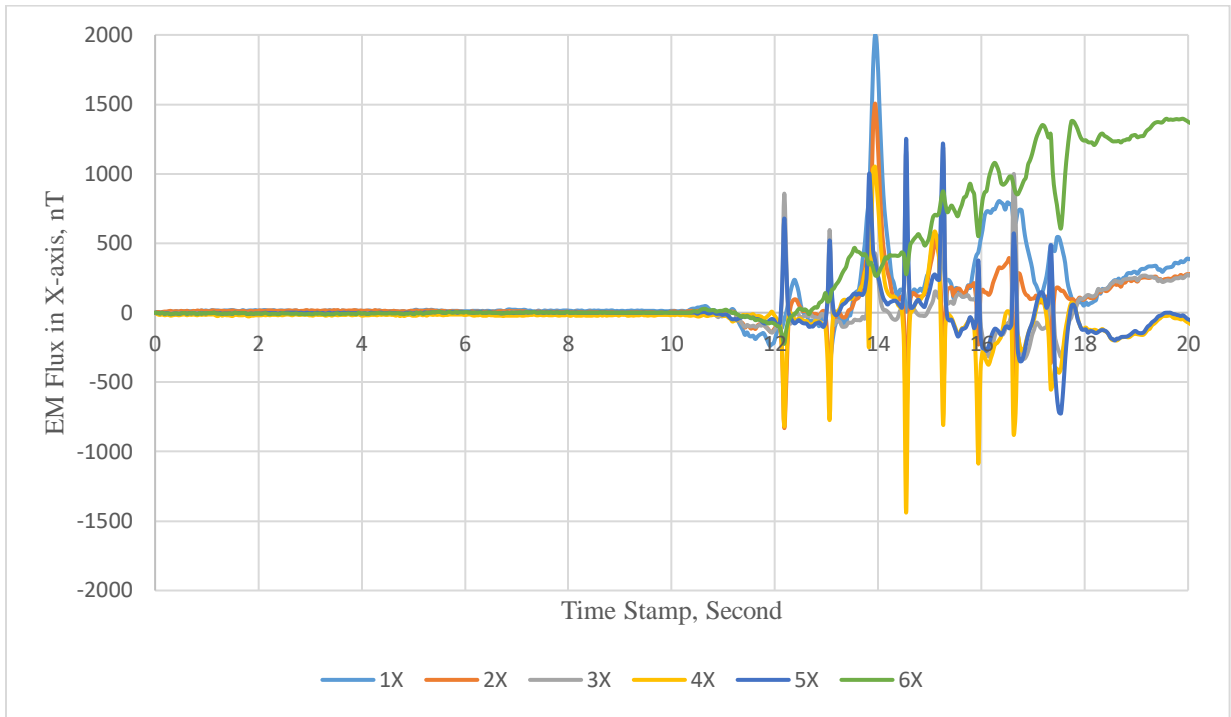
Figure 117. Graph. High-frequency filtered EM flux for sensors in X-axis (Case #1).
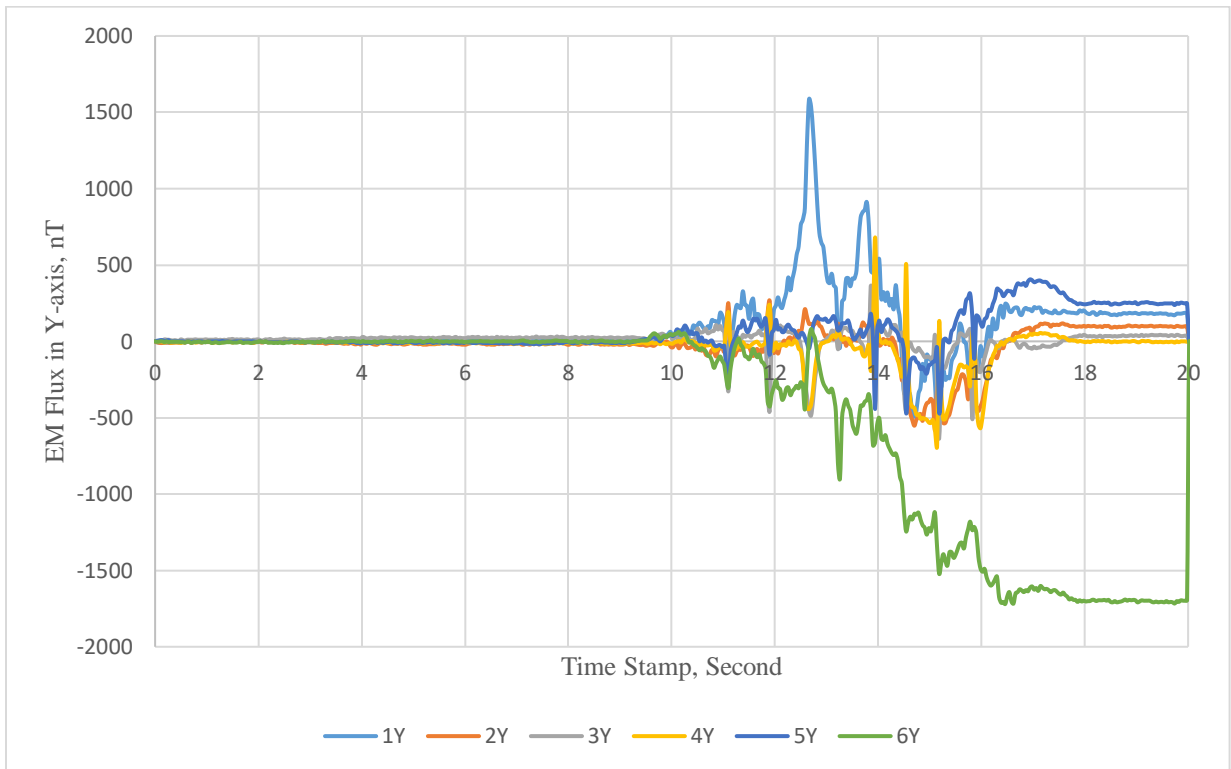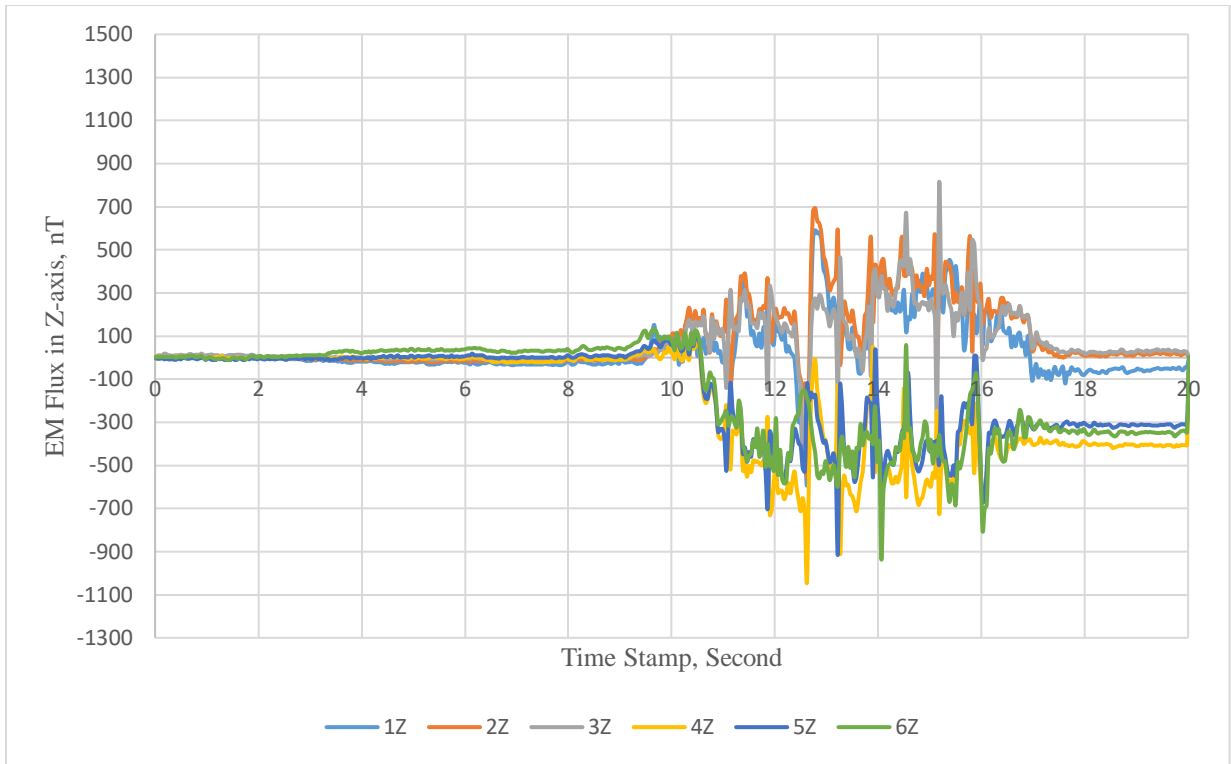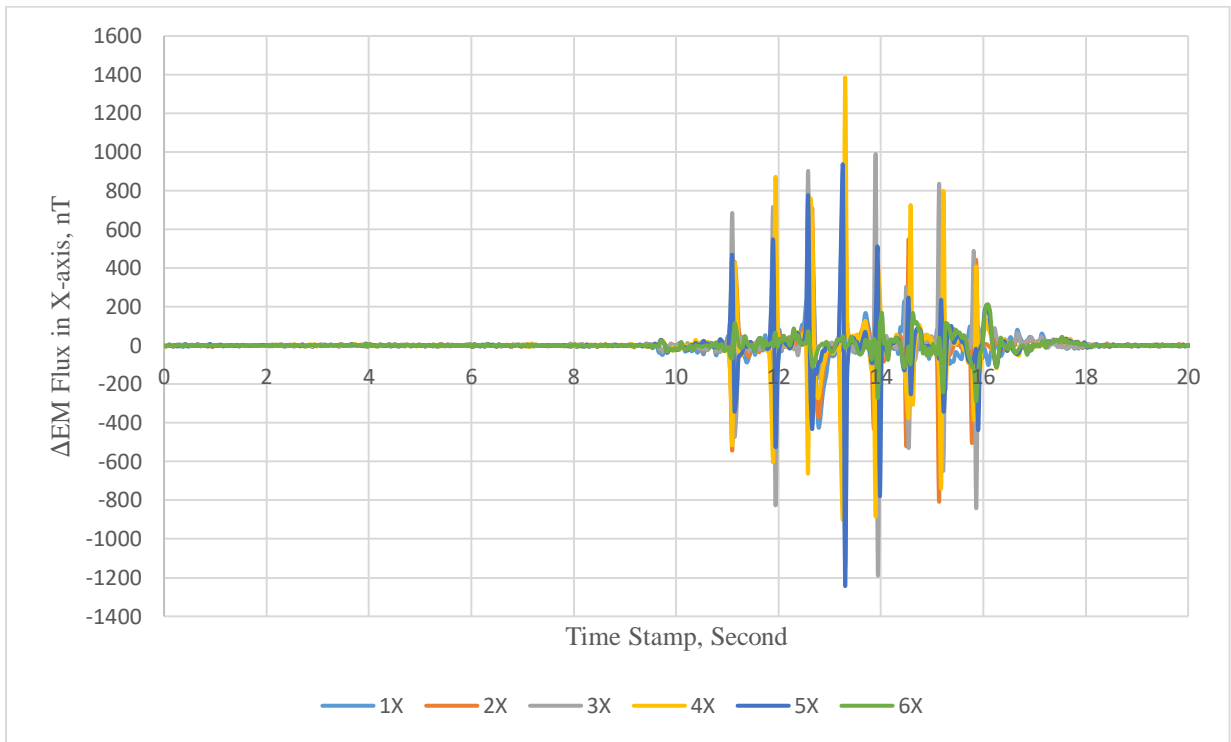

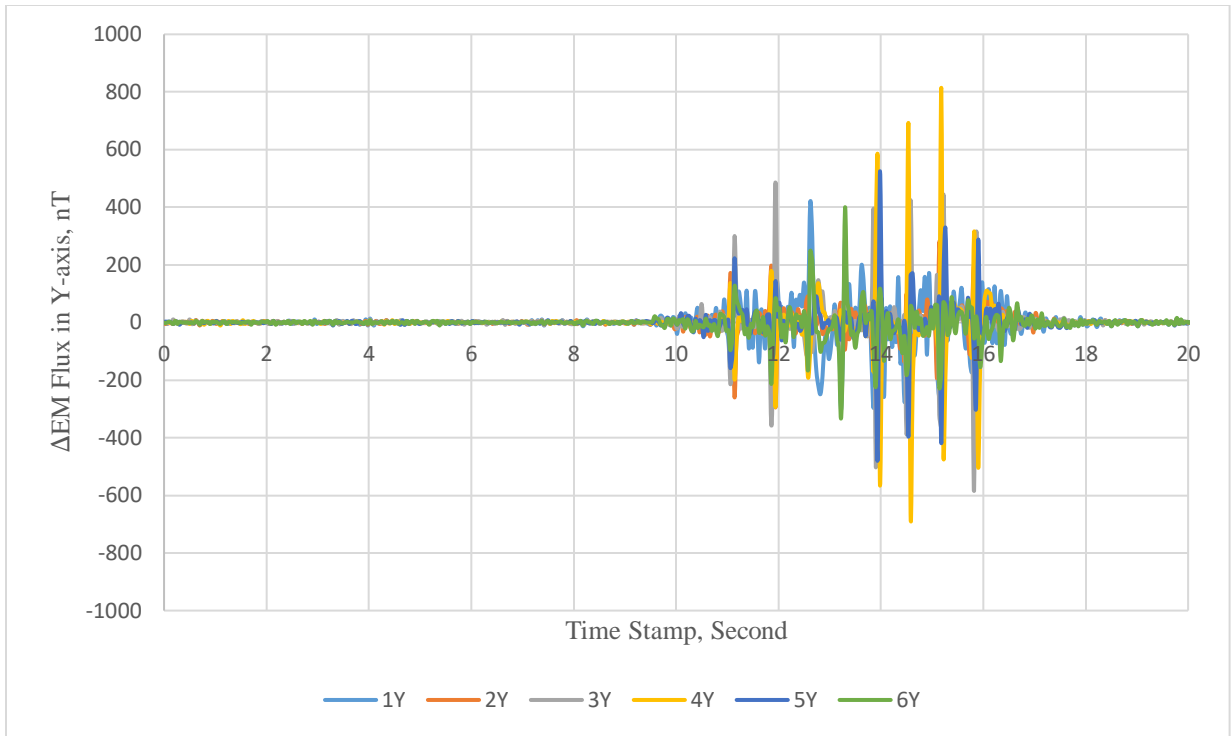Figure 118. Graph. High-frequency filtered EM flux for sensors in Y-axis (Case #1).

Figure 119. Graph. High-frequency filtered EM flux for sensors in Z-axis (Case #1).

Low- and High-Frequency Filtered EM Flux

Figure 120. Graph. Low- and high-frequency filtered ∆EM flux for sensors in X-axis (Case #1).
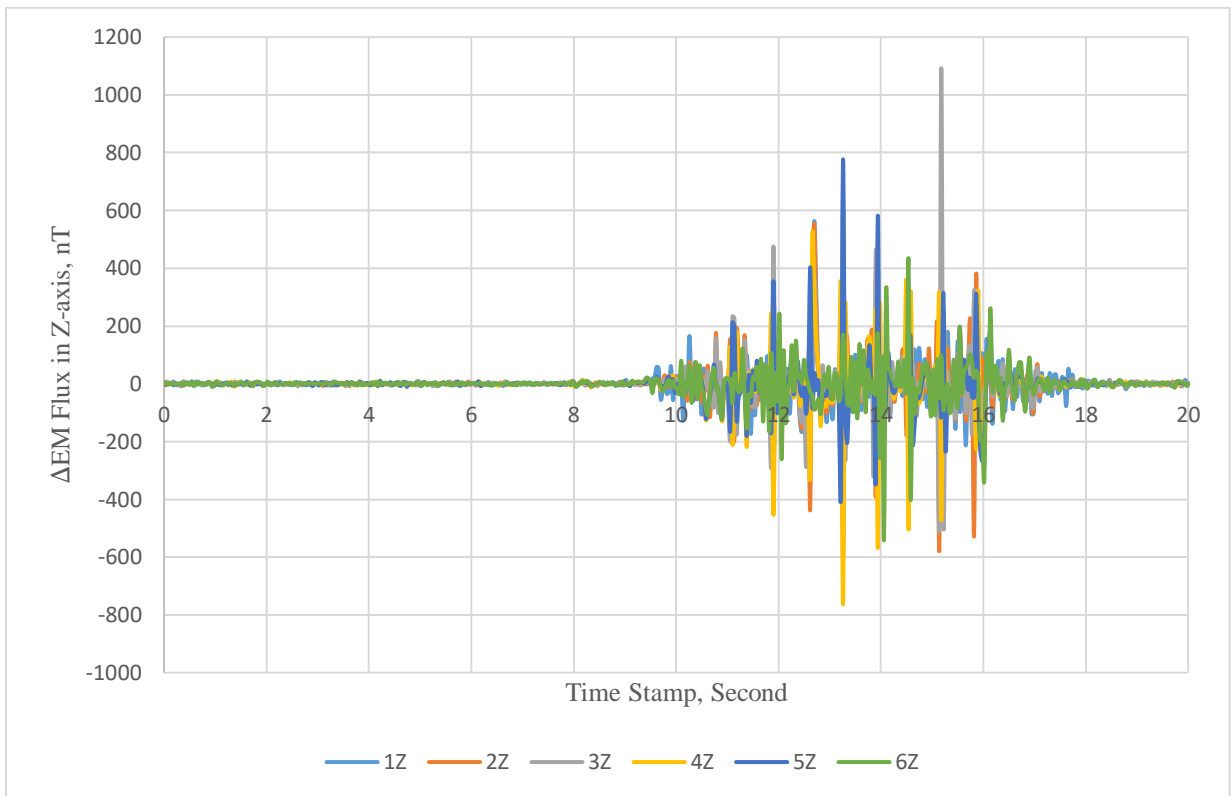
Figure 121. Graph. Low- and high-frequency filtered ΔEM flux for sensors in Y-axis (Case #1).

Figure 122. Graph. Low- and high-frequency filtered ΔEM flux for sensors in Z-axis (Case #1).

CASE #2

Raw EM Flux

Figure 123. Graph. Raw EM flux signals for sensors in X-axis (Case #2).

Figure 124. Graph. Raw EM flux signals for sensors in Y-axis (Case #2).

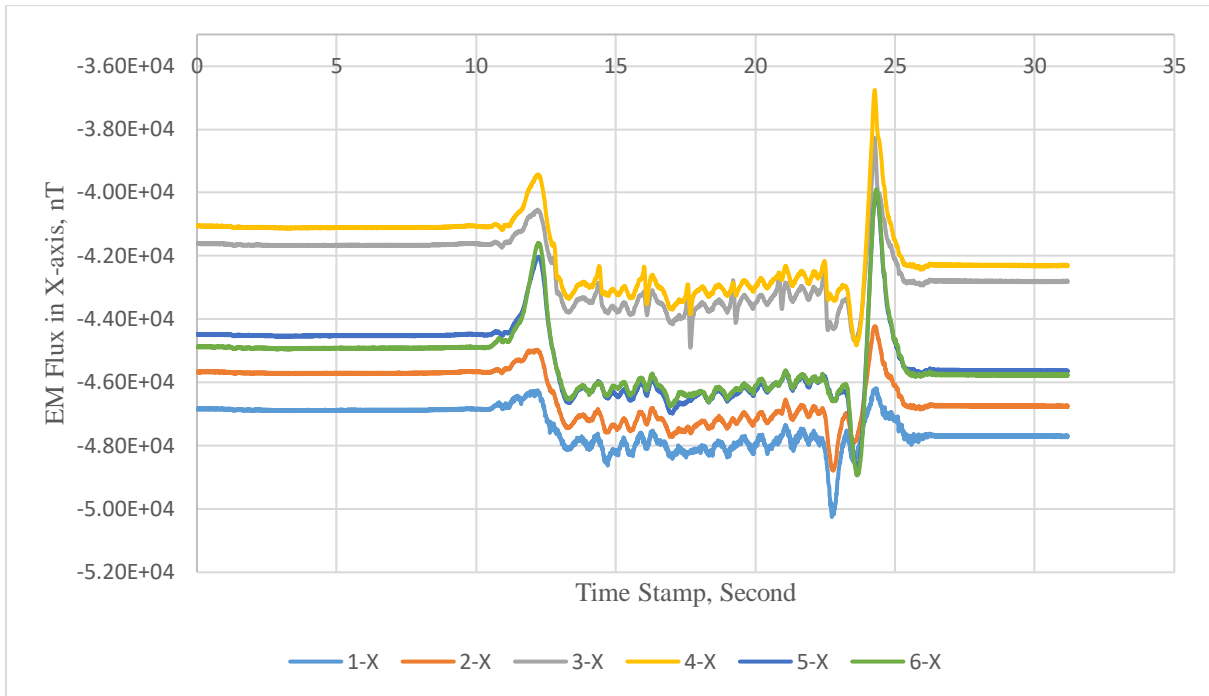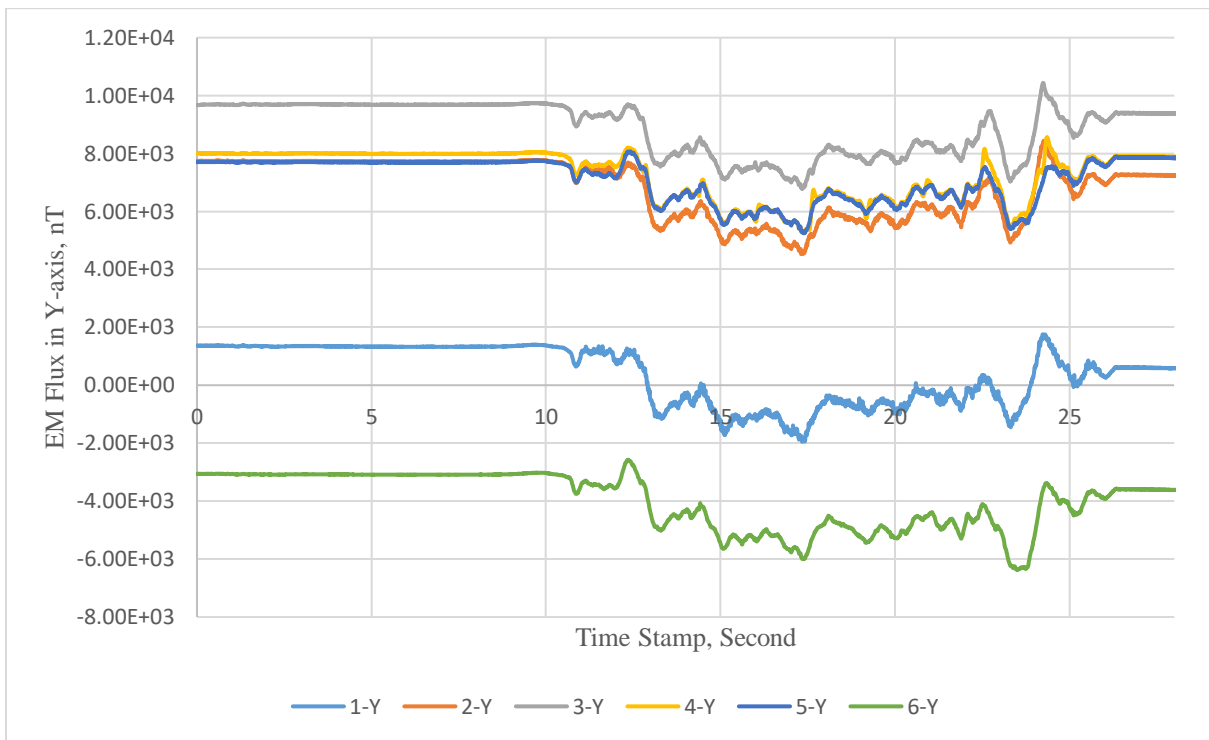**Figure 125. Graph. Raw EM flux signals for sensors in Z-axis (Case #2).**

Referenced EM Flux Signal after Initializing Initial Reading Value at Zero and Gradiometer Processing

Figure 126. Graph. Referenced EM Flux Signal after initializing initial reading value at zero and gradiometer processing for sensors in X-axis (Case #2).

Figure 127. Graph. Referenced EM Flux Signal after initializing initial reading value at zero and gradiometer processing for sensors in Y-axis (Case #2).

Figure 128. Graph. Referenced EM Flux Signal after initializing initial reading value at zero and gradiometer processing for sensors in Z-axis (Case #2).

High-Frequency Filtered EM Flux

Figure 129. Graph. High-frequency filtered EM flux for sensors in X-axis (Case #2).

Figure 130. Graph. High-frequency filtered EM flux for sensors in Y-axis (Case #2).

Figure 131. Graph. High-frequency filtered EM flux for sensors in Z-axis (Case #2).

Low- and High-Frequency Filtered EM Flux

Figure 132. Graph. Low- and high-frequency filtered ΔEM flux for sensors in X-axis (Case #2).

Figure 133. Graph. Low- and high-frequency filtered ΔEM flux for sensors in Y-axis (Case #2).

Figure 134. Graph. Low- and high-frequency filtered ΔEM flux for sensors in Z-axis (Case #2).

CASE #3

Raw EM Flux

Figure 135. Graph. Raw EM flux signals for sensors in X-axis (Case #3).

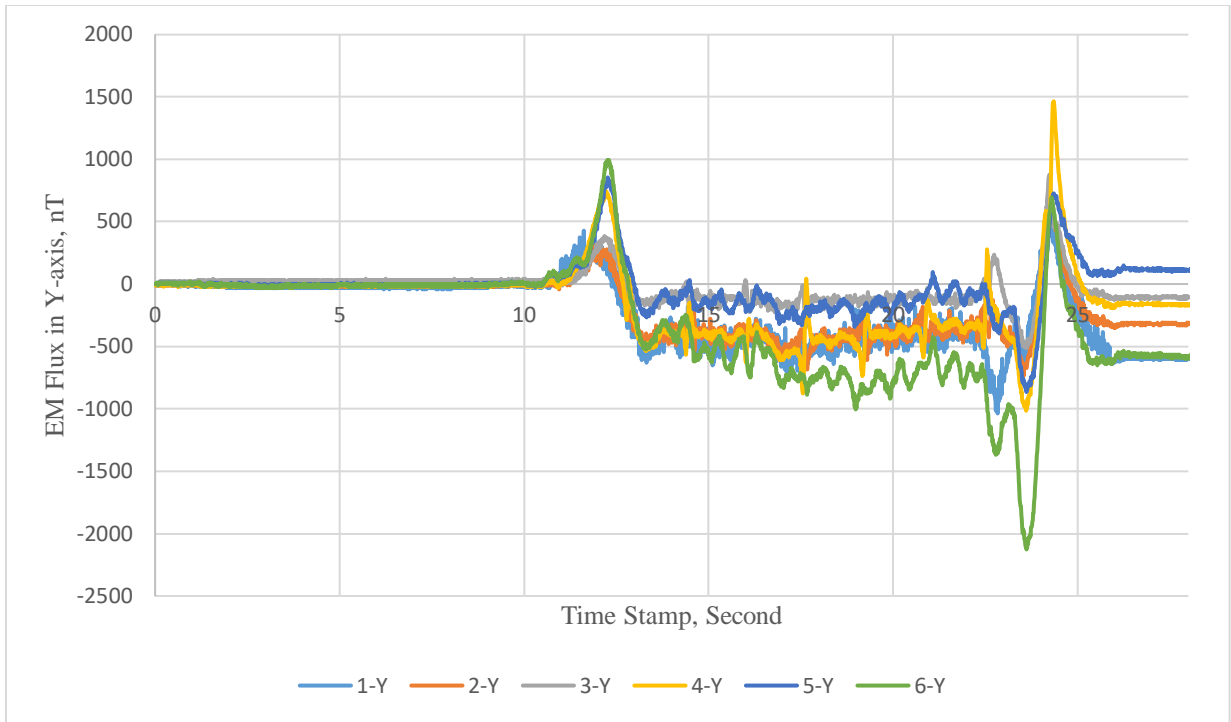**Figure 136. Graph. Raw EM flux signals for sensors in Y-axis (Case #3).**
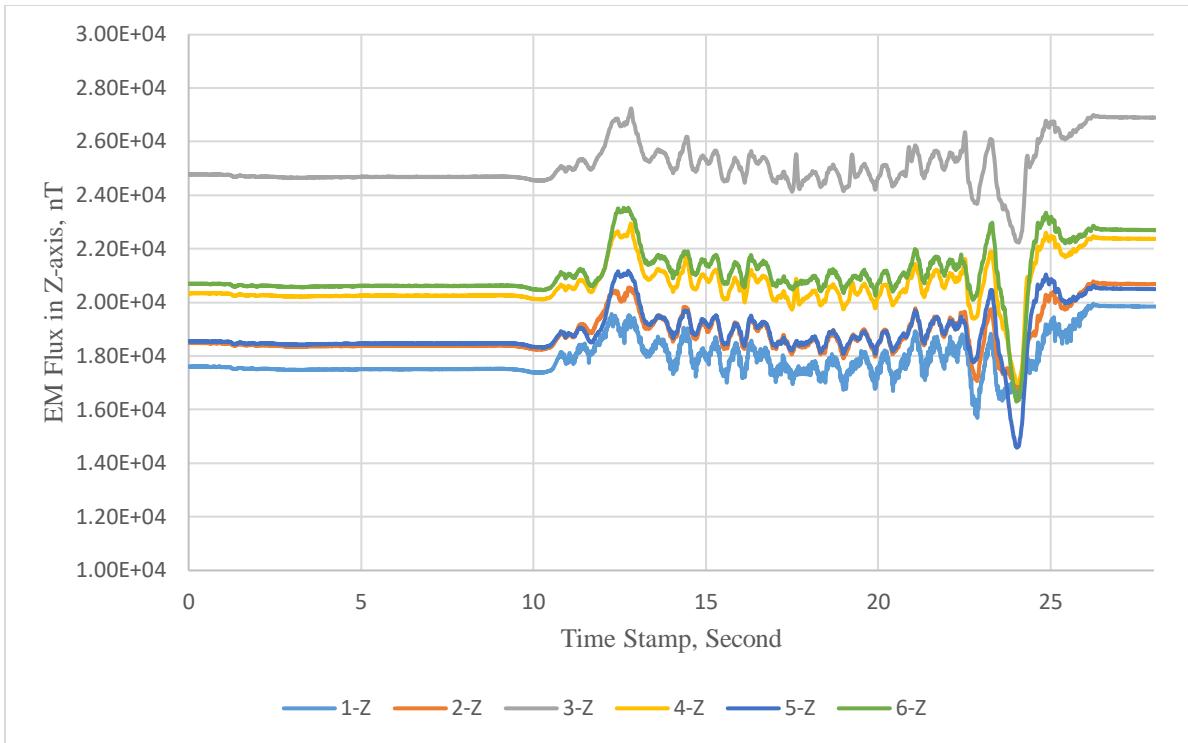
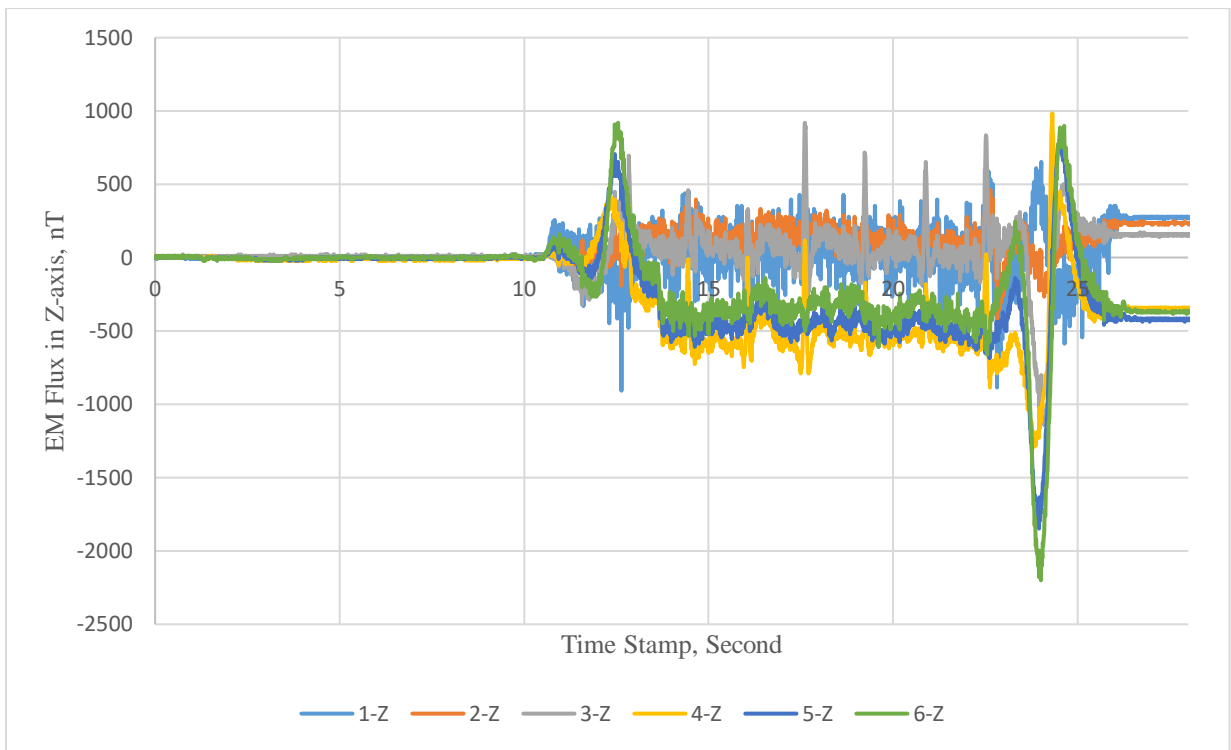**Figure 137. Graph. Raw EM flux signals for sensors in Z-axis (Case #3).**

Referenced EM Flux Signal after Initializing Initial Reading Value at Zero and Gradiometer Processing
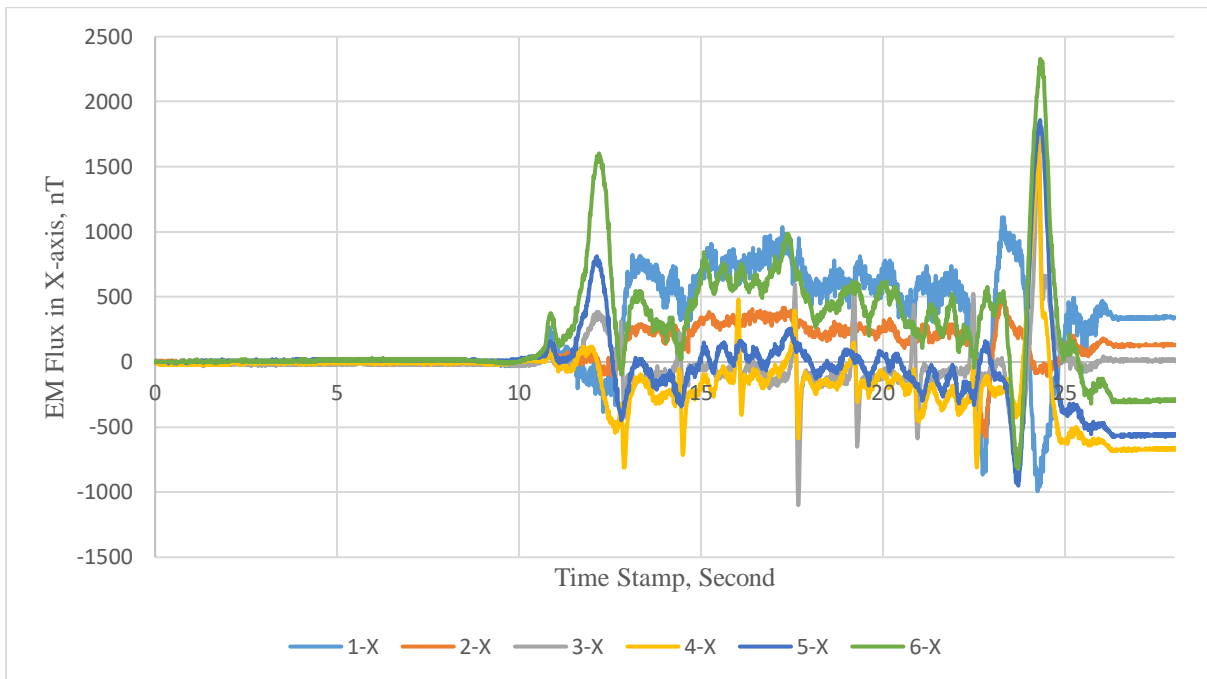
Figure 138. Graph. Referenced EM flux signal after initializing initial reading value at zero and gradiometer processing for sensors in X-axis (Case #3).

Figure 139. Graph. Referenced EM flux signal after initializing initial reading value at zero and gradiometer processing for sensors in Y-axis (Case #3).

Figure 140. Graph. Referenced EM flux signal after initializing initial reading value at zero and gradiometer processing for sensors in Z-axis (Case #3).
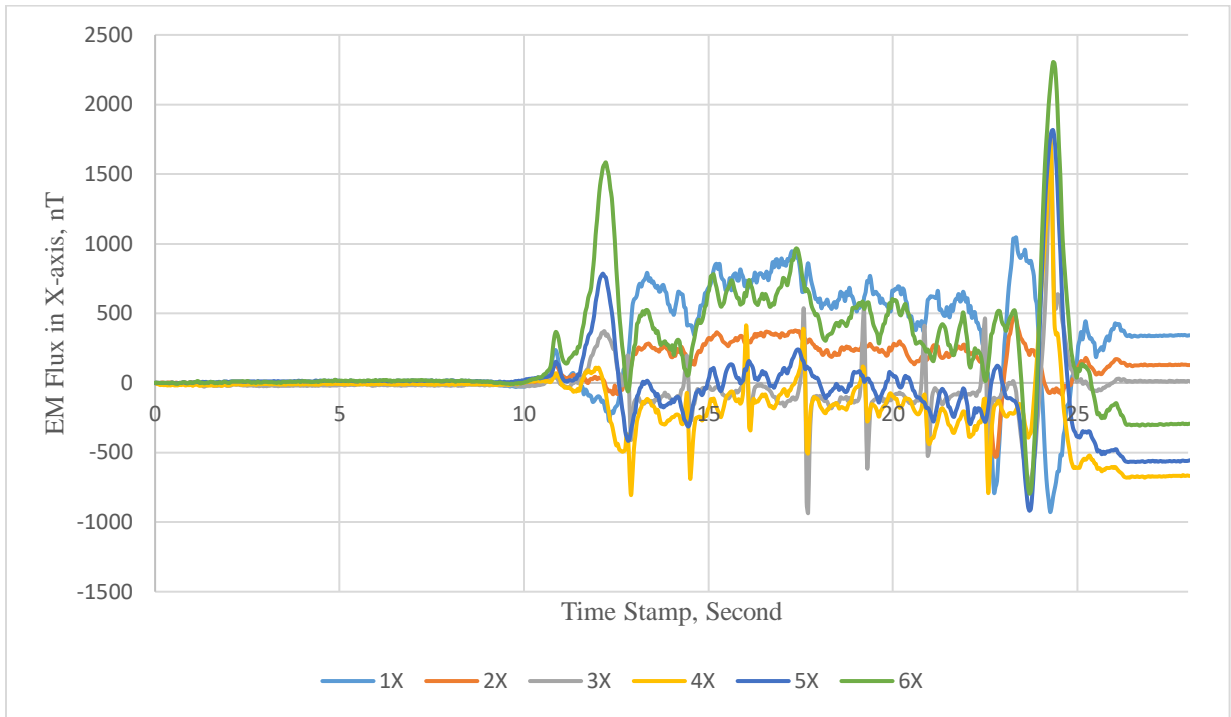
High-Frequency Filtered EM Flux

Figure 141. Graph. High-frequency filtered EM flux for sensors in X-axis (Case #3).
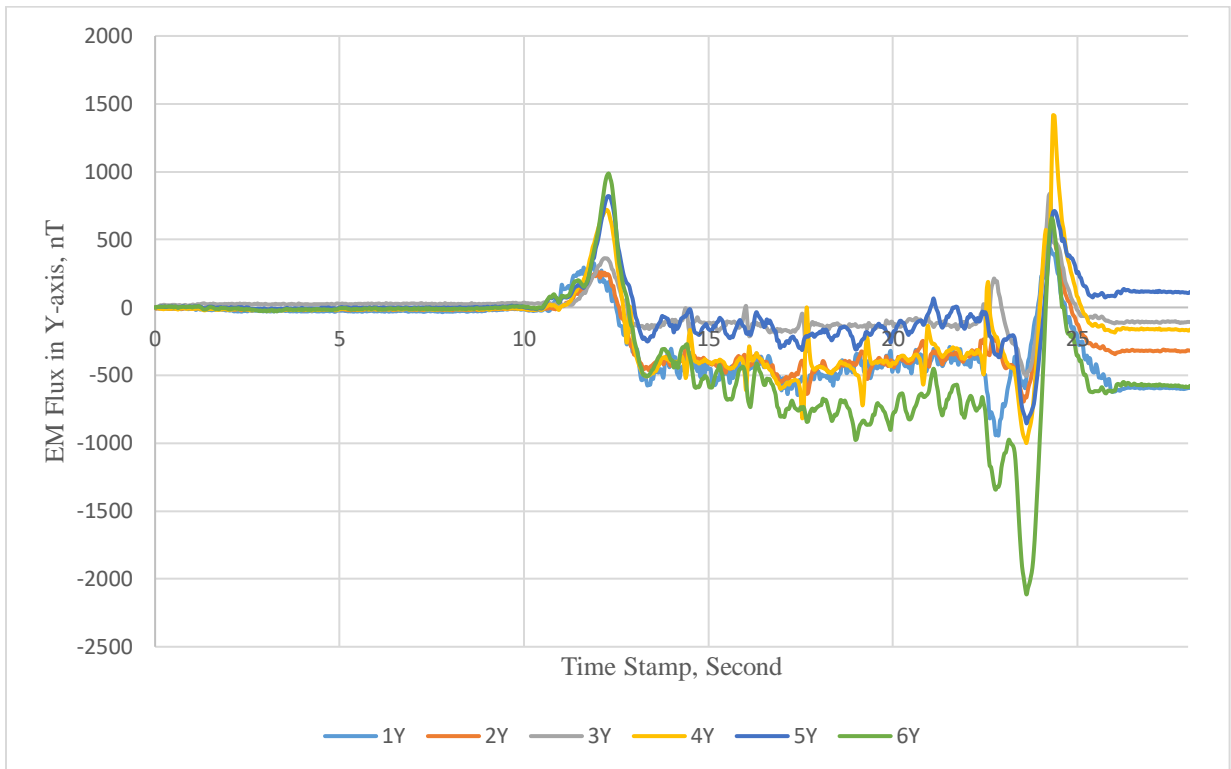

Figure 142. Graph. High-frequency filtered EM Flux for sensors in Y-axis (Case #3).
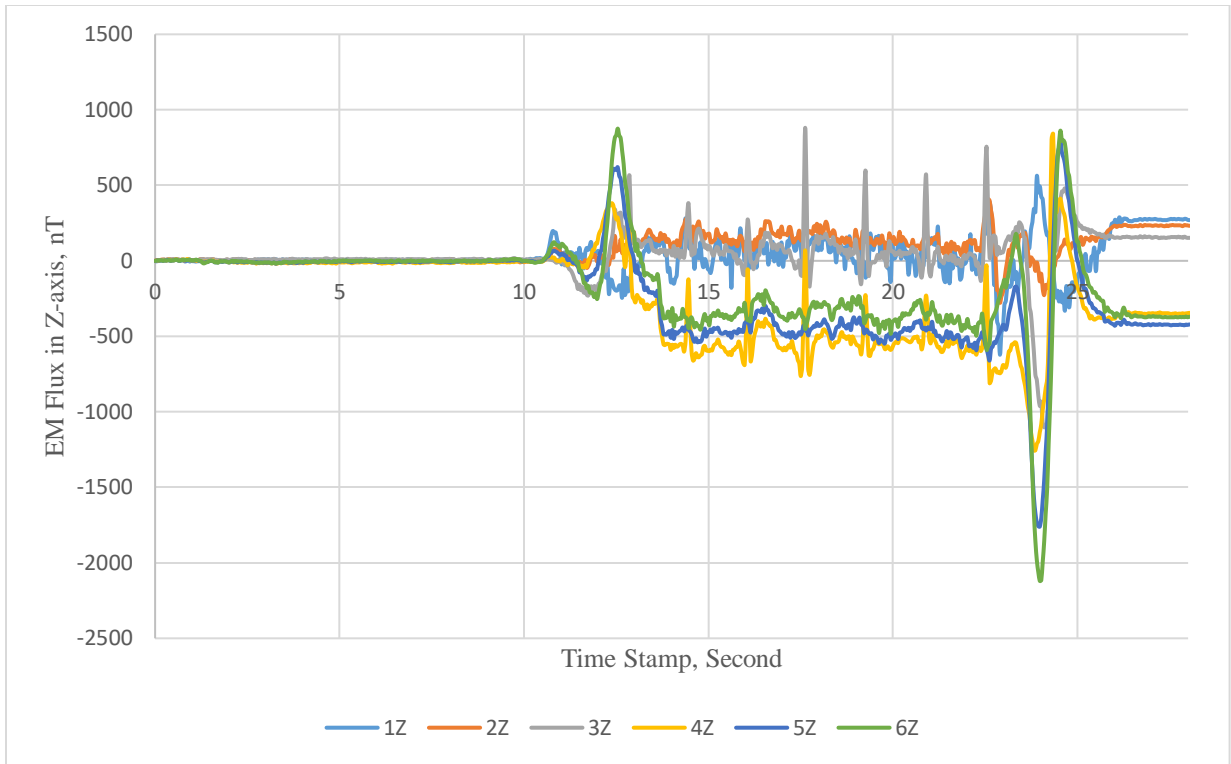
Figure 143. Graph. High-frequency filtered EM flux for sensors in Z-axis (Case #3).
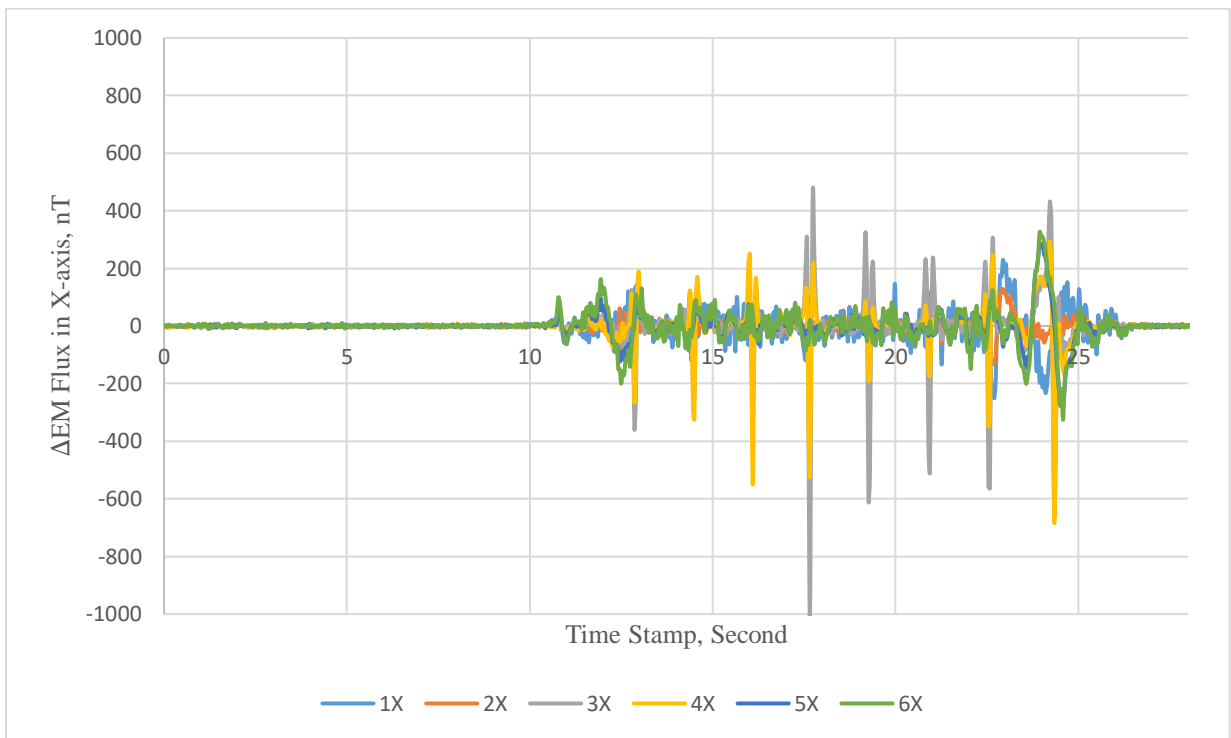
Low- and High-Frequency Filtered EM Flux

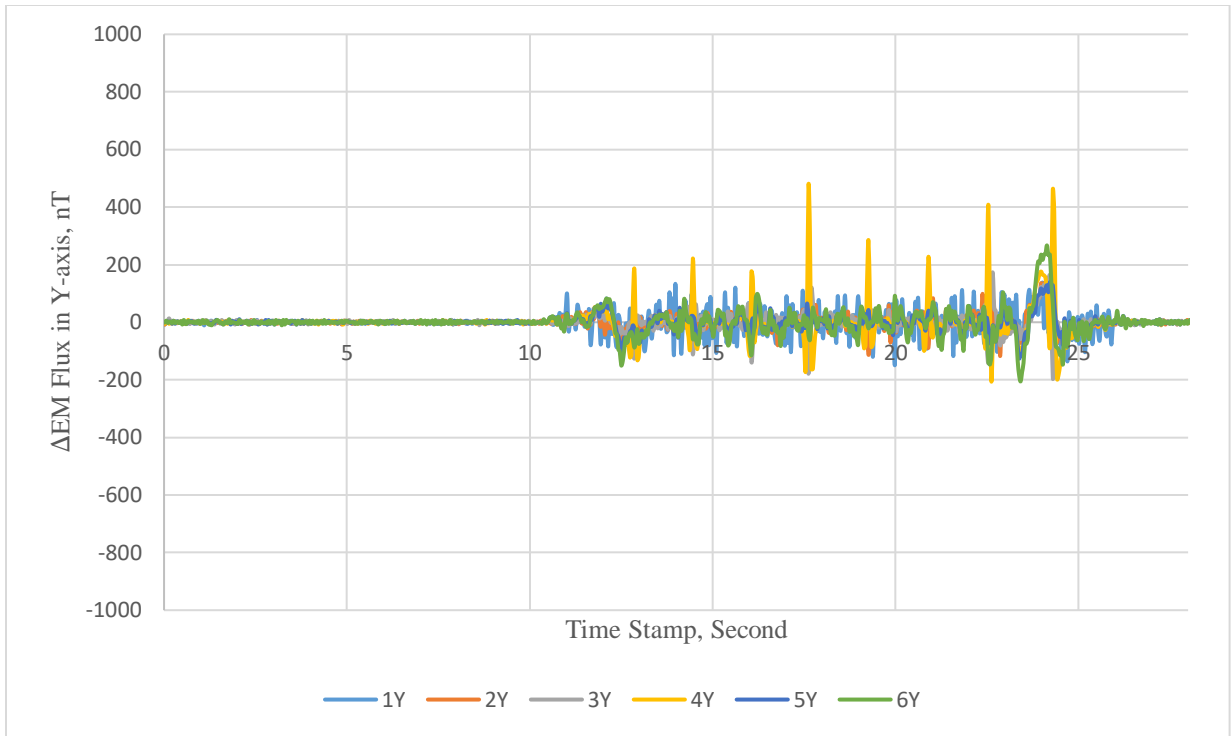**Figure 144. Graph. Low- and high-frequency filtered ∆EM flux for sensors in X-axis (Case #3).**

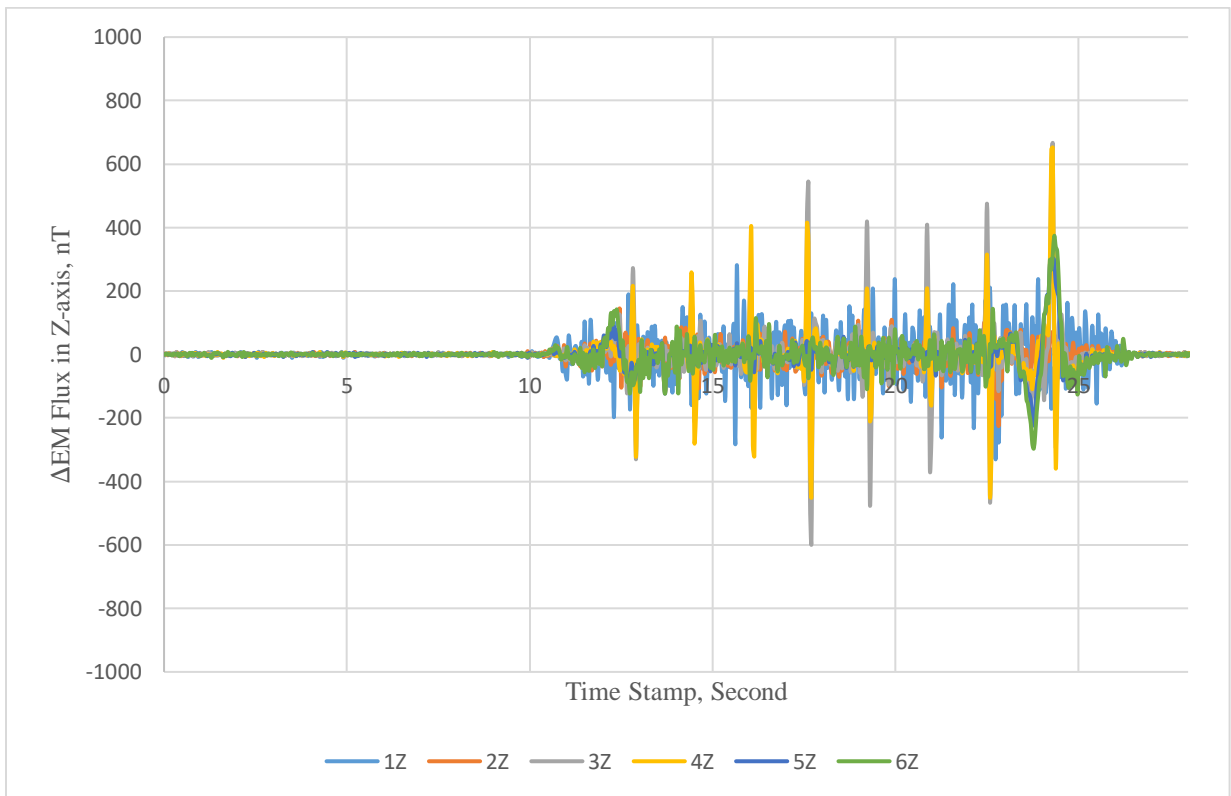**Figure 145. Graph. Low- and high-frequency filtered ΔEM flux for sensors in Y-axis (Case #3).**

Figure 146. Graph. Low- and high-frequency filtered ΔEM flux for sensors in Z-axis (Case #3).